Numerical Simulation of 3-Dimensional Flow in Straight and Curved Ducts of Rectangular Cross Section

Gervang, Bo Groht; Larsen, Poul Scheel

Publication date:
1989

Document Version
Publisher's PDF, also known as Version of record

AFM 89–09
ISSN 0590-8809

November 1989

NUMERICAL SIMULATION OF 3–DIMENSIONAL FLOW IN STRAIGHT AND CURVED DUCTS OF RECTANGULAR CROSS SECTION

BO GERVANG

DEPARTMENT OF FLUID MECHANICS

TECHNICAL UNIVERSITY OF DENMARK

Trykkeår 1990
Afdelingen for Fluid Mekanik,
Bygning 404, DTH
DK–2800 Lyngby

PREFACE

This dissertation is submitted in partial fulfilment of the requirements for the Danish licentiate (Ph.D.) degree. The dissertation is based on theoretical work carried out during the period February 1987 to October 1989 at the Department of Fluid Mechanics, The Technical University of Denmark.

The candidate wishes to express his sincere gratitude to his director of studies, Professor P. Scheel Larsen, Ph.D. for supervision, advice and encouragement throughout the period of research and during the preparation of this dissertation.

Thanks are also due to Professor A.D. Gosman, Ph.D. for supervision during a 10 weeks stay at Imperial College, London, providing the Department with the computer code ROBOT. This visit was made possible through a research grant (16–4226.M) from the Danish Technical Research Council (STVF). Thanks are also due to lektor A. Vincent Barker, M.Sc. for fruitful discussion on the topic of numerical analysis. I want also to thank all my colleaques at the Department for their cooperation and assistance. I am indepted to Mogens Krighaar and Niels Finderup Nielsen for their kind assistance in preparing some figures.

Finally, I would like to give a special thank to the Danish Sugar Corporation, DDS, for their encouragement and invaluable financial support during the last part of the work.

October 1989
Bo Gervang

ABSTRACT

The velocity field in straight and curved ducts of Newtonian and Non–Newtonian fluids is investigated numerically in order to determine the secondary flow descending either from curvature effects and/or from non–linear rheology. Physical phenomena inherent to duct flows are frictional pressure drop, heat transfer, mass transfer, and mixing rates. These phenomena may largely be changed by the presence of secondary flow which is a part of the present study considering only laminar flow. The investigated ducts have cross section geometry of 4×4 mm, 3×5.33 mm, 2×8 mm, and 1×16 mm with the width being equal to or greater than the height. This gives aspect ratios from 1 to 16.

The fluid dynamic model incorporates the finite volume method combined with an orthogonal curvilinear coordinate formulation of the governing equations in semi–strong conservative form. The velocity–pressure coupling is based on the PISO method in which an ADI solver is used to solve the momentum equations and a preconditioning conjugate gradient method is used to solve the pressure–corrector equations.

The influence of secondary flow on the primary flow in a curved duct with water is seen to depend on the Reynolds number. At low Reynolds numbers the highest value of the primary flow is situated near the inner wall whereas it is situated near the outer the wall at high Reynolds numbers.

Modeling 2% viscarin in a straight duct with the CEF–equation two vortices in each quadrant are observed for unity and moderate aspect ratio whereas 3 vortices are observed for the aspect ratio 16. The direction of the streamlines are only changed by changing the sign on the second normal stress coefficient.

The effect of secondary flow on pressure drop was not observed through measurements. Calculations showed a significant difference on the pressure drop using the powerlaw model and the CEF–equation at high velocities where the CEF–equation gave higher pressure drop.

ABSTRAKT (in Danish)

Hastighedsfeltet i lige og krumme kanaler er undersøgt numerisk for Newtonske og ikke–Newtonske fluider med henblik på større information om sekundærstrømninger stammende fra enten krumningseffekter og/eller ikke–lineær rheologi. Fysiske fænomener relateret til kanalstrømninger er friktions tab, varme– og massetransport og blandings rater. Disse fænomener kan ændres betragteligt ved tilstedeværelse af sekundærstrømninger, hvor kun sekundærstrømning ved laminære strømninger er undersøgt. De undersøgte kanaler har et tværsnitsareal på $16 \cdot 10^{-6}$ m^2 med dimensioner for højde og bredde på henholdsvis 4×4 mm, 3×5.33 mm, 2×8 mm og 1×16 mm, hvilket giver et sideforhold spændende fra 1 til 16.

En finit volumen model kombineret med en ortogonal kurvelineær koordinat formulering af de styrende ligninger på semi–stærk konservativ form er benyttet. Tryk–hastigheds koblingen er baseret på PISO–algoritmen, hvor en ADI ligningsløser er benyttet til løsning af bevægelsesmomentligningerne, og en prækonditioneret konjugeret gradient metode er brugt til løsning af trykkorrektionsligningerne. Indflydelsen af sekundærstrømning på primærstrømningen i krumme kanaler med vand afhænger af Reynolds tallet. Viskos domineret strømning (lave Reynolds tal) giver de største hastigheder nærmest indervæggen, mens inerti domineret (høje Reynolds tal) giver de største hastigheder nærmest ydervæggen.

Med brug af CEF–ligningen til modellering af 2% viscarin i lige kanaler blev 2 hvivler observeret i hvert kvadrant af tværsnittet ved små sideforhold. Ved sideforholdet 16 blev 3 hvivler observeret i hvert kvadrant givende 12 hvivler i hele tværsnittet. Retningen af strømlinierne afhænger udelukkende af fortegnet på anden normal spændingskoefficient.

Sekundærstrømningens indflydelse på tryktabet er ikke observeret ud fra målinger. Dette er derimod for høje hastigheder observeret ud fra numeriske beregninger. CEF–ligningen, der giver sekundærstrømning, giver et højere tryktab end powerlaw modellen, der ikke giver sekundærstrømning.

CONTENTS

NOMENCLATURE

To distingushed between scalars, vectors, and second order tensors the following notation is used,

s = scalar (lightface italic)

$\boldsymbol{v}$ = vector (boldface italic)

$\boldsymbol{\tau}$ = second–order tensor (boldface Greek)

Italic symbols

a	Coefficient in discretised, integrated momemtum equation.
a_{ij}	Coefficient in matrix A.
A	Coefficient matrix.
ΔA	Area.
$\boldsymbol{b}$	Source vector.
B	Preconditioning matrix.
C	Mass flow rate.
$\boldsymbol{d}$	Search vector.
D	Diagonal matrix.
D	Diffusion coefficient.
e^i	Contravariant base vector.
e_i	Covariant base vector.
E	Factored matrix of B ($EE^T = B$).
f	Error function.
F	F–function in eq. (8.6).
$\boldsymbol{g}$	Residual vector.
$\boldsymbol{h}$	Vector used in the PCG–method.
h_i	Scale factor.
H	Linear operator used in a compact form of the discretised and integrated momentum equations.
$\boldsymbol{i}$	Cartesian base vector.
I	Unit matrix.
J	Jacobian.
k	Coefficient in powerlaw model of viscosity.
k_1	Coefficient in powerlaw model of first normal stress coefficient.
$k(\cdot)$	Spectral condition number.

l Characteristic length.

$\boldsymbol{L}$ Lower triangular matrix.

$\boldsymbol{M}$ One part of the decomposed matrix $\boldsymbol{A}$ ($\boldsymbol{A} = \boldsymbol{M} + \boldsymbol{R}$).

n Exponent in powerlaw model of viscosity.

n_1 Exponent in powerlaw model of first normal stress coefficient.

N_1 First normal stress difference.

N_2 Second normal stress difference.

p pressure.

Pe Peclet number.

$\boldsymbol{R}$ One part of the decomposed matrix $\boldsymbol{A}$ ($\boldsymbol{A} = \boldsymbol{M} + \boldsymbol{R}$).

s Elememtal arc length.

s_φ Source term of dependent variable.

s_p Coefficient in linearization of $s_\varphi = s_p\varphi + s_c$.

s_c Coefficient in linearization of $s_\varphi = s_p\varphi + s_c$.

u Velocity component in physical domain (primary flow).

u_{ij} Coefficient in upper triangular matrix.

U Characteristic velocity.

$\boldsymbol{U}$ Upper triangular matrix.

v Velocity component in physical domain (secondary flow).

ΔV A volume.

V Orthogonal matrix used in PCG.

$v(i)$ Physical componets of a vector.

v^i Contravariant component of a vector.

v_i Covariant component of a vector.

x dependent variable vector.

x' Solution vector.

x_i Orthogonal coordinates.

X Orthogonal coordinate system.

y_i Cartesian coordinates.

Y Cartesian coordinate system.

z Transformed dependent variable vector.

w Velocity component in physical domain (secondary flow).

Greek symbols

α Angle to describe change in unit vector due to curvature.

β Angle to describe change in unit vector due to curvature.

$\dot{\gamma}$ Magnitude of $\dot{\boldsymbol{\gamma}}$.

$\dot{\boldsymbol{\gamma}}$ Rate of strain tensor.

$\overset{\Delta}{\dot{\boldsymbol{\gamma}}}$ Lower–convected derivative of rate of strain tensor.

Γ Diffusion coefficient.

$\boldsymbol{\delta}$ Unit tensor.

ϵ Error.

η Shear rate dependent viscosity.

λ_u, λ_v, λ_w Relaxation parameters used in the momentum equations.

λ_i Eigenvalues.

Λ $\Lambda = \text{diag}(\lambda_i)$

μ Newtonian viscosity.

π Diffusion flux momentum tensor.

ρ Density.

$\rho(\cdot)$ Spectral radius.

τ Coefficient in the PCG–method.

$\boldsymbol{\tau}$ Extra–stress tensor.

φ Dependent variable (a scalar quantity).

Ψ_1 First normal stress coefficient.

Ψ_2 Second normal stress coefficient.

ω Relaxation factor.

Invariants

I First invariant defined as $\mathrm{I} = \sum_i \dot{\gamma}_{ii}$

II Second invariant defined as $\mathrm{II} = \sum_i \sum_j \dot{\gamma}_{ij}\dot{\gamma}_{ji}$

III Third invariant defined as $\mathrm{III} = \sum_i \sum_j \sum_k \dot{\gamma}_{ij}\dot{\gamma}_{jk}\dot{\gamma}_{ki}$

Subscript

e, n, w, s, u, d Indicate the cell faces east, north, west, south, up, down in relation to a main grid point.

E, N, W, S, U, D Indicate the neighbour grid points east, north, west, south, up, down in relation to a main grid point.

CHAPTER 1

INTRODUCTION

1.1 BACKGROUND FOR THE PRESENT WORK

Considerable attention has been devoted to the study of the flow in rectangular ducts from the frequent use in engineering practice of non–circular duct flows of various forms. Perhaps the most important class of exact solutions is that of fully developed Newtonian flow in straight ducts of arbitrary but constant shapes. By fully developed we mean that our attention is focused far downstream of the duct entrance, so that the initial growing shear layer and acceleration effects have vanished and the velocity is purely axial and varies only in the cross plane. Whenever the ducts become curved or the fluid is of a Non–Newtonian type an exact solution is usually not obtainable. This counts for both fully developed flow and in particular developing flow, why numerical simulations are of great importance in understanding the physics of duct flows. Most non–circular duct flows have a primary velocity field in the direction of the duct and a secondary velocity field in the cross plane normal to the direction of the duct. Only Newtonian fluids in straight ducts show a rectilinear flow. The secondary flow is usually one or several orders lower than the primary flow. Therefore it usually does not have an important influence on the total velocity field, but it may play an important role in fluid mechanics because of its relevance to various engineering applications. Physical phenomena inherent to duct flows are frictional pressure drop, heat transfer, mass transfer, and mixing rates. These phenomena may largely be changed by the presence of secondary flow which becomes a part of the present study.

The present work is closely connected to a Brite project in which the Department of Fluid Mechanics (DFM) at the Technical University of Denmark (TUD) participate. The brite project is based on the need of more knowledge of ultrafiltration systems, where the study of duct flows equipped with a membrane at one wall is the main concern of the TUD work. Pressure–driven membrane processes have been used since the mid nineteensixties by the Danish Sugar Corporation, DDS (the filtration division is now a division under DANISCO, Ltd.). The pressure–driven membrane processes are used to fractionate molecules of different size by filtration, see Madsen (1977). The flow through the membrane,

the permeate flow, depends, among other things, on the concentration polarization i.e. the development of increased concentration near the membrane surfaces owing to removal of solvent. A desirable feature of pressure–driven membrane processes would be to minimize the concentration polarization to obtain higher permeate flow. In order to minimize the concentration polarization it is indeed a requirement to have a detailed information about the fluid mechanics in the ducts. Madsen (1977) studies the influence of primary flow and the corresponding shear rates on concentration polarization where mainly straight ducts are considered. The present study is devoted to a detailed investigation of the flow aspects of membrane filtration, including the secondary flow in curved ducts of a Newtonian fluid and in straight and curved ducts of a Non–Newtonian fluid. A greater knowledge of secondary flow will hopefully be of use in pressure–driven membrane processes to increase the permeate flow as mentioned is the case of heat transfer processes.

Rectilinear flow takes place in straight ducts with Newtonian fluid. However, if the duct is equipped with a membrane at one wall a striping phenomena is observed on the surface of the membrane in the direction along the duct when using died solutes. Madsen (1977) states that these stripes have a great influence on the concentration polarization and may occur due to either a wave pattern in the duct, or vortices, or both. Jonsson (1984) also observes stripes and evidence of a moving boundary layer flowing along the membrane surface in the duct direction. The concentration boundary layer was accumulated in the stripes and left the membrane nearly visible between the stripes. This pattern was stated to appear due to secondary flow perpendicular to the primary flow direction. This kind of secondary flow is believed to appear due to an instability arising from a coupling between primary flow, concentration boundary layer, and permeate flow, Larsen (1989) and it is believed to be confined to the concentration boundary layer. The secondary flow arising from curvature effects and non–linear rheology, however, extends all over the cross section. Even though the striping phenomenon may increase the mass transfer through the membrane only the type of secondary flow which arises from curvature effects and non–linear rheology is considered in the present study.

Secondary flow in ducts arising from either curvature effects or non–linear rheology has earlier been studied by others. Secondary flows arising from curvature effects have been studied for an aspect ratio (width/height) ranging from 1 towards zero and the secondary flow arising from non–linear rheology has been studied using a perturbation method. For the present work, aspect ratios

larger than or equal to unity will be studied and for the chosen Non–Newtonian model the full equations will be simulated numerically. The ducts considered all have a rectangular cross section with an aspect ratio ranging from 1 to 16 with corresponding dimensions ranging from 4×4 mm to 1×16 mm and all having a constant cross sectional area of $16 \cdot 10^{-6}$ m^2, see figs. 1.1 and 1.2 for the geometry. The two fluids which will be used are the Newtonian fluid water and the Non–Newtonian fluid 2% viscarin which is a solution of 2% viscarin in water. Viscarin is a polymeric solution chosen because it is found to be a suitable transparent model fluid to simulate certain dairy products. The constitutive equation used to describe the viscarin solution is the CEF–equation which takes account of the shear thinning behavior of the viscosity and the first and the second normal stress differences. The range of Reynolds numbers which will be simulated will be confined to laminar flows. The simulations are carried out using a finite volume discretisation, employing primitive variables. A straggered grid is involved in which the control volumes for each velocity component is staggered a half control volume in the direction of each velocity component relative to the main control volume. The solution procedure for the flow problems is based on a pressure–velocity coupling involving the PISO algorithm in which the momentum equations are solved with an ADI solver and the pressure equation with a preconditioned conjugate gradient method.

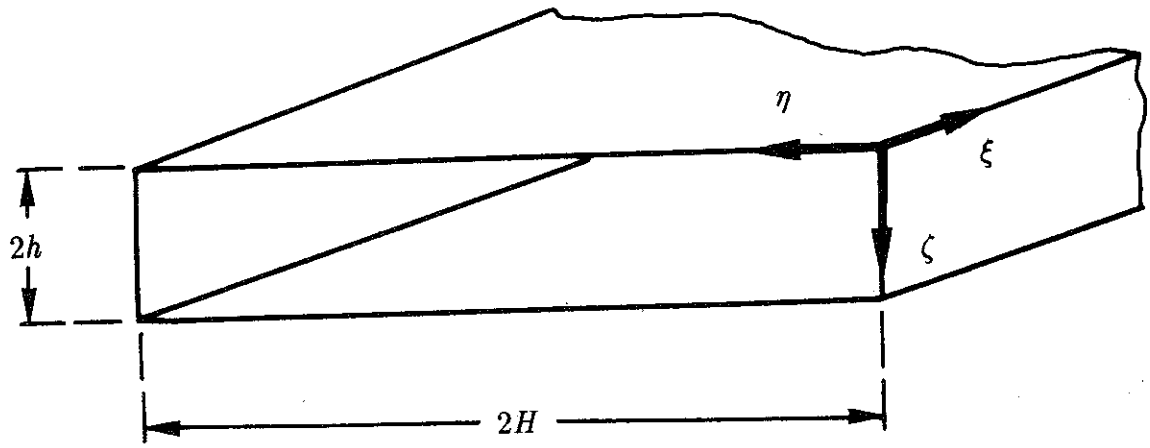

Fig. 1.1 *Geometry and coordinate system for straight duct,* $2h \equiv$ *height and* $2H \equiv$ *width.*

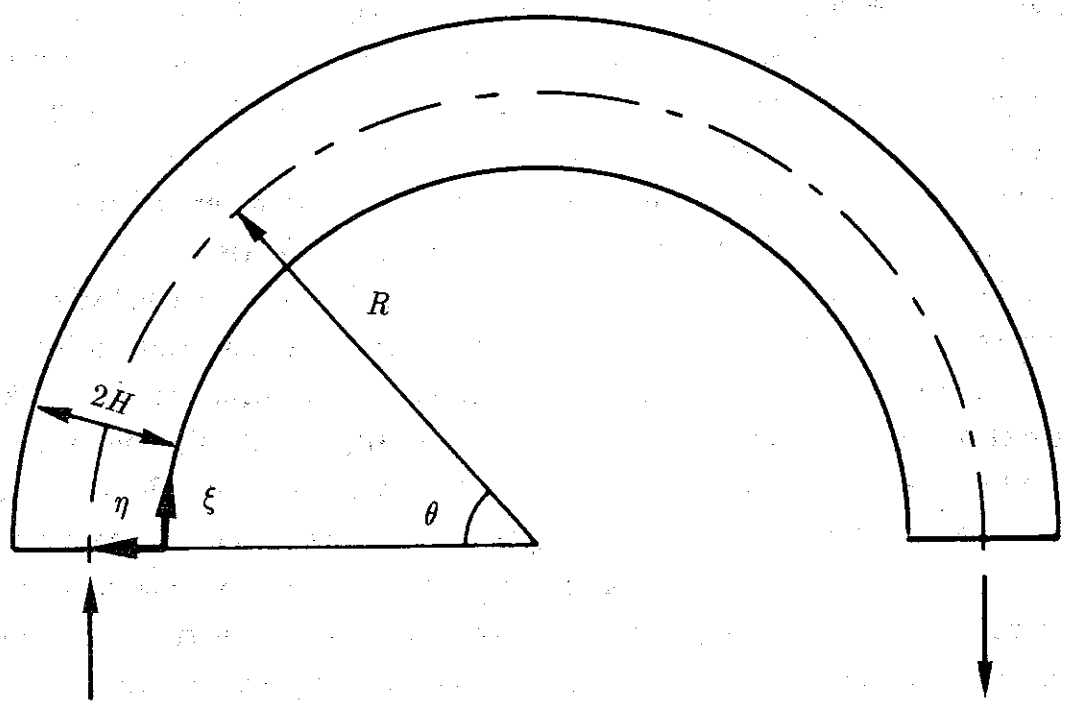

Fig. 1.2 *Geometry and coordinate system for curved duct,* $2H \equiv$ *width and* $R \equiv$ *radius, see fig.* 1.1 *for cross section geometry.*

CHAPTER 2

MATHEMATICAL DESCRIPTION OF PHYSICAL PHENOMENA

2.1 INTRODUCTION

In solving differential transport equations a coordinate system which describes the geometry of the domain has to be chosen. Complex geometries need advanced coordinate systems, but the complexity of the transport equations rise with the more advanced coordinate system. In section 2.2 the various coordinate systems are considered with their drawbacks and merits.

In section 2.3 the conservation equations of mass, momentum, and an arbitrary scalar quantity are formulated in an orthogonal curvilinear coordinate system

Each individual fluid material has its own characteristics which is described through its nature laws or constitutive relations which are the subject of section 2.4

Closing remarks are given in section 2.5

Some characteristics of orthogonal curvilinear coordinate systems are given in appendix A and for those who are not familiar with curved coordinate systems it is recommended to read appendix A before starting on chapter two.

2.2 COORDINATE SYSTEM

The coordinate system in which the differential transport equations is used should be chosen according to the geometri of the considered problem. A general non–orthogonal curvilinear coordinate system can be used in all geometries, but it is only used in complex geometries in which cartesian and orthogonal curvilinear coordinate systems are not adequate to describe the complexity of the problem. When a non–orthogonal curvilinear coordinate system is used the form of the differential equations can take different forms depending on how the base vectors are defined and depending on with which reference the vectors and tensors are expressed. In an orthogonal coordinate system the contravariant and the covariant vectors point in the same direction, and as base vectors are chosen the unit vectors. This gives a "natural" reference in which the vectors and the tensors are expressed according to the chosen coordinate system.

The range of coordinate frames to match a geometri may be classified into three categories, namely

- "Standard" orthogonal systems such as the cartesian, cylindrical–polar and spherical frames,
- Other orthogonal–curvilinear systems,
- Non–orthogonal systems.

The first of these categories possesses the disadvantage that it only can map domains of a limited range of geometries. The second category can, from a theoretical point of view, map all geometries, but under the condition that the coordinate lines are mutually orthogonal. For some geometries, this condition gives a poor resolution of the flow because there is only a limited control for the required grid spacing. The third category can map all geometries without any limitation on the grid lines (except that the grid lines normal to the boundaries are usually chosen to be orthogonal for ease of computation).

The flow field in complex geometries were earlier calculated or rather tried to be calculated in cartesian coordinates where the boundary of the geometry then was modified to fit the chosen coordinate system. A modification of the geometrical boundary condition of the real problem then gives inaccurate result. Consequently, to solve differential transport equations in complex geometries it is necessary to use a coordinate system which follows

the boundary of the geometry.

The three categories of coordinate frames give each a range of geometries to handle, but also the range of complexity of the governing equations in each individual system. The first category shows the simplest form of the governing equations and the third category the most complex form.

In a finite control volume formulation, the orthogonal property of the grid is essential for the application of the method. Since a diffusion flux across a control volume face is calculated in terms of the unknowns at two grid points, it is convenient that the face is normal to the line joining the two points, see Patankar (1980). The introduction of a non–orthogonal grid in the finite volume formulation does not cause severe problems, but the grid is generated not to deviate too much from an orthogonal grid to limit the numerical errors. The non–orthogonality of the grid involves more than two unknowns to calculate the diffusion flux across a control volume face, see Peric (1985).

For the present work, an orthogonal coordinate system is chosen. Two of the directions are curvilinear and orthogonal to each other while the third is cartesian to the two others. Fig. 2.1 shows an orthogonal curvilinear coordinate system. The Y–system is the cartesian system in which the $\boldsymbol{i}_i$–vectors are unit vectors belonging to each y_i–direction and the X–system is the orthogonal curvilinear system in which the $\boldsymbol{e}_i$–vectors are unit, tangent vectors belonging to each x_i–direction.

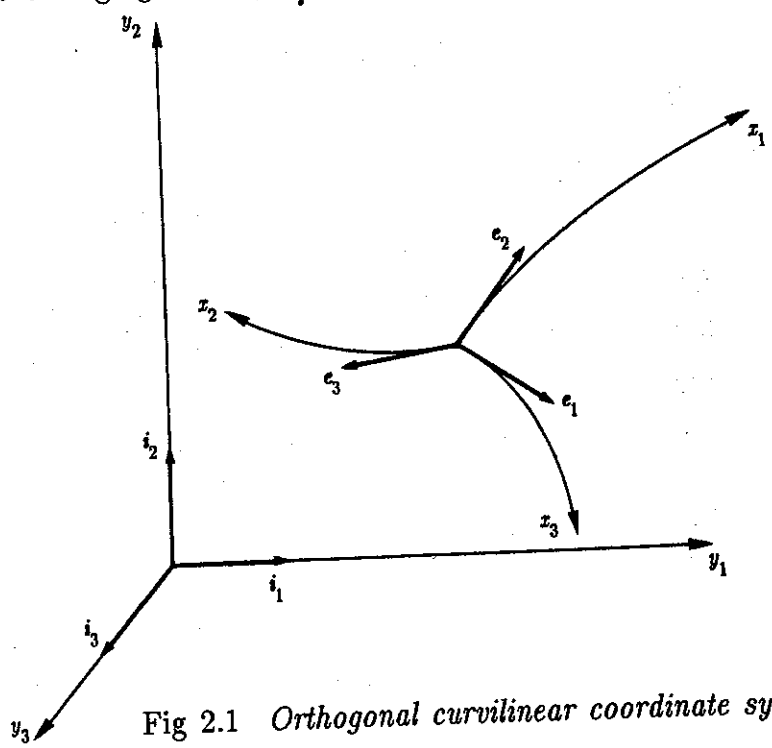

Fig 2.1 *Orthogonal curvilinear coordinate system.*

2.3 THE GOVERNING EQUATIONS

The motion of any fluid is described in a compact form by use of the Gibbs notation where the equation of conservation of mass, momentum, and an arbitrary scalar quantity is written as

$$\frac{\partial}{\partial t}\rho + \nabla\cdot\rho\boldsymbol{v} = 0, \tag{2.1a}$$

$$\frac{\partial}{\partial t}(\rho\boldsymbol{v}) + \nabla\cdot(\rho\boldsymbol{v}\boldsymbol{v}) = -\nabla\cdot\boldsymbol{\pi} + \boldsymbol{s}_v, \tag{2.1b}$$

$$\frac{\partial}{\partial t}(\rho\varphi) + \nabla\cdot(\rho\boldsymbol{v}\varphi) = \nabla\cdot(\Gamma_\varphi\nabla\varphi) + s_\varphi. \tag{2.1c}$$

Here, ρ is density, $\boldsymbol{v}$ velocity vector, $\boldsymbol{\pi}$ diffusion momentum flux tensor or stress tensor (see later), φ a scalar quantity (e.g. temperature or mass fraction), Γ_φ a diffusion coefficient for the quantity φ, and $\boldsymbol{s}_v$ and s_φ source terms associated with the momentum and scalar equations, respectively. The product between $\boldsymbol{v}$ and $\boldsymbol{v}$ is the dyadic product, often written $\otimes$, which gives a second order tensor as shown in fig. 2.2.

$$\boldsymbol{v}\boldsymbol{v} = \begin{bmatrix} v(1)v(1) & v(1)v(2) & v(1)v(3) \\ v(2)v(1) & v(2)v(2) & v(2)v(3) \\ v(3)v(1) & v(3)v(2) & v(3)v(3) \end{bmatrix}$$

Fig. 2.2 *Components of the convective momentum tensor.*

The tensor represents the convective momentum flux tensor. The physical meaning of a momentum flux tensor is explained later when the diffusion momentum flux is considered.

In the following, only steady, incompressible flows will be considered why eq. (2.1) takes the form

$$\nabla\cdot\boldsymbol{v} = 0, \tag{2.2a}$$

$$\nabla\cdot(\rho\boldsymbol{v}\boldsymbol{v}) = -\nabla\cdot\boldsymbol{\pi} + \boldsymbol{s}_v, \tag{2.2b}$$

$$\nabla\cdot(\rho v\varphi) = \nabla\cdot(\Gamma_{\varphi}\nabla\varphi) + s_{\varphi}. \qquad (2.2c)$$

The equation of conservation of mass, eq. (2.2a), is also called the equation of continuity.

The symbolic notation, ∇ and $\nabla\cdot$ (for the gradient and divergence operator), used in the conservation equations to describe transport of mass, momentum and scalar quantities can not be used in a computer program until a coordinate system is chosen. The transport equation will be described in an orthogonal curvilinear coordinate system where physical components of the vectors will be used. In appendix A the notation is explained and the metric coefficients in an orthogonal curvilinear system are given as well.

2.3.1 THE EQUATION OF CONTINUITY

In a steady, incompressible flow the equation of continuity states that the divergence of the velocity field is zero physically implying that the net outflow per unit volume is zero. With the divergence, written div, eq. (2.2a) may also be written as $\mathrm{div}(v) = 0$.

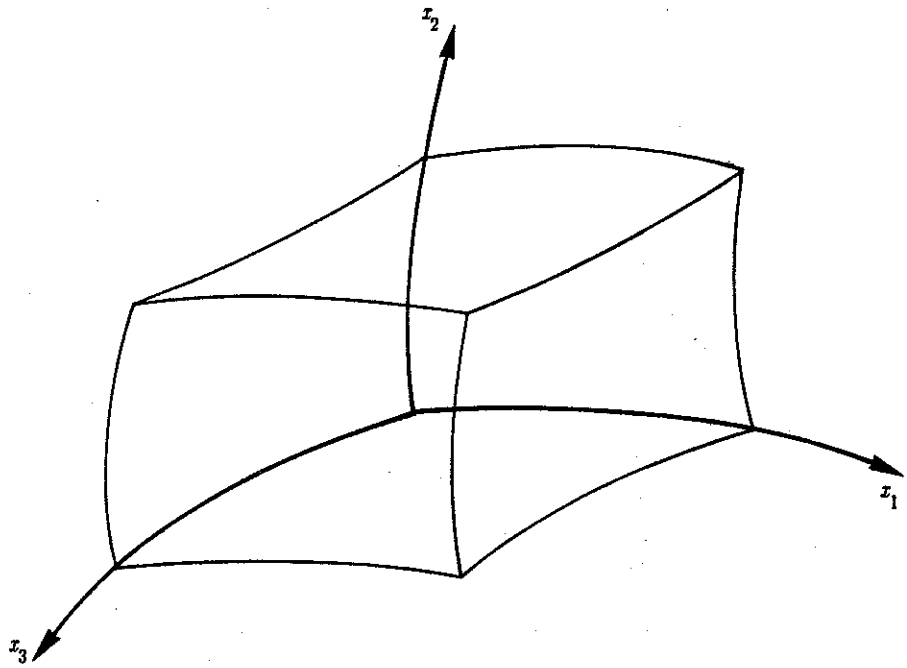

Fig. 2.3 *Finite volume in orthogonal curvilinear coordinates.*

Consider the x_1, x_2, x_3 coordinate system in fig. 2.3, with scale functions h_1, h_2, and h_3 (see appendix A), defining length increments $h_i dx_i$ along

coordinate axis x_i. Let $\boldsymbol{v} = v(1)\boldsymbol{e}_1 + v(2)\boldsymbol{e}_2 + v(3)\boldsymbol{e}_3$ be the vector field given in terms of the unit vectors $\boldsymbol{e}_1$, $\boldsymbol{e}_2$, and $\boldsymbol{e}_3$. The divergence of $\boldsymbol{v}$ will be calculated as the flux $\boldsymbol{v}$ out of the sides of the box in fig. 2.3, divided by the volume of the box. The flux density normal to the x_2, x_3–plane is $\boldsymbol{v}\cdot\boldsymbol{e}_1 = v(1)$ and the area of this face is $h_2h_3dx_2dx_3$. Therefore, the flux entering from that face is $v(1)h_2h_3dx_2dx_3$, while the flux leaving the opposite face is $\{v(1)h_2h_3 + [\partial(v(1)h_2h_3)/\partial x_1]dx_1\}dx_2dx_3$ (remember that $v(1)$, h_2, and h_3 are functions of x_1 as we move along the x_1–coordinate curve). Thus, the net flux in the x_1–direction is $[\partial(v(1)h_2h_3)/\partial x_1]dx_1dx_2dx_3$. Adding the contributions of the x_2 and x_3–directions the total flux through the volume sketched in fig. 2.3 is

$$\left[\frac{\partial}{\partial x_1}[v(1)h_2h_3] + \frac{\partial}{\partial x_2}[v(2)h_1h_3] + \frac{\partial}{\partial x_3}[v(3)h_1h_2]\right]dx_1dx_2dx_3. \tag{2.3}$$

The divergence of the velocity field in curvilinear coordinates is now obtained by dividing the expression in eq. (2.3) by the volume $h_1h_2h_3dx_1dx_2dx_3$. Hence

$$\mathrm{Div}(\boldsymbol{v}) = \frac{1}{h_1h_2h_3}\left[\frac{\partial}{\partial x_1}[v(1)h_2h_3] + \frac{\partial}{\partial x_2}[v(2)h_1h_3] + \frac{\partial}{\partial x_3}[v(3)h_1h_2]\right] \tag{2.4a}$$

or, written with summation indices,

$$\mathrm{Div}(\boldsymbol{v}) = \frac{1}{h}\left[\frac{h}{h_i}v(i)\right]_{,i}, \tag{2.4b}$$

where $h = h_1h_2h_3$. The equation of continuity for a steady, incompressible fluid states that eq. (2.4) must be equal to zero.

2.3.2 THE EQUATION OF MOTION

In the equation of balance of momentum, eq. (2.2b), the divergence operator operates on second order tensors, the convective and the diffusive momentum fluxes. The convective momentum flux $\rho\boldsymbol{vv}$ which is associated with the bulk flow of the fluid represents the convective transport. The diffusion momentum flux $\boldsymbol{\pi}$ is due to the molecular motion and interaction within the

fluid. Before the divergence of a second order tensor is worked out in an orthogonal curvilinear coordinate system it is appropriate to look at the physics behind the diffusion flux tensor of momentum, also called the stress tensor.

In the stress tensor $\boldsymbol{\pi}$ the component π_{ij} represents the force per unit area acting in the positive j-direction on a surface perpendicular to the i-direction. With the sign convection adopted from Bird et al (1960) and Bird et al (1987), it means that the fluid on the negative side of an element with area ds will exert a force of $\boldsymbol{n}\cdot\boldsymbol{\pi}ds$ on the fluid on the positive side of ds where the positive side corresponds to the orientation of the unit normal vector $\boldsymbol{n}$. Since force per unit area, which takes place between the individual parts of the fluid whenever a velocity difference occurs, is due to the diffusion process within the fluid, it is often more appropriate to talk about a momentum diffusion transport process. $\boldsymbol{\pi}$ is then given the name the diffusion momentum flux tensor.

Later it will be shown that the diffusion momentum flux for a Newtonian fluid is in the direction of the negative velocity gradient. It means that the momentum goes from a region of high velocity to a region of low velocity. Let us consider shear flow between two large parallel plates where the x_1-direction is in the direction of the flow and the x_2-direction is perpendicular to the x_1-direction. Newtons law of viscosity then states that

$$\pi_{21} = -\mu\frac{\partial v(1)}{\partial x_2}. \tag{2.5}$$

The reason for the adopted sign convection, see Bird et al (1960) and Bird et al (1987), is that it follows Fourier's heat conduction law $\boldsymbol{q} = -k\nabla T$ and Fick's mass diffusion law $\boldsymbol{j} = -D\nabla\rho$, where k is thermal conductivity, T is temperature, $\boldsymbol{q}$ is heat flux, D is mass diffusion coefficient, and $\boldsymbol{j}$ is mass flux. Fig. 2.4a shows the stresses on a finite fluid element whereas fig. 2.4b shows, the corresponding diffusion momentum fluxes. In principle there is no difference between the diffusion momentum flux tensor and the stress tensor why both convensions can be used.

Divergence of $\boldsymbol{\pi}$ in an orthogonal curvilinear coordinate system.

Tensor analysis is a widely used tool to express the sense of the operators used in Gibbs notation in any coordinate system. The tensor

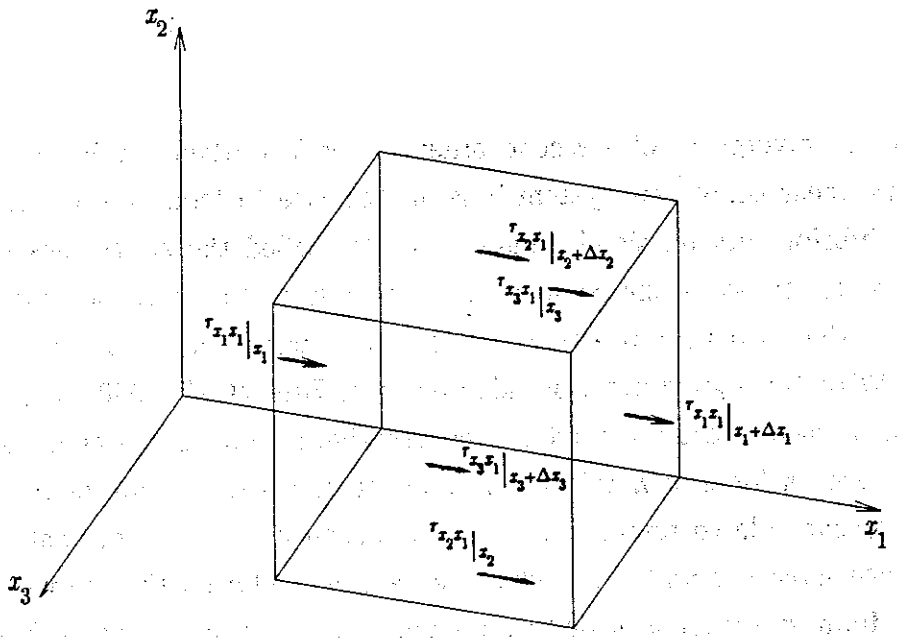

Fig. 2.4a *Volume element with arrows indicating the direction of the x–component of the stresses.*

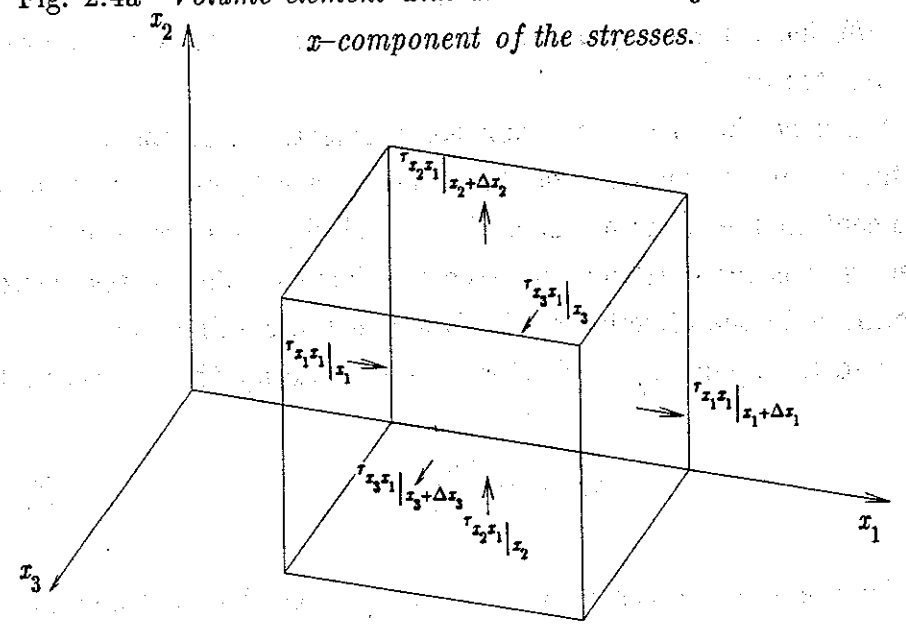

Fig. 2.4b *Volume element with arrows indicating the direction in which the x–component of the momentum is transported through the surfaces.*

analysis forms an algebra which can be used to simplify rather complex expressions, but at the same time it can hide some of the physics behind the problem. To use tensor algebra when dealing with orthogonal curvilinear coordinate systems, it is necessary to start out with a non–orthogonal coordinate system and then simplify it to the orthogonal case. To avoid the general tensor algebra, Prager (1961) uses only orthogonal unit vectors (base vectors) and their components with respect to the rectangular Cartesian coordinates to express the different operators in general orthogonal coordinates. He then uses only contravariant components, but it is rather cumbersome

and will not be recommended. To avoid hiding any of the physics behind the tensor algebra simple projection techniques will be used in our case. In the derivation of the divergence of a second order tensor in an orthogonal curvilinear coordinate system the technique will only be shown for a 2–D case.

From fig. 2.5 it is seen that all quantities must be referred to the local coordinate system in the middle of the element and that the components of the diffusion momentum flux tensor at the cell faces has to be projected on the axes of the local coordinate system. The angles of rotation of the cell faces relative to the local coordinate system is, to first order,

$$\alpha_e = [(h_1 + \tfrac{1}{2}\frac{\partial h_1}{\partial x_2}\mathrm{d}x_2)\mathrm{d}x_1 - h_1\mathrm{d}x_1]/h_2\mathrm{d}x_2 = \tfrac{1}{2}\frac{1}{h_2}\frac{\partial h_1}{\partial x_2}\mathrm{d}x_1,$$

$$\alpha_w = -[(h_1 - \tfrac{1}{2}\frac{\partial h_1}{\partial x_2}\mathrm{d}x_2)\mathrm{d}x_1 - h_1\mathrm{d}x_1]/h_2\mathrm{d}x_2 = \tfrac{1}{2}\frac{1}{h_2}\frac{\partial h_1}{\partial x_2}\mathrm{d}x_1,$$

$$\alpha_n = [(h_2 + \tfrac{1}{2}\frac{\partial h_2}{\partial x_1}\mathrm{d}x_1)\mathrm{d}x_2 - h_2\mathrm{d}x_2]/h_1\mathrm{d}x_1 = \tfrac{1}{2}\frac{1}{h_1}\frac{\partial h_2}{\partial x_1}\mathrm{d}x_2,$$

$$\alpha_s = -[(h_2 - \tfrac{1}{2}\frac{\partial h_2}{\partial x_1}\mathrm{d}x_1)\mathrm{d}x_2 - h_2\mathrm{d}x_2]/h_1\mathrm{d}x_1 = \tfrac{1}{2}\frac{1}{h_1}\frac{\partial h_2}{\partial x_1}\mathrm{d}x_2.$$

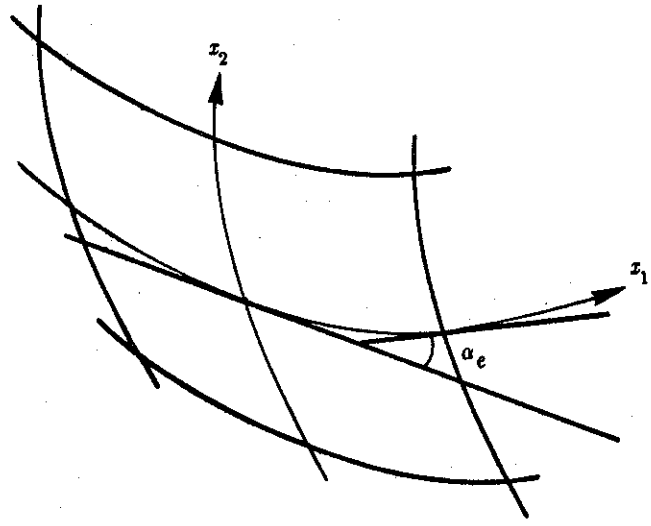

Fig. 2.5 *2–D orthogonal curvilinear element.*

The components along the x_1–axis of the divergence of $\boldsymbol{\pi}$ take the form

$$[(\pi_{11} + \tfrac{1}{2}\frac{\partial \pi_{11}}{\partial x_1}dx_1)\cos\alpha_e + (\pi_{12} + \tfrac{1}{2}\frac{\partial \pi_{12}}{\partial x_1}dx_1)\sin\alpha_e](h_2 + \tfrac{1}{2}\frac{\partial h_2}{\partial x_1}dx_1)dx_2 -$$

$$[(\pi_{11} - \tfrac{1}{2}\frac{\partial \pi_{11}}{\partial x_1}dx_1)\cos\alpha_w + (\pi_{12} - \tfrac{1}{2}\frac{\partial \pi_{12}}{\partial x_1}dx_1)\sin(-\alpha_w)](h_2 - \tfrac{1}{2}\frac{\partial h_2}{\partial x_1}dx_1)dx_2 +$$

$$[(\pi_{21} + \tfrac{1}{2}\frac{\partial \pi_{21}}{\partial x_2}dx_2)\cos\alpha_n + (\pi_{22} + \tfrac{1}{2}\frac{\partial \pi_{22}}{\partial x_2}dx_2)\sin(-\alpha_n)](h_1 + \tfrac{1}{2}\frac{\partial h_1}{\partial x_2}dx_2)dx_1 -$$

$$[(\pi_{21} - \tfrac{1}{2}\frac{\partial \pi_{21}}{\partial x_2}dx_2)\cos\alpha_s + (\pi_{22} - \tfrac{1}{2}\frac{\partial \pi_{22}}{\partial x_2}dx_2)\sin\alpha_s](h_1 - \tfrac{1}{2}\frac{\partial h_1}{\partial x_2}dx_2)dx_1.$$

Knowing that $\cos\alpha \simeq 1 - \alpha^2/2! + \alpha^4/4! - \ldots$ and $\sin\alpha \simeq \alpha - \alpha^3/3! + \alpha^5/5! - \ldots$ the expression, after reduction to first order, takes the form

$$\frac{\partial}{\partial x_1}(\pi_{11}h_2)dx_1dx_2 + \frac{\partial}{\partial x_2}(\pi_{21}h_1)dx_1dx_2 + \pi_{12}\frac{\partial h_1}{\partial x_2}dx_1dx_2 - \pi_{22}\frac{\partial h_2}{\partial x_1}dx_1dx_2. \tag{2.6}$$

The components along the x_2-axis of the divergence of $\boldsymbol{\pi}$ take the form

$$[(\pi_{22} + \tfrac{1}{2}\frac{\partial \pi_{22}}{\partial x_2}dx_2)\cos\alpha_n + (\pi_{21} + \tfrac{1}{2}\frac{\partial \pi_{21}}{\partial x_2}dx_2)\sin\alpha_n](h_1 + \tfrac{1}{2}\frac{\partial h_1}{\partial x_2}dx_2)dx_1 -$$

$$[(\pi_{22} - \tfrac{1}{2}\frac{\partial \pi_{22}}{\partial x_2}dx_2)\cos\alpha_s + (\pi_{21} - \tfrac{1}{2}\frac{\partial \pi_{21}}{\partial x_2}dx_2)\sin(-\alpha_s)](h_1 - \tfrac{1}{2}\frac{\partial h_1}{\partial x_2}dx_2)dx_1 +$$

$$[(\pi_{12} + \tfrac{1}{2}\frac{\partial \pi_{12}}{\partial x_1}dx_1)\cos\alpha_e + (\pi_{11} + \tfrac{1}{2}\frac{\partial \pi_{11}}{\partial x_1}dx_1)\sin(-\alpha_e)](h_2 + \tfrac{1}{2}\frac{\partial h_2}{\partial x_1}dx_1)dx_2 -$$

$$[(\pi_{12} - \tfrac{1}{2}\frac{\partial \pi_{12}}{\partial x_1}dx_1)\cos\alpha_w + (\pi_{11} - \tfrac{1}{2}\frac{\partial \pi_{11}}{\partial x_1}dx_1)\sin\alpha_w](h_2 - \tfrac{1}{2}\frac{\partial h_2}{\partial x_1}dx_1)dx_2,$$

which after reduction becomes

$$\frac{\partial}{\partial x_2}(\pi_{22}h_1)dx_1dx_2 + \frac{\partial}{\partial x_1}(\pi_{12}h_2)dx_1dx_2 + \pi_{21}\frac{\partial h_2}{\partial x_1}dx_1dx_2 - \pi_{11}\frac{\partial h_1}{\partial x_2}dx_1dx_2. \tag{2.7}$$

The divergence of a second tensor in orthogonal curvilinear coordinate is now obtained by dividing eq. (2.6) and (2.7) by the volume of the element, hence the x_1 and x_2 components of $\nabla \cdot \pi$ are, respectively,

$$x_1: \quad \frac{1}{h_1 h_2}\left[\frac{\partial}{\partial x_1}(\pi_{11} h_2) + \frac{\partial}{\partial x_2}(\pi_{21} h_1)\right] + \frac{1}{h_1 h_2}\pi_{12}\frac{\partial h_1}{\partial x_2} - \frac{1}{h_1 h_2}\pi_{22}\frac{\partial h_2}{\partial x_1}, \tag{2.8a}$$

$$x_2: \quad \frac{1}{h_1 h_2}\left[\frac{\partial}{\partial x_1}(\pi_{12} h_2) + \frac{\partial}{\partial x_2}(\pi_{22} h_1)\right] + \frac{1}{h_1 h_2}\pi_{21}\frac{\partial h_2}{\partial x_1} - \frac{1}{h_1 h_2}\pi_{11}\frac{\partial h_1}{\partial x_2}. \tag{2.8b}$$

The derivation of the divergence of a second order tensor has been shown for a 2–D case. The same procedure can be used in a 3–D case where the x_1, x_2, and x_3 components of the divergence of π are, respectively,

$$x_1: \quad \frac{1}{h_1 h_2 h_3}\left[\frac{\partial}{\partial x_1}(\pi_{11} h_2 h_3) + \frac{\partial}{\partial x_2}(\pi_{21} h_1 h_3) + \frac{\partial}{\partial x_3}(\pi_{31} h_1 h_2)\right] +$$

$$\frac{1}{h_1 h_2}\pi_{12}\frac{\partial h_1}{\partial x_2} + \frac{1}{h_1 h_3}\pi_{13}\frac{\partial h_1}{\partial x_3} - \frac{1}{h_1 h_2}\pi_{22}\frac{\partial h_2}{\partial x_1} - \frac{1}{h_1 h_3}\pi_{33}\frac{\partial h_3}{\partial x_1}, \tag{2.9a}$$

$$x_2: \quad \frac{1}{h_1 h_2 h_3}\left[\frac{\partial}{\partial x_1}(\pi_{12} h_2 h_3) + \frac{\partial}{\partial x_2}(\pi_{22} h_1 h_3) + \frac{\partial}{\partial x_3}(\pi_{32} h_1 h_2)\right] +$$

$$\frac{1}{h_1 h_2}\pi_{21}\frac{\partial h_2}{\partial x_1} + \frac{1}{h_2 h_3}\pi_{23}\frac{\partial h_2}{\partial x_3} - \frac{1}{h_1 h_2}\pi_{11}\frac{\partial h_1}{\partial x_2} - \frac{1}{h_2 h_3}\pi_{33}\frac{\partial h_3}{\partial x_2}, \tag{2.9b}$$

$$x_3: \quad \frac{1}{h_1 h_2 h_3}\left[\frac{\partial}{\partial x_1}(\pi_{13} h_2 h_3) + \frac{\partial}{\partial x_2}(\pi_{23} h_1 h_3) + \frac{\partial}{\partial x_3}(\pi_{33} h_1 h_2)\right] +$$

$$\frac{1}{h_3 h_1}\pi_{31}\frac{\partial h_3}{\partial x_1} + \frac{1}{h_3 h_2}\pi_{32}\frac{\partial h_3}{\partial x_2} - \frac{1}{h_3 h_1}\pi_{11}\frac{\partial h_1}{\partial x_3} - \frac{1}{h_3 h_2}\pi_{22}\frac{\partial h_2}{\partial x_3}. \tag{2.9c}$$

Written with summation indices, eq. (2.9) takes the form

$$\mathrm{Div}(\boldsymbol{\pi}) = \frac{1}{h}\left[\frac{h}{h_j}\,\pi_{ij}\right]_{,j} + \frac{1}{h_i h_j}\left[\pi_{ij}\,h_{i,j} - \pi_{jj}\,h_{j,i}\right], \tag{2.10}$$

where $h = h_1 h_2 h_3$.

The diffusion momentum flux tensor has been used as the second order tensor of which the divergence in orthogonal curvilinear coordinates is shown. In the equation of motion eq. (2.2b) it is seen that the divergence of the convective momentum flux appear too. Following, the same procedure for the dyadic product of $\boldsymbol{v}$ and $\boldsymbol{v}$, the x_1, x_2, and x_3 components of the divergence of $\rho\boldsymbol{vv}$ are, respectively,

$$x_1\text{:}\quad \frac{1}{h_1 h_2 h_3}\left[\frac{\partial}{\partial x_1}(\rho v(1)v(1)h_2h_3) + \frac{\partial}{\partial x_2}(\rho v(2)v(1)h_1h_3) + \frac{\partial}{\partial x_3}(\rho v(3)v(1)h_1h_2)\right] +$$

$$\frac{1}{h_1h_2}\rho v(1)v(2)\frac{\partial h_1}{\partial x_2} + \frac{1}{h_1h_3}\rho v(1)v(3)\frac{\partial h_1}{\partial x_3} - \frac{1}{h_1h_2}\rho v(2)v(2)\frac{\partial h_2}{\partial x_1} - \frac{1}{h_1h_3}\rho v(3)v(3)\frac{\partial h_3}{\partial x_1}, \tag{2.11a}$$

$$x_2\text{:}\quad \frac{1}{h_1 h_2 h_3}\left[\frac{\partial}{\partial x_1}(\rho v(1)v(2)h_2h_3) + \frac{\partial}{\partial x_2}(\rho v(2)v(2)h_1h_3) + \frac{\partial}{\partial x_3}(\rho v(2)v(3)h_1h_2)\right] +$$

$$\frac{1}{h_1h_2}\rho v(2)v(1)\frac{\partial h_2}{\partial x_1} + \frac{1}{h_2h_3}\rho v(2)v(3)\frac{\partial h_2}{\partial x_3} - \frac{1}{h_1h_2}\rho v(1)v(1)\frac{\partial h_1}{\partial x_2} - \frac{1}{h_2h_3}\rho v(3)v(3)\frac{\partial h_3}{\partial x_2}, \tag{2.11b}$$

$$x_3\text{:}\quad \frac{1}{h_1 h_2 h_3}\left[\frac{\partial}{\partial x_1}(\rho v(1)v(3)h_2h_3) + \frac{\partial}{\partial x_2}(\rho v(2)v(3)h_1h_3) + \frac{\partial}{\partial x_3}(\rho v(3)v(3)h_1h_2)\right] +$$

$$\frac{1}{h_1h_3}\rho v(3)v(1)\frac{\partial h_3}{\partial x_1} + \frac{1}{h_2h_3}\rho v(3)v(2)\frac{\partial h_3}{\partial x_2} - \frac{1}{h_1h_3}\rho v(1)v(1)\frac{\partial h_1}{\partial x_3} - \frac{1}{h_2h_3}\rho v(2)v(2)\frac{\partial h_2}{\partial x_3}, \tag{2.11c}$$

and in summation notation eq. (2.11) is given by

$$\mathrm{Div}(\rho \boldsymbol{v}\boldsymbol{v}) = \frac{1}{h}\left[\frac{h}{h_j}\,\rho v(i)v(j)\right]_{,j} + \rho\frac{v(j)}{h_i h_j}\left[v(i)\,h_{i,j} - v(j)\,h_{j,i}\right]. \qquad (2.12)$$

The equation of motion eq. (2.2b), with eq. (2.10) and eq. (2.12), can be written in orthogonal curvilinear coordinates as

$$\frac{1}{h}\left[\frac{h}{h_j}\,\rho v(i)v(j)\right]_{,j} + \rho\frac{v(j)}{h_i h_j}\left[v(i)\,h_{i,j} - v(j)\,h_{j,i}\right] =$$

$$\frac{1}{h}\left[\frac{h}{h_j}\,\pi_{ij}\right]_{,j} - \frac{1}{h_i h_j}\left[\pi_{ij}\,h_{i,j} - \pi_{jj}\,h_{j,i}\right] + s_i. \qquad (2.13)$$

The terms in the second pair of brackets on each side on the equation sign in eq. (2.13) are due to the curvature of the coordinate lines and are called the curvature terms. The contribution of the curvature terms from the convective part may be recognized as the centrifugal and the coriolis forces.

The difference between the divergence of a vector and the divergence of a second order tensor becomes clear by comparing eq. (2.11) and eq. (2.4a). It is seen that the terms in the brackets in eq. (2.11a) are equal to eq. (2.4a) where the tensor components now are velocity components. The extra terms in eq. (2.11a) are due to the curvature of the coordinate lines which also can be seen from the projection technique used to derive the divergence of a second order tensor. Similar equalities can be seen for the other coordinates lines.

2.3.3 THE EQUATION OF TRANSPORT OF A SCALAR

In the equation of conservation of a scalar quantity, eq. (2.2c), does the gradient of a scalar appear. The gradient operating on a scalar gives a vector on which the divergence operate. The divergence of a vector in orthogonal curvilinear coordinates has already been worked out, whereas the gradient of a scalar still need to be derived in orthogonal curvilinear coordinates.

The components of $\nabla\varphi$ in the e_1 direction is given by $d\varphi/d\xi$, the rate of change of φ with respect to distance in the e_1 direction. Since e_1, e_2, and e_3 are mutually orthogonal unit vectors $\nabla\varphi$ can be expressed in terms of these as

$$\nabla\varphi = \frac{d\varphi}{d\xi}\,e_1 + \frac{d\varphi}{d\eta}\,e_2 + \frac{d\varphi}{d\zeta}\,e_3$$

or, with use of the metrics also called the scale factors (see appendix A, where also the definition of ξ, η, and ζ is given) the gradient of a scalar in orthogonal curvilinear coordinates is given by

$$\nabla\varphi = \frac{1}{h_1}\frac{d\varphi}{dx_1}e_1 + \frac{1}{h_2}\frac{d\varphi}{dx_2}e_2 + \frac{1}{h_3}\frac{d\varphi}{dx_3}e_3 = \frac{1}{h_i}\varphi_{,i}e_i \tag{2.14}$$

With use of eq. (2.4a), (2.14), and (2.2c) the equation of conservation of a scalar quantity in orthogonal curvilinear coordinates is written

$$\frac{1}{h_1h_2h_3}\left[\frac{\partial}{\partial x_1}(\rho v(1)\varphi h_2h_3) + \frac{\partial}{\partial x_2}(\rho v(2)\varphi h_1h_3) + \frac{\partial}{\partial x_3}(\rho v(3)\varphi h_1h_2)\right] =$$

$$\frac{1}{h_1h_2h_3}\left[\frac{\partial}{\partial x_1}(\frac{h_2h_3}{h_1}\Gamma\frac{d\varphi}{dx_1}) + \frac{\partial}{\partial x_2}(\frac{h_1h_3}{h_2}\Gamma\frac{d\varphi}{dx_2}) + \frac{\partial}{\partial x_3}(\frac{h_1h_2}{h_3}\Gamma\frac{d\varphi}{dx_3})\right] + s_\varphi \tag{2.15}$$

or, with summation indices

$$\frac{1}{h}\left[\frac{h}{h_i}\rho\varphi v(i)\right]_{,i} = \frac{1}{h}\left[\frac{h}{h_i^2}\Gamma\varphi_{,i}\right]_{,i} + s_\varphi \tag{2.16}$$

2.4 CONSTITUTIVE RELATIONS

When the equation for transport of an arbitrary scalar was set up, eq. (2.1c), it was already pointed out that a diffusion coefficient Γ_φ associated with the medium φ was needed. The term $-\Gamma_\varphi\nabla\varphi$ decribes a flux (e.g. a heat flux or a mass flux) where Γ_φ depends on the medium and then is a characteristic of each specific medium. The relations which describe the behavior of a medium is named the constitutive relations and is a nature law. Many different constitutive relations can be made, but only relations involving the determination of the diffusion momentum flux tensor is considered in this section. Throughout the report we deal only with nonpolar fluids which state the symmetri of the diffusion momentum flux tensor, see Arpaci & Larsen (1984),

$$\pi_{ij} = \pi_{ji}$$

This implies the absence of intrinsic angular momemtum and surface and body couples.

2.4.1 NEWTONIAN FLUIDS

A rather big class of fluids, such as, see Bird et al (1987), the gases, gaseous mixtures, and low–molecular–weight liquids and their mixtures, are named Newtonian fluids. They show the simplest constitutive relation which fluids can take.

As stated above the diffusion momentum flux tensor is a symmetric tensor and every symmetric tensor can be divided into an isotropic part and a deviatoric part, whence $\boldsymbol{\pi}$ takes the form

$$\boldsymbol{\pi} = p\boldsymbol{\delta} + \boldsymbol{\tau}, \tag{2.17}$$

where p is pressure, $\boldsymbol{\delta}$ is a unit tensor and the deviatoric tensor $\boldsymbol{\tau}$ is a tensor where the trace per definition is zero and is then called traceless. The trace of a tensor is written $\mathrm{tr}(\boldsymbol{\tau}) = \tau_{ii}$ (i.e. sum of the diagonal elements). The deviatoric tensor is named the extra–stress tensor. The pressure p is, according to eq. (2.17) and the definition of a deviatoric tensor, in a Newtonian fluid defined as

$$p = \pi_{ii}/3.$$

The pressure represents a local state property and is given through the thermodynamic equation of state $p = p(\rho, T)$ why the pressure is called the thermodynamic pressure, which also is static pressure, see Arpaci & Larsen (1984). The deviatoric tensor contains the stresses which try to distort the fluid without changing the volume and the isotropic tensor gives the stresses which try to dilatate the fluid without shape distortion.

In order to provide a well–posed problem for the solution of the equation of motion under the condition of incompressibility it is necessary to require additional relationship between the extra–stress tensor and the kinematic variables. A general linear model based on the asumption that the extra–stress tensor is proportional to rate–of–deformation tensor leads to, see e.g. Prager

(1961), Batchelor (1967), and Arpaci & Larsen (1984)

$$\tau = -\mu[\nabla \boldsymbol{v} + (\nabla \boldsymbol{v})^{\mathrm{T}}] + (\tfrac{2}{3}\mu - \kappa)(\nabla \cdot \boldsymbol{v})\boldsymbol{\delta}, \tag{2.18}$$

where $\dot{\gamma} = \nabla \boldsymbol{v} + (\nabla \boldsymbol{v})^{\mathrm{T}}$ is rate–of–deformation tensor or rate–of–strain tensor, μ the dynamic viscosity, and κ the bulk viscosity. The bulk viscosity is written $\frac{2}{3}\mu + \lambda$, where λ denotes the second viscosity. The rate–of–deformation tensor is composed of the gradient of the velocity field and its transposed. The gradient of a vector field is named the dyadic and represents a tensor. The dyadic of a velocity field $\nabla \boldsymbol{v}$ in *Cartesian* coordinates takes the form

$$\nabla \boldsymbol{v} = \begin{bmatrix} \frac{\partial u}{\partial x} & \frac{\partial v}{\partial x} & \frac{\partial w}{\partial x} \\ \frac{\partial u}{\partial y} & \frac{\partial v}{\partial y} & \frac{\partial w}{\partial y} \\ \frac{\partial u}{\partial z} & \frac{\partial v}{\partial z} & \frac{\partial w}{\partial z} \end{bmatrix}$$

With the introduction of eq. (2.18) in eq. (2.17) we obtain after the usual splitting of $\boldsymbol{\pi}$

$$\boldsymbol{\pi} = (p_1 - \kappa \nabla \cdot \boldsymbol{v})\boldsymbol{\delta} - \mu[\nabla \boldsymbol{v} + (\nabla \boldsymbol{v})^{\mathrm{T}}], \tag{2.19}$$

where p_1 is named an arbitrary pressure. The shown linear model consists of all possible combinations of first derivatives of velocity components that are allowed when the fluid is nonpolar and has no directional preference, see Prager (1961).

The bulk viscosity is only known to become of practical importance in processes involving rapid volume changes which will not be considered here, why the Stokes hypothesis, stating $\frac{2}{3}\mu = -\lambda$, is assumed to apply to most Newtonian processes. The Stokes hypothesis is based on the assumption of local thermodynamic equilibrium. In our case, where only incompressible fluids are studied, $\nabla \cdot \boldsymbol{v}$ vanishes and eq. (2.19) takes the form

$$\boldsymbol{\pi} = p\boldsymbol{\delta} - \mu\dot{\gamma}. \tag{2.20}$$

The equation of motion eq. (2.1b) combined with the constitutive relation, eq.

(2.20) gives the well known Navier–Stokes equations.

In section 2.3.2 dealing with the equation of motion it was shown how the equation of transport of momentum can be expressed in orthogonal curvilinear coordinates. To express the full Navier–Stokes equations in orthogonal curvilinear coordinates we only need to show how of the constitutive relation, eq. (2.20), is expressed in orthogonal curvilinear coordinates.

The isotropic part of the diffusion momentum flux tensor does not need any rewriting, but the deviatoric part which contains the dyadic $\nabla \cdot \boldsymbol{v}$ needs to be rewritten. The components of $\nabla \cdot \boldsymbol{v}$ in the $\boldsymbol{e}_1$–direction is given by $\partial \boldsymbol{v}/\partial \xi$, the rate of change of $\boldsymbol{v}$ with respect to distance in the $\boldsymbol{e}_1$–direction. Since $\boldsymbol{e}_1$, $\boldsymbol{e}_2$, and $\boldsymbol{e}_2$ are mutually orthogonal unit vectors $\nabla \cdot \boldsymbol{v}$ can be expressed in terms of these as

$$\nabla \cdot \boldsymbol{v} = \frac{\partial \boldsymbol{v}}{\partial \xi}\, \boldsymbol{e}_1 + \frac{\partial \boldsymbol{v}}{\partial \eta}\, \boldsymbol{e}_2 + \frac{\partial \boldsymbol{v}}{\partial \zeta}\, \boldsymbol{e}_3. \tag{2.21}$$

The introduction of ξ, η, and ζ is given in appendix A. When dealing with the gradient of a scalar it was easy to introduce the scale factors and write the gradient in orthogonal curvilinear coordinates, but when dealing with a vector field it is necessary to evaluate the derivatives of the unit vectors $\boldsymbol{e}_i$ with respect to distance in the x_1, x_2, and x_3 directions, respectively. This can be seen by writting $\boldsymbol{v}$ in components as $\boldsymbol{v} = v(1)\boldsymbol{e}_1 + v(2)\boldsymbol{e}_2 + v(3)\boldsymbol{e}_3$ and introduce this expression in eq. (2.21). The derivative of the unit vectors with respect to distance in the x_1, x_2, and x_3 directions give the curvature of the coordinate lines. The curvature of $\boldsymbol{e}_1$ due to change in the x_1 and x_2 directions for a 2–D case will be shown, while the generalization to 3–D for the curvature of $\boldsymbol{e}_1$, $\boldsymbol{e}_2$, and $\boldsymbol{e}_3$ should be straight forward. With the help of fig. 2.6a it is seen that the change in $\boldsymbol{e}_1$ due to change in x_1 is $-\boldsymbol{e}_2\alpha$, where

$$\alpha = \mathrm{d}x_1 \mathrm{d}x_2 \, \frac{\partial h_1}{\partial x_2} / (h_2 \mathrm{d}x_2),$$

whence $\partial \boldsymbol{e}_1/\partial x_1$ is expressed as

$$\frac{\partial \boldsymbol{e}_1}{\partial x_1} = -\frac{\boldsymbol{e}_2}{h_2}\frac{\partial h_1}{\partial x_2}.$$

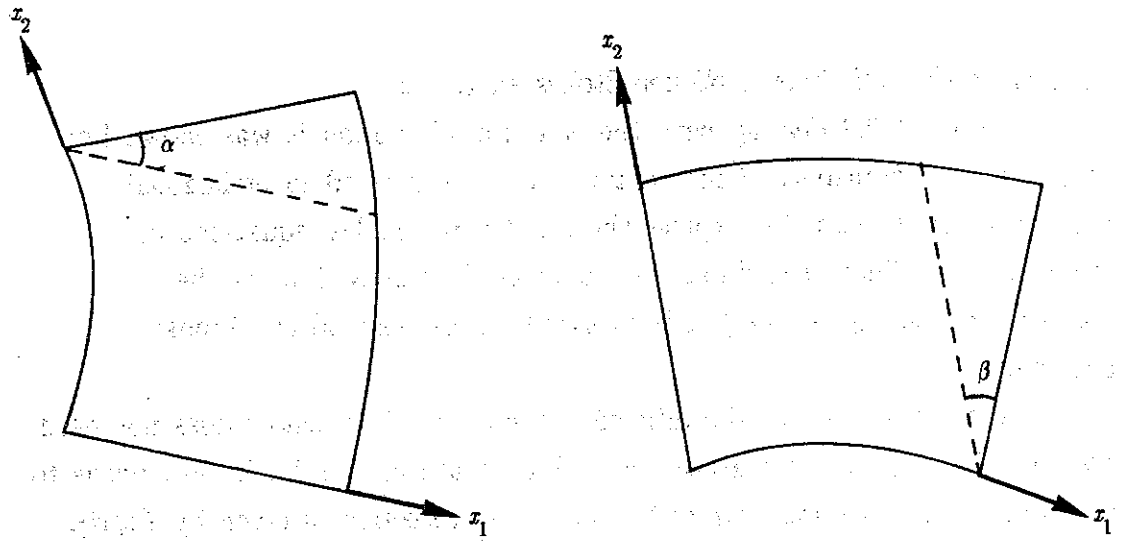

Fig. 2.6 *Chance in unit vectors due to curvature.*

The change in e_1 due to change in x_2 is $e_2\beta$, see fig. 2.6b, where

$$\beta = \mathrm{d}x_1\mathrm{d}x_2 \frac{\partial h_2}{\partial x_1}/(h_1\mathrm{d}x_1).$$

Therefore,

$$\frac{\partial e_1}{\partial x_2} = \frac{e_2}{h_1}\frac{\partial h_2}{\partial x_1}.$$

When dealing with a 3–D case an extra component along the x_3–direction need to be added for the derivative of e_1 along the x_1–direction why $\partial e_1/\partial x_1$ in 3–D is expressed as

$$\frac{\partial e_1}{\partial x_1} = -\frac{e_2}{h_2}\frac{\partial h_1}{\partial x_2} - \frac{e_3}{h_3}\frac{\partial h_1}{\partial x_3}.$$

The curvature of the unit vectors in a 3–D orthogonal curvilinear coordinate system can according to the above derivatives, see Morse & Feshbach (1953), be summarized as

$$\frac{\partial e_1}{\partial x_1} = -\frac{e_2}{h_2}\frac{\partial h_1}{\partial x_2} - \frac{e_3}{h_3}\frac{\partial h_1}{\partial x_3}; \quad \frac{\partial e_1}{\partial x_2} = \frac{e_2}{h_1}\frac{\partial h_2}{\partial x_1}; \quad \frac{\partial e_1}{\partial x_3} = \frac{e_3}{h_1}\frac{\partial h_3}{\partial x_1};$$

$$\frac{\partial e_2}{\partial x_2} = -\frac{e_3}{h_3}\frac{\partial h_2}{\partial x_3} - \frac{e_1}{h_1}\frac{\partial h_2}{\partial x_1}; \quad \frac{\partial e_2}{\partial x_3} = \frac{e_3}{h_2}\frac{\partial h_3}{\partial x_2}; \quad \frac{\partial e_2}{\partial x_1} = \frac{e_1}{h_2}\frac{\partial h_1}{\partial x_2};$$

$$\frac{\partial e_3}{\partial x_3} = -\frac{e_1}{h_1}\frac{\partial h_3}{\partial x_1} - \frac{e_2}{h_2}\frac{\partial h_3}{\partial x_2}; \quad \frac{\partial e_3}{\partial x_1} = \frac{e_1}{h_3}\frac{\partial h_1}{\partial x_3}; \quad \frac{\partial e_3}{\partial x_2} = \frac{e_2}{h_3}\frac{\partial h_2}{\partial x_3}.$$

The dyadic field of $\boldsymbol{v}$ can now be expressed in terms of curvature of the coordinates lines, components of the $\boldsymbol{v}$-vector, and eq. (2.21). It must be remembered that the product of the unit vectors is the dyadic product, why the result is a tensor. With use of $\nabla\boldsymbol{v}$ and its transposed the components of the diffusion momentum tensor eq. (2.20) are written

$$\pi_{11} = -p - 2\mu\left[\frac{1}{h_1}\frac{\partial(v(1))}{\partial x_1} + \frac{v(2)}{h_1 h_2}\frac{\partial h_1}{\partial x_2} + \frac{v(3)}{h_1 h_3}\frac{\partial h_1}{\partial x_3}\right], \tag{2.22a}$$

$$\pi_{22} = -p - 2\mu\left[\frac{1}{h_2}\frac{\partial(v(2))}{\partial x_2} + \frac{v(3)}{h_2 h_3}\frac{\partial h_2}{\partial x_3} + \frac{v(1)}{h_1 h_2}\frac{\partial h_2}{\partial x_1}\right], \tag{2.22b}$$

$$\pi_{33} = -p - 2\mu\left[\frac{1}{h_3}\frac{\partial(v(3))}{\partial x_3} + \frac{v(1)}{h_1 h_3}\frac{\partial h_3}{\partial x_1} + \frac{v(2)}{h_2 h_3}\frac{\partial h_3}{\partial x_2}\right], \tag{2.22c}$$

$$\pi_{12} = \pi_{21} = -\mu\left[\frac{h_1}{h_2}\frac{\partial}{\partial x_2}\left[\frac{v(1)}{h_1}\right] + \frac{h_2}{h_1}\frac{\partial}{\partial x_1}\left[\frac{v(2)}{h_2}\right]\right], \tag{2.22d}$$

$$\pi_{13} = \pi_{31} = -\mu\left[\frac{h_1}{h_3}\frac{\partial}{\partial x_3}\left[\frac{v(1)}{h_1}\right] + \frac{h_3}{h_1}\frac{\partial}{\partial x_1}\left[\frac{v(3)}{h_3}\right]\right], \tag{2.22e}$$

$$\pi_{23} = \pi_{32} = -\mu\left[\frac{h_2}{h_3}\frac{\partial}{\partial x_3}\left[\frac{v(2)}{h_2}\right] + \frac{h_3}{h_2}\frac{\partial}{\partial x_2}\left[\frac{v(3)}{h_3}\right]\right]. \tag{2.22f}$$

With the equation of motion eq. (2.2b) and the components of the diffusion momentum flux tensor eq. (2.22) the Navier–Stokes equations become, in orthogonal curvilinear coordinates,

$$\frac{1}{h}\left[\frac{h}{h_k}\rho v(i)v(k)\right]_{,k} + \rho\frac{v(k)}{h_i h_k}\left[v(i)\,h_{i,k} - v(k)\,h_{k,i}\right] =$$

$$
\begin{aligned}
&- \frac{1}{h_i} p_{,i} + \frac{1}{h}\Big\{2\Big[\mu\frac{h}{h_i^2}\,(v(i)_{,i} + \sum_s \frac{v(s)}{h_s}\,h_{i,s})\Big]_{,i} \\
&+ \sum_j \Big[\mu\,\frac{h}{h_j}\Big(\frac{h_i}{h_j}\,\Big(\frac{v(i)}{h_i}\Big)_{,j} + \frac{h_j}{h_i}\,\Big(\frac{v(j)}{h_j}\Big)_{,i}\Big)\Big]_{,j}\Big\} \\
&+ \sum_j \mu\,\frac{h_{i,j}}{h_i h_j}\Big[\frac{h_i}{h_j}\Big(\frac{v(i)}{h_i}\Big)_{,j} + \frac{h_j}{h_i}\,\Big(\frac{v(j)}{h_j}\Big)_{,i}\Big] \\
&- \sum_j 2\mu\,\frac{h_{j,i}}{h_i h_j}\Big[\frac{1}{h_j}v(j)_{,j} + \sum_l \frac{v(l)}{h_j h_l}\,h_{j,l}\Big]. \qquad (2.23)
\end{aligned}
$$

$$(s \neq i, \quad j \neq i, \quad l \neq j)$$

Equations (2.23) have been worked out in a three–dimensional orthogonal curvilinear coordinate system. However, in the present study, dealing with straight and curved ducts of general cross sections, we have chosen to work in curvilinear orthogonal in two directions and cartesian orthogonal in the third. The resulting special form is obtained by making h_1 and h_2 functions of only x_1 and x_2, and to make h_3 independent of coordinate directions. The scale factors then take the form

$$
\begin{aligned}
h_1 &= h_1(x_1, x_2), \\
h_2 &= h_2(x_1, x_2), \\
h_3 &= 1.
\end{aligned} \qquad (2.24)
$$

2.4.2 NON–NEWTONIAN FLUIDS

All fluids which do not obey the natural law described in eq. (2.20), where the extra–stress tensor is proportional to the rate–of–deformation tensor, are classified as Non–Newtonian fluids. Examples of materials which definitely are "fluid–like", see Coleman et al (1966), but not are well described by eq. (2.20) are molten polymers, concentrated and even dilute polymer solutions, protein solutions, synthetic latices (i.e. colloidal suspensions of synthetic rubber in water), special soap solutions, and examples encountered in daily life include asphalts, paints, pitch, starch suspensions, certain glues, and certain honeys. The term "fluid–like" refers to the fact that the fluid behavior results

in flow when subjected to stress. These fluids are referred to as elastico–viscous fluids or, as already mentioned, Non–Newtonian fluids. Materials which do deform, but do not flow, are termed viscoelastic materials and belong to the elastico solid group. A new science has originated in elastico–viscous fluids, Rheology, which is the study of deformation of flow of matter. The necessity of this study is needed because the equation of motion and the equation of continuity cannot alone predict the behavior of a particular fluid within the conditions of a flow situation. A constitutive equation which relates stress and deformation is needed.

In trying to relate stress and deformation, one model, as for the Newtonian case, cannot be made for the Non–Newtonian case. Only one parameter, the dynamic viscosity, which is material dependent, appears in the constitutive relation for a Newtonian fluid. To represent the complex behavior of Non–Newtonian fluids we need constitutive equations with several material parameters (constants) and nonlinear as well as linear terms. We still expect stress to depend on rate of deformation.

In the work of modeling the diffusion momentum flux tensor the usual decomposition, as in the Newtonian case, is made

$$\pi = p\delta + \tau, \tag{2.25}$$

but the decomposition is not necessarily composed of an istropic tensor and a deviatoric tensor. In eq. (2.25) p is an arbitrary pressure and takes the form as a dynamic variable, but it may not be a state proporty. From a computational point on view it is important to realize that the arbitrary pressure is only used as a variable to obtain the equation of continuity in junction with the equation of motion, see chapter 5. The extra–stress tensor τ is usually not a deviatoric tensor and for that reason not traceless. The pressure, which is defined as $\pi_{ii}/3$ (see the section of Newtonian fluids), is then, for a Non–Newtonian fluid, composed of the arbitrary pressure and the trace of the extra–stress tensor. The rotating rod example shows one of the many peculiar differences between dynamics of Non–Newtonian and Newtonian fluids. The non–traceless form of the extra–stress tensor of the Non–Nowtonian fluid, for this example, gives rise to the rod–climbing phenomenon.

The Navier–Stokes equations can be non–dimensionalized using a suitable characteristic velocity V and length L. The equations then involve one non–dimensional parameter called the Reynolds number Re, defined by

$$\mathrm{Re} = \frac{\rho V L}{\mu}. \tag{2.26}$$

For a Non–Newtonian fluid, additional dimensionless parameters appear. One is the ratio of the elastic forces to the viscous forces (remember that the Non–Newtonian fluids are called elastico–viscous fluids too). This number is the Deborah number De, defined as the ratio of a characteristic time of the fluid λ to a characteristic time of the deformation or the flow process, t_{flow}, see Crochet et al (1984) and Bird et al (1987),

$$\mathrm{De} = \lambda / t_{flow}. \tag{2.27}$$

It is seen that the Newtonian case is obtained in the limit De $\to$ 0, and in the limit De $\to \infty$ the viscoelastic case is obtained. The characteristic time of the fluid λ, or the characteristic times λ_i if the fluid is characterized by several time constants, is for example used when a memory effect is modeled. An example of a process where an elastico–viscous fluid shows memory effect is the extrudate swell. In the rest of the thesis memory characteristics will not be considered even if the fluid considered contains memory. Only two rheometrical differences from the Newtonian case will be considered, the shear rate dependent viscosity $\eta = \eta(\dot{\gamma})$ and the normal stress differences (η is also used to describe the physical distance along the x_2–direction, but this should cause no problems).

The shear rate dependent viscosity.

In the Newtonian case, the dynamic viscosity is a constant for each material. This is not the case for Non–Newtonian fluids where the viscosity is a function of the shear rate. A typical example of shear rate dependent viscosity is shown in fig. 2.7, where the two plateaus are called the first Newtonian plateau, denoted η_0, and the second Newtonian plateau, denoted η_2. The axes in fig. 2.7 are logarithmic so the variation of η between η_0 and η_2 is often approximated by a powerlaw, of the form

$$\eta = k\dot{\gamma}^{n-1}. \tag{2.28}$$

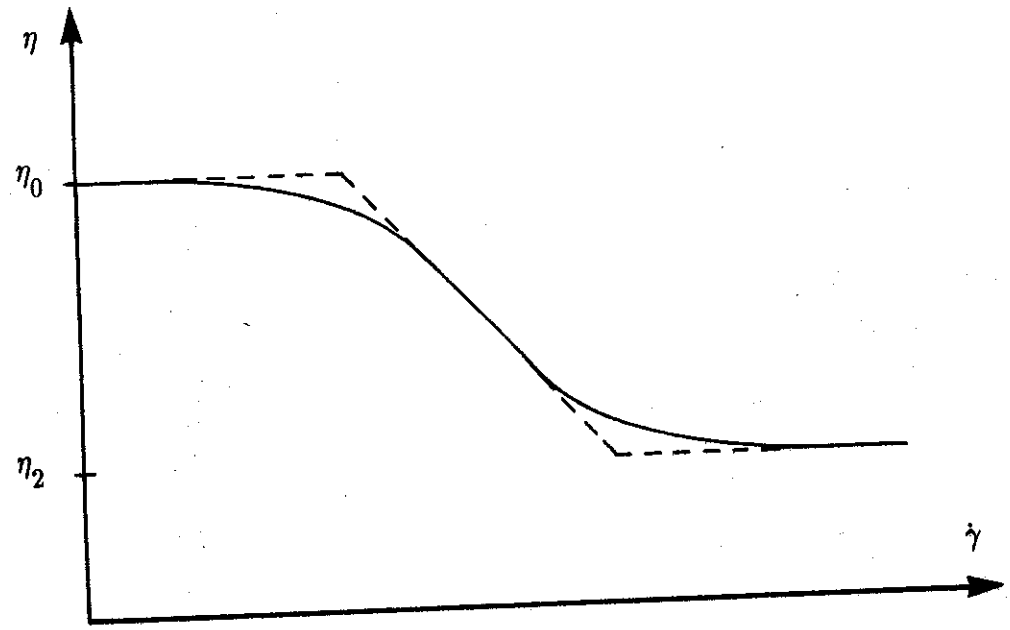

Fig. 2.7 *Viscosity as function of shear rate.*

Employing the four constants η_0, η_2, k, and n , the viscosity variation is approximated with the dashed line in fig. 2.7. Fluids which have a decreasing value of η with increasing $\dot{\gamma}$, as in fig. 2.7, are called shear thinning fluids whereas shear thickening fluids have an increasing value of η with increasing $\dot{\gamma}$. It is seen that n must be less than 1 for shear thinnning fluids and greater than 1 for shear thickening fluids. The Newtonian case is obtained for $n = 1$ and $k = \mu$.

First & second normal stress coefficients.

The normal stress differences observed in Non–Newtonian fluids were already touched on when the decomposition of the diffusion momentum flux tensor was described. It was stated that the extra–stress tensor was not always traceless why normal stress differences can occour. The first and second normal stress differences are denoted N_1 and N_2, respectively, see Crochet et al (1984) and Bird et al (1987),

$$\tau_{11} - \tau_{22} = -N_1(\dot{\gamma}),$$

$$\tau_{22} - \tau_{33} = -N_2(\dot{\gamma}),$$

where $\dot{\gamma} = |\dot{\gamma}| = \sqrt{\frac{1}{2}\sum_i\sum_j \dot{\gamma}_{ij}\dot{\gamma}_{ji}} = \sqrt{\frac{1}{2}\text{II}}$. II is the second invariant of a tensor, also written $\text{II} = \text{tr}(\dot{\gamma}\cdot\dot{\gamma}) = \text{tr}\dot{\gamma}^2$. Two more invariants of a tensor can be defined as $\text{I} = \text{tr}(\dot{\gamma})$ and $\text{III} = \text{tr}\dot{\gamma}^3$ which are the first and third invariant, respectively. Invariants are quantities which are independent of the choice of coordinate system to which the components of $\dot{\gamma}$ are referred. The normal stress differences are modeled as linear functions of the square of the magnitude of the rate–of–deformation tensor,

$$-N_1(\dot{\gamma}) = -\Psi_1(\dot{\gamma})\dot{\gamma}^2,$$

$$-N_2(\dot{\gamma}) = -\Psi_2(\dot{\gamma})\dot{\gamma}^2,$$

where Ψ_1 and Ψ_2 are the first and second normal stress coefficients, respectively. For many fluids, the normal stress coefficients show a similar dependency of shear rate as the viscosity, why a power law model is used as well.

The viscosity, and the first and second normal stress differences, are usually referred to as the three viscometric functions, the viscosity being especially important in many engineering applications. The magnitude of N_2 is much smaller than N_1, about one order of magnitude, but this does not mean that N_2 does not have a prominent influence. For example, rectilinear flow in straight channels with non–circular cross section is usually not possible with a elastico–viscous fluid, and some secondary flow is to be expected when N_2 is non–zero. This fact was studied in detail in a paper by Dodson et al (1973), where a perturbation method was used. In the present work, the full equations are used in their original form when studying the nature of the secondary flow.

It was mentioned that Non–Newtonian fluids are attempted modeled with several methods. Here, however only two models will be described. The first model is the generalized Newtonian model which only contains the shear rate dependent viscosity η, and the other model is the Criminale–Ericksen–Filbey (CEF) model which contains all three viscometric functions η, Ψ_1, and Ψ_2.

Generalized Newtonian Fluid.

In the Newtonian case, the extra–stress tensor has the form

$$\tau = -\mu\dot{\gamma}, \tag{2.29}$$

where μ is a constant for the given material at a given temperature and pressure. In the generalized Newtonian model, the extra–stress tensor is given by

$$\tau = -\eta(\dot{\gamma})\dot{\gamma}. \tag{2.30}$$

Letting the viscosity η be dependent on the magnitude of $\dot{\gamma}$, it is to be independent of coordinate system, hence only a function of combinations of the invariants of $\dot{\gamma}$, see Bird et al (1987). Of the three possible invariants I, II, and III, I is zero due to the incompressibility condition and III turns out to be zero for shearing flows. It is not considered to be a serious restriction if III is omitted for nearly shearing flow, see Bird et al (1987), why II is the only invariant on which η depends. As already mentioned, instead of using the second invariant the magnitude of the rate–of–deformation tensor is used, hence $\eta = \eta(\text{II})$ for incompressible flow of the generalized Newtonian model.

The Criminale–Ericksen–Filbey (CEF) equation.

Each model of a Non–Newtonian fluid has its own limitations. It is therefore important to know which flow situation can be handled with which model. An important class of flows are shear flows. Various categories of shear flows are studied in Bird et al (1987), but we only will look at one type of flows, *the viscometric flows*, for which a constitutive equation will be obtained.

According to Bird et al (1987) from which the definition is taken the viscometric flow is defined to be a flow in which

- There is a one–parameter family of material surfaces, the shearing surfaces, which move isometrically, that is, the distance between any two neighboring particles in the surface is constant; and
- The volume of every fluid element is constant; and
- The lines of shear are material lines; and

- The velocity gradient $\dot{\gamma}_{21}$ is independent of time at a given particle.

The velocity gradient $\dot{\gamma}_{21}$ is the gradient seen from the shear axes at a particle where the x_1–direction is tangent to a shearing surface and the x_2–direction is normal to a shearing surface. The first two requirements define *general shear flow* and, with the third requirement, the definition of *unidirectional shear flow* is obtained. *Rectilinear shear flow* is defined by the first 3 requirements and

- The fluid particle pathlines are straight lines.

It is seen that steady rectilinear shear flow is a viscometric flow.

A constitutive equation based on the three viscometric functions is the CEF–equation, see Criminale et al (1958),

$$\tau = -\eta(\dot{\gamma})\dot{\gamma} + \tfrac{1}{2}\Psi_1(\dot{\gamma})\overset{\Delta}{\dot{\gamma}} - (\Psi_1 - \Psi_2)\{\dot{\gamma}\cdot\dot{\gamma}\}, \tag{2.31}$$

where $\overset{\Delta}{\dot{\gamma}}$ represents the lower–convected derivatives and defined as

$$\overset{\Delta}{\dot{\gamma}} = \frac{D}{Dt}\dot{\gamma} + \{(\nabla v)^{\mathrm{T}}\cdot\dot{\gamma} + \dot{\gamma}\cdot(\nabla v)\}, \tag{2.32}$$

with $\frac{D}{Dt}$ as the substantial derivative

$$\frac{D}{Dt} = \frac{\partial}{\partial t} + (v\cdot\nabla).$$

In the previous sections, the transport equations and the constitutive relations have been worked out in an orthogonal curvilinear coordinate system, but the CEF–equation will only be worked out in a cartesian system because the model will be used in modeling the flow in straight channels. Attempts to extend the study to that of a curved channel using the same model is justified when curvature effects on diffusion of momentum is neglible.

In employing the generalized Newtonian model in the solution of a flow problem, the basic equations are necessarily more complicated in detail than the corresponding Navier–Stokes equations for a constant η, but no new

conceptual difficulties are encountered, Crochet et al (1984). The first term in the CEF–equation is then handled mainly as in the Newtonian case and only the second and third terms will be written with summation indices for a cartesian coordinate system. In the second term, where the substantial derivative appears, only the convective term is of interest since only steady situations are considered. The second term $\frac{1}{2}\Psi_1 \overset{\Delta}{\dot{\gamma}} = \frac{1}{2}\Psi_1[\boldsymbol{v}\cdot\nabla\dot{\gamma} + \{(\nabla\boldsymbol{v})^{\mathrm{T}}\cdot\dot{\gamma} + \dot{\gamma}\cdot(\nabla\boldsymbol{v})\}]$ is given by

$$\tfrac{1}{2}\Psi_1 \overset{\Delta}{\dot{\gamma}}_{ik} = \tfrac{1}{2}\Psi_1\left\{v(j)\frac{\partial\dot{\gamma}_{ik}}{\partial x_j} + \frac{\partial v(j)}{\partial x_i}\dot{\gamma}_{jk} + \frac{\partial v(j)}{\partial x_k}\dot{\gamma}_{ij}\right\}, \tag{2.33}$$

and, with $\dot{\gamma}_{ik} = \frac{\partial v(i)}{\partial x_k} + \frac{\partial v(k)}{\partial x_i}$, the second term takes the form

$$\tfrac{1}{2}\Psi_1 \overset{\Delta}{\dot{\gamma}}_{ik} = \tfrac{1}{2}\Psi_1\left\{v(j)\left[\frac{\partial^2 v(i)}{\partial x_j \partial x_k} + \frac{\partial^2 v(k)}{\partial x_j \partial x_i}\right] + 2\frac{\partial v(j)}{\partial x_k}\frac{\partial v(j)}{\partial x_i} + \frac{\partial v(j)}{\partial x_i}\frac{\partial v(k)}{\partial x_j} + \frac{\partial v(j)}{\partial x_k}\frac{\partial v(i)}{\partial x_j}\right\}. \tag{2.34}$$

The third term is given by

$$(\Psi_1 - \Psi_2)\{\dot{\gamma}_{ij}\dot{\gamma}_{jk}\} = (\Psi_1 - \Psi_2)\left\{\frac{\partial v(j)}{\partial x_k}\frac{\partial v(i)}{\partial x_j} + \frac{\partial v(i)}{\partial x_j}\frac{\partial v(k)}{\partial x_j} + \frac{\partial v(j)}{\partial x_k}\frac{\partial v(j)}{\partial x_i} + \frac{\partial v(j)}{\partial x_i}\frac{\partial v(k)}{\partial x_j}\right\}. \tag{2.35}$$

The second and third terms are outlined in component form in appendix B.

2.5 CLOSURE

We have chosen to work in an orthogonal coordinate system which is curvilinear in two direction and cartesian in the third direction. In outlining the governing equations they have been worked out in a 3–D orthogonal curvilinear coordinate system which easily can be simplified to the

environment we have chosen to work in.

In modeling the nature of fluids, the well known Navier–Stokes equations have been outlined for the Newtonian fluids. The Non–Newtonian fluids have been modeled with the viscometric functions η, Ψ_1, and Ψ_2. Two constitutive relations have been given. The first one, the generalized Newtonian model, which takes into account the shear rate dependent viscosity η, and the other model which, in addition to η, takes into account the normal stress differences. The second model, the CEF–model, which will mainly be used in straight channels, is for that reason written in cartesian coordinates.

CHAPTER 3

DISCRETISATION

3.1 INTRODUCTION

In order to solve the differential equations proposed in chapter 2 it is necessary to discretise the equations. An interpolation practice which expresses the cell face values in terms of the neighbour node values in order to obtain a closed set of algebraic equations is outlined.

From a mathematical point of view, a differential equation can take different forms without loss of information, but from a numerical point of view the form of the equations is important for the accuracy of the calculation. Section 2 describes the different conservation forms and give the form which is used for the present work.

In the preceding chapter the governing equations were derived with use of the scale factors. In section 3 these equations are written in a form where all quantities are in physical dimensions.

With the equations set up in section 3, the general form which they may take is shown in section 4 where the assembled equations yield a system of linear algebraic equations. The associated matrix structure is outlined for a 7 point discretisation molecule.

In section 5, the desired properties for differencing schemes are described. In the following section 6, several discretisation schemes are considered. The final form of the equations with the chosen differencing scheme is given in section 7.

Closing remarks are given in section 8.

3.2 CONSERVATION FORM

In using the finite volume approach for discretization of the transport equations it is desirable to keep the equations on a conservative form. A differential equation on a conservative form is given by, see Berge (1982),

$$\frac{\partial}{\partial t}A + \frac{\partial}{\partial x_j}B_j + C = 0, \tag{3.1}$$

where A, B, and C are functions of the unknowns and C does not contain derivatives of the unknowns.

The unique proporties of the conservative form, see Hirsch (1988), is illustrated by a little example.

With u being velocity in the x direction and f the x component of the flux vector the conservation law is given by

$$\frac{\partial u}{\partial t} + \frac{\partial f}{\partial x} = q. \tag{3.2}$$

The discretization of eq. (3.2) at a point i with a central difference applied to the mesh of fig. 3.1 is

$$\frac{\partial u_i}{\partial t} + \frac{f_{i+\frac{1}{2}} - f_{i-\frac{1}{2}}}{\Delta x} = q_i. \tag{3.3}$$

The same discretization applied to point i+1 gives

$$\frac{\partial u_{i+1}}{\partial t} + \frac{f_{i+\frac{3}{2}} - f_{i+\frac{1}{2}}}{\Delta x} = q_{i+1}, \tag{3.4}$$

and at i–1

$$\frac{\partial u_{i-1}}{\partial t} + \frac{f_{i-\frac{1}{2}} - f_{i-\frac{3}{2}}}{\Delta x} = q_{i-1}. \tag{3.5}$$

The sum of these three equations is a consistent discretization of the conservation law for the cell AB

$$\frac{\partial}{\partial t}\frac{(u_i + u_{i+1} + u_{i-1})}{3} + \frac{f_{i+\frac{3}{2}} - f_{i-\frac{3}{2}}}{3\Delta x} = \frac{1}{3}(q_i + q_{i+1} + q_{i-1}), \tag{3.6}$$

since the flux contribution at internal points have cancelled out.

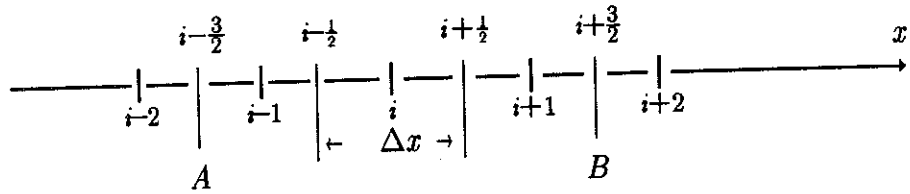

Fig. 3.1 *Mesh cells in one–dimension with equidistant mesh (grid point spacing) Δx; cell AB has the length $3\Delta x$.*

In general, if a summation is made of the difference equations for all the cells in a domain, the inner fluxes cancel, leaving the net transport flux across the solution domain balanced by internal sources and boundary fluxes. This guaranties overall conservation of the transported quantity, see Roache (1976), and for that reason equations which possess this property are said to be written in a *strong conservation form.*

With f a function of the unknown u, eq. (3.2) can be expressed as

$$\frac{\partial u}{\partial t} + \frac{\partial f}{\partial u}\frac{\partial u}{\partial x} = q, \tag{3.7}$$

and with $\frac{\partial f}{\partial u} = a(u)$ eq. (3.7) takes the form

$$\frac{\partial u}{\partial t} + a\frac{\partial u}{\partial x} = q, \tag{3.8}$$

which is in a *non–conservative* form. Applying second–order central difference at mesh point i results in

$$\frac{\partial u_i}{\partial t} + a_i\frac{u_{i+\frac{1}{2}} - u_{i-\frac{1}{2}}}{\Delta x} = q_i,$$

where a_i can be estimated as $a_i = (a_{i+\frac{1}{2}} + a_{i-\frac{1}{2}})/2$. If similar equations are written for i+1 and i–1 and summed, a discretised equation for the cell AB in fig. 3.1 is obtained,

$$\frac{\partial}{\partial t}\frac{(u_i + u_{i+1} + u_{i-1})}{3} + (a_{i+\frac{3}{2}} + a_{i-\frac{3}{2}})\frac{u_{i+\frac{3}{2}} - u_{i-\frac{3}{2}}}{6\Delta x} - \frac{q_i + q_{i+1} + q_{i-1}}{3} =$$

$$- (a_{i+\frac{1}{2}} - a_{i-\frac{3}{2}})\frac{u_{i+\frac{3}{2}} - u_{i-\frac{1}{2}}}{6\Delta x} + (a_{i+\frac{3}{2}} - a_{i-\frac{1}{2}})\frac{u_{i+\frac{1}{2}} - u_{i-\frac{3}{2}}}{6\Delta x}. \tag{3.9}$$

A direct discretisation of eq. (3.8) on the cell AB would have given the left–hand side of eq. (3.9) with a vanishing right–hand side. It is therefore seen that the discretisation of the non–conservative form of the equation gives rise to internal sources, equal in this case to the right–hand side of eq. (3.9). From a mathematical point of view there is no difference between eq. (3.2) and eq. (3.7), but it is obvious that the corresponding discretised equations (eq. (3.6) and eq. (3.9)) are different. It is seen that the internal sources do vanish as $\Delta x \to 0$, but this is of little consolation in practical computation with finite Δx. From a numerical point of view, the internal sources appearing in the non–conservative form are considered as a numerical error and in order to avoid this error a conservative formulation is preferred. It can be achieved if the base vectors at any point are expressed in terms of arbitrary, but spacially constant base vectors and the obvious choice would be to use cartesian base vectors i_i as a fixed basis, see Peric (1985). On a staggered grid this approach will cause problems and oscillations are usually encontered, but since the staggered grid is used as a remedy to remove the zig–zag field which the pressure field might cause (see chapter 4 for grid arrangement) we are not going to use constant base vectors and a strong conservative form is not obtained. We already know from chapter 2 that the chosen base vectors are unit base vectors which follow the curved coordinate lines. When using a set of base vectors which follow the curvilinear coordinates the curvature terms (see chapter 2) will appear as undifferentiated terms and the form of the equations is said to be a *semi–strong conservation form* which is the form we are going to use.

The semi–strong conservation form has the advantage that it can be cast into a form which follows a general transport equation. A general transport

equation contains convective and diffusive terms in the actual directions of base vectors and source terms. The advantage of this form is that the same solution procedure can be used in solving different transport equations since it contains common terms. The main difference is the terms contained in the source term. A general transport equation in orthogonal curvilinear coordinates is

$$\frac{1}{h}\left\{\frac{h}{h_k}\rho v(k)\varphi\right\}_{,k} = \frac{1}{h}\left\{\frac{h}{h_k^2}\Gamma_\varphi \varphi_{,k}\right\}_{,k} + s_\varphi, \tag{3.10}$$

where φ is the unknown quantity which is transported. The continuity equation is obtained from eq. (3.10) by setting $\varphi = 1$ and $s_\varphi = 0$ and the equation of motion is obtained by setting $\varphi = v(i)$ and $\Gamma = \mu$. Comparing eq. (3.10) with eq. (2.16) it is seen that they take exactly the same form and eq. (3.10), as it stands, is in a conservative form and it incorporates variation in both density and as diffusion coefficient. The source term contains all the other terms which cannot be cast into the convection and diffusion terms.

In using a semi–strong conservation form the non–conservative terms appear among other expressions in the source term. In the equation of continuity the source term is zero, whereas in the equation of motion the pressure gradient and the curvature terms are contained in source terms. In the Navier–Stokes equations, where $\varphi = v(i)$ and $\Gamma = \mu$ in eq. (3.10), the source terms take the form

$$\rho \frac{v(k)}{h_i h_k}\left\{v(k)h_{k,i} - v(i)h_{i,k}\right\}; \tag{3.11a}$$

$$-\frac{1}{h_i}p_{,i} + \frac{1}{h}\left\{\left[\mu\frac{h}{h_i^2}\left(v(i)_{,i} + 2\sum_s \frac{v(s)}{h_s}h_{i,s}\right)\right]_{,i}\right.$$

$$\left. + \sum_j\left[\mu\frac{h}{h_j}\left(\frac{h_j}{h_i}\left(\frac{v(j)}{h_j}\right)_{,i} - \frac{v(i)}{h_i h_j}h_{i,j}\right)\right]_{,j}\right\} \tag{3.11b}$$

$$+ \sum_j \mu\frac{h_{i,j}}{h_i h_j}\left[\frac{h_i}{h_j}\left(\frac{v(i)}{h_i}\right)_{,j} + \frac{h_j}{h_i}\left(\frac{v(j)}{h_j}\right)_{,i}\right] - 2\mu\sum_j \frac{h_{j,i}}{h_i h_j}\left[\frac{1}{h_j}v(j)_{,j} + \sum_l \frac{v(l)}{h_j h_l}h_{j,l}\right].$$

$$s \neq i,\ j \neq i,\ l \neq j$$

Equation (3.11a) gives the curvature terms being due to the convective flow, whereas eq. (3.11b) contains the pressure gradient and the curvature terms being due to the diffusion flow.

In this work, the general transport equation will be used in handling both Newtonian and Non-Newtonian fluids. Non-Newtonian fluids with "memory" are usually simulated with the equation of motion and a transport equation for the stress, see Crochet et al (1984). In using the power law model eq. (2.28) to describe the shear-rate dependent viscosity the flow problem can be solved as for a Newtonian viscous fluid with variable viscosity and eq. (3.10) and eq. (3.11) together with the powerlaw model describe to full extent the generalized Newtonian fluid.

In using the general transport equation to describe the conservation of momentum and the CEF-model to express the constitutive relation it is seen that only the term which contains the shear dependent viscosity is contained in the diffusion terms. Whereas the terms which describe the normal stress differences must be contained in the source term. When treating the normal stress difference terms as source terms they will be handled in an explicit manner.

The advantage of treating the normal stress terms as explicit terms is that no special attention has to be taken to the boundary conditions. The boundary conditions are treated in chapter 6. The disadvantage of explicit terms compared to implicit terms is usually larger cpu consumption for the same accuracy of the computation. Larger cpu consumption might not be the case in our problem because the generalized Newtonian term in the CEF-model has a much bigger influence on the flow field than the first and second normal stress differences. In other words, the main flow couples strongly to the secondary flow or the main flow drives the secondary flow which has little influence on the main flow. This coupling justifies the splitting of the extra-stress tensor in a part which is treated fully implicitly and a part which is treated explicitly. The main disadvantage of the splitting in our case is the accuracy of the computation. For the splitting used, to obtain the same accuracy as in a full implicit treatment, a finer grid is needed and through that, larger cpu consumption occurs. But again, because of the coupling, the accuracy of the secondary flow is mainly determined through the accuracy of the main flow, why the grid density is determined from the conditions of the main flow. The cpu consumption is given in chapter 8.

3.3 THE TRANSPORT EQUATION

In the preceding section, the general transport equation is shown. It takes a semi-strong conservation form when used in orthogonal curvilinear coordinates and will be used for Newtonian fluids as well as for Non-Newtonian fluids. The reason why the general transport equation can be used for the Non-Newtonian fluids of interest is that the geometries which will be considered have a flow field with a dominant velocity component.

In finite volume calculations, the computational domain is discretized into a number of cells, or control volumes, formed by coordinate surfaces. The volume of a control volume (CV) in physical dimension, see appendix A, is

$$\Delta V = h dx_1 dx_2 dx_3 = \Delta\xi\Delta\eta\Delta\zeta. \tag{3.12}$$

It is seen that when working in the physical domain (ξ,η,ζ) it is not necessary to use the scale factors directly. The coordinate system ξ, η, and ζ follows the x_1, x_2, and x_3 system, but the distances along the coordinate lines are always in physical dimension of length. Since the volume of a CV can be given in physical dimensions, as the last equality of eq. (3.12), it can also be convenient to cast the general transport equation into a form where all quantities are in physical dimensions (the velocity components are already given in physical dimension of length per time, see chapter 2 and also appendix A). With the scale factors given by eq. (2.24), the physical distances by eq. (A8), and the velocities $v(1)$, $v(2)$, and $v(3)$ by u, v, and w, respectively, the transport equation (3.10) takes the form, see also Antonopoulos et al (1976)

$$\frac{1}{\Delta\eta}\frac{\partial}{\partial\xi}(\rho u\Delta\eta\varphi) + \frac{1}{\Delta\xi}\frac{\partial}{\partial\eta}(\rho v\Delta\xi\varphi) + \frac{\partial}{\partial\zeta}(\rho w\varphi) =$$

$$\frac{1}{\Delta\eta}\frac{\partial}{\partial\xi}(\Gamma_\varphi\Delta\eta\frac{\partial\varphi}{\partial\xi}) + \frac{1}{\Delta\xi}\frac{\partial}{\partial\eta}(\Gamma_\varphi\Delta\xi\frac{\partial\varphi}{\partial\eta}) + \frac{\partial}{\partial\zeta}(\Gamma_\varphi\frac{\partial\varphi}{\partial\zeta}) + s_\varphi. \tag{3.13}$$

In table 3.1, the expressions for s_φ are given for the components of the momentum equations when φ stands for the velocity components. Note, that these forms assume a coordinate system which is curvilinear orthogonal in the ξ and η direction and cartesian orthogonal in the ζ-direction.

The equation of continuity which is a special case of the general transport equation (3.10) takes the corresponding form

φ	s_φ
u	$-\frac{\partial p}{\partial \xi} - \frac{\rho uv}{\Delta\xi}\frac{\partial \Delta\xi}{\partial \eta} + \frac{\rho v^2}{\Delta\eta}\frac{\partial \Delta\eta}{\partial \xi}$ $+ \frac{1}{\Delta\eta}\frac{\partial}{\partial \xi}\left\{\Delta\eta\mu\left[\frac{\partial u}{\partial \xi} + 2\frac{v}{\Delta\zeta}\frac{\partial \Delta\xi}{\partial \eta}\right]\right\}$ $+ \frac{1}{\Delta\xi}\frac{\partial}{\partial \eta}\left\{\Delta\xi\mu\left[\frac{\partial v}{\partial \xi} - \frac{v}{\Delta\eta}\frac{\partial \Delta\eta}{\partial \xi} - \frac{u}{\Delta\xi}\frac{\partial \Delta\xi}{\partial \eta}\right]\right\}$ $+ \frac{\mu}{\Delta\xi}\frac{\partial \Delta\xi}{\partial \eta}\left\{\frac{\partial v}{\partial \xi} + \frac{\partial u}{\partial \eta} - \frac{v}{\Delta\eta}\frac{\partial \Delta\eta}{\partial \xi} - \frac{u}{\Delta\xi}\frac{\partial \Delta\xi}{\partial \eta}\right\}$ $- \frac{2\mu}{\Delta\eta}\frac{\partial \Delta\eta}{\partial \xi}\left\{\frac{\partial v}{\partial \eta} + \frac{u}{\Delta\eta}\frac{\partial \Delta\eta}{\partial \xi}\right\} + \frac{\partial}{\partial \zeta}\left\{\mu\frac{\partial w}{\partial \xi}\right\}$
v	$-\frac{\partial p}{\partial \eta} - \frac{\rho uv}{\Delta\eta}\frac{\partial \Delta\eta}{\partial \xi} + \frac{\rho u^2}{\Delta\xi}\frac{\partial \Delta\xi}{\partial \eta}$ $+ \frac{1}{\Delta\xi}\frac{\partial}{\partial \eta}\left\{\Delta\xi\mu\left[\frac{\partial v}{\partial \eta} + 2\frac{u}{\Delta\eta}\frac{\partial \Delta\eta}{\partial \xi}\right]\right\}$ $+ \frac{1}{\Delta\eta}\frac{\partial}{\partial \xi}\left\{\Delta\eta\mu\left[\frac{\partial u}{\partial \eta} - \frac{v}{\Delta\eta}\frac{\partial \Delta\eta}{\partial \xi} - \frac{u}{\Delta\xi}\frac{\partial \Delta\xi}{\partial \eta}\right]\right\}$ $+ \frac{\mu}{\Delta\eta}\frac{\partial \Delta\eta}{\partial \xi}\left\{\frac{\partial v}{\partial \xi} + \frac{\partial u}{\partial \eta} - \frac{v}{\Delta\eta}\frac{\partial \Delta\eta}{\partial \xi} - \frac{u}{\Delta\xi}\frac{\partial \Delta\xi}{\partial \eta}\right\}$ $- \frac{2\mu}{\Delta\xi}\frac{\partial \Delta\xi}{\partial \eta}\left\{\frac{\partial u}{\partial \xi} + \frac{v}{\Delta\xi}\frac{\partial \Delta\xi}{\partial \eta}\right\} + \frac{\partial}{\partial \zeta}\left\{\mu\frac{\partial w}{\partial \eta}\right\}$
w	$-\frac{\partial p}{\partial \zeta} + \frac{\partial}{\partial \zeta}\left\{\mu\frac{\partial w}{\partial \zeta}\right\} + \frac{1}{\Delta\eta}\frac{\partial}{\partial \xi}\left\{\mu\Delta\eta\frac{\partial u}{\partial \zeta}\right\}$ $+ \frac{1}{\Delta\xi}\frac{\partial}{\partial \eta}\left\{\mu\Delta\xi\frac{\partial v}{\partial \zeta}\right\}$

Table 3.1 *Expressions for the source term s_φ in the momentum equations when φ takes either the value u, v, or w for an orthogonal coordinate system which is curvilinear in the ξ* and *η direction and cartesian in the ζ direction.*

$$\frac{1}{\Delta\eta}\frac{\partial}{\partial\xi}(\rho u\Delta\eta) + \frac{1}{\Delta\xi}\frac{\partial}{\partial\eta}(\rho v\Delta\xi) + \frac{\partial}{\partial\zeta}(\rho w) = 0. \qquad (3.14)$$

3.4 FORM OF DISCRETISED EQUATION

A difference equation corresponding to eq. (3.13) can be derived by use of the finite volume approach which has been adapted here. In the finite volume approach equations are integrated over a finite volume of CVs, in order to ensure the conservation property of the differential equations. In this process, using Gauss' theorem, the volume integrals can be convected into surface integrals over the six faces of the control volumes. Thus, eq. (3.13) takes the following discrete form

$$C_e\varphi_e - C_w\varphi_w + C_n\varphi_n - C_s\varphi_s + C_u\varphi_u - C_d\varphi_d =$$

$$D_e(\varphi_E - \varphi_P) - D_w(\varphi_P - \varphi_W) + D_n(\varphi_N - \varphi_P) - D_s(\varphi_P - \varphi_S)$$

$$+ D_u(\varphi_U - \varphi_P) - D_d(\varphi_P - \varphi_D) + s_\varphi\Delta V, \qquad (3.15)$$

where e.g. $C_e = (\rho u\Delta A)_e$ is the mass flow rate normal to the "e" face of the CV and $D_e = (\Gamma\Delta A/\Delta x)_e$ is the diffusion coefficient at the "e" face, see fig. 3.2 for location of E, e, W, w, etc. ΔV and ΔA are the volume and the face area of the CV, respectively.

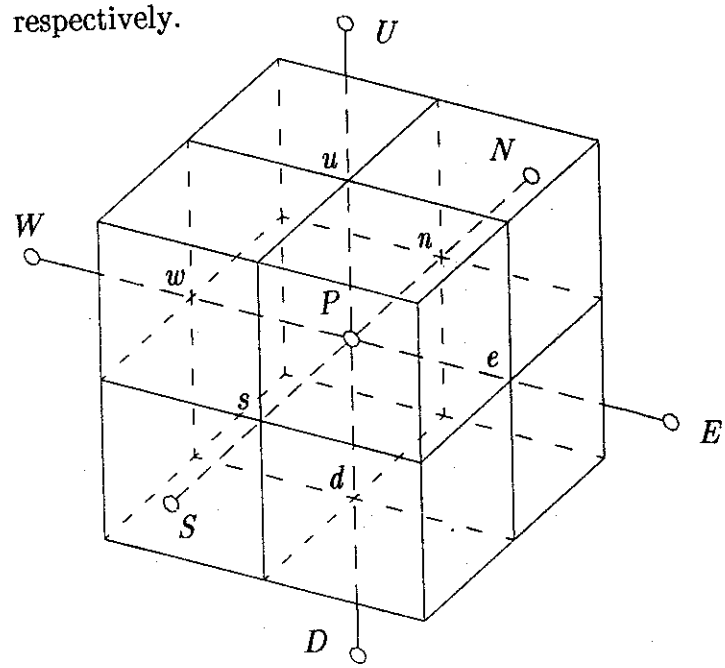

Fig. 3.2 *A control volume showing face locations and associated neighbours.*

The ratio of the mass flow rate C_e and the diffusion coefficient D_e gives the ratio of convection to diffusion. The ratio is named the cell Peclet number and defined by

$$\mathrm{Pe}_e = \frac{\rho u \Delta x}{\Gamma}.$$

Similar cell Peclet numbers are given for the other cells. A global Peclet number is also defined and take the form

$$\mathrm{Pe} = \frac{\rho UL}{\Gamma},$$

where U and L are a characteristic velocity and a characteristic length of the problem, respectively.

In order to derive eq. (3.15) from eq. (3.13) it is seen that the variation of φ along coordinate lines approximated by some function of distance is needed to fit selected nodes. Central differencing has been used for the diffusion term whereas no approximation has yet been made for the convected face values φ_e, φ_n, etc. These values are considered in detail in a following section. The unknown φ and the fluxes are regarded as uniformly distributed over the CV and the control surfaces, respectively, which requires that the CV is small. The source term is approximated by a constant as seen from eq. (3.15).

Even if the source term is considered as a constant in the discretisation procedure it is important to account for the variable φ on which the source term might depend. The source term will be linearized according to

$$s_\varphi = s_p \varphi_P + s_c, \tag{3.16}$$

where s_p is the coefficient of φ_P and s_c is the constant part of s_φ. A linearization as eq. (3.16) is only done if s_p takes a negative value in order to stabilise the equations and ensure fast convergence, see Patankar (1980).

After the convective face values φ_e, φ_n, etc. are calculated through interpolation from their neighbouring nodal values the discretised equation is cast into the general form

$$a_p \varphi_P = \sum_m a_m \varphi_m + b, \tag{3.17a}$$

$$a_p = \sum_m a_m + s_p, \tag{3.17b}$$

where a's and b express combined effects of transport and sources, $\sum_m \equiv$ summation over coefficients linking to neighbours, and a_p is the center node coefficient. Every node P is assembled by an equation as eq. (3.17), yielding a closed set, see Gosman et al (1969). Since eq. (3.17) exists for each interior computational node the numerical solution procedure entails solving a system of N equations in N unknowns where N is the total number of nodes. The total system of linear algebraic equations results in the matrix equation

$$\boldsymbol{A}\boldsymbol{x} = \boldsymbol{b} \tag{3.18}$$

where $\boldsymbol{A}$ is coefficient matrix, $\boldsymbol{x}$ is solution vector containing the unknowns φ, and $\boldsymbol{b}$ is right hand side containing sources.

The diagonal elements of the coefficient matrix $\boldsymbol{A}$ consist of the a_p coefficients and the non–zero off–diagonal elements correspond to the $-a_m$ coefficients. Row i in eq. (3.18) corrosponds to eq. (3.17a) rewritten as $a_p\varphi_p - \sum_m a_m\varphi_m = b$. Fig. 3.3 shows the structure of the coefficient matrix $\boldsymbol{A}$ which possesses seven non–zero diagonal elements in three dimensions. The matrix is of banded form. The total number of unknowns in each coordinate direction are given by N_i, N_j and N_k and ordered such that index i is increasing first, then j and lastly k. In chapter 7, several ways to solve the system given by eq. (3.18) are outlined.

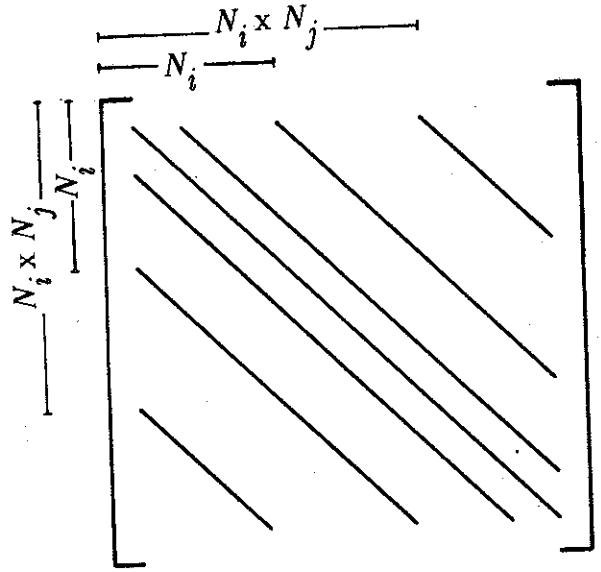

Fig. 3.3 *Matrix structure using a 7 point "molecule" for discretisation in 3–D.*

3.5 DESIRED PROPORTIES FOR DIFFERENCING SCHEMES

Conservation.

In section 3.2 it was stated that keeping the governing equations in a conservative form will be an advantage numerically since it gives rise to no numerical sources. Roache (1976) gives examples where a non–conservative form in compressible flows can give a more accurate solution than a conservative form but in general, conservative systems give more accurate results.

To satisfy the conservation law a value φ_e must be represented by the same value at the "e" face of CV P and the "w" face of CV E. This guaranties that the conservation of φ represented by eq. (3.13) must hold, whether the intergral is over the entire domain or a single CV. The flux leaving one CV face must be equal to the flux entering the adjacent CV face which, by Patankar (1980), is named the *consistency at control volume faces.*

The consistency at CV faces is obtained by having the same derivative with respect to distance of φ along a normal to a face, approaching the face either along the positive or negative side. From this it can be deduced that at least a linear variation between two adjacent points must be taken. Parabola and higher ordens variations do not violate the consistency rule, but if a stepwise profile is taken a slope at the CV face is not defined and the consistency rule is violated. In integrating eq. (3.13) a stepwise variation is assumed for the source term and it is hereby seen why our formulation is named a semi–strong conservation form since the curvature terms, which are included in the source term, do not take the same value approaching a CV face from either the positive or negative side.

Stability and boundedness.

In order to avoid overshoot, undershoot, or wiggles a differencing scheme has to be bounded. In a steady state problem and in absence of sources the interior of a domain should be bounded by the minimun and maximum values of the boundaries, see Carrier & Pearson (1976),

$$\min(\varphi_B) \leq \varphi \leq \max(\varphi_B). \tag{3.19}$$

To obtain the boundedness of eq. (3.19) it is sufficient to require that all coefficients have the same sign, positive sign is chosen, and that the sum of the neighbours is equal to the coefficient of the main node. Including sources, linearized according to eq. (3.16) for s_p negative, the main node coefficient must include the negative s_p coefficient in addition to the sum already obtained according to eq. (3.17b). The positive sign requirement states that an increase in a value φ at one node should, with other conditions remaining unchanged, lead to an increase in the value at the neighbouring nodes. The other requirement implies that the value φ_p at the central node is a weighted avarage of the neighbour values φ_m.

With the requirement that the sum of the neighbour coefficients is equal to the main node coefficient and with a Dirichlet boundary condition imposed it will hold, at least for one node, that

$$\sum_{j \neq i} \left| \frac{a_{ij}}{a_{ii}} \right| < 1,$$

which with the requirement of positive coefficients implies that the matrix is *positiv definit* ($\boldsymbol{x}^T \boldsymbol{A} \boldsymbol{x} > 0$, $0 \neq \boldsymbol{x} \in R^n$). A positiv definit matrix is an adequate condition to ensure convergence for all iterative solution methods. If one of the requirements is violated instabilities may occour, but even if boundedness is a desired feature of the discretisation scheme not all schemes are bounded. Unbounded schemes may be used to enhance the accuracy according to a Taylor series expansion analysis, (TSE) analysis, see next section.

Transportiveness.

A differencing scheme is said to possess the ability of transportiveness if a perturbation in a transport property is convected only in the direction of the velocity, Roache (1976). Due to diffusion the perturbation will spread in all directions, but it should only be carried in the direction of velocity. With no flow (Pe = 0) the perturbation will diffuse evently in all directions and a constant value of φ is indicated by a circle in fig 3.4, whereas flow with no diffusion (Pe $\rightarrow \infty$) gives a straight line of constant φ. Intermediate values of the Peclet number give elliptical contours of constant φ, see fig 3.4. Failure to obey the transportiveness requirement may give rise to unrealistic results.

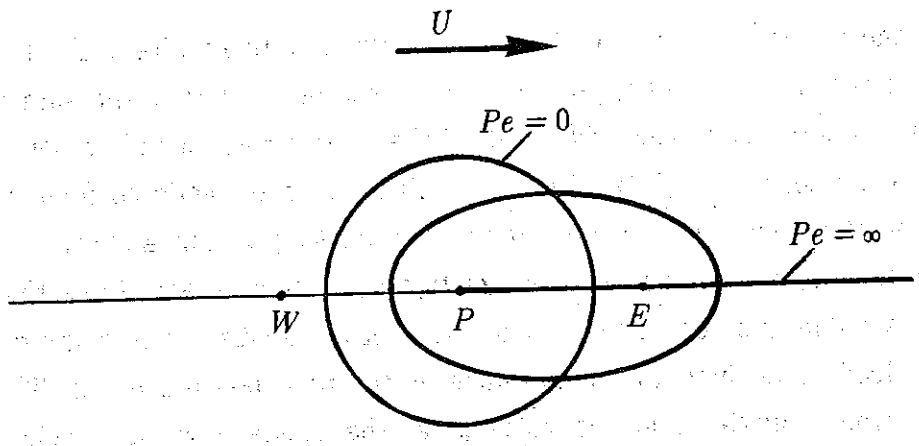

Fig. 3.4 *Transport property shown for constant value of φ at different global Peclet numbers.*

3.6 DIFFERENCING SCHEME

In order to obtain the face values φ_e, φ_n etc an interpolation practice has to be described in evaluating the convective fluxes. In the following schemes only face values at the "e" faces are going to be considered. The other face values can easily be derived when the expression for the "e" face is known.

Central Differencing Scheme (CDS).

Central differencing was used in approximating the diffusive fluxes. With the same approximation for the convective fluxes the face value between P and E takes the form

$$\varphi_e = \varphi_E f_e + (1-f_e)\varphi_P, \tag{3.20}$$

where $f_e = \dfrac{\xi_e - \xi_P}{\xi_E - \xi_P}$, see fig. 3.5.

Thus, φ_e is by eq. (3.20) given through a linear variation between of φ P and E. With a uniform grid f_e becomes $\frac{1}{2}$ and φ_e would take the same form with a quadratic interpolation.

With the "e" face value given by eq. (3.20) the E coefficient a_e, with eq.

(3.15), is given by

$$a_e = D_e - C_e f_e. \tag{3.21}$$

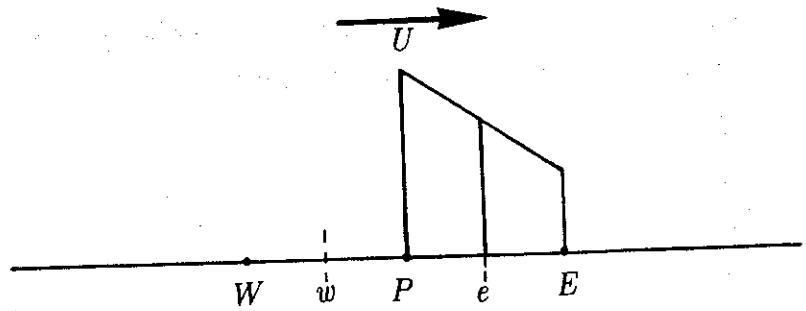

Fig. 3.5 *Interpolation in central differencing.*

To obtain boundedness it was earlier stated that the coefficients had to have the same sign, positive sign was chosen. When the Peclet number (defined earlier as C/D) becomes greater than $1/f_e$ the coefficient a_e becomes negative. To avoid negative coefficients it is seen that the CDS only can be used for low Peclet numbers (on a uniform grid the Peclet number must be lower than 2), high Peclet numbers make the matrix non–diagonal dominant and convergence is not assured, Spalding (1972).

Imploying a TSE analysis it is shown that the CDS is second order accurate with the truncation error $\frac{1}{6}\rho u(\Delta\xi)^2\frac{\partial^3\varphi}{\partial\xi^3}$ (the leading higher order neglected term). As stated above, the boundedness requirement is not obained at high Peclet numbers, but the transport property is also violated because it is physically unrealistic that downstream information should influence face values for Pe $\to \infty$.

Upwind Differencing Scheme (UDS).

In order to obtain a scheme which does not have the drawbacks of the CDS, the upwind differencing scheme can be used. In the UDS, the cell face value is taken as the value from the upstream "doner" cell, see fig. 3.6a and fig. 3.6b, along the same coordinate line, thus

$$\varphi_e = \begin{cases} \varphi_P \text{ if } C_e > 0 \\ \varphi_E \text{ if } C_e < 0 \end{cases}. \tag{3.22}$$

Employing eq. (3.22) and eq. (3.15), the a_e coefficient takes the form

$$a_e = D_e + \max(-C_e, 0). \tag{3.23}$$

This scheme is both bounded and has the transportive property which makes the resulting matrix unconditionally diagonal dominant.

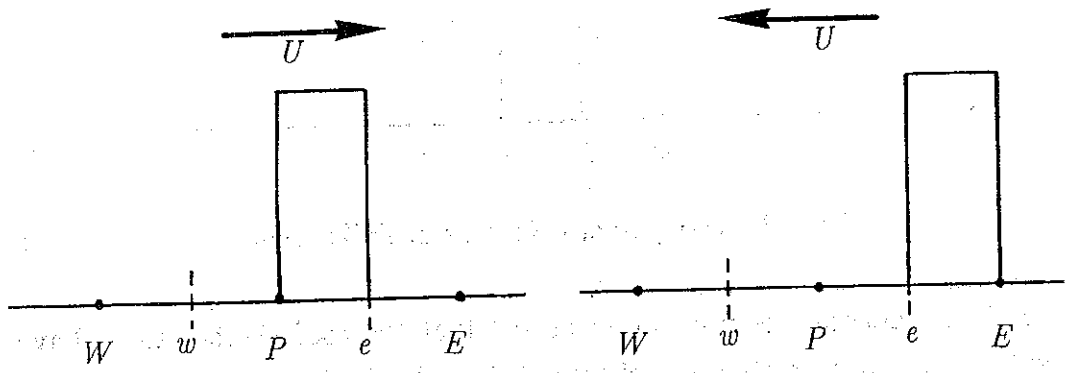

Fig. 3.6 *Interpolation in upwind differencing.*

A TSE analysis shows that the UDS is only first order accurate with the truncation error $-\frac{1}{2}\rho u \Delta\xi \frac{\partial^2 \varphi}{\partial \xi^2}$. Since the truncation error is proportional to $\frac{\partial^2 \varphi}{\partial \xi^2}$ the error is said to be diffusion–like with an artificial viscosity $\Gamma_a = \frac{1}{2}\rho u \Delta\xi$. The artificial viscosity in the truncation error should not be considered as an undesired feature of the UDS, at least at high Peclet numbers, but rather a term which makes the scheme stable. In a paper by Raithby (1976a), the transportive property of the UDS is highly appreciated, whereas "false" diffusion is stated as a drawback of the UDS. False diffusion is encountered when flow to grid alignment is violated and if a strong gradient of the dependent variable normal to the flow exist. An approximate expression for the false diffusion coefficient for a two–dimensional situation is given by Patankar (1980),

$$\Gamma_{\text{false}} = \frac{\rho U \Delta\xi \Delta\eta \sin 2\theta}{4(\Delta\eta \sin^3\theta + \Delta\xi \cos^3\theta)}, \tag{3.24}$$

where U is the resulting velocity and θ the angle made between the velocity vector and the ξ–direction. It is seen that no false diffusion is present when the flow is aligned with grid. On the other hand, the false diffusion is most serious when the angle is 45^0.

Linear Upwind Differencing Scheme (LUDS).

The previous two one–dimensional schemes are based on the closest neighbour nodes, whereas the linear upwind differencing scheme is based on the two closest upstream neighbour nodes on the same coordinate line, see fig. 3.7a and fig. 3.7b. Here, the cell face value is given by

$$\varphi_e = \begin{cases} \varphi_P + (\varphi_P - \varphi_W)(1-f_w) & \text{if } C_e > 0 \\ \varphi_E + (\varphi_E - \varphi_{EE})f_e & \text{if } C_e < 0 \end{cases}, \tag{3.25}$$

where $f_e = \dfrac{\xi_{EE} - \xi_e}{\xi_{EE} - \xi_E}$, $f_w = \dfrac{\xi_e - \xi_W}{\xi_P - \xi_W}$, and φ_{EE} is the unknown at the node next to E away from the P node.

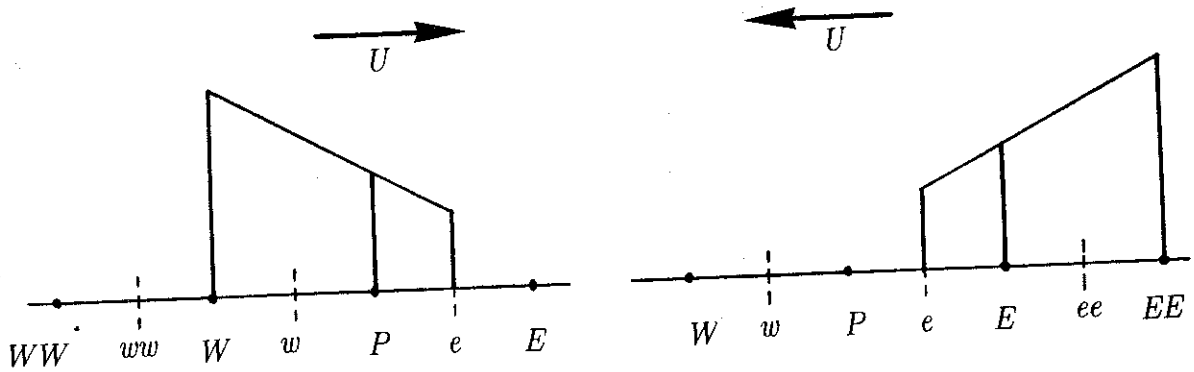

Fig. 3.7 *Extrapolation in linear upwind differencing.*

In order to use a "higher" order scheme, as the LUDS, it is necessary to use 9 points for discretization whereas only 5 points are needed if the CDS or UDS is used in two–dimensions. In three dimensions, the LUDS requires 13 points where only 7 points are needed when using CDS or UDS. With the face value given by eq. (3.25), the a_e and a_{ee} coefficients are expressed as

$$\begin{aligned} a_e &= D_e + \max(-C_e,0)f_e + \max(-C_w,0)f_p \\ a_{ee} &= -\max(-C_e,0)f_e, \end{aligned} \tag{3.26}$$

where $f_p = \dfrac{\xi_P - \xi_W}{\xi_E - \xi_P}$ and a_{ee} now enters the sum in eq. (3.17).

It is seen that the transportive proporty requirement is obeyed, but the

far neighbouring points *EE*, *WW*, *NN*, *SS*, *UU*, and *DD* are either negative or zero depending on flow direction. This gives a scheme which is not unconditionally bounded and hence not a diagonal dominant matrix which might give overshoots and/or undershoots in a solution procedure. A TSE analysis gives a leading truncation error of $-\frac{1}{3}\rho u(\Delta\xi)^2\frac{\partial^3\varphi}{\partial\xi^3}$ and compared with UDS which also preserve transportiveness it is expected that LUDS is more accurate than UDS. This is confirmed by Peric (1985) among others, but also that LUDS produces overshoots and undershoots if the variation of φ is not sufficiently "smooth".

In the LUDS the cell face value is extrapolated from the two closests points whereas in the Quadratic Upwind Differencing Scheme (QUDS) the cell face values are interpolated from a quadratic function. The situation is outlined in fig. 3.8a and fig. 3.8b.

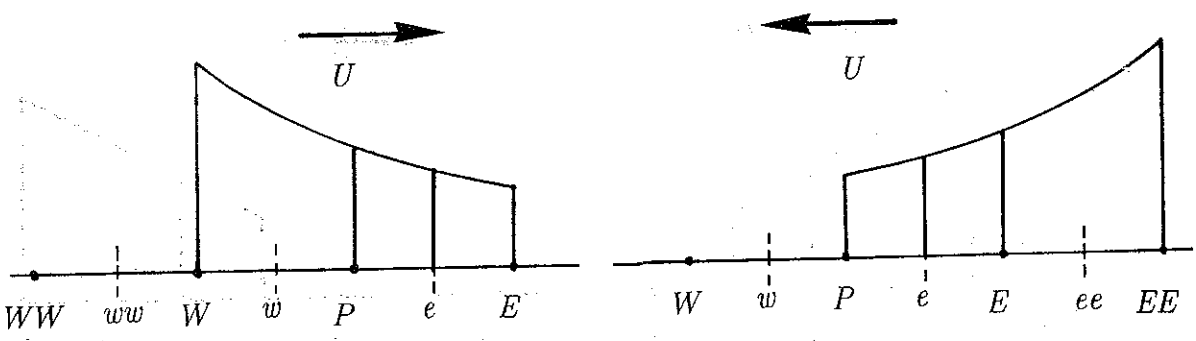

Fig. 3.8 *Interpolation in quadratic upwind differencing.*

Even though the leading truncation error $\frac{1}{24}\rho u(\Delta\xi)^2\frac{\partial^3\varphi}{\partial\xi^3}$ is lower than in the LUDS case not only the far neighbours might become negative, but also the closest neighbours can become negative if the Peclet number is greater than 8/3 on a uniform grid, see Lai (1983). Also, the transportive proporty is not obtained since a downstream point is used in the discretization. Even if the QUDS is the most accurate scheme considered until now (seen from a TSE analysis) it is not used to a great extent because of the violation of boundedness and transportiveness.

Skew Upwind Differencing Scheme (SUDS).

In order to take advantage of boundedness and transportiveness of the UDS Raithby (1976b) designed a scheme which evaluates the cell face value

by tracking back along the local streamline and then using linear interpolation. A two–dimensional situation where the "e" face value is found by linear interpolation between φ_P and φ_S is shown in fig. 3.9 . In a 2–D flow calculation the scheme uses 9 points whereas 27 points are needed in a 3–D situation.

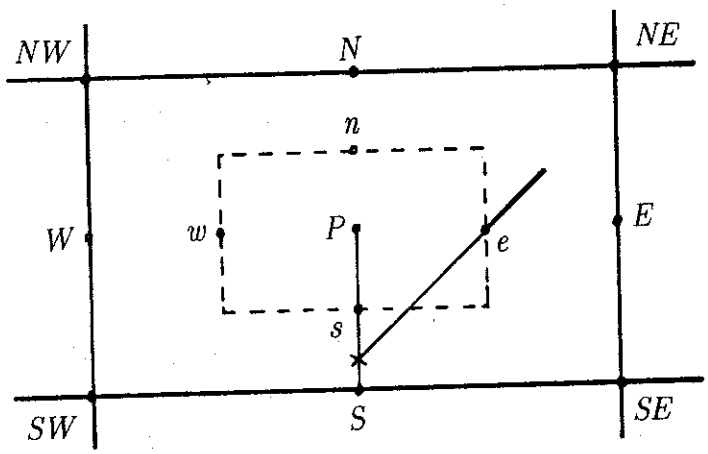

Fig. 3.9 *Interpolation in skew upwind differencing*

The main advantage by the SUDS is that false diffusion is highly reduced compared with UDS, but the scheme is still only first order accurate, see Lai (1983). The transportiveness is maintained, but the scheme is not always bounded. The corner coefficients (*SE*, *SW*, *NE*, and *NW*) are always positive whereas the other coefficients (*E*, *S*, *W*, and *N*) might become negative. To obtain the stable and bounded features of the UDS and the high accuracy of the SUDS an elegant blending of the two schemes has been developed by Lai (1983) and named Bounded Skew Upwind Differencing Scheme (BSUDS). The blending of the two schemes takes the form

$$\text{BSUD} = \sigma \cdot \text{SUD} + (1-\sigma) \cdot \text{UD}. \tag{3.27}$$

The blending factor σ is chosen to maximise BSUD contribution while maintaining boundedness e.g. by requiring $a_m \geq 0$. Usually the UDS is used to obtain boundedness and/or transportiveness in blending schemes, but other "higher" order schemes than the SUDS can be chosen. Neither the BSUDS nor the SUDS is widely used, at least in 3–D calculations, because of the 27 diagonal matrix that the schemes produces.

Discussion.

From the above differencing schemes it is seen that the leading truncation error derived from a TSE analysis does not give information about the accuracy of the scheme when relatively high Peclet numbers are considered. This is because the desired properties of a differencing scheme, covered in section 3.5, is violated. Lai (1983) states that a TSE analysis is only valid for $|Pe| \leq 1$. At large Peclet numbers, truncated higher order terms may dominate the discretization error and a TSE analysis can only indicate the "nature" of the error. The error can be categorised as either

- dispersive

or

- diffusive.

The dispersive error is the error which is encountered when the scheme is unbounded, e.g. the CDS for $|Pe| > 2$. It is an error which gives rise to overshoots, undershoots, or wiggles. The diffusive error is characterised by smearing of a gradient which is observed with the UDS. The truncation error is proportional to $\frac{\partial^n \varphi}{\partial \xi^n}$ where odd values of n give a dispersive type of error and even values of n give a diffusive type of error. Both types of errors thus appear in each differencing scheme, but the leading truncation term determines the nature of the error.

Hybrid Scheme (HS).

In all the schemes described so far, the conservation property is preserved, but only the UDS (except from BSUDS with the right blending factor) possesses all the desired proporties of a differencing scheme. LUDS and SUDS have the ability of transportiveness, but are not unconditionally bounded. QUDS will under certain circumstances be unbounded and does only partially satisfy the transportivê proporty. The CDS possesses the same disadvantage as the QUDS, but is very attractive for low Peclet numbers where it is both bounded and give highly accurate results. Unfortunately, to keep the CDS bounded, a very fine grid is needed which is rarely possible for practical applications in view of computer storage and cpu consumption. The only scheme which then seems usable for practical applications is the UDS. Even if UDS has all the desired proporties it will, at least at low Peclet

numbers and for the cases discussed in the section of UDS, suffer from excessive false diffusion which can outweigh the actual diffusion of the flow considered, Raithby (1976a) and Lai (1983).

To take advantage of the desired properties of UDS and the high accuracy of CDS, Spalding (1972) designed the hybrid scheme. The HS can be thought of as a simple blending scheme where either the CDS is used or the UDS is used, depending on the cell Peclet number. On a uniform grid the CDS is used whenever $|\mathrm{Pe}| < 2$ and otherwise the UDS. This ensure positive coefficients and hence a bounded scheme.

Until now only the convective terms have been considered in the differencing schemes whereas central differencing has been used for the diffusive fluxes in all schemes. In the HS, central differencing is only used for the diffusive fluxes when the Peclet number is less than 2 on an uniform grid and otherwise the diffusion term is set to zero. The reason why no diffusion is applied at high Peclet numbers is described in the following section.

In the convective term the "e" face value is given by

$$\varphi_e = \begin{cases} \varphi_P, & \text{if } \mathrm{Pe} > \frac{1}{f_e} \\ \varphi_E f_e + (1-f_e)\varphi_P, & \text{if } \frac{1}{1-f_e} \leq \mathrm{Pe} \leq \frac{1}{f_e} \\ \varphi_E, & \text{if } \mathrm{Pe} < -\frac{1}{1-f_e} \end{cases} \qquad (3.28)$$

and the diffusive conductance is given by

$$D_e = \begin{cases} D_e & \text{if } \frac{1}{1-f_e} \leq \mathrm{Pe} \leq \frac{1}{f_e} \\ 0 & \text{otherwise} \end{cases}. \qquad (3.29)$$

With the convective term and the diffusive term treated as in eq. (3.28) and eq. (3.29), respectively, the a_e coefficient is given by

$$a_e = \max(f_e C_e, -(1-f_e)C_e, D_e) - f_e C_e. \qquad (3.30)$$

The HS is used in a few applications for the present work (e.g. the inlet problem).

The Exponential Scheme (ES) and the Power–Law Scheme (PLS).

The governing convection and diffusion equation in one dimension is

$$\frac{d}{d\xi}(\rho u\varphi) = \frac{d}{d\xi}(\Gamma\frac{d\varphi}{d\xi}) \tag{3.31}$$

with the convection flux $\rho u\varphi$ and the diffusion flux $-\Gamma\frac{d\varphi}{d\xi}$. An analytical solution with ρ, u, and Γ taken as constants and subject to the boundary conditions

$$\varphi = \varphi_P \quad \text{at } \xi = 0$$
$$\varphi = \varphi_E \quad \text{at } \xi = L$$

the solution of eq. (3.31) is

$$\frac{\varphi - \varphi_P}{\varphi_E - \varphi_P} = \frac{\exp(\mathrm{Pe}\cdot\xi/L) - 1}{\exp(\mathrm{Pe}) - 1}, \tag{3.32}$$

where $\mathrm{Pe} = \rho uL/\Gamma$.

In fig. 3.10 eq. (3.32) is plottet for different values of the Peclet number. When $|\mathrm{Pe}|$ is large $\frac{d\varphi}{d\xi}$ is nearly zero at $\xi = L/2$ and diffusion is almost absent. This shows why the diffusion term was set to zero in the hybrid scheme for numerically large Peclet numbers. It also shows it to be legitimate to set the face value equal to the upstream node value for numerically large Peclet numbers.

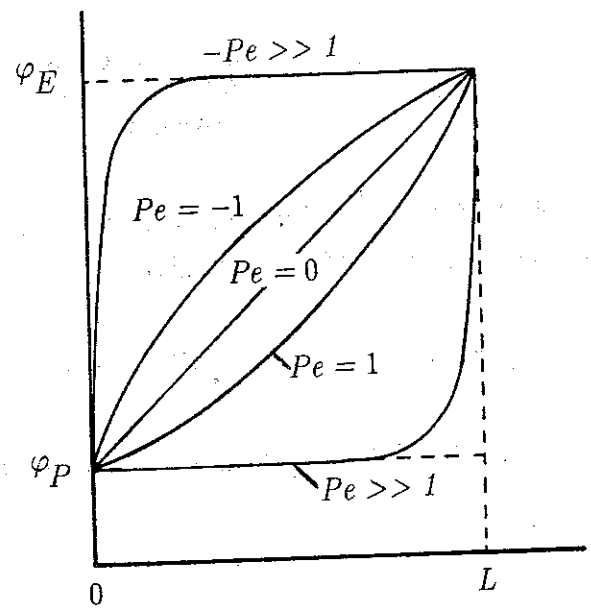

Fig. 3.10 *Plot of equation (3.32) for different Peclet numbers.*

With the total flux J made up of the convective flux and the diffusive flux eq. (3.31) is written

$$J = \rho u \varphi - \Gamma \frac{d\varphi}{d\xi}, \tag{3.33}$$

and with use of the conservation law in one dimension eq. (3.31) is given by

$$\frac{dJ}{d\xi} = 0, \tag{3.34}$$

which, when integrated over a one–dimensional control volume, gives

$$J_e - J_w = 0. \tag{3.35}$$

Using eq. (3.33) and eq. (3.32), the "e" face flux is given by

$$J_e = C_e\left[\varphi_P + \frac{\varphi_P - \varphi_E}{\exp(\mathrm{Pe}) - 1}\right]. \tag{3.36}$$

Substitution of eq. (3.36) and a similar expression for J_w into eq. (3.35) gives, after a little algebra, see Patankar (1980),

$$a_p \varphi_P = a_e \varphi_E + a_w \varphi_W, \tag{3.37}$$

where

$$a_e = \frac{C_e}{\exp(\mathrm{Pe}_e) - 1}, \tag{3.38a}$$

$$a_w = \frac{C_w \exp(\mathrm{Pe}_w)}{\exp(\mathrm{Pe}_w) - 1}, \tag{3.38b}$$

$$a_p = a_e + a_w. \tag{3.38c}$$

Equation (3.37), with eq. (3.38c), is now cast in the standard form, see the general form in eq. (3.17). From a computational point of view the a_w coefficient is never calculated as stated in eq. (3.38b), but as $a_e + C_e$ where a_e and C_e must be taken from the previous CV to the "west" of P. This should be obvious to the reader since the scheme is conservative.

Since the scheme is exact in one–dimension it may then be regarded as an attractive scheme. Even if it looks attractive, the scheme does not make

allowance for two– and three–dimensional situations which do not justifie the use of the exp–function which is very cpu consuming. Patankar (1980) then suggests a scheme which has the same advantages as the exponential scheme and is inexpensive to compute; the power–law scheme. With eq. (3.38a) rewritten as

$$\frac{a_e}{D_e} = \frac{\mathrm{Pe}_e}{\exp(\mathrm{Pe}_e) - 1}, \tag{3.39}$$

and plottet as function of Peclet number, fig. 3.11 gives with the solid line the exact variation of a_e/D_e and with the dotted line the variation of the HS. In the PLS the variation of a_e/D_e is approximated with a power–law function to fit the exact curve. The expression of the a_e coefficient is given by

$$a_e = D_e \cdot \max\left[0, \left\{1 - \frac{0.1\,|C_e|}{D_e}\right\}^5\right] + \max(0, -C_e). \tag{3.40}$$

The difference between the exact variation of a_e/D_e and the variation obtained with the PLS is not visible in fig. 3.11. The PLS is used in all the flow calculations for the present work except for a few cases to be mentioned where the HS is used.

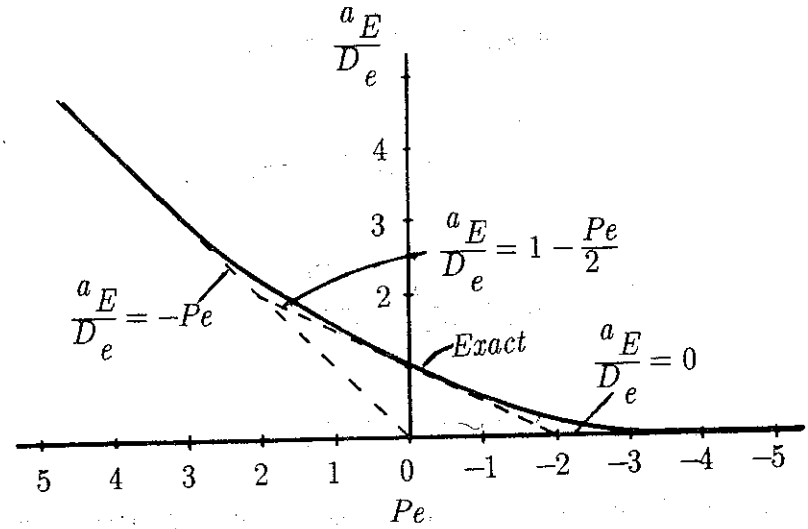

Fig. 3.11 *Variation of a_e/D_e in the power–law scheme and in the hybrid scheme.*

COntrolled Numerical Diffusion with Internal Feedback (**CONDIF** scheme).

Except for the SUDS and the BSUDS all the schemes are based on an one–dimensional analysis. Many attempts to take into account the cross–stream fluxes have been made. In compressible flow, where schock capturing is essential, it is of great importance to take into account the cross–stream fluxes for the accuracy of the flow calculation. In papers by especially Harten et al (1987) the technique for incorporating the cross–stream fluxes is outlined and can perhaps be used also with advantage for incompressible flow situations.

One remedy to get rid of false diffusion is to use an adaptable grid where the grid is aligned with the flow direction. In practise, grid adaptation can lower the angle between grid and flow direction but usually not ensure a perfect alignment why accurate differencing schemes are still a big challenge in CFD.

In all the schemes worked out only convection–diffusion terms have been considered whereas the source term has been neglected. Thiart (1988) has proposed a scheme where a one–dimensional exact solution to the convection–diffusion problem with source term has been used in a form similar to the power–law scheme. The scheme has been extended by Thiart (1989) to take into account the cross–stream fluxes by treating them as source expressions in an explicit manner.

Even though cross–stream fluxes and source terms are important factors in obtaining accurate differencing schemes the CONDIF scheme which will be outlined in the following for a one–dimensional case does not take these factors into account. The CONDIF scheme retains the essential nature of the CDS, but eliminates the over– and undershoots, see Runchal (1986). This is done by introducing a controlled amount of numerical diffusion based on local gradients of the unknown. It is known from the earlier section on central differencing scheme that this may be written, on an uniform grid, as

$$(a_e + a_w)\varphi_P = a_e\varphi_E + a_w\varphi_W \tag{3.41}$$

where

$$a_e = D_e - C_e/2; \qquad a_w = D_w + C_w/2.$$

In the CONDIF scheme, eq. (3.41) is modified as

$$(a_e^* + a_w^*)\varphi_P = a_e^*\varphi_E + a_w^*\varphi_W + \tilde{a}_e(\varphi_P - \varphi_E) + \tilde{a}_w(\varphi_P - \varphi_W) \tag{3.42}$$

where

$$a_e^* = D_e + (|C_e| - C_e)/4; \quad a_w^* = D_w + (|C_w| + C_w)/4,$$

$$\tilde{a}_e = (|C_e| + C_e)/4; \quad \tilde{a}_w = (|C_w| - C_w)/4.$$

With the introduction of the terms

$$g_e = \tilde{a}_e(\varphi_P - \varphi_E) = \tilde{a}_e R_e(\varphi_W - \varphi_P); \quad \varphi_P \neq \varphi_W$$

$$R_e = (\varphi_E - \varphi_P)/(\varphi_P - \varphi_W)$$

and

$$g_w = \tilde{a}_w R_w(\varphi_E - \varphi_P); \quad \varphi_P \neq \varphi_E$$

$$R_w = (\varphi_P - \varphi_W)/(\varphi_E - \varphi_P) = \frac{1}{R_e},$$

eq. (3.42) is rewritten as

$$(a'_e + a'_w)\varphi_P = a'_e\varphi_E + a'_w\varphi_W \tag{3.43}$$

where

$$a'_e = a_e^* + \tilde{a}_w R_w; \qquad a'_w = a_w^* + \tilde{a}_e R_e.$$

All the coefficients in eq. (3.42) are non–negative whereas the coefficients in eq. (3.43) can be negative through the R–parameter. An examination of the R–parameter shows that for the "e" face it may be written as

$$R_e = \left[\frac{\partial\varphi}{\partial\xi}\right]_e \Big/ \left[\frac{\partial\varphi}{\partial\xi}\right]_w$$

Thus, R_e represents the ratio of the gradient of φ at the two interfaces of the integration cell. R_e is then positive for monotonically increasing or decreasing values of φ and only when φ goes through an extremum within the integration cell R_e becomes negative. This motivates to use of UDS whenever the R–parameter is negative. Whenever the R–parameter is positive and $|\mathrm{Pe}| < 2$ the CDS is used and elsewhere the CONDIF scheme is used.

The R–parameter determines the amount by which the gradient varies

from one grid node to the next one and plays the role of introducing a controlled amount of numerical diffusion in the scheme. A sharp variation in R may give numerical instabilities why a limit is imposed so that

$$R \leq R_{max}. \tag{3.44}$$

The R_{max} value does usually not exceed 10, Runchal (1986).

Use of the HS whenever the R-parameter becomes negative ensures boundedness for the CONDIF scheme. The transportive proporty is also ensured because a downstream value is not used explicitly in the differencing. Instead, the downstream gradient of the unknown is used. This provides the scheme with a hyperbolic nature which is essential at high Peclet numbers.

Several test examples made by Runchal (1986) show that CONDIF is second order accurate, it contains very little false diffusion when flow to grid is not aligned, and it gives very accurate results even for source dominated flows. The only drawback of the scheme is that eq. (3.43) has become quasi–linear since the R–parameter has become a function of the unknown. This non–linearity is rather weak since the coefficients in eq. (3.43) depend on the gradient of the unknown and not on the unknown itself. The non–linearity gives rise to extra computation in solving the equations, but the higher accuracy justifies the extra computation.

The technique used in the CONDIF scheme can as well be used in a "higher" order scheme to eliminate over– and undershoots. This has been done with the LUDS where good results have been obtained, Collins (1988). Lately a refinement of the CONDIF scheme has been made to obtain quasi–linear, positive coefficients in the extremum points too. This scheme is named NONDIF (NO Numerical Diffusion with Internal Feedback), Hedberg (1989).

3.7 THE FINAL DISCRETISATION EQUATION

In the above schemes only a discretization in the E–W (East – West) direction has been applied. The same can be done in the N–S (North – South) direction as well as in the U–D (Up – Down) direction in a three–dimensional case. With the general transport equation cast into the form

$$a_p \varphi_P = \sum_m a_m \varphi_m + b,$$

$$a_p = \sum_m a_m + s_p,$$

and the PLS used as the interpolation practice for the face values, the coefficients are

$$a_e = D_e \cdot \max\left[0, (1 - 0.1|\mathrm{Pe}_e|)^5\right] + \max(0, -C_e),$$

$$a_w = D_w \cdot \max\left[0, (1 - 0.1|\mathrm{Pe}_w|)^5\right] + \max(0, C_w),$$

$$a_n = D_n \cdot \max\left[0, (1 - 0.1|\mathrm{Pe}_n|)^5\right] + \max(0, -C_n),$$

$$a_s = D_s \cdot \max\left[0, (1 - 0.1|\mathrm{Pe}_s|)^5\right] + \max(0, C_s),$$

$$a_u = D_u \cdot \max\left[0, (1 - 0.1|\mathrm{Pe}_u|)^5\right] + \max(0, -C_u),$$

$$a_d = D_d \cdot \max\left[0, (1 - 0.1|\mathrm{Pe}_d|)^5\right] + \max(0, C_d).$$

The mass flow rates and the diffusion conductances are given by

$$C_e = (\rho u \Delta\eta\Delta\zeta)_e; \qquad D_e = (\Gamma\Delta\eta\Delta\zeta/\Delta\xi)_e,$$

$$C_w = (\rho u \Delta\eta\Delta\zeta)_w; \qquad D_w = (\Gamma\Delta\eta\Delta\zeta/\Delta\xi)_w,$$

$$C_n = (\rho v \Delta\xi\Delta\zeta)_n; \qquad D_n = (\Gamma\Delta\xi\Delta\zeta/\Delta\eta)_n,$$

$$C_s = (\rho v \Delta\xi\Delta\zeta)_s; \qquad D_s = (\Gamma\Delta\xi\Delta\zeta/\Delta\eta)_s,$$

$$C_u = (\rho w \Delta\xi\Delta\eta)_u; \qquad D_u = (\Gamma\Delta\xi\Delta\eta/\Delta\zeta)_u,$$

$$C_d = (\rho w \Delta\xi\Delta\eta)_d; \qquad D_d = (\Gamma\Delta\xi\Delta\eta/\Delta\zeta)_d.$$

3.8 CLOSURE

In order to avoid numerical errors due to the form of the equations it is

shown that a strong conservation form is preferred. For the present work a semi–strong conservation form is chosen. The equations are outlined in physical dimensions with the matching source terms which contain the curvature terms and give rise to the semi–strong conservation form.

The discretised equations are cast into a general form where neighbour node values give the influence on the center node value. In order to obtain high accuracy and stability it is desirable that a differencing scheme possesses the conservativeness, boundedness, and transportiveness. A violation of these requirements may introduce overshoots, undershoots or wiggles. Among the investigated differencing schemes the power–law scheme has been chosen and the final discretised equation is given.

CHAPTER 4

GRID

4.1 INTRODUCTION

In the preceding chapter the discretised transport equation was given. In order to solve the equations it is necessary to divide the domain into control volumes where the variables are held at nodes. The velocity and pressure nodes do not need to be held in the same control volume and even the three velocity components do not need to coincide.

In section 2 two alternative ways to derive a grid are given, on which the discretised equations can be solved.

The third section introduces the staggered grid in which the three velocity components and the pressure are staggered relative to each other.

Closing remarks are given in section 4.

4.2 GRID ARRANGEMENT

Two types of grid arrangements are encountered when control volume faces are to be located in relation to grid points. Fig. 4.1 shows the practice where a grid point is placed at the intersection of two grid lines (for ease of illustration the grid is drawn for a two–dimensional case). The control volume faces are drawn halfway between the grid lines, giving a main node which is not placed at the geometric center of the control volume.

The other practice is shown in fig. 4.2 where the grids lines give the control volume faces. The main node can then be placed at the center of the control volume, but the control volume faces are not placed halfway between two main nodes. Even if the control volume faces are not placed halfway between two main nodes the second approach of grid arrangement will be used for the present work. The advantage of the first practice is that higher accuracy may be obtained in calculating the flux across the face. Providing a linear variation of the unknown between P and E the halfway value takes the same expression as if a parabolic variation was used. The disadvantage is that the value at a main node may not represent the whole control volume very well because it is not in the geometric

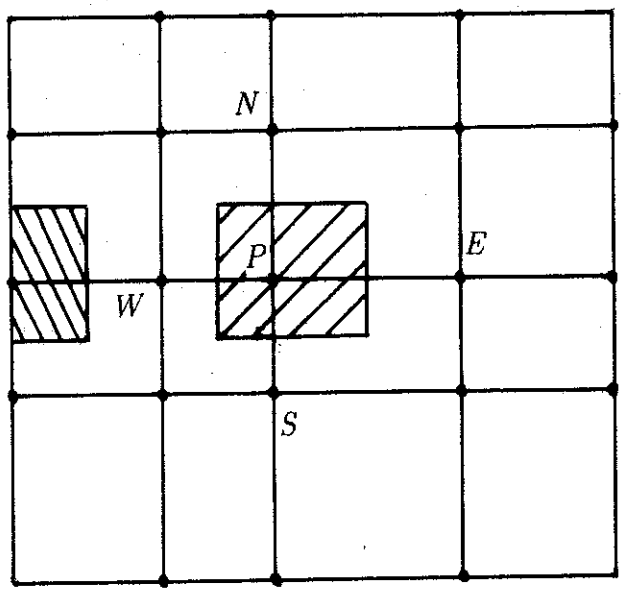

Fig. 4.1 *Main nodes placed at grid intersections defining control volume faces halfway between grid lines.*

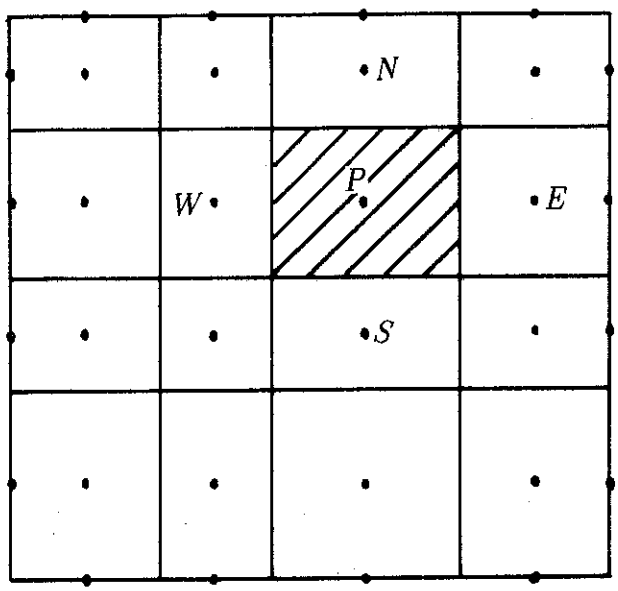

Fig. 4.2 *Main node placed at the geometric center of the control volume. Grid lines define control volume faces.*

center. Also the face fluxes are not calculated in the middle of the faces why the flux, which is assumed to prevail over the entire face, entails some inaccuracy. These disadvantages do not apply to the second practice why the second practice is preferred in a finite–volume formulation. The first practice is usually used in finite–difference formulations.

The control volumes adjacent to the boundary leads to additional consideration for the first practice because a half control volume is needed, see fig. 4.1. The second practice does not need any special treatment, because one control volume face coincides with the boundary, see fig. 4.2. The different boundary conditions are treated in chapter 6.

4.3 LAYOUT OF VARIABLES

In the above section, the node in a control volume was named the main node. All the unknowns could be located at the main node, but this practice will not be used. Before the location of the different unknowns are given it is necessary to take into account the pressure term or rather the pressure gradient term. With reference to fig. 4.3 it is seen that the pressure difference in the P control volume of unit length on an uniform grid is

$$p_w - p_e = \frac{p_W - p_P}{2} - \frac{p_P - p_E}{2} = \frac{p_W - p_E}{2}. \qquad (4.1)$$

This implies that if the velocity u_P were held at the same node as pressure p_P, as sketched in fig. 4.3, the pressure p_P would not take part in the pressure gradient acting in the momentum equation involving u_P.

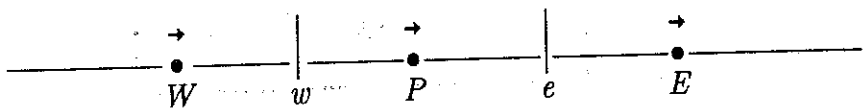

Fig. 4.3 *Pressure and velocity held at the same nodes.*

Each velocity node "feels" the two adjacent pressure nodes, but not the pressure held at the same node. This gives a velocity field which is influenced by a pressure field from a coarser grid than the one actually employed. The coarser grid influence not only gives a lower accuracy but it also creates a velocity field

and a pressure field which have zig–zag structure. A pressure field where every second pressure node has the same value different from the other values will satisfy the momentum equations as well as an uniform pressure field would do. A zig–zag pressure field arising during the iterative solution will persist until convergence, Patankar (1980). The problem arises in two– and three–dimensions as well.

One remedy, to get rid of the zig–zag fields and at the same time obtain the accuracy which the actual pressure field allows, is to use a staggered grid. In the staggered grid, which will be used for the present work, the u velocities are stored at the center of the "e" and "w" faces, v velocities are stored at the center of the "n" and "s" faces, and w velocities are stored at the "u" and "d" faces. The velocity control volumes have been displaced half a main control volume in their respective directions, see fig. 4.4a, fig. 4.4b, and fig. 4.4c. Only the velocities are staggered from the main node whereas all other quantities are stored in the main node, e.g. pressure, viscosity, concentration etc. This staggering was suggested by Harlow & Welch (1965) and named the MAC (Marker And Cell) arrangement.

The advantage is neatly seen in fig. 4.4 where the pressures adjacent to a velocity control volume "drive" the momentum associated with the velocity. In chapter 3 the general transport equation was cast into the form

$$a_p \varphi_p = \sum_m a_m \varphi_m + b. \tag{4.2}$$

When dealing with transport of momentum it is convenient to separate the pressure term from the rest of the source term, so eq. (4.2) is written

$$a_p \varphi_p = \sum_m a_m \varphi_m + A\delta(p) + b, \tag{4.3}$$

where A is an area and the operator δ is a difference operator. Taking the u–momentum equation as an example eq. (4.3) for an "e" face of a main volume is written

$$a_e \varphi_e = \sum_m a_m \varphi_m + A(p_W - p_E) + b_u, \tag{4.4}$$

The "driving" pressure term in eq. (4.4) consists of the two adjacent pressures. This arrangement avoids zig–zag fields and consequently gives a higher accuracy.

Recently a non–staggered arrangement without the disadvantages mentioned has been proposed. A special interpolation practice has been introduced to

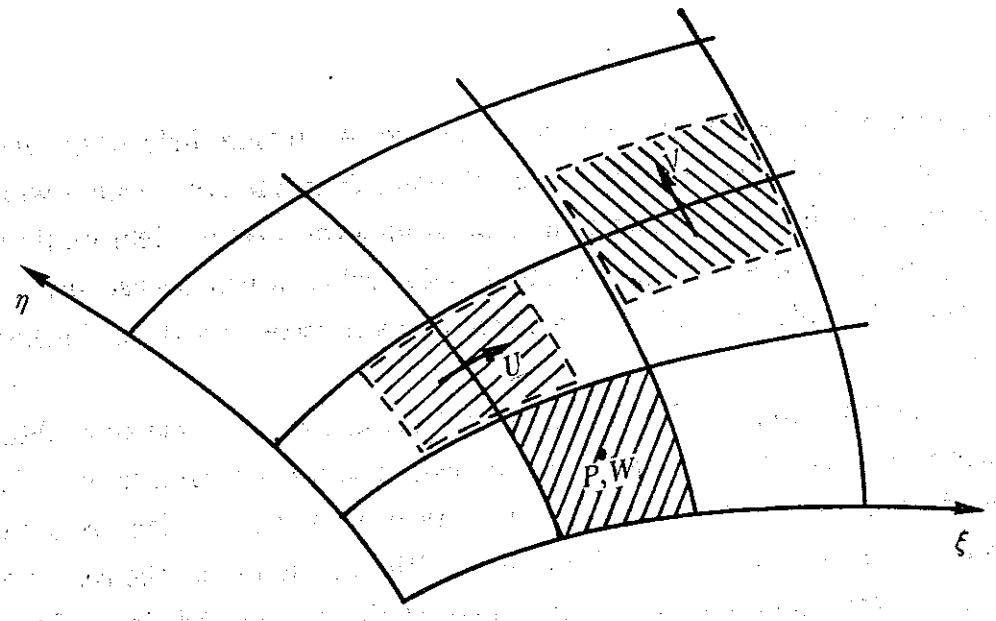

Fig. 4.4a *ξη plane of main control volumes showing layout of variables.*

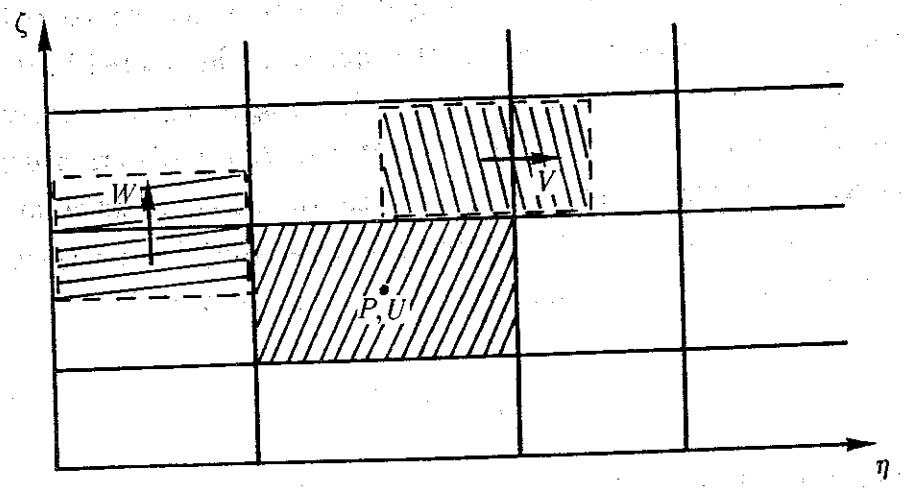

Fig. 4.4b *ηζ plane of main control volumes showing layout of variables.*

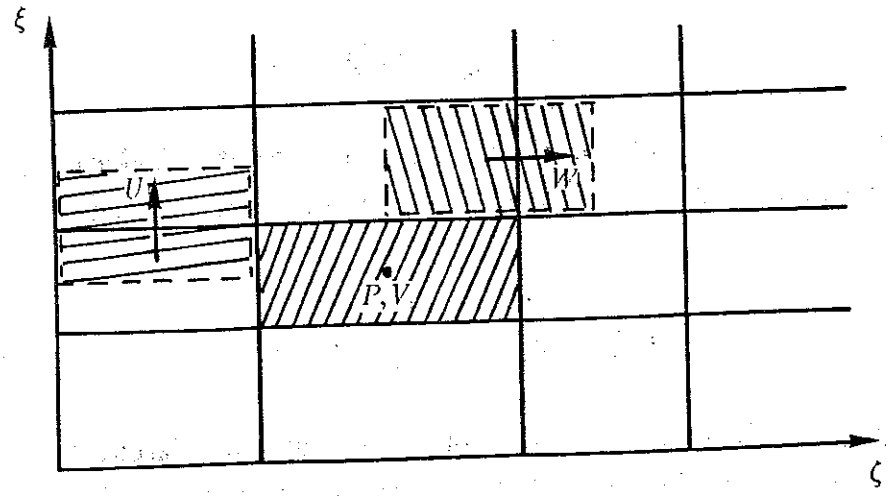

Fig. 4.4c *ζξ plane of main control volumes showing layout of variables.*

evaluate the face velocities of the main control volume to avoid the zig–zag field, see Peric (1985), among others. The face velocities are needed in solving the continuity equation (the face values are easily found in our case where the "e" face velocity, for example, is found from eq. (4.4)). A comparison of the staggered arrangement to the non–staggered arrangement is made by Peric et al (1988) where the accuracy of the two arrangements is nearly identical with a little advantage to the staggered grid. The main advantages of the non–staggered grid, also named the colocated grid, to the staggered grid is a little faster convergence and easier extension to multigrid and non–orthogonal grids.

4.4 CLOSURE

Two grid arrangements have been considered, one with main control volume nodes located at grid line intersections and one with main control volume faces made of grid lines. For the present work the last practice is chosen because the main node is located in the geometric center and the flux is evaluated in the center of a boundary surface.

To avoid a pressure field and a velocity field which have a zig–zag structure the velocity control volumes are staggered in each individual direction from the main control volume. The velocity nodes are located on the boundary of the main control volume. This arrangement will evidently not necessarily place the velocity node in the geometric center of a velocity control volume.

CHAPTER 5

SOLUTION ALGORITHMS

5.1 INTRODUCTION

In chapter three, the discretised general transport equation was set up with no special attention given neither to the continuity equation nor to the pressure term in the momentum equations. In this chapter, algorithms based on the pressure–velocity coupling in incompressible flow problems are described. Probably the most widely used algorithm is the SIMPLE method (Semi–Implicit Method for Pressure Linked Equations). Proposed by Patankar & Spalding (1972), later Patankar (1980) presented the SIMPLER method (SIMPLE Revised), and Issa (1985) the PISO method (Pressure Implicit with Splitting of Operators). Below, the aforementioned three methods will be described. However, other methods have been proposed, for example, SIMPLEC, Van Doormaal & Raithby (1984), FIMOSE, Latimer & Pollard (1985) and PUP, Raithby & Scheider (1979). These methods also work with pressure–velocity coupling.

In section 2, the vorticity–stream function formulation contra the primitive variable formulation is discussed and their merits and the drawbacks are outlined.

In the following three sections the SIMPLE method, the SIMPLER method, and the PISO method are described.

Final remarks are given in section 6.

5.2 THE PRESSURE TERM AS THE MISSING "LINK"

In incompressible flow the pressure does not have its own governing equation. It has to be determined through the equation of continuity. If the correct pressure field is substituted into the momentum equations, the resulting velocity field satisfies the continuity equation. Several methods to determine the pressure field together with the momentum equations are developed.

A method which does not calculate the pressure field explicitly is the vorticity–stream function method. It is restricted to two–dimensions and involves two equations, those of the stream function and the vorticity. In order to enforce boundary conditions, the vorticity is a major difficulty and may cause convergence problems in the vorticity–stream function formulation, Patankar (1980). On the other hand, the primitive variable formulation causes no problems, in order to enforce the boundary conditions, see chapter 6. The major problem of the vorticity–stream function formulation is that no stream function exists in three–dimensions. A velocity–vorticity formulation can be made in three–dimensions, but 6 equations have to solved, the three components of the velocity vector and the three components of the vorticity vector. This compares to only 4 equations in the primitive variable formulation. Because of ease in handling boundary conditions, simple extension from two– to three–dimensions, and less computation in three–dimensions compared to other methods the primitive variable formulation is preferred for the present work.

Writing the incompressible, unsteady Navier–stokes equations in two–dimensions in a conservative form

$$u_t + \frac{\partial u^2}{\partial \xi} + \frac{\partial uv}{\partial \eta} = -\frac{\partial p}{\partial \xi} + \frac{1}{Re}\left(\frac{\partial^2 u}{\partial \xi^2} + \frac{\partial^2 u}{\partial \eta^2}\right) \tag{5.1}$$

$$v_t + \frac{\partial uv}{\partial \xi} + \frac{\partial u^2}{\partial \eta} = -\frac{\partial p}{\partial \eta} + \frac{1}{Re}\left(\frac{\partial^2 v}{\partial \xi^2} + \frac{\partial^2 v}{\partial \eta^2}\right), \tag{5.2}$$

a Poisson equation for the pressure is obtained by differentiation and addition of eq. (5.1) and eq. (5.2), see Ames (1977) who incorporates the continuity equation. Solving eq. (5.1), eq. (5.2), and the Poisson equation in a iterative manner with appropriate boundary conditions ensures balance of momentum and mass through the pressure term. The pressure term thus becomes the term which links the continuity to the momentum equations. This method is not used in practice because instabilities are often encountered.

Instead, in the finite volume method, the coupling between the velocities

and the pressure is obtained by satisfying the continuity equation for each main control volume. With the grid arrangement chosen, where the calculated velocities are located on the cell faces of a main control volume, the pressure is used to correct these velocities to ensure continuity. The pressure becomes again the "link" between the momentum equations and the continuity equation or, in other words, the continuity equation becomes the equation from which the pressure is determined. In compressible flow where the pressure has its "own" equation the continuity equation is a conservation equation of the density. In the folowing section, three algorithms for coupling of the velocity field and the pressure field are outlined for incompressible flow of concern here.

5.3 SIMPLE ALGORITHM

The momentum equations already derived as eq. (3.17) can be written as

$$a_p u_{i,P} = H(u_{i,m}) + A\delta_i(p) + b_i, \tag{5.3}$$

where $u_{i,P}$ is one of the three velocity components, $u_1 = u$, $u_2 = v$ or $u_3 = w$, in the central point P, $H(u_{i,m}) = \sum_m a_m u_{i,m}$, m is the neighbor points to the central point, A is an area, $\delta_i(\cdot)$ is a difference operator in direction i, and b_i is the source term associated with u_i.

In the following, superscript n denotes the solution at step n in the iterative process, while $*$ denotes the solution at the predictor level, and $**$ denotes the solution at the corrector level.

Predictor level.

At the predictor level the velocity field u_i^* is solved for an estimated pressure field which will be taken as the pressure from the previous iteration step,

$$a_p u^*_{i,P} = H(u^*_{i,m}) + A\delta_i(p^n) + b_i. \tag{5.4}$$

The velocity field u_i^* satisfies the momentum equation for the predicted pressure field but in general it does not satisfy the continuity equation. The

source terms b_i and the coefficients a_p and a_m are all functions of the velocity field which is taken from step n.

Corrector level.

A correction to the pressure field is sought such that the matching velocity field satisfies the continuity constraint. Therefore corrections to both pressure and velocity fields are introduced,

$$p^* = p^n + p'$$
$$u_i^{**} = u_i^* + u_i'.$$

Subtraction of eq. (5.4) from eq. (5.3) will result in a corrector equation

$$a_p u'_{i,P} = H(u'_{i,m}) + A\delta_i(p'). \tag{5.5}$$

The velocity correction u_i', if determined according to eq. (5.5), is found in a fully implicit manner and the term $H(u'_{i,m})$ will have to be expressed in terms of the pressure corrections and the velocity corrections at the neighbors of $u_{i,m}$. Solution of eq. (5.5) together with the continuity constraint is very complex and is not recommended. Therefore the velocity correction is obtained by omitting the H–term, resulting in

$$a_p u'_{i,P} = A\delta_i(p') \tag{5.6}$$

or

$$u^{**}_{i,P} = u^*_{i,P} + d\delta_i(p'), \tag{5.7}$$

where

$$d = A/a_p. \tag{5.8}$$

The pressure correction equation is obtained by substituting eq. (5.7) into the discretized continuity equation eq. (3.14) around the main grid node which has the following form

$$a_p p'_P = H(p'_i) + b, \tag{5.9}$$

where

$$H(p'_i) = a_e p'_E + a_w p'_W + a_s p'_S + a_n p'_N + a_u p'_U + a_d p'_D,$$

$$a_e = (\rho A d)_e,\ a_w = (\rho A d)_w,\ a_s = (\rho A d)_s,\ a_n = (\rho A d)_n,$$
$$a_d = (\rho A d)_d,\ a_u = (\rho A d)_u.$$

$$b = F_w - F_e + F_s - F_n + F_u - F_d,$$

where

$$F_w = (\rho u^* A)_w,\ F_e = (\rho u^* A)_e,\ F_s = (\rho v^* A)_s,\ F_n = (\rho v^* A)_n,$$
$$F_u = (\rho w^* A)_u,\ F_d = (\rho w^* A)_d.$$

The source term b in eq. (5.9) represents a mass defect which is equal to zero if the continuity is satisfied.

After solution of eq. (5.9) the velocity field is updated by eq. (5.7) and the pressure field is updated as $p^* = p^n + \lambda p'$, where λ is a relaxation parameter. u_i^{**} and p^* are taken as the new values at step n+1. In summary, the sequence of steps in the SIMPLE algorithm are,

1) Calculate the coefficients of the momentum equation [eq.(5.4)] and solve the equation with a predicted pressure field p, taken from the previous iteration step.
2) Solve the pressure corrector equation [eq.(5.9)].
3) Calculate p^* as $p^* = p^n + \lambda p'$.
4) Update velocities u_i [eq.(5.7)].
5) Treat the corrected velocities and the underrelaxed pressure as new values at the next step and repeat from step 1) until convergence is reached.

The updated velocity field u_i^{**} is the solution to the momentum equation, where the H–term is treated in an explicit manner. This can be seen if eq. (5.6) is added to eq. (5.4) to give the approximate momentum equation

$$a_p u^{**}_{i,P} = H(u^*_{i,m}) + A\delta_i(p^*) + b_i. \qquad (5.10)$$

Omitting the $H(u'_{i,m})$ term in the velocity correction equation results in strong underrelaxation, suppressing the effects of the nonlinearities. Patankar (1980) suggests a relaxation factor of about 0.5 for the velocity field and about 0.8 for the pressure field. One reason for the small relaxation factors and, at the same time, the main reason for the drawback of the SIMPLE method is that the continuity constraint is not kept in the H–term in eq. (5.10). This violation results in a strong sensitivity to the values of relaxation factors. It implies a considerable increase in computational effort if optimum relaxation is not chosen (see the discussion of relaxation later).

5.4 SIMPLER ALGORITHM

Omitting the H–term in the velocity correction equation causes a slow convergence of the pressure field but the equation does a good job correcting the velocity field, Patankar (1980). This fact is used in the SIMPLER algorithm where the pressure field is solved in another way. To explain this, let eq. (5.3) be written as

$$u_{i,P} = \frac{H(u_{i,m}) + b_i}{a_p} + d\delta_i(p). \tag{5.11}$$

If $[H(u_{i,m}) + b_i]/a_p$ is defined as a pseudo velocity $\hat{u}_{i,P}$ then eq. (5.11) takes the form

$$u_{i,P} = \hat{u}_{i,P} + d\delta_i(p), \tag{5.12}$$

which is similar to eq. (5.7) in the SIMPLE method. Eq. (5.7) was used to define a pressure correction equation, while eq. (5.12) is now used to define a pressure equation on the form

$$a_p p_P = H(p_i) + b, \tag{5.13}$$

where

$$H(p_i) = a_e p_E + a_w p_W + a_n p_N + a_s p_S + a_d p_D + a_u p_U$$

$$b = (\rho A\hat{u})_w - (\rho A\hat{u})_e + (\rho A\hat{v})_s - (\rho A\hat{v})_n + (\rho A\hat{w})_u - (\rho A\hat{w})_d$$

Sequence of steps in the SIMPLER algorithm are,

1) Calculate the pseudo velocities $\hat{u}_{i,P}$ from a predicted velocity field often taken from the previos iteration step.
2) Calculate the coefficients of the pressure equation [eq. (5.13)] and solve for the updated pressure field.
3) Use the updated pressure field as a predicted pressure field and solve the momentum equation.
4) Solve the pressure corrector equation [eq. (5.9)] as in the SIMPLE method.
5) Correct the velocity field by the velocity correction equation [eq. (5.7)].
6) Repeat from step 1) until convergence.

The main advange of SIMPLER is that if a correct velocity field is known the correct pressure field is calculated in one iteration. In SIMPLE, on the other hand, the situation deteriorates in the first iteration which creates a wrong pressure distribution.

Even though SIMPLER requires also the calculation of pseudo velocities and a pressure equation in every iteration the overall computational effort is lowered compared with that of the SIMPLE method. Another advange is that the overall stability is greater with SIMPLER than with SIMPLE. This means that optimum relaxation is not very critical.

5.5 PISO ALGORITHM

The PISO algorithm develop by Issa (1985) was aimed to handle time marching unsteady compressible flows, with no iterations in each time step. Both SIMPLE and SIMPLER has been extended to handle unsteady and compressible flow situations but require several iterations in each time step.

The PISO algorithm will be described for an unsteady incompressible situation. In the following, the superscript n and *** are taken as time level and value at the second corrector step, respectively. The superscripts * and ** have the same meaning as in the SIMPLE method.

The time–dependent momentum equation has the form

$$(a_p + \frac{\rho \Delta V}{\Delta t}) u_{i,P}^{n+1} = H(u_{i,m}^{n+1}) + A\delta_i(p^{n+1}) + b_i + \frac{\rho \Delta V}{\Delta t} u_{i,P}^{n}, \tag{5.14}$$

in a fully implicit scheme, where an implicit Euler time step is used.

Predictor level.

The velocity field u_i^* is implicitly expressed as

$$\tilde{a}_p u_{i,P}^* = H(u_{i,m}^*) + A\delta_i(p^n) + b_i + f u_{i,P}^n, \tag{5.15}$$

where

$$f = \frac{\rho \Delta V}{\Delta t}; \qquad \tilde{a}_p = a_p + f.$$

The pressure field from the previous time step is used in the solution of the predicted velocity field u_i^* which in general does not satisfy the zero divergence condition.

First correction.

A corrected form of the momentum equation is written as

$$\tilde{a}_p u_{i,P}^{**} = H(u_{i,m}^*) + A\delta_i(p^*) + b_i + f u_{i,P}^n, \tag{5.16}$$

which is of explicit type because the H–term is not updated. Subtracting eq. (5.16) from eq. (5.15) gives the increment equation for the velocity

$$u_{i,P}^{**} = \hat{u}_{i,P} + d\delta_i(p^*), \tag{5.17}$$

where

$$\hat{u}_{i,P} = u_{i,P}^* - d\delta_i(p), \tag{5.18}$$

$$d = A/\tilde{a}_p. \tag{5.18a}$$

Substitution of eq. (5.17) into the continuity equation results in a pressure equation on the same form as eq. (5.13) for the SIMPLER method, with the pseudo velocities taken as eq. (5.18). With a known pressure field p^* the corrected velocity field u_i^{**} can be obtained and it should be recalled that the zero–divergence condition is satisfied.

If the strategy from the SIMPLE method were used one would end up with a pressure corrector equation which would give the same corrected velocity field u_i^{**}. It is worthwhile noticing that no overall difference will appear using a SIMPLER or a SIMPLE version on the corrector levels in PISO.

Second corrector.

When the first corrected form of the momentum equation was used the continuity was not satisfied in the H–term. The second corrector equation contains a new velocity field u_i^{***} and a new pressure field p^{**}, where the velocity field u_i^{***} should satisfy the zero–divergence condition,

$$\tilde{a}_p u_{i,P}^{***} = H(u_{i,m}^{**}) + A\delta_i(p^{**}) + b_i + f u_{i,P}^{n}. \tag{5.19}$$

Subtracting eq. (5.19) form eq. (5.16) results in the second corrector equation for the velocity field

$$u_{i,P}^{***} = \hat{u}_{i,P} + d\delta_i(p^{**}), \tag{5.20}$$

where d is given by eq. (5.18a) and

$$\hat{u}_{i,P} = u_{i,P}^{**} + [H(u_{i,m}^{**}) - H(u_{i,m}^{*})]/\tilde{a}_p - d\delta_i(p^*). \tag{5.21}$$

Again, as for the first corrector step, the new velocity field is solved with use of the continuity equation and the updated values $u_{i,P}^{***}$ and p^{**} are taken as

the values at the new time level, $n+1$. More corrector steps could be taken but the increase in accuracy per time step would increase the overall computational effort, Issa (1985). In appendix C is given a discussion of an estimation of the accuracy and stability. Jang et al. (1986) have made a comparison between SIMPLEC, SIMPLER and PISO and have shown that PISO is superior to SIMPLER and SIMPLEC conserning computational effort when solving the momentum equations alone. However, when a active scalar is involved both SIMPLER and SIMPLEC are faster than PISO. Neither SIMPLER nor SIMPLEC is superior to each other. In dealing with the PISO method together with an active scalar they found that it was only robust for small time steps. This has to do with the accuracy and, as shown in appendix C, an extra corrector step might make the PISO method superior to SIMPLER and SIMPLEC when an active scalar is involved too. Issa et al. (1985) have shown PISO's very substantial stability when used on steady–state calculations and have demonstrated the stability, even for very large time–steps. Because of PISO's great stability the method is excellent for both unsteady and steady–state flow problems.

Discussion of relaxation.

Solution of eq. (5.3) as described in the SIMPLE method needs underrelaxation to suppress the effects of nonlinearities, but in the PISO method no under relaxation is needed for the velocity and pressure fields. Instead, the relaxation is obtained through the time step Δt. There is a close relationship between underrelaxation in steady–state iteration methods and relaxation through the time step in time–dependent methods. Underrelaxation has the form

$$u_{i,P}^{n+1}(\text{used}) = \lambda u_{i,P}^{n+1} + (1-\lambda) u_{i,P}^{n}, \tag{5.22}$$

in which $u_{i,P}^{n+1}(\text{used})$ is the updated velocity field which is used in the next iteration. The relaxationship between the underrelaxation factor λ and the time term $\rho \Delta V/\Delta t$ can be seen if eq. (5.22) is substitutet into eq. (5.14) without the time term, to obtain

$$\frac{a_p}{\lambda} u_{i,P}^{n+1}(\text{used}) = H(u_{i,m}^{n+1}) + A\delta_i(p^{n+1}) + b_i + \frac{1-\lambda}{\lambda} a_p u_{i,P}^{n}. \tag{5.23}$$

By comparison of eq.s (5.3) and (5.14) follows

$$\frac{1-\lambda}{\lambda} a_p = \frac{\rho \Delta V}{\Delta t} \quad \text{or} \quad \lambda = \frac{a_p}{a_p + \rho \Delta V / \Delta t}, \tag{5.24}$$

which states that λ dependends on a_p which in turn dependends on the spatial discretisation and on u_i. It can then be stated that λ evolves with the spatial discretisation and the intermediate solution in time–marching algorithms. This is unlike the steady–state iteration where λ usually does not evolve during the computations.

Two cases of the dependency of λ and a_p is considered.

1) In a convection dominated flow ($\Gamma = 0$), the coefficient a_p can be described as $a_p = \rho u \Delta y \Delta z + \rho v \Delta x \Delta z + \rho w \Delta x \Delta y$. Combination of this expression of a_p and eq. (5.24) gives

$$\frac{\lambda}{1-\lambda} = a_p / \frac{\rho \Delta V}{\Delta t} = \frac{u \Delta t}{\Delta x} + \frac{v \Delta t}{\Delta y} + \frac{w \Delta t}{\Delta z}. \tag{5.25}$$

In cases where one velocity component is dominating, for instance u, eq. (5.25) is given by

$$\frac{\lambda}{1-\lambda} = \frac{u \Delta t}{\Delta x} = C \quad \text{or} \quad \lambda = \frac{C}{1+C}, \tag{5.26}$$

where C is the Courant number.

In explicit methods, the Courant number has to be less than one to obtain stability during the solution. In semi–implicit methods a value around one is usually used. In the PISO method the Courant number can easily be one order higher than for the semi–implicit methods without loosing stability.

2) In a diffusion dominated flows the coefficient a_p can be described as

$$a_p = 2\Gamma \frac{\Delta y \Delta z}{\Delta x} + 2\Gamma \frac{\Delta x \Delta z}{\Delta y} + 2\Gamma \frac{\Delta x \Delta y}{\Delta z}.$$

Combining a_p and eq. (5.24), gives

$$\frac{\lambda}{1-\lambda} = 2\frac{\Gamma \Delta t}{\rho \Delta x^2} + 2\frac{\Gamma \Delta t}{\rho \Delta y^2} + 2\frac{\Gamma \Delta t}{\rho \Delta z^2}. \qquad (5.27)$$

In general, the relaxation factor λ is a combination of eq. (5.26) and eq. (5.27). In iterative steady–state calculations, where underrelaxation is necessary, it is usually not possible to find an optimum value of λ unless ad hoc methods are used. It means that the optimum has to be found from calculations with different values of λ. The PISO method has only been described as a time marching method which is based on no iterations in each time step. However, a simplified iterative version for steady–state calculation can be extracted from the time version. The iterative version can be interpreted as an extension of the SIMPLE method, in which a second corrector level is added. As in the time marching version of PISO, no relaxation is needed when updating the pressure field but when updating the velocity field underrelaxation is necessary. In the SIMPLE method, underrelaxation of about 0.5 is used but in the iterative version of PISO, underrelaxation as high as 0.95 is used. Because of the great stability of the PISO method, and of the iterative version as well, the optimum value of λ is not that critical for the cost of the computation.

5.6 CLOSURE

To avoid the difficulties associated with the determination of pressure a vorticity–stream function formulation can be used in a two–dimensional flow calculation. In a three–dimensional flow calculation a primitive variable formulation is to be preferred to a velocity–vorticity formulation because of less computation. The velocity–pressure coupling used for the present work is the PISO algorithm which is used in a iterative version even though the method is developed for unsteady flow calculations. Here, an underrelaxation factor of about 0.9 is used for the momentum equations The PISO algorithm is built around the SIMPLE algorithm which has been the most used algorithm in the past and is still widely used.

CHAPTER 6

BOUNDARY CONDITIONS

6.1 INTRODUCTION

In order to get an uniquely solution to the linearised and discretised equations appropriate boundary conditions have to be applied. Even if the linearised equations with appropriate boundary conditions have a unique solution there is no guarantee of convergence towards the unique solution with iterative solvers. One necessary requirement, as discussed in chapter 3, is use of a bounded differencing scheme. Contrary to a linear differential equation, a non–linear differential equation does not always have an unique solution. For the present work, where only laminar flows are considered, uniqueness is always encountered and in order to obtain a converged solution of the overall non–linear equations splitting technique and relaxation as discussed in chapter 5 are used.

Most boundary conditions are usually of a Dirichlet type (specified function value), a Neumann type (specified normal gradient) or a Robbin type (a mixed type, where a weighted linear combination of a Dirichlet condition and a Neumann condition are specified). The two first conditions are often used in computational fluid dynamics whereas the last one is limited to a few applications. It is, for example, used in potential flows to enhance stability and accuracy near sharp corners.

In section 2, three physical boundaries are encountered and their incorporation into the discretised equations are described.

Two types of numerical boundaries, the symmetry boundary and the cyclic boundary, are described in section 3.

The physical boundaries and the numerical boundaries hold for the general transport equation and thereby for the momentum equations too which are a special case of the transport equation. The physical and numerical boundaries count as well for the pressure field, but the pressure field gives usually only rise to a Neumann condition and thereby the problem does not become a boundary value problem. This is discussed in section 4.

Closing remarks are given in section 5.

6.2 PHYSICAL BOUNDARY CONDITIONS

The physical boundaries which are going to be introduced in the manner in which they appear in the discretised equations are a wall boundary, an inlet boundary, and an outlet boundary.

Walls.

In the near wall region where steep variation in the dependent variables occur a large number of control volumes are needed, but because of limitations in numbers of control volumes, especially in three–dimensional calculations, a wall function is usually introduced. A wall is modeled with a Dirichlet condition where the velocity at the wall is specified. A no–slip condition indicates that the velocity at the wall is zero whereas a slip condition indicates a non zero velocity at the wall. We will apply a no–slip condition at the wall which leads to high amount of diffusive fluxes because of the steep variation in the dependent variables. In order to calculate the diffusive fluxes with high order of accuracy without an excessive number of control volumes a one–dimensional Couette flow behavior is assumed in the near–wall region. The wall shear stress in laminar flow in a one–dimensional Couette flow is given by

$$\tau_W^{\xi\eta} = \frac{\text{viscosity} \cdot u_P}{\eta_p},$$

where viscosity is the apparent viscosity, either the constant viscosity μ or the shear dependent viscosity η, u_P is the parallel velocity at the edge of the near–wall region, and η_p is thickness of the layer.

The incorporation of the constant τ_W is done via the source term. First, the coefficients which link the control volumes next to the wall to the wall node are set to zero. Second, the source coefficient s_p for the u–velocity is set to

$$s_p = -\frac{\text{viscosity} \cdot A}{\eta_p},$$

where A is area of control volume face. The constant wall shear stress is treated in the same way when the v and w velocities are considered.

Inlet.

At the inlet, the values of the dependent variables are normally known and no special numerical treatment has to be done. If the values are not known an estimation can be dangerous because a deviation from the one which actually should have been applyed is carried downstream and will influence the calculation. If the influence region is limited to a small part of the domain the inlet boundary can for some geometries be placed further upstream to minimize errors, but at the expense of more grid points and consequently larger cpu consumption. Another way to obtain inlet values is to extract them from experimental or analytical data.

Because the boundary condition is of dominant importance in computational fluid dynamics it is worth to notice the restriction different boundary conditions make on the calculation. Let a Neumann condition be given by $\partial f / \partial \xi = 0$ which states that the gradient of a function f along the ξ-direction is zero, but nothing is stated about the value or the gradients in the other directions. Any constant added to f does still satisfy the Neumann condition. A Neumann condition is said to be less restrictive than a Dirichlet condition and if higher order boundary conditions ($\partial^n f / \partial \xi^n$ with n bigger than 1) are used they are even less restrictive. It might seem preferable to use a less restrictive boundary condition, but instabilities and loss of convergence can occur. Roache (1976) suggests to use a boundary condition which is most restrictive for the particular problem and when a solution is obtained the restriction of the boundary condition can be reduced.

At the inlet boundary where the flux is known, a Dirichlet condition is usually applyed for each velocity component. Thus, if the flux is normal to the inlet plane the main flow component is given a value according to inlet flux and the others are set to zero. A two-dimensional situation would give

$$u = \text{const},$$
$$v = 0.$$

A less restrictive inlet boundary condition would be to apply a Neumann condition, according to the equation of continuity, to the variables which at the first condition were set to zero. This gives for a two-dimensional situation

$$u = \text{const},$$
$$\frac{\partial v}{\partial \xi} = 0.$$

The last condition might be a physically more correct condition because a boundary layer which is built at the wall is "felt" already at the inlet and does not have to have a zero component normal to the main flow.

The two different boundary conditions were tried and gave different results in the near inlet region where it was observed that the boundary layer was built faster with the second condition than with the first condition. A more detailed study of inlet and outlet boundary conditions is made by Sørensen & Loc (1989).

Outlet.

Even if the inlet boundary condition can be crucial for the accuracy of the flow calculation the outlet boundary condition can be even more crucial if the outlet is not located a suitable place. Normally, the values of the dependent variables are not known at an outlet boundary why the outlet has to be placed where the flow is expected to be everywhere outwards–directed and a Neumann condition must be imposed. The Neumann condition at the outlet, stating that the gradient of the dependent variables should be zero, can legitimately be used where the downstream conditions do not influence upstream regions and the flow is said to be parabolic.

The parabolic flow condition at the outlet is implemented by setting the coefficients linking the upstream node to the node prevailing at the outlet boundary to zero. This corresponds to equating the boundary node value with the node value immediately upstream. A linear or a quadratic extrapolation could be used as well.

When dealing with fluid flow the velocities at the outlet have to be estimated according to a parabolic flow condition, but the equation of continuity must also be satisfied. In chapter 5, several methods to satisfy the equation of continuity together with the momentum equations were outlined, but there is no guarantee of convergence if the equation of continuity is not satisfied overall. This is done by correcting the outlet values in a way that the outlet flux is equal to the inlet flux. The final solution will satisfy both the equation of continuity and the parabolic flow condition at the outlet.

At first sight, the outlet condition might not be that critical because a deviation from a more correct outlet condition is neither convected into the computational domain nor transported by diffusion provided the outlet is placed where the flow is everywhere directed outwards. Yet, a deviation might influence

the calculation domain through the pressure field which is always fully elliptic. Nevertheless, the elliptic influence from a perturbation of the pressure field in a given point is rapidly reduced with distance from the point and in practice only a limited region of the domain is influenced.

6.3 NUMERICAL BOUNDARY CONDITIONS

The physical boundary conditions described in the preceding section are the most often encountered boundary conditions in flow calculations, but often the numerical problem can be reduced if a plane or an axis of symmetry appears in the domain or/and a cyclic boundary condition can be introduced in the problem. Symmetry and cyclic boundary conditions are described in this section.

Symmetry.

At a plane or an axis of symmetry, two conditions can be stated

- zero convective flux;
- zero normal gradient of the dependent variables which implies zero diffusion flux.

No modification of the coefficients have to be introduced from the first condition, only the velocity normal to the symmetry plane or axis has to be initialized to zero value. The last condition can be introduced by setting the coefficients for the dependent variables linking nodes next to the symmetry plane to nodes prevailing at the symmetry plane to zero. The values at the symmetry plane must then take the same values as the immediate neighbours next from the symmetry plane.

Cyclic boundaries.

Cyclic boundaries can be used in two cases. The first case is flow where a periodic relation appears in the flow and only one period of the flow has to be calculated. The outlet is linked by some cyclic relations with conditions at the inlet. This is, for example, used in calculations of flow in rod bundles, see

Antonopoulos et al (1976). The other case where cyclic boundary conditions are used is when a fully developed solution is sought. In both cases the periodic relations can be handled by a guess–and–correct technique, see Antonopoulos et al (1976) by which a guess is initially made of the inlet conditions and the outlet is handled as if the flow is parabolic. Then, the resulting outlet conditions are feed in as a new set of inlet conditions and this is repeated until the inlet and outlet conditions are equal. This method works but does not ensure the fastest convergence. A faster convergence is obtained if inlet and outlet are treated numerically as if they were linked together. This means that the outwards–directed coefficients should not be set equal to zero as if the flow were parabolic, but the coefficients should link the outlet node with the corresponding inlet node. The same procedure should be used at the inlet where the coefficients which point upstream should be linked to the corresponding outlet nodes. The corresponding coefficient matrix does not have the same structure as sketched in fig. 3.3, but now an extra small band in the outer corners are now added. The extra computation is small compared with the gain in convergence rate.

6.4 BOUNDARY CONDITIONS FOR THE PRESSURE

The boundary conditions described in the preceding sections are given for the general transport equation of which the momentum equations are special cases. In chapter 5, the pressure equation was outlined or more correctly the pressure correction equation was outlined and since it is not a special case of the general transport equation it has to be treated separately.

As in the general case, either a Dirichlet condition or a Neumann condition can be applied at the boundary. With a Dirichlet condition, the pressure at the boundary is given and consequently the value of p' at the boundary will be zero and no modification of the boundary coefficients take place. In most flow calculations, the normal velocity at the boundary is given which is the case of all the boundary conditions considered until now. Since the normal velocities are given, no correction must take place through the pressure, and a pressure correction normal to a boundary is not needed. But because the pressure correction at the interior of the domain is influenced, the pressure correction at a boundary node and the corresponding neighbour node normal to the boundary must take the same value. This is equivalent to impose a Neumann condition on the boundary, stating that the gradient normal to the boundary must be zero for

the pressure correction equation. Thus, the coefficients linking an interior pressure node with that at the boundary are set to zero.

With a Neumann condition imposed at all the boundaries the problem does not become a boundary value problem and no unique solution can be obtained. With one solution obtained all other solutions which differ by a constant from the first are also solutions. This is in no contradiction to the Navier–Stokes equations in which the pressure field itself does not appear, but instead the pressure gradient. It means that if one pressure field is a part of a solution to the Navier–Stokes equations an unlimited number of pressure fields which differ only by a constant are also a part of a solution. It counts also for fluids which do not satisfy the Navier–Stokes equations.

The associated coefficient matrix to the pressure field is not diagonal dominant and hence not positive definite. Instead, the coefficient matrix becomes semi–positive definite. A semi–positive definite matrix has eigenvalues which are all non–negative in contrast to a positive definite matrix which has only positive eigenvalues. The presence of zero eigenvalues gives rise to special attention in computing the preconditioning matrix used in the conjugate gradient method to solve the pressure–corrector equations. This is discussed in details in chapter 7.

6.5 CLOSURE

The two most often encountered boundary conditions when solving partial differential equations, the Dirichlet condition and the Neumann condition, were introduced. The numerical treatment of the physical boundaries, a wall, an inlet, and an outlet boundary, involves either a Dirichlet or a Neumann condition. The Dirichlet condition is associated with the values of the dependent variables at the boundary and the Neumann condition is associated with the flux at the boundary. Problems which involve either a symmetry plane or axis and/or a cyclic relation can reduce the computational domain with the implementation of symmetry boundary conditions and/or cyclic boundary conditions.

The boundary condition of the pressure field is usually of a Neumann type where the normal gradient is specified to zero value. The associated coefficient matrix is semi–positive definite and consequently has eigenvalues which are zero.

CHAPTER 7

SOLUTION OF DISCRETISED EQUATIONS

7.1 INTRODUCTION

When the momentum and continuity equations are discretised and linearised a linear system of algebraic equations result,

$$\boldsymbol{A}\boldsymbol{x} = \boldsymbol{b}. \tag{7.1}$$

$\boldsymbol{A}$ is a sparse square matrix of order N, where N is the number of interior points multiplied by a number of dependent variables, $\boldsymbol{x}$ is the dependent variable vector and $\boldsymbol{b}$ the source vector. The number of non–zero elements in each row of $\boldsymbol{A}$ is depending on whether it is a two – or three – dimensional problem, on the grid arrangement and on the differencing scheme used. On a rectangular grid arrangement, each row possesses five and seven non–zero elements for hybrid schemes in two – and three – dimensional problems, respectively.

There are two groups of methods by which eq. (7.1) can be solved: direct and iterative. By a direct method, the exact solution can be achieved directly in one pass by manipulation of the coefficient matrix if no roundoff errors occur. An iterative method will, at each iteration, generate an approximate solution which will converge towards the exact one in the limit.

The two most well–known direct methods are Gauss elimination and factorization. Computation involves operations on all elements in the coefficient matrix which for sparse matrices implies the creation of fill–ins. For large sparse matrices this requires a lot of computation and a lot of storage and consequently is not advisable. A direct method employing sparse matrix techniques, which means that fill–ins less than a certain value are neglected, may be used to minimize creation of fill–ins and only an approximate solution will be obtainable. The resulting approximate solution can be adjusted by iterative refinement. Direct methods for elliptic problems have been developed and for the Poisson equation very fast solvers using Fast Fourier Transformation (FFT) and/or cyclic reduction are used. The direct solution of the Poisson equation is described, for example, by Dorr (1970), Buzbee et al. (1970) and Swarztrauber (1977). For a general non–separable elliptic equation, direct methods, such as FFT and cyclic reduction

must be used iteratively. This involves large execution times and the conjugate gradient method (see later) looks more attractive for this case, Hockney (1980). Because the direct methods do not (or only partially) take advantage of the sparsity, iterative methods, which succeed in this respect, are more likely to be used.

A class of iterative methods is the stationary iterative methods, in which the matrix A is decomposed into two matrices M and R, where M is a nonsingular matrix

$$A = M + R. \tag{7.2}$$

Equation (7.2) is called a splitting of A. Equation (7.1) and eq. (7.2) can be combined to the stationary iterative method,

$$Mx^{n+1} = -Rx^n + b, \qquad n = 0, 1, 2,... \tag{7.3}$$

where n is the iteration number. x^0 is an arbitrary initial solution vector and x^n will converge to the solution if $\rho(-M^{-1}R) < 1$, where $\rho(\cdot)$ is the spectral radius, Hageman & Young (1981).

The simplest splitting of a stationary point iterative method is the Jacobi method where $M = D$ and $R = A - D$, D being the diagonal matrix of A, Jennings (1977). Other point iterative methods are Gauss–Seidel, SOR and SSOR, and their respective M matrices are: $D - L$, $D/\omega - L$, and $\omega/(2-\omega)(D/\omega - L)D^{-1}(D/\omega + L)$. L is a lower triangular matrix and ω is a relaxation parameter lying in the range $0 < \omega < 2$.

Another important group of iterative methods is the line iteration. It has a better rate of convergence than the point iteration methods but more computation in each iteration has to be done. A subset of an individual line is solved at once. On a rectangular mesh, it will be either a row or a column line. A splitting as shown for the point iterative methods can be derived in a similar way for the line iterative methods by considering M as a row or a column line relaxation matrix. The interchangeability of the sweep direction is used in the alternating direction implicit procedure (ADI) where the row and column directions, respectively, are swept alternately.

From eq. (7.3) it must be expected that the "closer" the matrix M is to the coefficient matrix A, the faster the rate of convergence. In the Stone's strongly

implicit procedure (SIP), Stone (1968), the solution matrix $\boldsymbol{M}$ is "closer" to the coefficient matrix $\boldsymbol{A}$ than for point and line iteration, which gives a more effective solver for a wider class of problems than the ADI, Jennings (1977). A systematic comparison between the ADI and the SIP on a Poisson like problem is made by Tsui (1987) who shows that the SIP is faster than the ADI.

It is characteristic of the above mentioned stationary iterative methods that a large fraction of the residual is reduced in the first few iterations, but then the convergence is lowered. This is because the high frequency errors die out more quickly than the low frequency ones, Brandt (1987). To overcome this the multigrid method has been developed. These methods use the fact that different error frequencies are smoothed on different grid densities. The method consists of three well known elements (Stuben & Trottenberg, 1982),

- error smoothing by relaxation,
- calculation of corrections on coarser grids and recursive application,
- combination with nested iteration.

Any solver can be used as a relaxation method, but often a simple method as a point iterative method is used because most of the solution is done on coarse grids where it is usually not necessary to use advanced solvers. Another widely used relaxation method is the zebra solver which is similar to the ADI solver, except that in each sweep the even lines are solved before the odd lines. Even though the zebra solver is more costly per iteration than the point solver it is usually to be preferred because of its faster convergence.

The last iterative solver to be mentioned is the conjugate gradient (CG) method. It is often considered as a direct solver because the solution is found in at most N iterations if rounding errors are absent, where N is the number of unknowns. The method was originally worked out for symmetric positive definite (SPD) matrices, but has been extended to handle nonsymmetric matrices as well. It is then called the generalized conjugate gradient method. The CG method is a minimization method where the rate of convergence is proportional to the spectral condition number $\kappa(\boldsymbol{A})$ of the coefficient matrix $\boldsymbol{A}$. The minimization problem is often solved with a preconditioning matrix $\boldsymbol{B}$, wherefore the method is called the preconditioning conjugate gradient method (PCG). The advantage of the PCG method is that the condition number is lowered compared with that of the CG method and hence it has a better rate of convergence. The preconditioning matrix $\boldsymbol{B}$ can be found from the splitting of $\boldsymbol{A}$ as shown in eq. (7.2) and eq. (7.3), and $\boldsymbol{B}$

can then be any of the M matrices described earlier or, as will be described latter, an incomplete factoriazation of A. The description of the CG method and, in addition, the PCG method is the outline of this chapter.

In section 2 a discussion about choice of solvers is given. The choice of solver used for the momentum equations is the ADI solver which is briefly discussed in section 3. General aspects of the gradient methods are discussed in section 4 and three gradient methods, the steepest descent method, the conjugate gradient method, and the preconditioned conjugate gradient method are outlined in section 5, 6, and 7, respectively. The assessment of CG and PCG is described in section 8 and conclusions and closure are given in section 9.

7.2 WHICH SOLVER FOR WHICH PROBLEM ?

Any of the aforementioned solution methods can not be unambiguously superior to the other, because the choice of solver is closely connected to the problem, the strategi of solution for the problem, and the boundary conditions. A line–solver will often be a good solver for parabolic and hyperbolic fluid mechanic problems because the information is carried in the direction of the streamlines, in which lines the line–solver should be used. Often the streamlines are not known in advance whence the line–solver used in alternating directions often is a better choice.

In elliptic problems there is no certain directions in which information is carried. Elliptic problems can be characterised as if a disturbance, taking place at one spot, can then be felt in whole the solution domain. The CG method does not take care of any information line(s) and with a good preconditioning it works very efficiently on elliptic problems. The method is used to solve the pressure–correction equation, which is a Poisson type equation.

As mentioned earlier the choice of an efficient solution method is problem dependent and in many cases the solution method can be the critical point for fast solutions of fluid mechanic problems.

7.3 THE ALTERNATING DIRECTION IMPLICIT PROCEDURE

The general transport equation is an elliptic equation, but by dropping diffusion terms and letting $s_\varphi = 0$ the equation becomes hyperbolic. In hyperbolic

equations the information is propagated along streamlines in the direction of flow from upstream to downstream. This is used when solving the momentum equations which, when discretised, should obey the transport proporty. Thus information is not propagated in lines, but rather in "directed clouds" as sketched in fig. 3.4. The ADI solver developed by Peaceman and Rachford (1955) is used to solve the momentum equations.

The ADI solver was originally developed for two–dimensional calculations where an interchangeability of the rows and columns can take place. The coefficient matrix A can according to the interchangeability be split into

$$A = H + V, \tag{7.4}$$

where H and V are tridiagonal matrices. For a five point difference molecule with equal grid spacing the row–wise listing of the mesh nodes of H and V are, respectively

$$[Hx]_j = -x_{i+1,j} + 2x_{i,j} - x_{i-1,j}, \tag{7.5a}$$

$$[Vx]_j = -x_{i,j+1} + 2x_{i,j} - x_{i,j-1}. \tag{7.5b}$$

The matrices H and V are employed in two alternating sweeps to produce an ADI iteration step as follows

$$(H + \omega I)x^{k+\frac{1}{2}} = b - (V - \omega I)x^k, \tag{7.6a}$$

$$(V + \omega I)x^{k+1} = b - (H - \omega I)x^{k+\frac{1}{2}}. \tag{7.6b}$$

In a three–dimensional calculation the coefficient matrix A is split into three tridiagonal matrices and the same procedure as outlined above is used to solve the matrix system where one ADI iteration step now is composed of three alternating sweeps. The relaxation parameter ω is set to one in our calculations, but it may take another fixed value or change from iteration to iteration.

7.4 GRADIENT METHODS

The error function.

The problem of solving a linear system of equations $\boldsymbol{Ax} = \boldsymbol{b}$ can be turned into the problem of finding a minimum of an error function. The residual vector $\boldsymbol{g}$ corresponding to the trial vector $\boldsymbol{x}$ is

$$\boldsymbol{g} = \boldsymbol{Ax} - \boldsymbol{b}. \tag{7.7}$$

In the following, the matrix $\boldsymbol{A}$ will be assumed symmetric and positive definite (SPD). An error function corresponding to the residual vector can be written

$$e(\boldsymbol{x}) = (\boldsymbol{g})^T \boldsymbol{Ag}. \tag{7.8}$$

When $\boldsymbol{A}$ is assumed SPD the inverse of $\boldsymbol{A}$ is also SPD and eq. (7.8) will only take positive values (or null if $\boldsymbol{g}$ is the null–vector which correspond to $\boldsymbol{x} = \boldsymbol{x}'$ in eq. (7.7), where $\boldsymbol{x}'$ is the solution vector). If eq. (7.7) is substituted into eq. (7.8) the error function takes the form

$$e(\boldsymbol{x}) = \boldsymbol{x}^T \boldsymbol{Ax} - 2\boldsymbol{b}^T \boldsymbol{x} + \boldsymbol{b}^T \boldsymbol{A}^{-1} \boldsymbol{b} \tag{7.9}$$

or, written in the more common way, the error function will subsequently be written as

$$f(\boldsymbol{x}) = \tfrac{1}{2} \boldsymbol{x}^T \boldsymbol{Ax} - \boldsymbol{b}^T \boldsymbol{x} + c, \tag{7.10}$$

which shows that $f(\boldsymbol{x})$ is quadratic in $\boldsymbol{x}$.

Level surfaces of the error function.

In the following, the error function eq. (7.10) will be examined more closely (a more thorough description is given in Axelsson & Barker, 1984).

It is easily seen that the gradient of f at $\boldsymbol{x}$ is the vector $\boldsymbol{g}(\boldsymbol{x})$ and then the gradient vector and the residual vector, according to eq. (7.7), are equal to each other. At $\boldsymbol{x} = \boldsymbol{x}'$ the gradient $\boldsymbol{g}$ vanishes and $\boldsymbol{x} = \boldsymbol{x}'$, which, besides being the solution vector, represents a stationary point and $f(\boldsymbol{x})$ represents a minimum. On that basis the error function can be written

$$f(x) = \tfrac{1}{2}(x - x')^T A(x - x') + c' \tag{7.11}$$

where

$$c' = -\tfrac{1}{2}b^T x' + c.$$

To the matrix A, a set of eigensolutions can be written as $\{\lambda_i, v_i\}_{i=1}^n$ where $Av_i = \lambda_i v_i$, $i = 1, 2, ..., N$. Since A is SPD the eigenvalues are ordered as $0 < \lambda_1 \leq \lambda_2 \leq, ..., \leq \lambda_N$ and the eigenvectors satisfy the orthogonality condition $v_i \cdot v_j = \delta_{ij}$, $i,j = 1, 2, ...N$. Let the eigenvalues be written as $\Lambda = \text{diag}(\lambda_i)$ and $V = [v_1, v_2, ... v_N]$ the eigensolution to A can be written $AV = \Lambda V$, where V is an orthogonal matrix for which the condition $V^{-1} = V^T$ is valid. With the information that $V^{-1} = V^T$ and with the introduction of the variable $z = V(x - x')$ eq. (7.11) can be written

$$\underset{\sim}{f}(z) = f(Vz + x') = \tfrac{1}{2}z^T VAVz + c' = \tfrac{1}{2}z^T \Lambda z + c' \tag{7.12}$$

or

$$\underset{\sim}{f}(z) = \frac{1}{2}\sum_{i=1}^{N} \lambda_i z_i^2 + c'. \tag{7.13}$$

Since $\underset{\sim}{f}(z) = f(x)$ under the transformation $z = V^T(x - x')$ our attention can be turned from $\underset{\sim}{f}$ to f.

Equation (7.13), for $\underset{\sim}{f}(z) = k > c'$, can be expressed as

$$k' = 2(k - c') = \sum_{i=1}^{N} \lambda_i z_i^2, \tag{7.14}$$

which represents an $N-$ dimensional ellipsoid with level surface k'. In fig. 7.1 level surfaces representing an ellipse for 3 different k' values are drawn.

For $N = 2$, eq. (7.14) can be written as $k' = \lambda_1 z_1^2 + \lambda_2 z_2^2$, which can be turned into the more commonly used equation for an ellipse

$$\frac{z_1^2}{(\sqrt{k'}/\lambda_1)^2} + \frac{z_2^2}{(\sqrt{k'}/\lambda_2)^2} = 1, \tag{7.15}$$

where $\sqrt{k'}/\lambda_1$ and $\sqrt{k'}/\lambda_2$ represent the length of the principal axes. It is seen that if $\lambda_1 = \lambda_2$ then eq. (7.15) represents a circle. The ratio λ_2/λ_1 is a measure of the distortion from a circle and for a general $N-$dimensional ellipsoid the ratio λ_N/λ_1 represents the spectral condition number $\kappa(A)$.

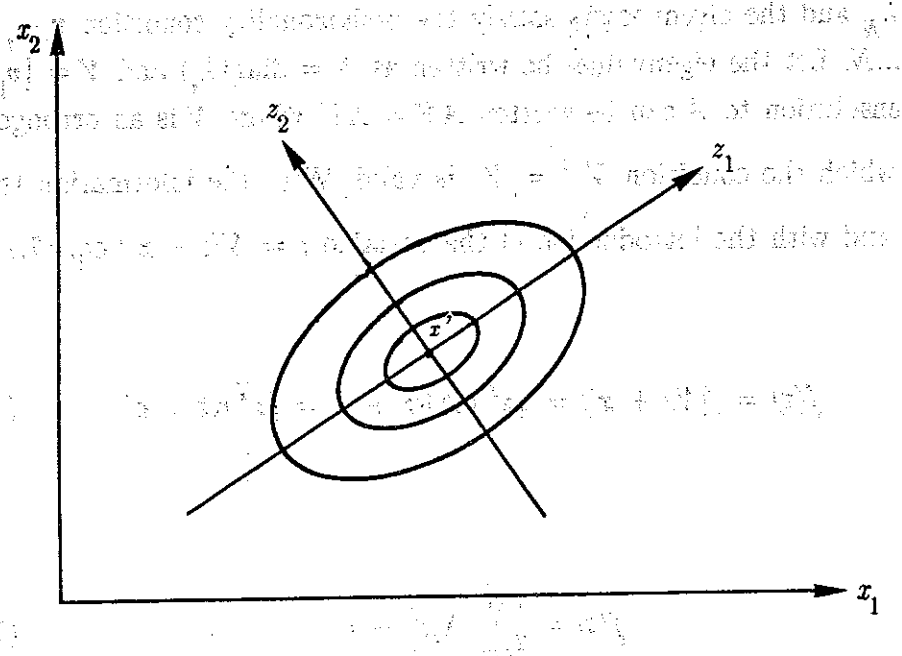

Fig. 7.1 *Level surface of a SPD matrix of order* 2.

Minimizing the error function.

As briefly described in the introdution, the stationary iteration methods find a new trial vector based on the old one through an iteration matrix. Each step in the gradient methods is governed by a line search which is given by

$$\boldsymbol{x}^{n+1} = \boldsymbol{x}^n + \tau_n \boldsymbol{d}^n, \tag{7.16}$$

where $\boldsymbol{x}^n$ is the trial vector at iteration n, $\boldsymbol{d}^n$ is a search vector, τ_n is a parameter proportional to the distance between $\boldsymbol{x}^n$ and $\boldsymbol{x}^{n+1}$, and $\boldsymbol{x}^{n+1}$ is the new trial

vector. The new trial is found through a minimization of $f(\boldsymbol{x})$ for $\boldsymbol{x} = \boldsymbol{x}^{n+1}$ which corresponds to a new lower value of the error function. Substitution of eq. (7.16) into the error function f eq. (7.10), gives

$$f(\boldsymbol{x} + \tau\boldsymbol{d}) = \tfrac{1}{2}(\boldsymbol{x} + \tau\boldsymbol{d})^T\boldsymbol{A}(\boldsymbol{x} + \tau\boldsymbol{d}) - \boldsymbol{b}^T(\boldsymbol{x} + \tau\boldsymbol{d}) + \mathrm{c} \tag{7.17}$$

or

$$f(\boldsymbol{x} + \tau\boldsymbol{d}) = \tfrac{1}{2}\tau^2\boldsymbol{d}^T\boldsymbol{A}\boldsymbol{d} + \tau\boldsymbol{d}^T\boldsymbol{g} + c', \tag{7.18}$$

where $c' = \frac{1}{2}\boldsymbol{x}^T\boldsymbol{A}\boldsymbol{x} - \boldsymbol{b}^T\boldsymbol{x} + c$ is independent of τ. Since $\boldsymbol{A}$ is SPD then $\boldsymbol{d}^T\boldsymbol{A}\boldsymbol{d} > 0$ and eq. (7.18) has a minimum at

$$\partial f/\partial\tau = \tau\boldsymbol{d}^T\boldsymbol{A}\boldsymbol{d} + \boldsymbol{d}^T\boldsymbol{g} = 0,$$

by which τ is determined as

$$\tau = -\boldsymbol{d}^T\boldsymbol{g}/\boldsymbol{d}^T\boldsymbol{A}\boldsymbol{d}. \tag{7.19}$$

7.5 THE METHOD OF STEEPEST DESCENT

In the last section it was seen that whenever a search direction is known a value of τ can be determined to minimize the error function f. A choice of the search direction is the direction in which the error function decreases most rapidly. The negative gradient of f represents this direction and it can be written as $\boldsymbol{d} = -\operatorname{grad}[f(\boldsymbol{x})] = \boldsymbol{b} - \boldsymbol{A}\boldsymbol{x} = -\boldsymbol{g}$. An algorithm where the search directions are based on the negative gradient of f is called the method of the steepest descent and it takes the following form

$$\boldsymbol{g}^n = \boldsymbol{A}\boldsymbol{x}^n - \boldsymbol{b} \tag{7.20a}$$

$$\tau_n = (\boldsymbol{g}^n)^T\boldsymbol{g}^n/(\boldsymbol{g}^n)^T\boldsymbol{A}\boldsymbol{g}^n \tag{7.20b}$$

$$x^{n+1} = x^n - \tau_n g^n, \tag{7.20c}$$

where $n = 0, 1, \ldots$ and $g^n = g(x^n)$.

From eq. (7.20) it is seen that two matrix vector products must be made at each iteration, but if eq. (7.20c) is multiplied and subtracted, respectively, with A and b, the relation

$$g^{n+1} = g^n - \tau_n A g^n \tag{7.20d}$$

is obtained according to eq. (7.20a). The initial residual vector has to be calculated as $g^0 = Ax^0 - b$.

The rate of convergence of the steepest descent method is very slow if the spectral condition number $\kappa(A)$ is large. Large $\kappa(A)$ corresponds to a very elongated ellipsoid where the minimum of the error function can be regarded as the lowest point on a very flat, steep – sided valley. The steps in the steepest descent method results in back and forth traverses in the valley rather than down the valley, Golub & Van Loan (1983)

Convergence analysis.

As shown in eq. (7.11) the error function f can be written

$$f(x) = \tfrac{1}{2}(x - x')^T A(x - x') + c'$$

where

$$c' = -\tfrac{1}{2} b^T x' + c$$

or

$$f(x) = \tfrac{1}{2}(x - x')^T A(x - x') + f(x'). \tag{7.21}$$

A measure of the error can then be quantified as $f(x) - f(x')$. If the energy inner product and energy norm are defined as

$$(x,y)_A = x^T Ay$$

and

$$\|x\|_A = (x,x)_A^{\frac{1}{2}} = (x^T Ax)^{\frac{1}{2}},$$

respectively, the error in the energy norm is defined as

$$f(x) - f(x') = \tfrac{1}{2}(x-x')^T A(x-x') = \tfrac{1}{2}\{\|x-x'\|_A\}^2. \tag{7.22}$$

When the energy norm is used as a measure for the error a convergence analysis can be made and the convergence of the steepest descent can be written

$$\|x^{n+1} - x'\|_A \leq \left[\frac{\kappa(A) - 1}{\kappa(A) + 1}\right]^n \|x^0 - x'\|_A, \tag{7.23}$$

or, if $p(\epsilon)$ is the smallest integer for which

$$\|x^n - x'\|_A \leq \epsilon \|x^0 - x'\|_A, \text{ and } \epsilon > 0,$$

then eq. (7.23) can be written

$$p(\epsilon) \leq \tfrac{1}{2}\kappa(A)\ln(1/\epsilon) + 1. \tag{7.24}$$

The difference between the energy norm and the more commonly used Euclidean norm is illustrated in fig. 7.2.

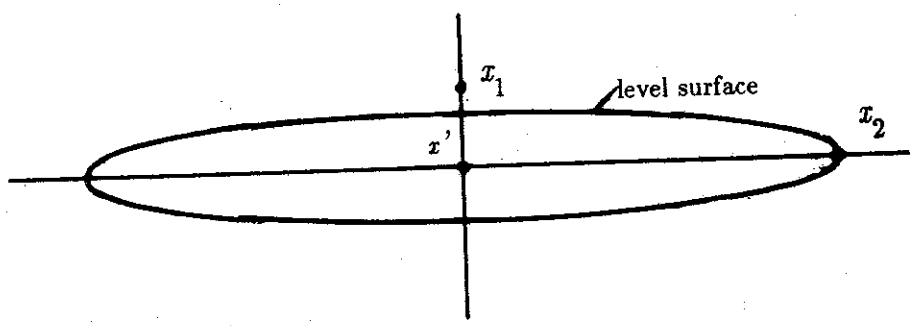

Fig. 7.2 *Level surfaces at which the "energy" is constant.*

Let eq. (7.21) represent a level surface at which the "energy" is constant then the energy at x_2 is lower than x_1 and according to that, $(x_2 - x')$ is smaller than $(x_1 - x')$ measured in the energy norm, but bigger if measured in the Euclidian norm. If the ellipse sketched had been a circle the measure in the two different norms would be equal.

7.6 THE CONJUGATE GRADIENT METHOD

In the preceding section the search direction was taken as the direction in which f decreased most rapidly in a neighborhood of the latest trial vector. In the conjugate gradient method the search direction is chosen such that it contains as much of the nature of the steepest descent method as possible, but with the overriding condition that vectors indicating the direction are mutually A–conjugate. To be A–conjugate means that the search vectors are orthogonal with respect to A which can be written

$$(d^i)^T A d^j = 0, \quad \text{for all } i \neq j.$$

To choose a set of search vectors d^0, d^1,..., which represents as nearly as possible the directions of the steepest descent a search vector spanned by the latest known residual vector and the search vector from the preceding iteration is formed

$$d^{n+1} = -g^{n+1} + \beta_n d^n, \qquad n = 0, 1,... \tag{7.25}$$

Geometrically the new search vector d^{n+1} points to the center of the intersection ellipse where its plane is determined by g^{n+1} and d^n, Fröberg (1965). The parameter β_n in eq. (7.25) is determined by using the condition that d^{n+1} is A–conjugate upon d^1,... d^n. By multiplying each side of eq. (7.25) with Ad^n the parameter β_n is given by

$$\beta_n = (g^{n+1})^T A d^n / (d^n)^T A d^n. \tag{7.26}$$

In eq. (7.20) it was shown that the residual vector in the method of the

steepest descent can be calculated iteratively as $g^{n+1} = g^n - \tau_n A g^n$. In the general case the residual is calculated as

$$g^{n+1} = g^n + \tau_n A d^n, \tag{7.27}$$

and if the inner product with $(d^n)^T$ is formed the relation

$$(d^n)^T g^{n+1} = (d^n)^T g^n - \tau_n (d^n)^T A d^n \tag{7.28}$$

is obtained. As was shown previosly, $\tau_n = -(d^n)^T g^n / (d^n)^T A d^n$ minimizes $f(x^n - \tau_n d^n)$, but it also has the proporty to make the gradient g^{n+1} orthogonal to the search direction d^n, which can be seen if the expression for τ_n is compared with eq. (7.28). Equation (7.28) is then equal to zero and by induction it can be shown that the orthogonality relation

$$(g^i)^T d^j = 0 \quad \text{for } i > j \tag{7.29}$$

is satisfied.

The relation $(g^{n+1})^T g^n$ can be written

$$(g^{n+1})^T g^n = (g^{n+1})^T (g^{n-1} + \tau_{n-1} A d^{n-1}) =$$

$$(g^{n+1})^T g^{n-1} + \tau_{n-1} (- d^{n+1} + \beta_n d^n)^T A d^{n-1} \tag{7.30}$$

and with the relation that the search vectors are mutually A–conjugate eq. (7.30) is written

$$(g^{n+1})^T g^n = (g^{n+1})^T g^{n-1}. \tag{7.31}$$

The procedure can be continued to obtain

$$(g^{n+1})^T g^n = (g^{n+1})^T g^1 = (g^{n+1})^T (g^0 - \tau_0 A g^0) =$$

$$(g^{n+1})^T g^0 - (g^{n+1})^T g^0 g^0 A g^0 / g^0 A g^0 = 0. \tag{7.32}$$

Equation (7.32) shows that after $n + 1$ iterations the residuals g^1, g^2,..., g^{n+1} are mutually orthogonal and the following orthogonal relation is satisfied

$$(g^i)^T g^j = 0 \quad \text{for } i \neq j. \tag{7.33}$$

Applying the orthogonality relation eq. (7.29) with eq. (7.19) and eq. (7.25) shows that τ_n can be expressed as

$$\tau_n = (g^n)^T g^n / (d^n)^T A d^n. \tag{7.34}$$

Using the other orthogonality relation eq. (7.33) with eqs. (7.25), (7.26), (7.27), and (7.29) shows that β_n can be expressed as

$$\beta_n = (g^{n+1})^T g^{n+1} / (g^n)^T g^n. \tag{7.35}$$

With the foregoing expressions, the conjugate gradient method takes the form

$$\tau_n = (g^n)^T g^n / (d^n)^T A d^n, \tag{7.36a}$$

$$x^{n+1} = x^n + \tau_n d^n, \tag{7.36b}$$

$$g^{n+1} = g^n + \tau_n A d^n, \tag{7.36c}$$

$$\beta_n = (g^{n+1})^T g^{n+1} / (g^n)^T g^n, \tag{7.36d}$$

$$d^{n+1} = - g^{n+1} + \beta_n d^n, \tag{7.36e}$$

where $n = 0, 1, \ldots$ The start vector x^0 can be chosen arbitrary and g^0 and d^0 are calculated, respectively, as $g^0 = Ax^0 - b$ and $d^0 = - g^0$.

Convergence analysis.

When Hestenes & Stiefel (1952) proposed the CG method it was originally thought as a direct solver, where the number of steps are equal to or lower than the order of $\boldsymbol{A}$. This can be verified from eq. (7.33) where it is known that $\boldsymbol{g}^n$ for $n = 0, 1, ..., N$ are mutually orthogonal. Since $\boldsymbol{g}^n$ has the dimension N the residual after N steps will be equal to zero. In fact, it can be shown that the number of steps is equal to the number of distinct eigenvalues which are lower or equal to the order of $\boldsymbol{A}$. Even if the theory says that the exact solution can be found in at most N steps it will not stand in practice. The reason is that rounding errors are not absent in practice. Consequently, it results in search directions that are not exactly $\boldsymbol{A}$–conjugate and the orthogonality is lost among residual vectors. Even though the effect of rounding errors will not show up until the residual is very low the CG method is not used as a direct solver, but it has gained a considerable interest as an iterative method for sparse matrices. To quantify the error $f(\boldsymbol{x}) - f(\boldsymbol{x}')$ after a number of iterations, the energy norm is used as in the method of the steepest descent. The number of iterations used to lower the error a factor ϵ is shown in Axelsson & Barker (1984) to be

$$p(\epsilon) = \tfrac{1}{2}\sqrt{\kappa(\boldsymbol{A})}\ln(2/\epsilon) + 1. \tag{7.37}$$

Let eq. (7.37) be compared with the corresponding equation in the method of steepest descent, eq. (7.24). Then it is seen that the spectral condition number for the CG method enters as the square root of its value whereas it enters without the square root in the method of steepest descent. Equation (7.37) is usually pessimistic and is not principally dependent on the values of the limiting eigenvalues but on the grouping of the full spectrum of eigenvalues, Stewart (1975). Even if a grouping of the eigenvalues gives a faster convergence than predicted by eq. (7.37) the rate of convergence is still too slow to be used as an efficient iterative solver and the CG method is usually not used as it stands alone.

7.7 THE PRECONDITIONED CONJUGATE GRADIENT METHOD

The number of iterations required to reach a certain error level can be

estimated with eq. (7.37) but for ill–conditioned problems the rate of convergence is hopelessly slow. An important way around this problem is to precondition A. The original system to be solved is transformed to a system of improved conditions with a preconditioning nonsingular symmetric matrix B. Is B factored in the form $B = EE^T$ ($E = E^T$ because B is symmetric) $Ax = b$ can be transformed to the system

$$\underset{\sim}{A}\underset{\sim}{x} = \underset{\sim}{b}, \tag{7.38}$$

where $\underset{\sim}{A} = E^{-1}AE^T$, $\underset{\sim}{x} = E^Tx$, and $\underset{\sim}{b} = E^{-1}b$.

Since $x^TAx = \underset{\sim}{x}^T\underset{\sim}{A}\underset{\sim}{x}$ and $x^TAx > 0$, $\forall x \neq 0$ then $\underset{\sim}{x}^T\underset{\sim}{A}\underset{\sim}{x} > 0$, $\forall \underset{\sim}{x} \neq 0$ and $\underset{\sim}{A}$ is also positive definite. The similarity transformation

$$E^{-T}AE^T = E^{-T}E^{-1}A = B^{-1}A$$

shows that $\underset{\sim}{A}$ and $B^{-1}A$ have the same eigenvalues and with convergence rate described in eq. (7.37) the system $\underset{\sim}{A}\underset{\sim}{x} = \underset{\sim}{b}$ has the convergence properties according to the limiting eigenvalues of $B^{-1}A$. It is seen that the spectral condition number $\kappa(\underset{\sim}{A})$ is determined by A and the preconditioning matrix B, and not by E, even though $\underset{\sim}{A} = E^{-1}AE^T$.

The CG method can be used directly on the transformed system but the sparsity of $\underset{\sim}{A}$ might be less than that of A, and the trial vector $\underset{\sim}{x}^n$ is an approximation to $\underset{\sim}{x}'$ and not to x'. Let the transformation $\underset{\sim}{A} = E^{-1}AE^T$, $\underset{\sim}{x} = E^Tx$, and $\underset{\sim}{b} = E^{-1}b$ be substituted into the CG method of the transformed system. Then the preconditioned CG method (PCG) is defined as follows

$$\tau_n = (g^n)^Th^n/(d^n)^TAd^n, \tag{7.39a}$$

$$x^{n+1} = x^n + \tau_n d^n, \tag{7.39b}$$

$$g^{n+1} = g^n + \tau_n Ad^n, \tag{7.39c}$$

$$h^{n+1} = B^{-1}g^{n+1}, \tag{7.39d}$$

$$\beta_n = (g^{n+1})^T h^{n+1} / (g^n)^T h^n, \tag{7.39e}$$

$$d^{n+1} = -h^{n+1} + \beta_n d^n, \tag{7.39f}$$

$n = 0, 1, \ldots$ x^0 is chosen arbitrary and g^0, h^0 and d^0 are calculated as $g^0 = Ax^0 - b$, $h^0 = B^{-1}g^0$, and $d^0 = -h^0$.

To improve the PCG method over the CG method the preconditioning matrix B should be chosen to give $\kappa(B^{-1}A) < \kappa(A)$. Two extreme matrices for preconditioning would be $B^{-1} = A^{-1}$ and $B^{-1} = I$. $B^{-1} = A^{-1}$ gives the optimal choice, whereas $B^{-1} = I$ does not change the eigenvalue distribution. At first sight, B^{-1} should be as "close" to A^{-1} as possible but three other factors must also be kept in mind: 1) the determination of the coefficients in B should cost little computer time, 2) the solution of $Bh^n = g^n$ should be done very quickly, and 3) the storage of B, or rather, a factored form of B, should require no or little extra storage.

One class of preconditioning matrices is the stationary iterative methods where the form is given in eq. (7.3). The advange of this class is that the coefficients in B usually do not need to be calculated but can be taken directly from A. Thus no extra storage is needed and the solution of $Bh^n = g^n$ can be solved by a forward – backward substitution. This class of preconditioning gives a fast convergence and in section 6 the CG method is compared with the PCG method, where the preconditioning matrix is the M–matrix in the SSOR method. It was mentioned earlier that a preconditioning was made to improve the conditions of the original system to be solved, but with a preconditioning matrix, taken from a stationary iterative method the CG method can be classified as a dynamic acceleration method of the stationary iterative methods, Golub & Van Loan (1983). In the following, a preconditioning of a system $Ax = b$ will only be taken as a method to improve the conditions of the CG method.

Preconditioning by an incomplete factorization.

In the preceding, the stationary iterative methods have been considered as a source of preconditioning matrices, but in the following a class of incomplete

factorizations of A will be considered.

In the stationary iterative methods, a splitting of A in the form $A = M + R$ was used. The same form will be used in the incomplete factorization with the M–matrix written as $M = LU$, where L and U are lower and upper triangular matrices, respectively. The preconditioning matrix B will be taken as an incomplete matrix, $B = M = LU = LDL^T$, where $\mathrm{diag}(L) = I$. The defect matrix $R = A - LU$ depends on the factorization. When $R = 0$, i.e. $B = A$, a complete factorization of A is made, while $R \neq 0$ implies an incomplete factorization.

During each iteration of the PCG method the preconditioning system $Bh = g$ has to be solved. The cost of this has to be low and the factor L is therefore chosen as a sparse matrix. The incomplete factorization is based on an incomplete Cholesky factorization where a pointwise version will be described.

The pointwise version is the Relaxed Incomplete Cholesky factorization, RIC, which is a generalization of the Incomplete Cholesky factorization, IC, and the Modified Incomplete Cholesky factorization, MIC. The IC is described in Meijerink & Van der Vorst (1977) and Gustafsson (1983), and MIC is described in Gustafsson (1983) and Axelsson & Barker (1984).

Another version, which is used in the calculations presented in chapter 8, is the Relaxed Block Incomplete Cholesky factorization which is a generalization of the (Modified) Block Incomplete Cholesky factorization, (MBIC), BIC. This is described in Concus et al (1985), Axelsson et al (1984), Axelsson (1986), and Gervang (1989). The RBIC version gives a faster convergence as the one presented here, but more cpu time is needed to calculate the factorization.

The Relaxed (pointwise) Incomplete Cholesky factorization.

During an incomplete factorization the amount of fill–ins must be controlled somehow. The two main methods are either fill–ins controlled by size of the actual value, Munksgaard (1978), or by some chosen subset J of indices (i,j) in which fill–ins are permitted. Outside this subset fill–ins are ignored. The last one will be considered here.

A RIC factorization based on the notation in Axelsson & Barker (1984),presented in a relaxed form, takes the following algorithm. For $r = 1, 2, \ldots, N-1$ do

$$l_{ir} = a_{ir}^{(1)} (a_{rr}^{(r)})^{-1}$$

$$a_{ij}^{(r+1)} = \begin{cases} a_{ij}^{(r)} - l_{ir}a_{rj}^{(r)}, & (r+1 \le j \le N) \cap ((i,j) \in J) \\ 0, & (r+1 \le j \le N) \cap ((i,j) \notin J) \\ a_{ii}^{(r)} - l_{ir}a_{rj}^{(r)} + \omega \sum_{\substack{k=r+1 \\ (i,k) \notin J}}^{N} a_{ik}^{(r)} - l_{ir}a_{rk}^{(r)}, & j = i, \end{cases} \tag{7.40}$$

where $i = r + 1, r + 2, ..., N$. The matrices L and $A^{(r+1)}$, $r = 1, 2, ..., N$–1 are completely defined $N \times N$ matrices when we add

$$l_{ij} = \begin{cases} 0, \text{ for } j > i \\ 1, \text{ for } j = i \end{cases}$$

$$a_{ij}^{(r+1)} = \begin{cases} 0, & \text{for } j = 1, ..., r;\ i = j+1, ..., N \\ a_{ij}^{(i)} & \text{for } i = 1, ..., r;\ j = i, ..., N \end{cases}$$

and the matrix U is then given by

$$u_{ij} = \begin{cases} 0, & \text{for } j \neq i \\ a_{ii}^{(i)}, & \text{for } i = 1, 2, ..., N;\ j = i, i+1, ..., N. \end{cases}$$

The RIC factorization of A is then given by

$$B = LU = LDL^T,$$

where L and U are lower and upper triangular matrices, respectively, and D is a diagonal matrix.

The relaxation parameter ω takes the values $0 \le \omega \le 1$. The IC factorization is obtained by setting $\omega = 0$, and $\omega = 1$ corresponds to the MIC factorization. For $\omega = 0$ fill–ins are totally ignored, but for $\omega = 1$ the fill–ins are added to the diagonal elements. In the following, the subset J is only taken as $J = \{(i,j);\ a_{ij} \neq 0\}$, why L and D only will contain elements on the positions where A has elements.

In Axelsson & Barker (1984) it is shown that for A a SPD matrix and $\omega = 1$ the factorization shown in eq. (7.40) is stable. With $\omega = 1$ the rowsum (and

consequently the columnsum) of $\boldsymbol{B} = \boldsymbol{LDL}^T$ is retained, and the rowsum of the defect matrix $\boldsymbol{R}$ is equal to zero. For a symmetric semi–positive definite (SSPD) matrix the algorithm in eq. (7.40) will still be stable, but D_{NN} is zero and the solution of the preconditioned system $\boldsymbol{Bh} = \boldsymbol{g}$ in the PCG method is not possible. As already described the CG method was developed for SPD matrices but it works on SSPD matrices as well, Barker (1987). To work with the PCG method on SSPD matrices, where the precondition matrix $\boldsymbol{B}$ is found from an incomplete factorization, the relaxation parameter ω can take the values $0 \leq \omega < 1$. But it can take the value $\omega = 1$, too, if $\boldsymbol{A}$ is SPD, Barker (1988).

7.8 ASSESSMENT OF THE CG AND PCG METHODS

The problem selected to test the efficiencies of the CG and PCG methods is a two–dimensional Poisson equation with variable coefficients Γ, which resembles the pressure–correction equation of a Navier–Stokes solver

$$\text{div}[\Gamma \text{ grad}(\phi)] = S(x,y), \quad \text{in region } R, \tag{7.41}$$

where Γ is a function of x and y, and S is a source term subject to the constraint

$$\iint_R S\text{dA} = 0,$$

indicating that no net source exists in the domain. This corresponds to the requirement in the pressure–correction equations that the sum of the mass sources should be zero to satisfy overall continuity. Neumann boundary conditions are imposed on all boundaries, i.e.

$$\Gamma \frac{\partial \phi}{\partial \text{n}} = 0.$$

One pair of test functions which satisfy eq. (6.1), see Tsui (1987), is

$$\Gamma = 1/[\tfrac{1}{3}(a^2x^3 - y^3) - (x-y) + 2]$$

$$S = 2(a^2x - \text{y})$$

and the exact solution is

$$\phi = \frac{1}{18}(a^4x^6+y^6) - \frac{1}{3}(a^2x^4+y^4) + \frac{1}{3}a^2x^3y(1-\frac{1}{3}y^2) + \frac{1}{2}(x^2+y^2) - xy(1-\frac{1}{3}y^2) + 2[\frac{1}{3}(a^2x^3-y^3)-(x-y)]$$

in the region $-1/a \leq x \leq 1/a$ and $-1 \leq y \leq 1$. The parameter a is an aspect ratio parameter which can model the region from a square region ($a = 1$) to a non–square region ($a > 1$).

Equation (7.41) is discretised with a central differencing scheme and solved with a finite volume method. The convergence requirement is that the 1–norm (sum of the absolute residuals at all interior nodes) falls below 10^{-4}. The number of interior nodes is of course equal to the number of unknowns and gives the order of the coefficient matrix. For the chosen differencing scheme, a Poisson equation has a five banded matrix structure on a rectangular region.

The residual histories of the CG for the two values $a = 1$ and 5 of the aspect parameter are plotted in fig. 7.3 on two grid densities, 20×20 and 40×40. It is seen that on both grids the number of iterations to reach the stop criterion is doubled if a is raised from 1 to 5, and the number of iterations is doubled too if the number of nodes is doubled in each direction of the region R (the number of interior nodes is raised 4 times). From the convergence analysis of CG it was shown that the residual was a monotonic decreasing function of iterations. The wavy shape, especially in the beginning of the residual history, is due mainly to the use of an Euclidian norm instead of the energy norm. In practice, a Euclidian norm is used because it requires less computation, even if the convergence analysis is made in the energy norm. All figures show Euclidian norms.

The slope of the curves is lower in the beginning of the residual history than in the end. This has to do with the start vector. The components of the start vector might appear in a condition that the search vector is searching in a direction very far from the minimun and on that basis it can take a few iterations to "tune" the search vector to search in directions where the residual decreases rapidly. On the other hand, if the start vector consists of components which are important to the convergence, the convergence can be very fast already from the beginning. The influence of the start vector on the residual history is being studied in an accompanying paper.

Fig. 7.4 shows the residual history for the PCG method where the preconditioning matrix is the M–matrix from the SSOR method. The grids and the aspect parameters are the same as for the CG method and the relaxation

parameter in the SSOR method is $\omega = 1.5$. The residual history shows the same tendency as for the CG method, even if the curves are more wavy, but the total number of iterations to reach the stop criterion is lowered a factor 3–4.

The curves in fig. 7.4 are only shown for one value of the SSOR relaxation parameter ω. Tabel 1 shows the influence of ω upon the number of iterations for $a = 1$ and the grid density 20×20. It is seen that the convergence is very insensitive to ω in a large interval around $\omega = 1.5$.

Tabel 1. Number of iterations of PCG with SSOR, $a = 1$ and grid 20×20.

ω:	0.1	0.5	1.0	1.1	1.2	1.3	1.4	1.5	1.6	1.7	1.8	1.9	1.99
N:	40	63	40	37	34	33	30	30	30	31	33	43	66

Tabel 2 shows the sensitivity of ω for the SSOR preconditioning with $a = 1$ on the grid density 40×40. Again low sensitivity is seen if ω is selected near $\omega = 1.5$. In fig. 7.4 all the runs where made with $\omega = 1.5$ but, as seen in table 2, the optimal choice was not used on the grid density 40×40 with $a = 1$.

Tabel 2. Number of iterations of PCG with SSOR, $a = 1$ and grid 40×40.

ω:	0.1	0.5	1.0	1.1	1.2	1.3	1.4	1.5	1.6	1.7	1.8	1.9	1.99
N:	200	129	78	73	67	63	59	56	52	49	51	62	124

Fig. 7.5 shows the residual history for the RIC method. The same conditions as for the CG and the SSOR–PCG methods are used. The relaxation parameter in the incomplete factorization is chosen as $\omega = 0.9$. The rate of convergence is increased dramatic compared with the CG method. Compared with the SSOR–PCG method, the convergence is increased a factor 2–3 and has much less wavy curves. The sensitivity of ω on the convergence is shown in tabel 3 and tabel 4 for $a = 1$ and on grid densities 20×20 and 40×40, respectively. It is seen that the relaxation parameter takes the optimum much closer to one than to zero. This indicates that a partial addition of fill–ins on the diagonal is important for the rate of convergence. In the following plots of the residual histories the relaxation parameter ω is taken as $\omega = 0.9$.

Tabel 3. Number of iterations of RIC, $a = 1$ and grid 20×20.

ω:	0.1	0.2	0.3	0.4	0.5	0.6	0.7	0.8	0.9	0.95	0.99	0.9999
N:	22	22	21	20	20	19	18	17	16	16	17	20

Tabel 4. Number of iterations of RIC, $a = 1$ and grid 40×40.

ω:	0.1	0.2	0.3	0.4	0.5	0.6	0.7	0.8	0.9	0.95	0.97	0.9999
N:	41	41	39	38	37	35	33	30	27	24	23	32

Fig. 7.6 is the same plot as fig. 7.5, but the x–axis has been blown up. The figure should be used as reference for fig. 7.7 and fig. 7.8 where the number of nodes and aspect ratio is examined. In fig. 7.7 the residual history is shown over 13 decades for the RIC method on a square grid with respectively 20×20 and 40×40 interior nodes. It is seen that the number of iterations to reach a certain error level is raised less than 1.5, even if the number of points is raised a factor 4. In fig. 7.8 the conditions around the aspect ratio is examined for the RIC on a 40×40 grid with a values taken as 1, 10, 100, and 1000. The differences in the number of iterations to reach the stop criterion are due mainly to the phenomena at the first iteration. At the very first iteration, the CG, as well as the PCG, takes a steepest descent step and for high a values the spectral condition number may be assumed higher than for low a values. Because of the very fast convergence for ill–conditioned matrices in the first step of the steepest descent the RIC should give a very fast convergence at the first iteration when a is big, which is observed in fig. 7.8. Even for the very high value of a the slope of the curve is nearly as step as for the low value of a which indicates that the use of RIC as a preconditioning matrix is very attractive. An even more attractive preconditioning matrix is the RBIC which is chosen for the solution of the present problem as stated in subsection "Preconditioning by an incomplete factorization".

7.9 SOLUTION PROCEDURE FOR FLOW PROBLEM AND STOP CRITERION

In chapter 5 the solution algorithm for the non–linear problem was given where, to repeat, the sequence leading to the final solution was given by

1) Initialise all values.
2) Calculate the coefficients of the momentum equations and solve the equation, with suitable underrelaxation, employing a predicted pressure field.

   The predicted velocity fields are solved with the ADI solver and u^*, v^*, and w^* are obtained.
3) Calculate the coefficients of the pressure corrector equation and solve the

first pressure corrector equation with the PCG method.

4) Calculate the first corrected pressure field and velocity fields which are denoted, respectively, by p^*, u^{**}, v^{**}, and w^{**}.

5) Calculate a new right hand side and solve the second pressure correction equation with the PCG method.

6) Calculate the second corrected pressure field and velocity fields which are denoted, respectively, by p^{**}, u^{***}, v^{***}, and w^{***} and treat them as new value fields at the next step and repeat from step 2 until convergence is obtained.

The solution sequence involves stoping criteria for each momentum equation, each pressure corrector equation, and the non–linear equations in solving the steady state problem. The residual for each momentum equation is lowered a factor 100–1000 in each step which requires form 1 to 10 ADI iterations. The 1–norm is used to calculate the residuals. The large number of iterations is required when nonlinear fluid rheology of viscarin is simulated. The calculations are made at low Reynolds number due to the high viscosity which creates high amount of diffusive fluxes and makes the ADI solver less effective than when water is simulated.

At each pressure correction level the residual is lowered a factor 50–100 where again the 1–norm is used to calculate the residuals. The number of iterations required to reach the convergence criterion are from 1 to 30 dependent on whether it is a two– or a three–dimensional problem and on the type of flow fields encountered, but the number of iterations are very insensitive to the number of unknowns.

In order to solve the non–linear problem, several linear matrix systems have to be solved in each step leading to the final solution. A residual vector for each linearised matrix system based on an updated coefficient matrix and right hand side is written

$$\boldsymbol{r}^n = \boldsymbol{A}^n \boldsymbol{x}^{n-1} - \boldsymbol{b}, \tag{7.42}$$

or, if the general form, eq. (3.17), is used the residual at each point is written

$$r^n_{P,\varphi} = a^n_p \varphi^{n-1}_P - \sum_m a^n_m \varphi^{n-1}_m - b^n, \tag{7.43}$$

where n is number of steps. The total residual is calculated with use of the 1–norm

$$R_{\varphi}^{n} = \sum_{1}^{N} |r_{P,\varphi}^{n}|.$$

To non–dimensionalise the residual R_{φ}^{n}, the residual is normalised with the corresponding inlet flux

$$RNOR_{\varphi} = R_{\varphi}^{n}/\text{Inlet\_flux},$$

where, for example, the inlet flux used is the total mass inlet flux when solving the pressure corrector equations and the total momentum inlet flux when solving the momentum equations.

A solution to the total flow problem is usually obtained when the maximum $RNOR_{\varphi}$ is below 10^{-3}, but for viscarin at high velocities a residual as low as 10^{-4} is needed.

7.10 CLOSURE

In this chapter, the efficiencies of the conjugate gradient method, as well the preconditioned conjugate method, were examined. The two preconditioning methods employed were the SSOR and an incomplete factorization.

The conjugate gradient method showed, next to slow convergence, a high dependency on aspect ratio as well as on the the number of unknowns and is consequently not very attractive as a iterative solver. In the preconditioned conjugate gradient methods, the dependency on aspect ratio and number of nodes was considerably lowered. The incomplete factorization was superior to the SSOR and the number of iterations to reach a certain error level was lowered a factor 10 over the CG method and a factor 2–3 over the SSOR–PCG method.

In the overall solution algorithm for the non–linear problem the residuals of the momentum equations are lowered a factor 100–1000 and the residuals for the pressure corrector equations are lowered a factor 50–100 at each non–linear step. The overall problem is stopped when the residual for the linearised matrix systems with updated coefficient and normalised by their respective values at inlet falls below 10^{-3}–10^{-4}.

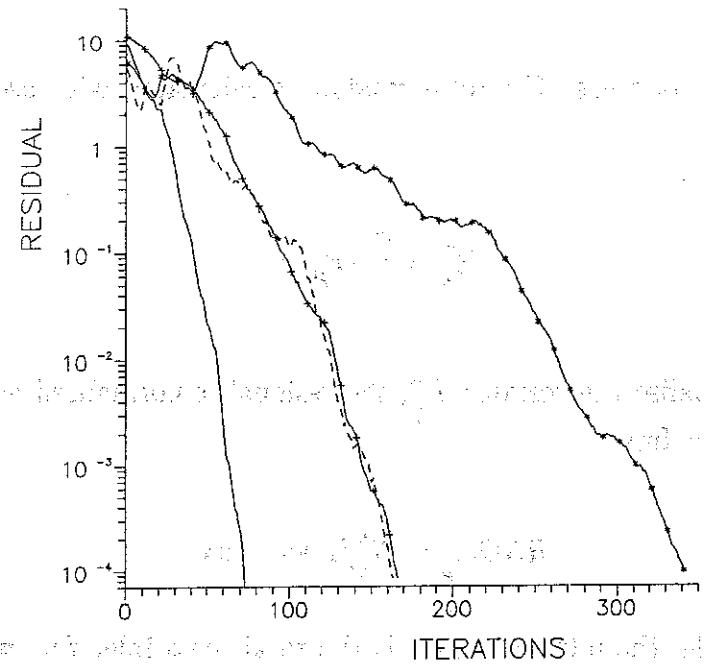

Fig. 7.3 *Residual historie for the CG method.*
——— 20×20, $a = 1$; — — — 20×20, $a = 5$;
+—+—+ 40×40, $a = 1$; *-*-* 40×40, $a = 5$.

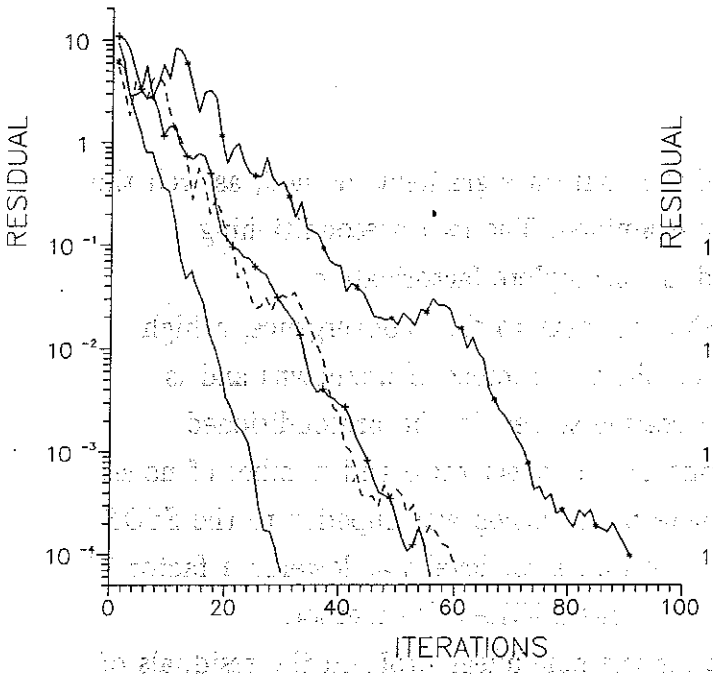

Fig. 7.4 *Residual historie for the SSOR–CG method.*
——— 20×20, $a = 1$; — — — 20×20, $a = 5$;
+—+—+ 40×40, $a = 1$; *-*-* 40×40, $a = 5$.

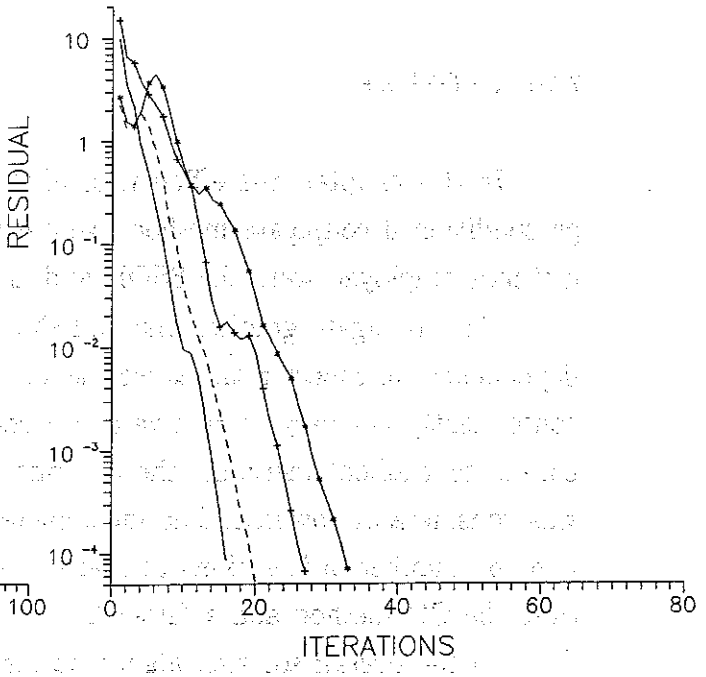

Fig. 7.5 *Residual historie for the RIC–CG method.*
——— 20×20, $a = 1$; — — — 20×20, $a = 5$;
+—+—+ 40×40, $a = 1$; *-*-* 40×40, $a = 5$.

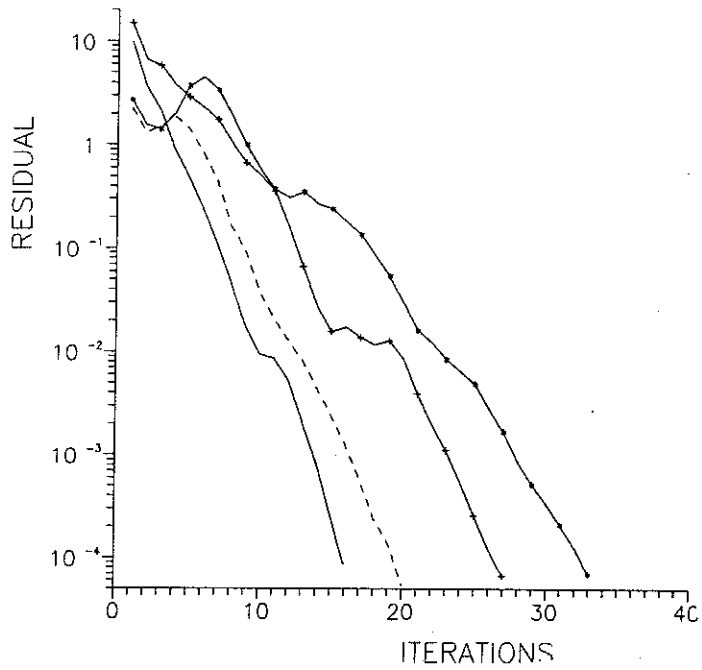

Fig. 7.6 *Residual historie for the RIC–CG method.*
——— 20×20, $a = 1$; — — — 20×20, $a = 5$;
+—+—+ 40×40, $a = 1$; *-*-* 40×40, $a = 5$.

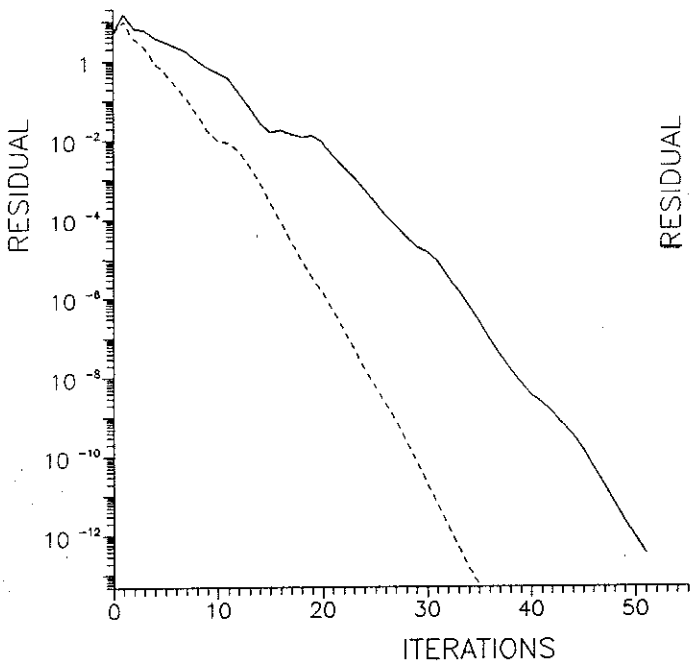

Fig. 7.7 *Residual historie for the RIC–CG method.*
——— 20×20, $a = 1$; — — — 40×40, $a = 1$.

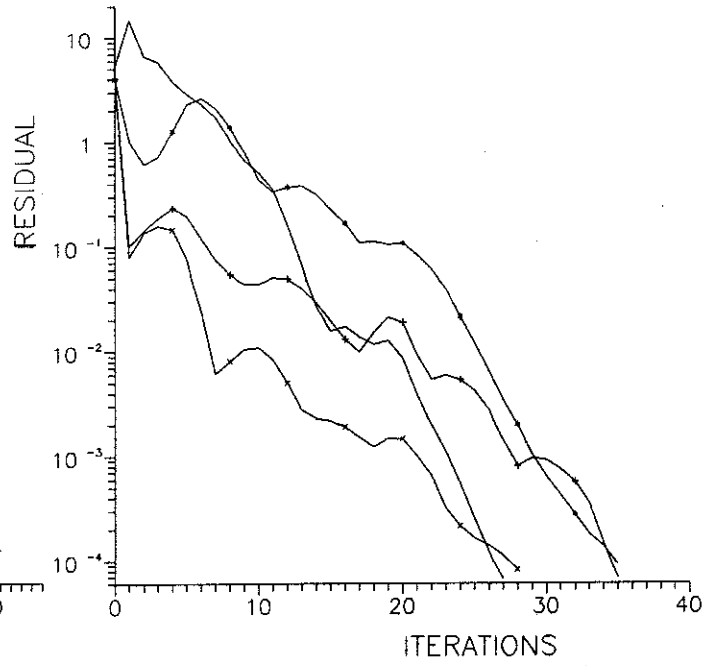

Fig. 7.8 *Residual historie for the RIC–CG method.*
--* 40×40, $a = 1$; ——— 40×40, $a = 10$;
+—+—+ 40×40, $a = 100$; ×–×–× 40×40, $a = 1000$.

CHAPTER 8

APPLICATIONS AND EXPERIMENTS

8.1 INTRODUCTION

The numerical model described in the preceding chapters will be applied to flows in straight and curved ducts, all with a cross section of $16 \cdot 10^{-6}$ m^2. The fluids which will be considered are the Newtonian fluid water and the Non–Newtonian fluid 2% viscarin which is a 2% solution of viscarin in water. The results will be compared with experimental results where possible.

First, in section 2, applications of the method to water flows are presented. The calculations are concentrated on the entrance problem of a straight duct and on primary and secondary flow of a curved duct.

Next, in section 3, a 2% viscarin solution is simulated and the results are presented for both straight and curved ducts with emphasis on the straight ducts.

Pressure drop experiments with 2% viscarin solution is carried out in section 4 and compared with the calculated results.

Finally, in section 5, closing remarks are given.

8.2 SIMULATION OF WATER IN DUCTS

The application of water in the entrance flow between parallel plates will mainly be used as a test case to compare the numerical result with numerical results obtained by other's calculations. Fully developed velocity profiles are also shown for a straight duct with cross section dimensions of 1×16 mm. The main study is the study of the secondary flow in the curved ducts. One geometry is studied for both fully developed flow and developing flow.

Throughout the simulations, the density ρ will be set to 1000 kg/m^3 and the dynamic viscosity μ is set to 0.001 Pa·s which are the values of water at 20^{0}C.

8.2.1 STRAIGHT DUCT

Entrance flow.

The entrance flow between parallel plates has been solved for the Reynolds numbers 20, 200, and 2000. The Reynolds number is referred to the height of the duct and to the mean velocity. The inlet boundary condition is that commonly used of uniform and parallel flow. The centerline velocity and the entrance length is of interest in the entrance flow. In fig. 8.1 (taken from Walter & Larsen, 1981) the centerline velocity normalized with the mean velocity is shown as function of distance from the inlet normalized with the half duct height and divided by the Reynolds number. The solution by Schlichting is based on a boundary layer formulation and is an approximation valid for Re $\rightarrow \infty$. The present results are shown in fig. 8.2 and it is seen that they agree very well with the results in fig. 8.1.

The calculation was carried out with the hybrid scheme. The grid involved 15 control volumes across the duct with a cell length ratio of 1.2 growing from the walls towards the centerline and 80 control volumes along the duct with a cell length ratio of 1.04 growing from the inlet to the outlet. The outlet boundary condition was set at $x/Re = 0.16$, where x denotes axial position from inlet normalized by half height.

Schlichting (1979) gives an expression for the entrance length which is $l_E = 0.08h(u2h/\nu) = 0.08hRe$, where h is half the height of the duct. With this expression the normalised velocity should reach its maximum value at $x/Re = 0.08$. This is not the case, and should not be, since the Reynolds numbers, in our

case, are finite.

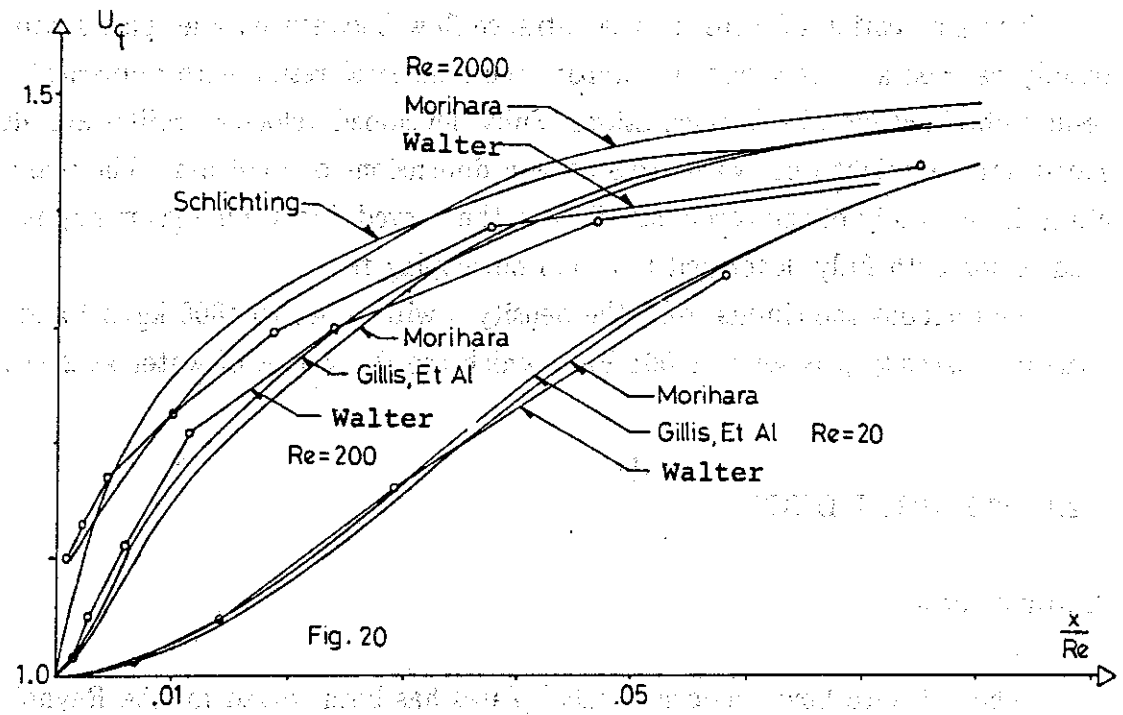

Fig. 8.1 *Centerline velocity on entrance flow* (*taken from Walter & Larsen*, 1981).

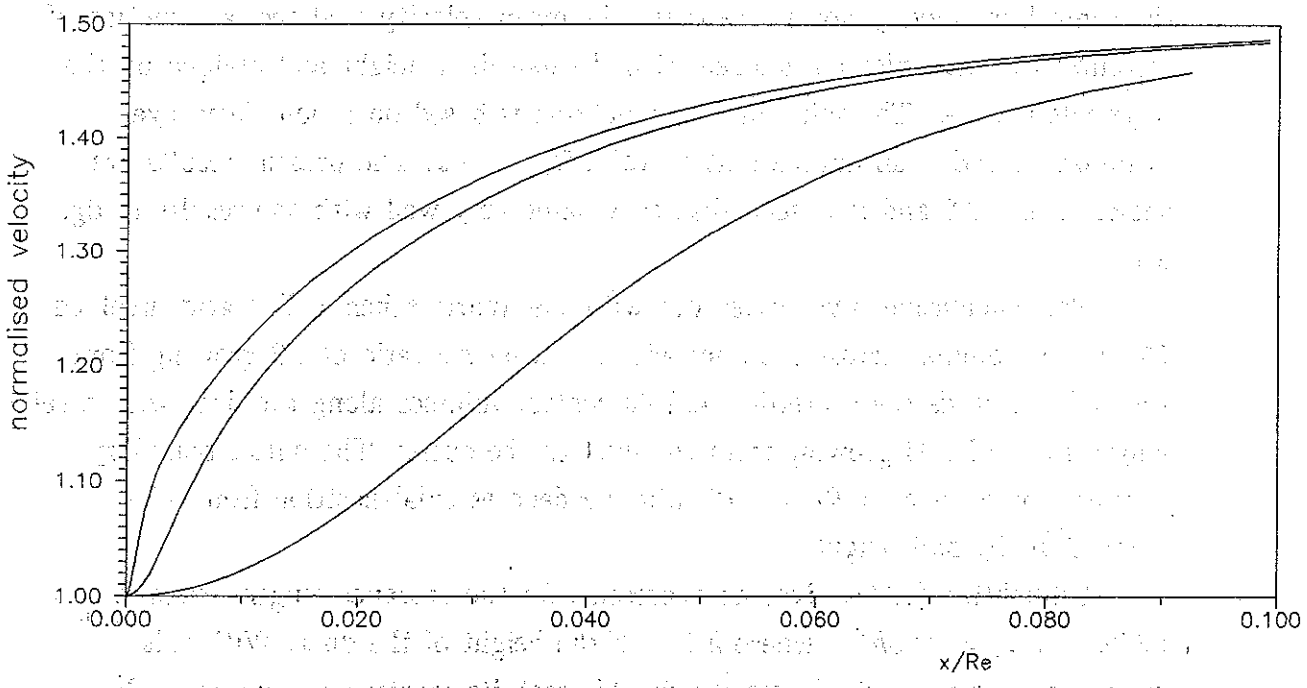

Fig. 8.2 *Centerline velocity on entrance flow* (*present calculations*).

Fully developed flow.

The geometry and the matching coordinate system of the straight duct is shown in fig. 8.3. With a cross section of 1×16 mm the computational grid is 13 control volumes in the 1 mm direction and 39 control volumes in the 16 mm direction, respectively. The ratio between successive grid cell lengths in each direction is 1.2 in the rectangular grid, strained according to geometric progression. The symmetry conditions at the midplanes were not used.

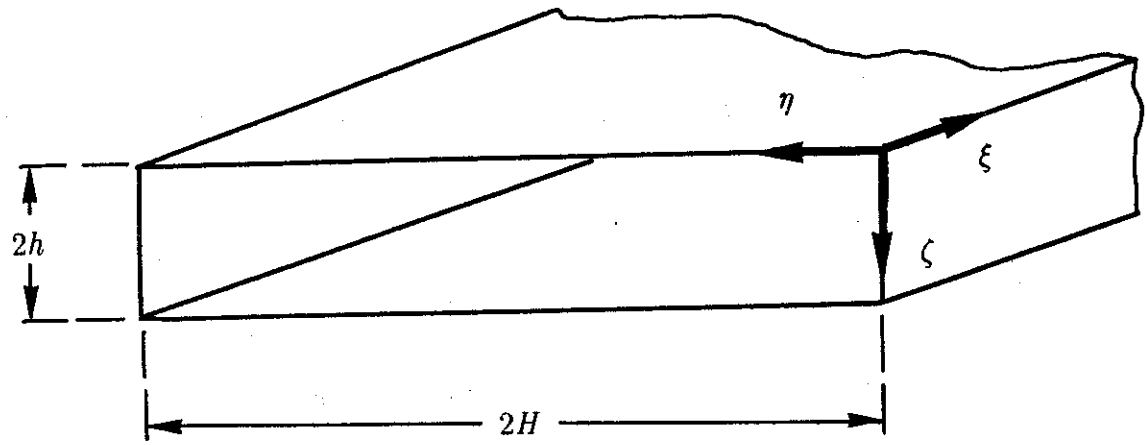

Fig. 8.3 *Geometry and coordinate system for straight duct,* $2h = 1$ mm *and* $2H = 16$ mm.

With the chosen geometry the aspect ratio of the total η dimension (width) and the total ζ dimension (height) becomes 16 and consequently the main velocity profile along the height at $\eta = 8$ mm is approximately a parabola. The velocity profile at midplane of height and midplane of width are shown in figs. 8.4 and 8.5, respectively, for a mean velocity of 0.5 m/s which gives a Reynolds number of 993.

Bardur et al (1987) have made a thorough study of primary velocity distributions for the chosen geometry and fluid where the Laser Doppler Anemometry (LDA) technique was used. They show both raw data and smoothed data and the present results agree very well with the measured results.

The problem considered has a simple geometry and very well agreement with experimental results is not surprising, but even if the problem is easy to handle the distribution of control volumes and the distance at which the inlet–outlet conditions are applied are of interest from a numerical point of view. The distribution of control volumes across the height of the duct was first evaluated

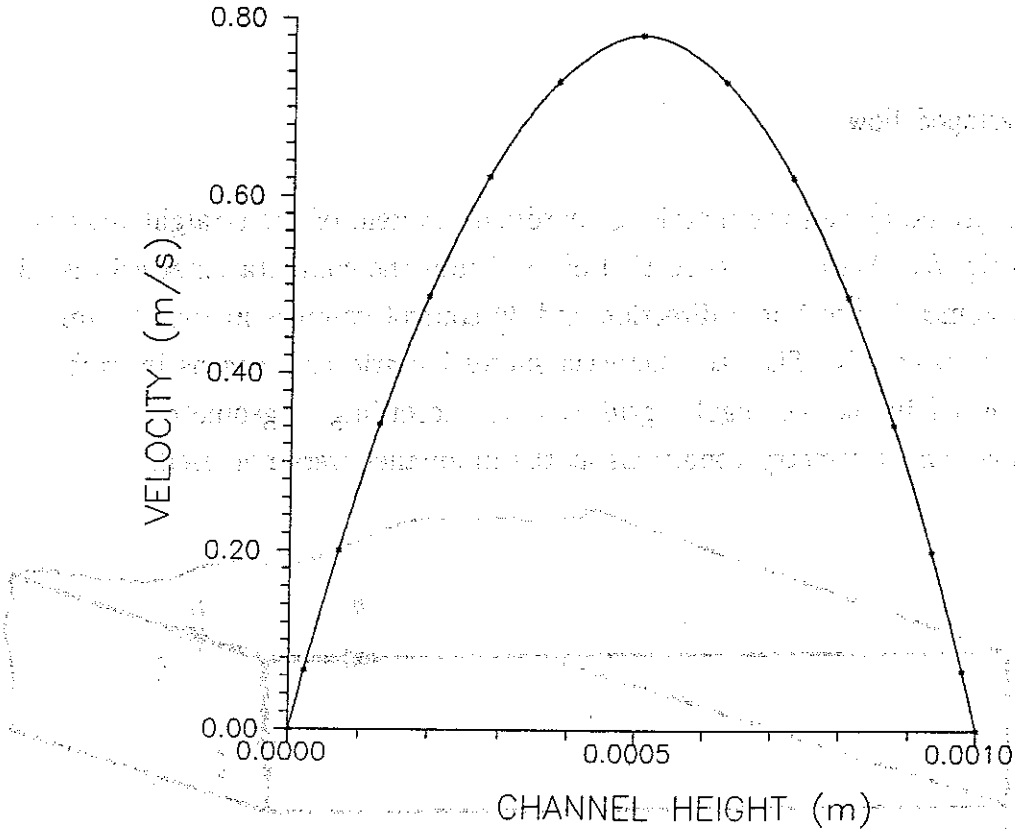

Fig. 8.4 *Velocity profile of water in straight duct shown at midplane of height.*

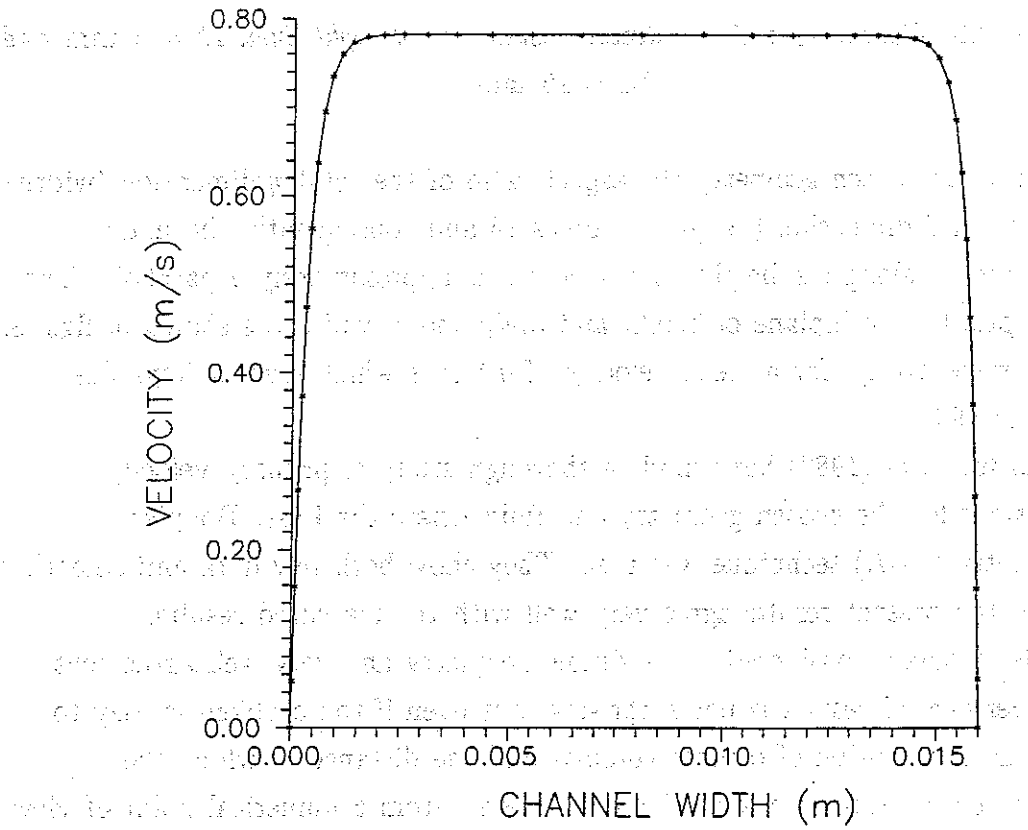

Fig. 8.5 *Velocity profile of water in straight duct shown at midplane of width.*

from the fully developed flow between parallel plates separated the height of the duct. It is well known that the analytical expression for the velocity profile is a parabola and the gradient of the velocity varies then linearly across the duct. The first distribution of control volumes was found by dividing the velocity profile evenly according to the number of control volumes and then assign a ζ–value to the corresponding velocity value. This gave high concentration of control volumes near the walls and little concentration around the middle of the duct and consequently the cell length ratio of successive control volumes is not a constant. The numerical solution of this distribution of control volumes was compared with solutions of distributions with a constant cell length ratio between successive control volumes and with the analytical solution. For a constant number of 13 control volumes the distribution which showed the highest level of accuracy was the one with a constant cell length ratio of 1.2. It was expected that the first distribution gave the best result, but because the cell length ratio was much higher near the center than near the walls the highest level of inaccuracies was encountered near the center and this gave worse results compared with the other distributions. The distribution which was found to be the best result for the fully developed flow between parallel plates separated the height of the duct was then used as the distribution across the height of the duct.

Several distributions across the width of the duct were tried. From fig. 8.5 it must be obvious that high concentration of control volumes are needed near the walls and very few are needed where no variation in the velocity occurs. This was tryed and it was found that the "shoulders" of the velocity profile became the critical areas in which high resolution was needed. The cell length ratio between control volumes in the "shoulder" areas where a variation in the velocity profile occurs and the middle of the width where no variation occurs is of great importance. A too high cell length ratio will introduce wiggles in the converged solution in the "shoulder" areas. A constant cell length ratio between successive control volumes of 1.2 was found to resolve the velocity profile for the chosen number of control volumes. This might be too conservative as seen from fig. 8.5 where several grid points are situated where no variation in the velocity profile occurs, but indeed no wiggles appear.

The other problem which is also of interest from a numerical point of view is the distance at which the cyclic boundary conditions at the inlet–outlet are applied in order to obtain a fully developed solution. Different distances will all give the same result, but the cpu consumption can vary dramatic. It turns out that the optimum distance is on the order of the inlet length at which a fully

developed solution is found in a developing flow for the same geometry. With a distance which is longer than the optimum the aspect ratio of the individual control volumes becomes large and this will introduce numerical errors and longer cpu time is needed to remove these errors before a fully developed solution is attained. Longer distances than the optimum will usually only increase the total cpu consumption slightly, but is the distance lowered compared with the optimum high increase in the cpu consumption can occur. This has to due with the way the velocity field develops during the calculations. The inlet condition at the first cycle is given through a Dirichlet condition for each velocity component where the primary velocity component is given the value corresponding to the mean velocity and the others are set to zero. The initial inlet conditions give rise to a flow pattern which during the calculations will move fluid from the walls towards the center. If the distance at which this occurs is shorter than the distance a fully developed solution is attained the number of cycles the outlet conditions are fed in at the inlet are increased and consequently an increase in cpu consumption occurs. The physics behind the acceleration of the inner core is further discussed in the section of developing flow in a curved duct.

8.2.2 CURVED DUCTS

Curved ducts are widely observed in engineering application where much attention has been paid to the flow. Owing to the presence of secondary flow caused by centrifugal forces, fluid flow in a curved geometry differs significantly from flow in a straight channel. Much larger pressure drop or friction, heat transfer, and mixing rates are expected for a flow in a curved duct, except for very slow flow.

The centrifugal force is proportional to u^2/R, where R is radius of curvature of the duct. See fig. 8.6 for the geometry and coordinate system where the cross section may be viewed in fig. 8.3. The centrifugal force acts outward from the center of curvature on the fluid particles and generate a streamwise vorticity, or secondary flow, within the duct. With the addition of the primary flow, the fluid particles follow helical trajectories. Eustice, see Soh & Berger (1984) was one of the first who discovered spiral motion in a curved pipe from dye–injection experiments. The secondary flow results, as already mentioned, in a pressure loss and increased heat transfer compared with a straight duct, but also in a spatial redistribution of streamwise velocity which in addition to the secondary flow will

Fully developed flow.

The fully developed flow in a curved duct with cross section 1×16 mm and curvature radius 0.1 m is shown in figs. 8.7 to 8.12. The grid used in each case consists of 9 control volumes across the height and 40 control volumes across the width. A symmetry condition is used at half the height why the calculations are carried out over only half the total height. The cell length ratio of successive grid cell lengths is 1.2 across the height and 1.25 across the width, respectively.

Table 8.1 shows the mean velocity, the corresponding Reynolds number, the maximum u-velocity, and the maximum v-velocity for 7 different runs of the considered geometry. The first 6 runs are shown graphically in figs. 8.7 to 8.12. Each figure shows three different plots for the same flow situation. Plot *a* shows the primary flow along the width at half the total height. Plot *b* shows the v-component of the flow at the same position as plot *b*. Plot *c* shows again the v-component of the flow, but along the height at half the total width. Only the variation of the v-component of half the height is shown in plot *c* due to the symmetry condition at $\zeta = \frac{1}{2}$ mm.

u_{mean} (m/s)	*Re* (–)	u_{max} (m/s)	v_{max} (m/s)	Re_v (–)	*Figure*
1	1882	1.80	$1.42 \cdot 10^{-1}$	267	8.12
0.5	941	$8.08 \cdot 10^{-1}$	$4.15 \cdot 10^{-2}$	78.1	8.11
0.25	471	$4.05 \cdot 10^{-1}$	$1.13 \cdot 10^{-2}$	21.3	8.10
$1 \cdot 10^{-1}$	188	$1.65 \cdot 10^{-1}$	$1.90 \cdot 10^{-3}$	3.68	8.9
$1 \cdot 10^{-2}$	19	$1.65 \cdot 10^{-2}$	$1.92 \cdot 10^{-5}$	$3.61 \cdot 10^{-2}$	8.8
$1 \cdot 10^{-3}$	1.9	$1.65 \cdot 10^{-3}$	$1.92 \cdot 10^{-7}$	$3.61 \cdot 10^{-4}$	8.7
$1 \cdot 10^{-4}$	0.19	$1.65 \cdot 10^{-4}$	$1.92 \cdot 10^{-9}$	$3.61 \cdot 10^{-6}$	–

Table 8.1 *Calculated u_{max} and v_{max} values for different Reynolds numbers and corresponding u_{mean} values. The Reynolds numbers for the secondary flow and figure numbers for 6 runs are also shown.*

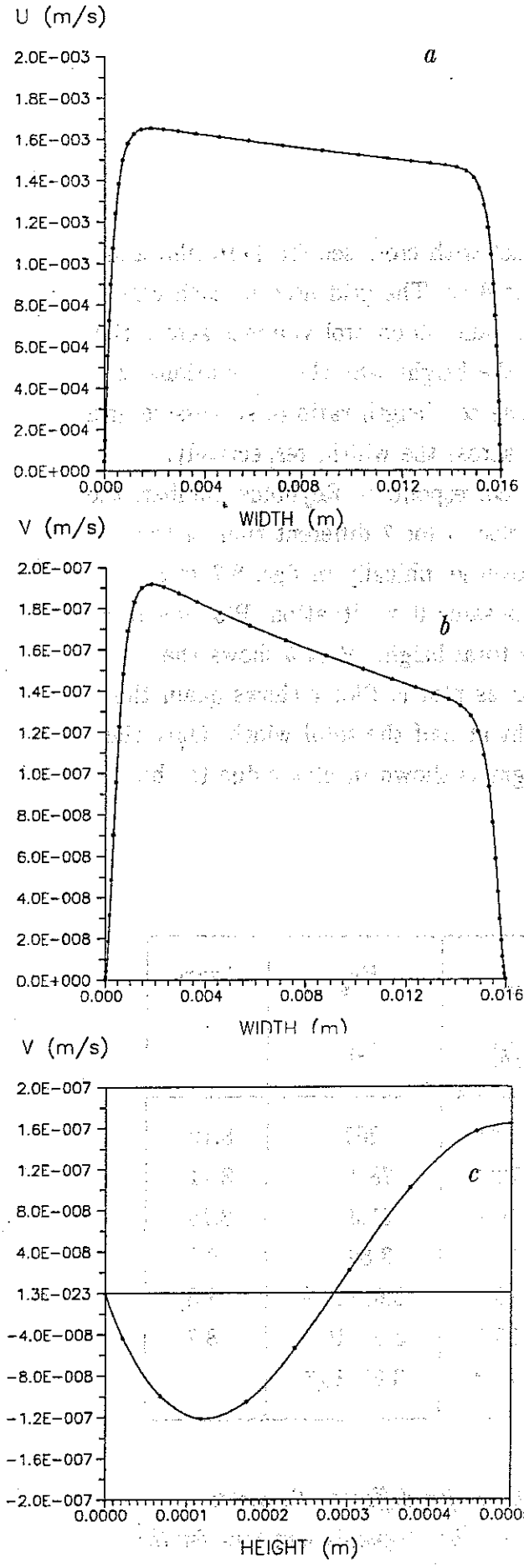

Fig. 8.7.

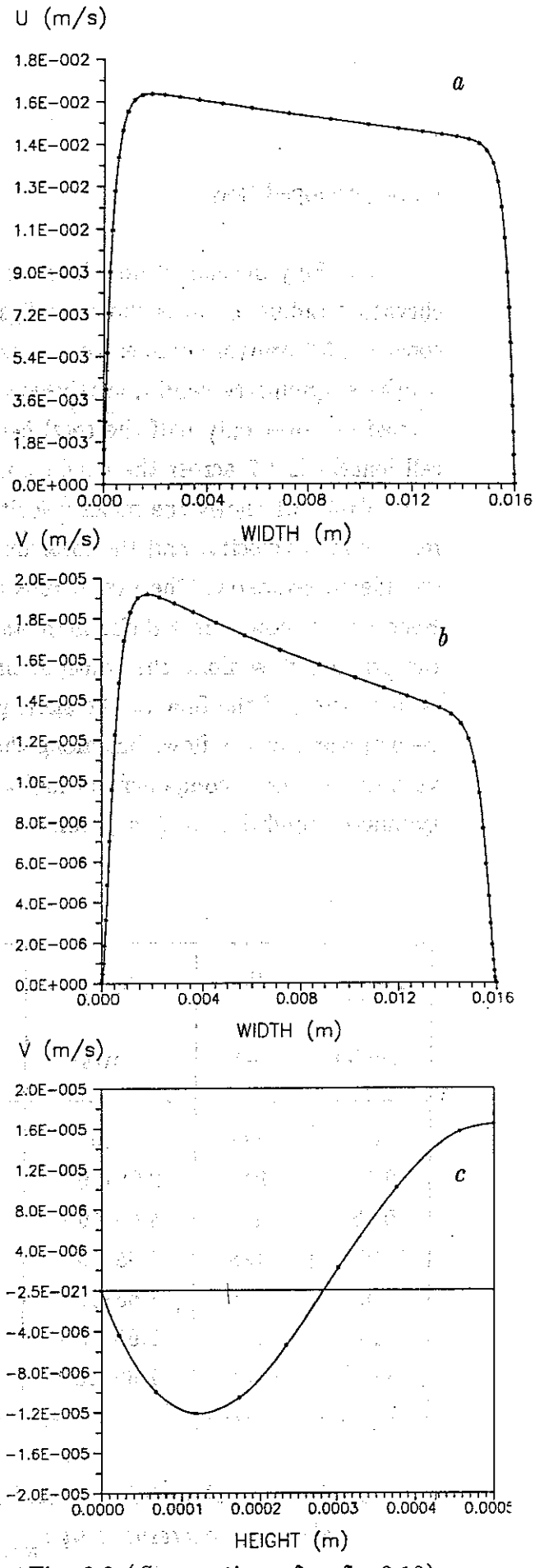

Fig. 8.8 (*See caption after fig.* 8.12).

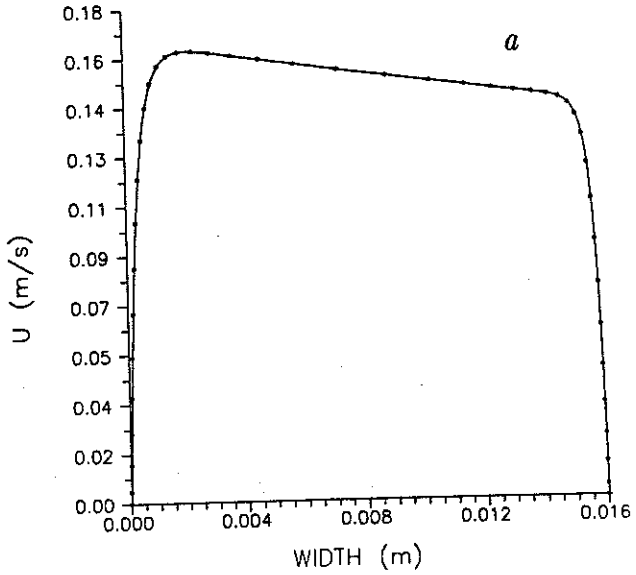

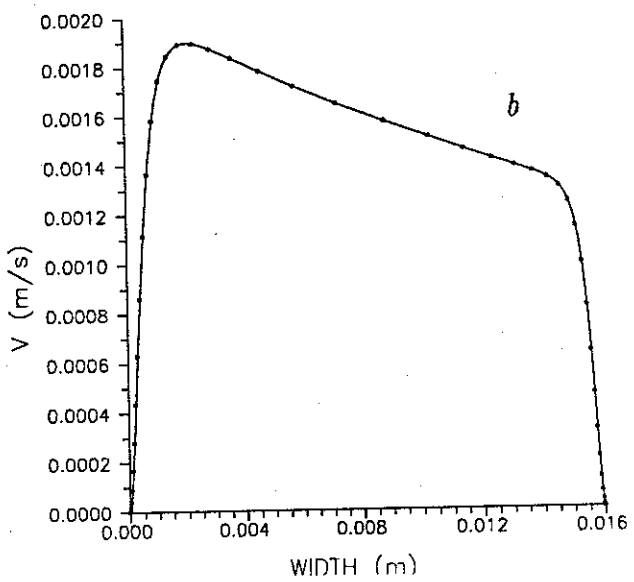

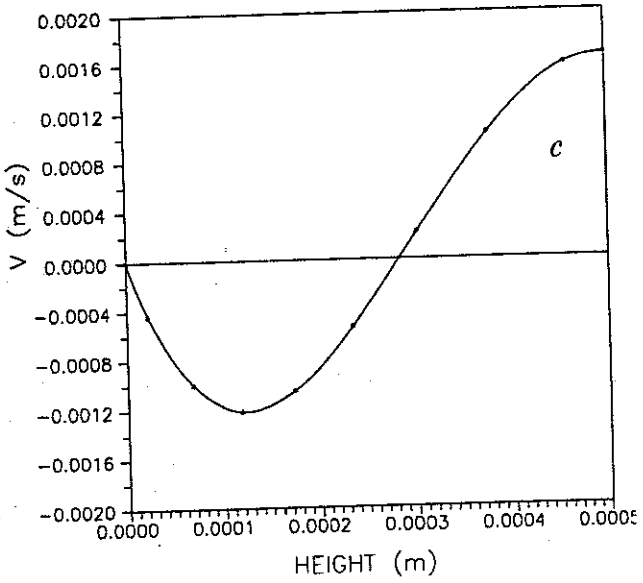

Fig. 8.9.

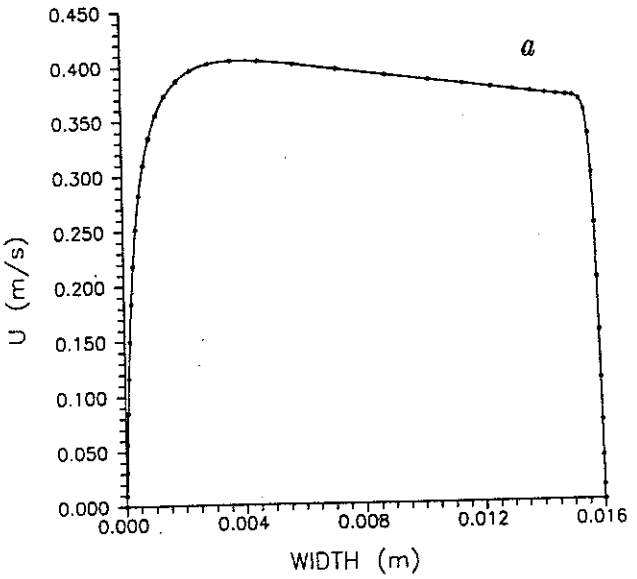

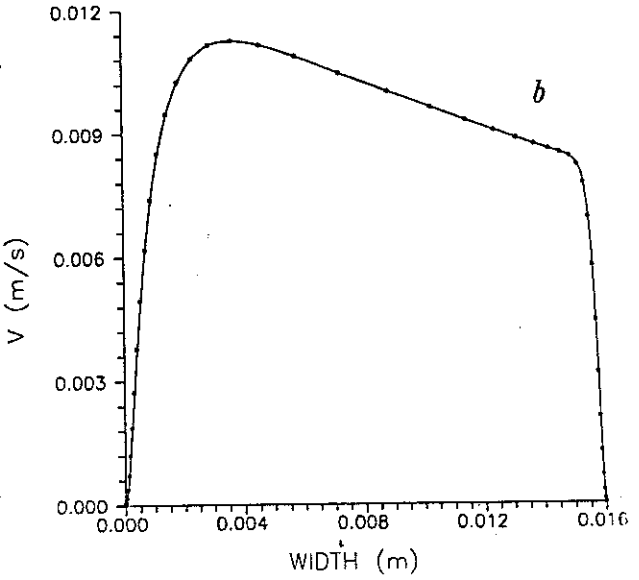

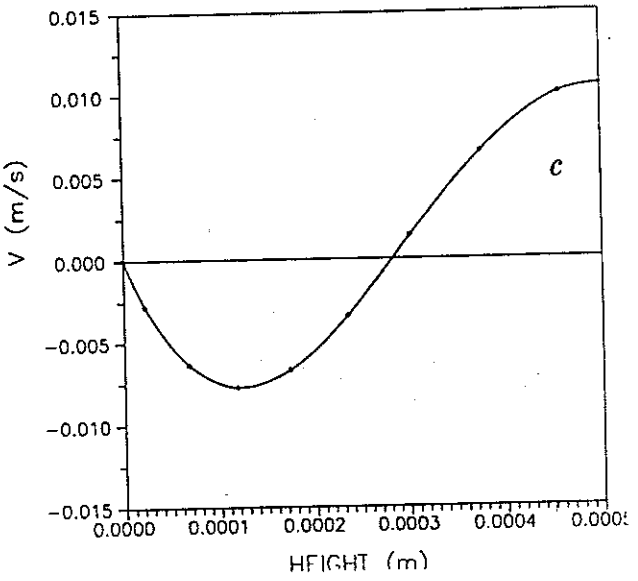

Fig. 8.10 (*See caption after fig.* 8.12).

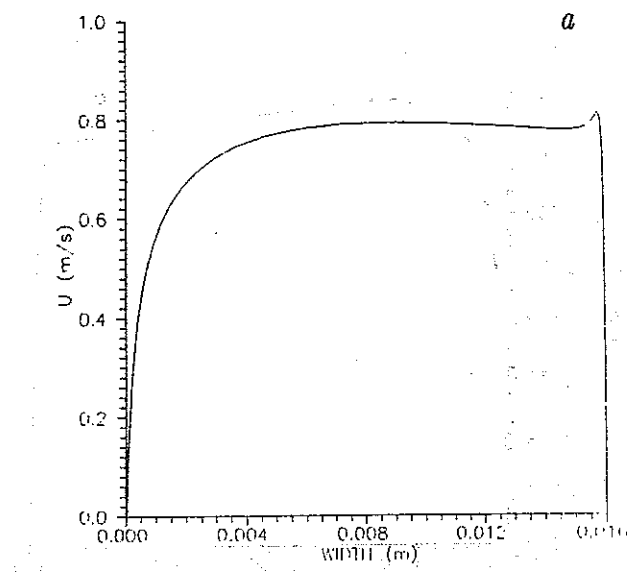

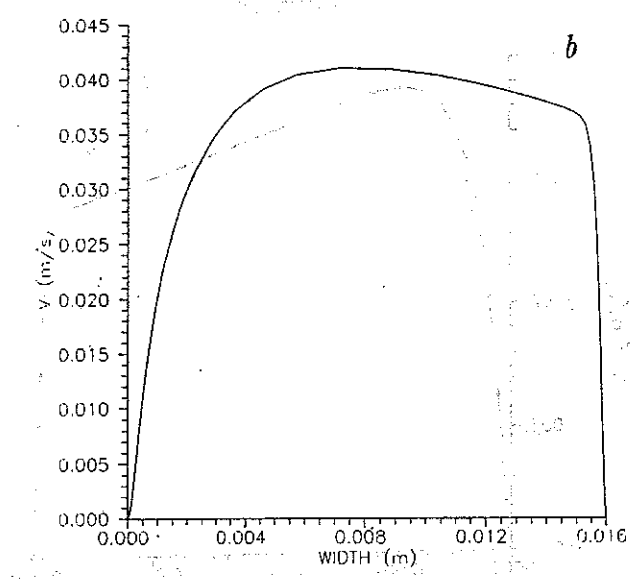

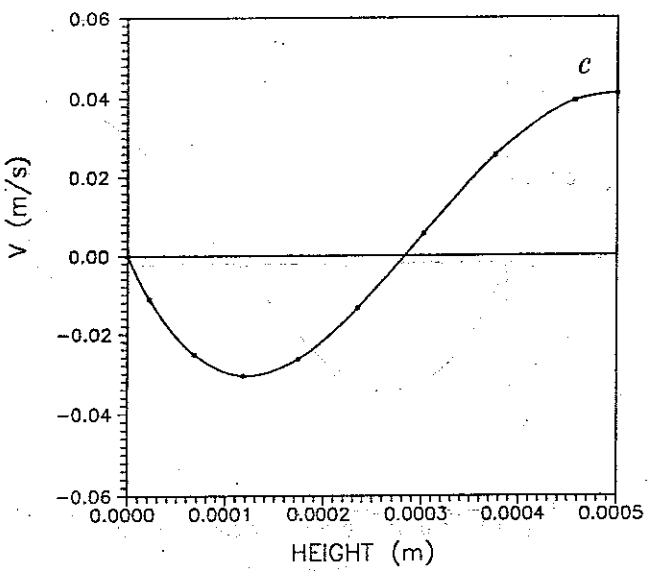

Fig. 8.11.

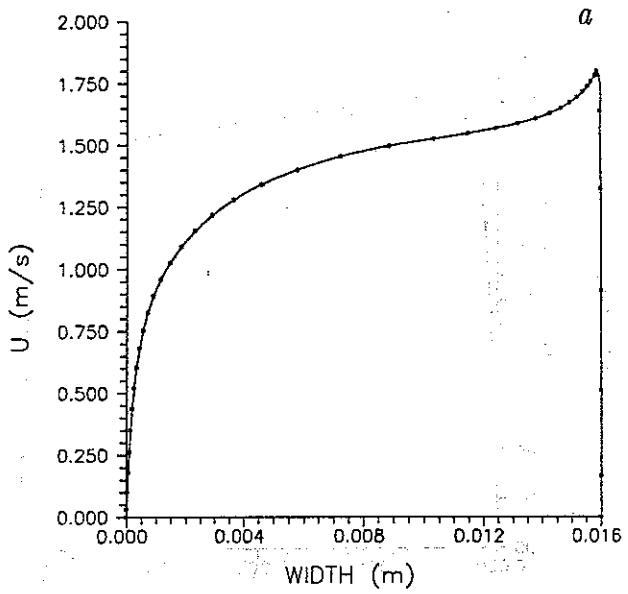

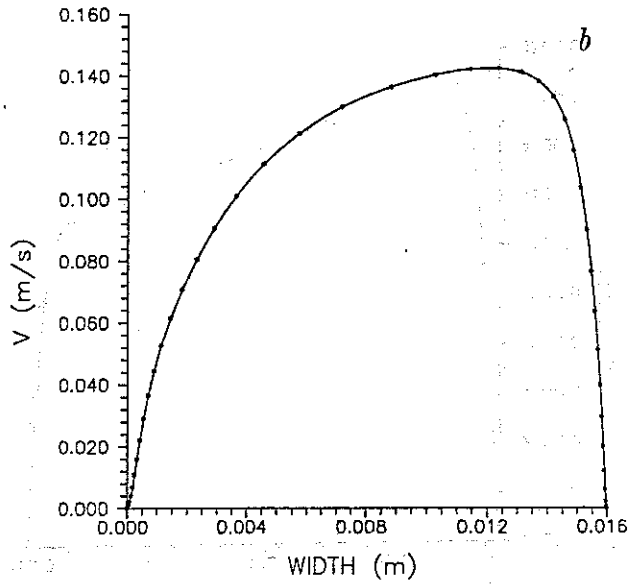

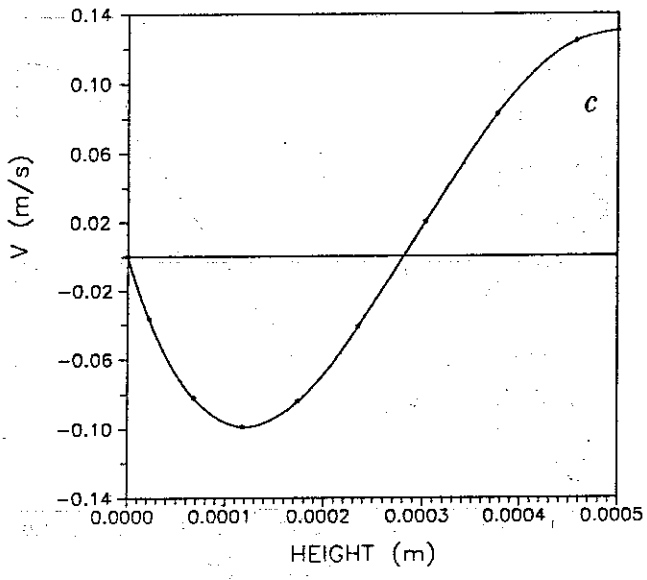

Fig. 8.12 (*See caption next page*).

Caption for figs. 8.7 to 8.12. *The 6 figures show plots for Reynolds numbers 1.9, 19, 188, 471, 941, and 1886 in the order shown. The a plots in each figure show the u-velocity profiles at midplane of width, the b plots show the v-velocity at midplane of width , and the c plots show the v-velocity at midplane of height.*

From the *c* plots it is seen that the nature of the secondary flow at half the width does not change as the Reynolds number is raised even if the velocity profile of the v-component along the width at midplane changes, which is seen from the *b* plots. For the chosen geometry the secondary flow follows the regular pattern of secondary flow in curved ducts and pipes with two main secondary flow vortices.

The secondary flow pattern is in general composed of 4 forces: pressure force, centrifugal force, viscous force, and inertia force. By defining a Reynolds number for the secondary flow as

$$Re_v = \frac{v_{max} \cdot \tilde{H}}{\nu},$$

where $\tilde{H}$ is the hydraulic diameter of the duct, we see, by comparing with table 8.1, that whenever u_{mean} is less than or equal to 0.1 m/s Re_v is less than or of the order of one. This means that the flow in the cross plane is of a creeping flow situation which is characterized as a flow dominated by viscous force. The secondary flow is then created by an interplay of pressure force, centrifugal force, and viscous force. The pressure force and centrifugal force dominate along the width at the midplane whereas the pressure force and viscous force dominate near the wall. If no viscous force appeared the centrifugal force and the pressure force would counterbalance each other with the highest pressure at the outer wall and the lowest at the inner wall and no secondary flow would occur. The primary velocity is moving more slowly near the walls due to the viscous force and consequently the centrifugal force can not counterbalance the pressure force and fluid will flow along the bottom and top walls towards the inner wall, see fig. 8.13 for a sketch of the secondary flow. At the midplane, where the primary velocity is highest, the pressure gradient across the duct can not counterbalance the centrifugal force and fluid will flow from the inner wall towards the outer wall. The pressure gradient built along the width of the duct at midplane in trying to balance the centrifugal force is enforced not only at midplane but, due

to the very little pressure drop along the inner and outer walls, nearly the same pressure gradient is applied along the bottom and top walls.

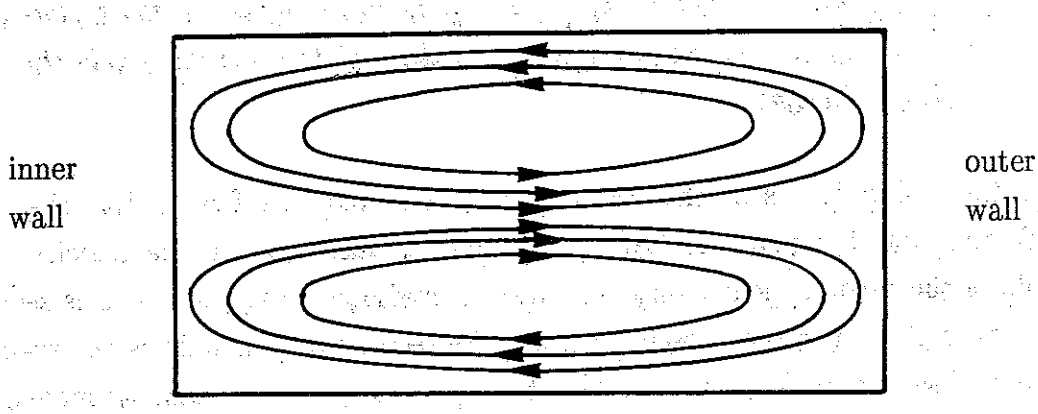

Fig. 8.13 *Sketch of secondary flow in curved rectangular duct.*

Isobars are shown in fig. 8.14 for a flow with the mean velocity of 0.5 m/s ($Re = 993$). The last isobar before the outer wall is curved slightly, but otherwise no pressure difference across the height is observed graphically. In incompressible flow, the specific pressure is of no interest from a numerical point of view, but rather the pressure difference. The pressure difference between the isobars in fig. 8.14 is 2.82 Pa which gives a total pressure difference between the outer and inner wall of 62.1 Pa, or a pressure gradient across the duct of 3875 Pa/m.

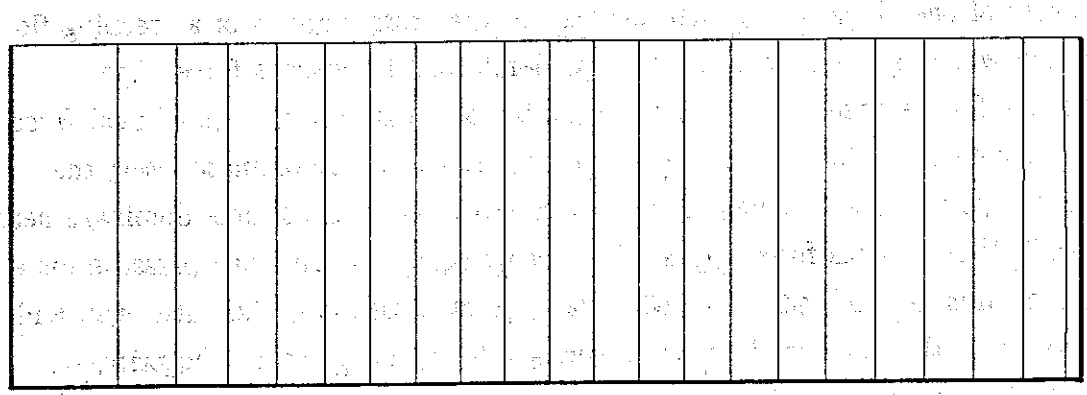

Fig. 8.14 *Isobars in curved duct with Re = 993. Height scaled* 1:10.

The physics behind the secondary flow just described holds for all 7 runs in table 8.1, but at the high Reynolds numbers the inertia force has an influence. This is observed by looking at the fourth column in table 8.1 where, going from the bottom towards the top, v_{max} is increased an order of two whenever the Reynolds number and mean velocity is increased an order of one. This continues

until the mean velocity is about 0.1 m/s whereafter v_{max} increases slightly less than an order of two due to the influence of inertia. The quadratic dependence of v_{max} on u_{mean} for a high range of Reynolds numbers is unsurprising since the centrifugal force is proportional to u^2/R. Fig. 8.15 shows v_{max} versus u_{mean} where the slope of the straight line is 1.976. The deviation from a slope of 2 comes from the influence of inertia at high Reynolds numbers.

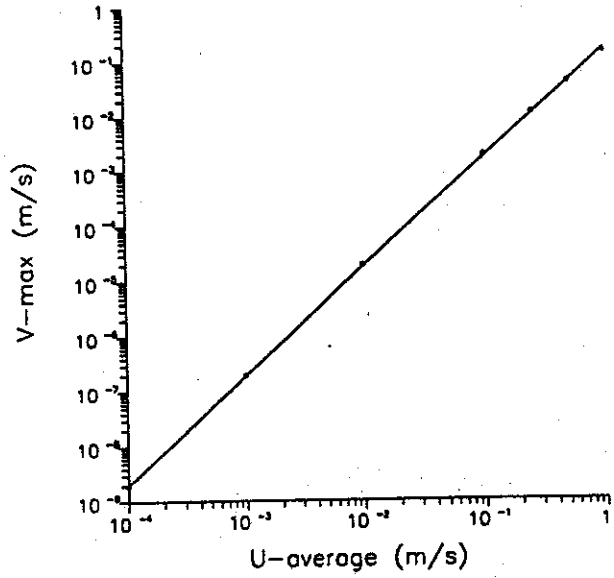

Fig. 8.15 v_{max} *versus* u_{mean}.

It was stated that the secondary flow does not change its pattern for the range of Reynolds numbers shown, but as seen from the *a* plots in figs. 8.7 to 8.12 the primary flow does. It is seen that maximum of the primary velocity is near the inner wall for low Reynolds numbers whereas the maximum moves towards the outer wall as the Reynolds number is raised. At low Reynolds numbers where the secondary flow grows with the square of the primary flow the secondary flow has no influence on the primary flow. In a fully developed flow the pressure gradient between two cross sections is the same all over the section. This means that the fluid near the inner wall fells a higher "driving" force than the fluid near the outer wall since the constant pressure gradient works over a shorter distance and consequently the fluid near the inner wall has a higher velocity than the fluid near the outer wall. As the Reynolds number grows, the secondary flow gets an influence on the primary flow. The faster moving fluid at the middle of the duct is moving outwards, pushing the fluid in the boundary layer at the outer wall to the top and bottom, and along the top and bottom walls towards the inner wall. Thus fresh fluid with high momentum is being continually brought

into the neighbourhood of the outer wall and then forced round towards the inner wall, being continually retarded. There is thus an accumulation of retarded fluid at the inner wall and an accumulation of high momentum fluid near the outer wall, Goldstein (1950). The change in primary flow along the width for different Reynolds numbers is viewed in the *a* plots in figs. 8.7 to 8.12. The corresponding v-velocity is shown in the *b* plots for the same position as the *a* plots where it is seen that the velocity towards the outer wall is highest for the high Reynolds numbers.

In trying to relate some of the calculated results to measurements isovelocity curves of the primary flow and streamlines of the secondary flow are calculated for $u_{mean} = 0.5$ m/s (Reynolds number = 993) and compared with measurements. Isovelocity curves are shown in fig. 8.16 where both calculated data and measured data are plotted. The 9 curves shown from the calculated data are equally distributed between the lowest value and the highest value which are zero and 0.804 m/s, respectively. With one isovelocity curve which coincides with the boundary each velocity jump is then (0.804 m/s)/9 = 0.089 m/s.

Streamlines are, of both calculated data and measured data, shown in fig. 8.17. The streamlines shown for the numerical part are distributed evenly between the lowest value, $\Psi_{low} = -5.2 \cdot 10^{-6}$ m^2/s and the highest value, $\Psi_{high} = 0$ m^2/s. 9 curves are shown where one coincedes with the boundary. This gives a difference between two streamlines of $-5.78 \cdot 10^{-7}$ m^2/s. Comparing the numerical results of figs. 8.16 and 8.17 to the experimental results, shown in the same figures, shows satisfactory agreement in view of the experimental uncertainty. The measured data are taken from Hansen et al (1988).

Developing flow.

Developing flow in a 1×16 mm duct for two Reynolds numbers are calculated over a total angel of 180^0, see fig. 8.6. The two Reynolds numbers are 64 and 1886, respectively, and correspond to a mean velocity of 0.0334 m/s and 1.0 m/s, respectively. Velocity vector plots at 5 cross sections (only one half of the height is shown due to the symmetry condition) located at 1.5^0, 5.8^0, 11.2^0, 23.6^0, and 91.4^0 from inlet are shown and the corresponding primary velocity at midplane along the width at the same locations are also shown. The inlet condition is taken as u_{mean} for the w-component and zero for the v and w-components.

The 5 velocity vector plots at Reynolds number 64 are shown in figs. 8.18a

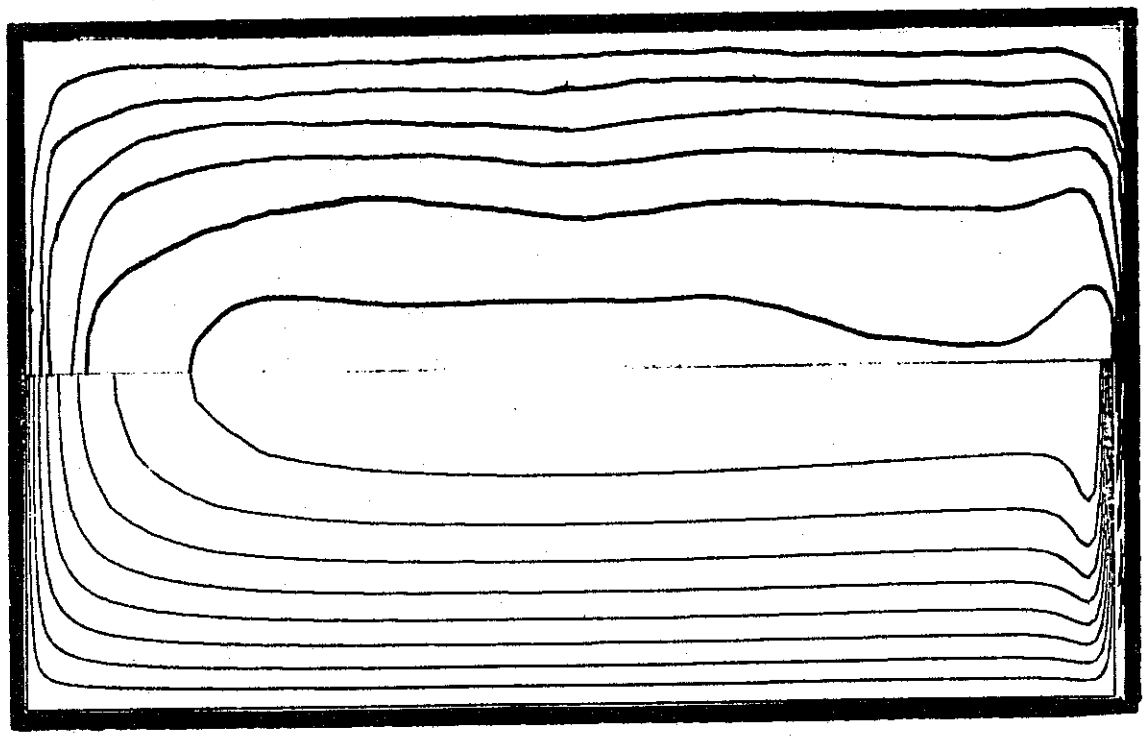

Fig. 8.16 *Calculated (a) and measured (b) isovelocity curves of secondary flow,* $u_{mean} = 0.5$ m/s.

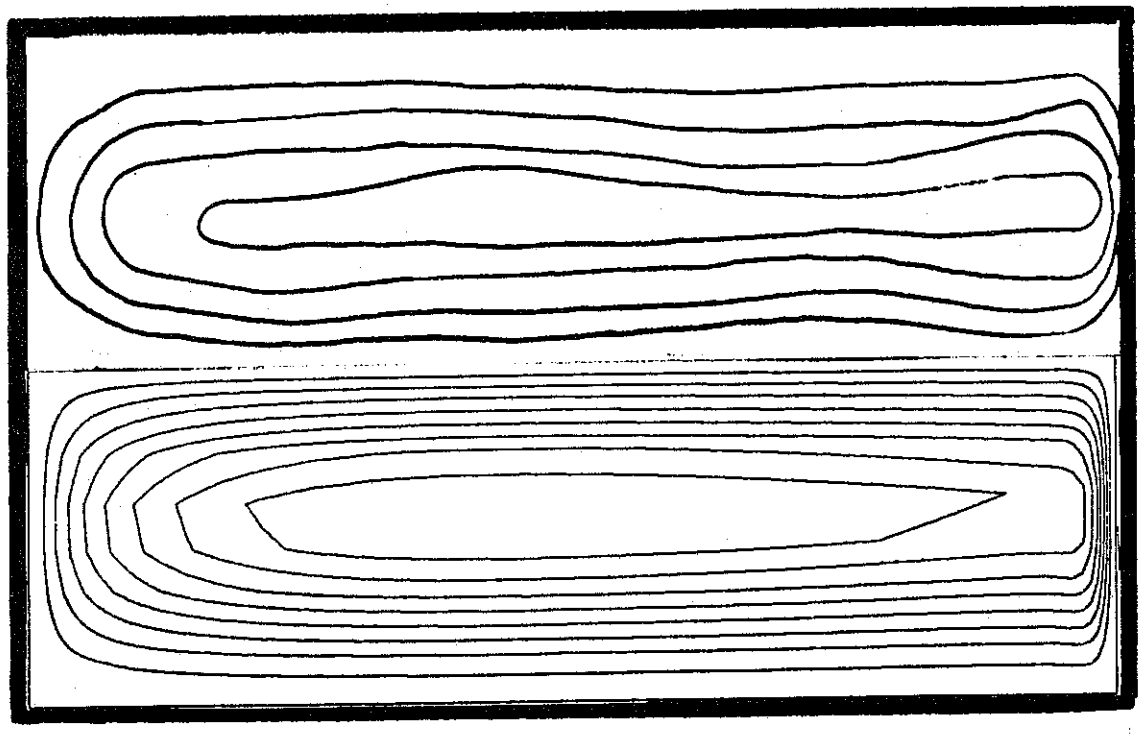

Fig. 8.17 *Calculated (a) and measured (b) streamlines of secondary flow,* $u_{mean} = 0.5$ m/s.

to 8.18e and the corresponding primary plots in fig 8.19. At the first 3 velocity vector plots no indication of a roll superposed the primary flow is seen. The vectors indicate that fluid is moved from the wall regions to the center region where it is accelerated. This is seen in fig. 8.19 where especially an acceleration between $\theta = 1.5^0$ and $\theta = 5.8^0$ take place. During the development of the velocity field the maximum of primary velocity is felt already at the first cross section where it is seen that fluid does not move evenly towards the symmetry plane, but rather towards the place where the maximum velocity is located. This is seen in fig. 8.18b too, but a tendency to inner and outer wall vorticity is viewed in addition. This tendency is further pronounced in fig. 8.18c, and in fig. 8.18d the fully developed solution is reached. This is seen both by comparing figs. 8.18d and 8.18c in which no difference is observed and in fig. 8.19 where there is no graphically difference in the plots for $\theta = 23.6^0$ and $\theta = 91.4^0$. From the graphical data it can be stated that the developing zone extend into 1/8 of the duct.

At Reynolds number 1886, the velocity vector plots at 5 cross sections are shown in figs. 8.20a to 8.20e and the corresponding primary velocity plots along the width at midplane are shown in fig. 8.21. The first velocity vector plot shows a movement of fluid from the wall regions to the center region in which the velocity vectors are distributed more regularly than for the low Reynolds number case. This must due to the fact that the fully developed flow field is attained much further downstream than for the low Reynolds number case and the maximum velocity attained near the outer wall is not felt near the inlet. Even if the fully developed solution is attained much further downstream than for the low Reynolds number case the roll pattern is attained already at the second cross plane, but the fully developed solution is first obtained after half the duct is reached. The difference between velocity vector plot in figs. 8.20d and 8.20e is only minor, but the primary velocity at midplane changes greatly from the second last cross section to the last cross section.

Even if a secondary flow is attained very early in the developing zone it does not have a great influence on the primary velocity distribution until the inner core of the flow is accelerated and has reached its maximum velocity on the mean. This is seen from fig. 8.21 where the increase in velocity is viewed for the first 4 plots, but no increase of velocity on the mean is seen in the last plot, only a redistribution of the primary velocity field. This was not observed for the low Reynolds number case, and it should not be, since the secondary flow has no or hardly any influence on the primary flow as discussed in the section on fully

developed flow.

The accelaration of the inner core is clearly viewed in fig 8.21, but the inner core is not accelerated evenly. This is best viewed in fig. 8.19 for $\theta = 1.5^0$ where it is seen that the area near the inner and outer walls is accelerated faster than the middle of the core. To understand this, we have to remember that fluid is moved from the wall regions towards the inner core and due to limited speed and fulfilment of the equation of continuity the velocity near the inner wall and outer wall is increased faster in the first part of the developing zone.

In the section of fully developed flow in a straight duct it was stated that the lowest cpu consumption was attained if the distance at which the cyclic boundary conditions was applied was approximately equal to the distance of the developing zone in a developing flow of the same geometry and Reynolds number. If the distance is shorter the cpu consumption increases dramatic. This has to do with the higher velocity in the "shoulder" areas which has to be moved into the center core. This is done very slowly if the distance is too short.

150^0 from the inlet, where the fully developed solution is reached, isovelocity curves of the primary flow and streamlines of the secondary flow are calculated for both Reynolds numbers. Calculated and measured isovelocity curves and streamlines for $Re = 64$ are shown in fig. 8.22 and 8.23, respectively. The calculated isovelocity curves in fig. 8.22 are evenly distributed between the lowest value (0 m/s) and the highest value (0.0548 m/s) and the jump between each curve becomes $6.09 \cdot 10^{-2}$ m/s. The maximum calculated value of the streamfunction is $\Psi_{max} = 2.67 \cdot 10^{-8}$ m^2/s and the minimum is $\Psi_{min} = 0$ m^2/s for $Re = 64$. This gives a jump between each curve of $2.97 \cdot 10^{-9}$ m^2/s. The plots in fig. 8.22 and 8.23 made from measured data are taken from Nielsen (1989). The wavy pattern, especially in fig. 8.22, is due to a combination of few measurements and a bad graphic packet, see Nielsen (1989).

Figs. 8.24 and 8.25 show only the calculated isovelocity curves and streamlines of the secondary flow for $Re = 1886$. Maximum velocity in fig. 8.24 is 1.81 m/s and minimum is 0 m/s. With evenly distributed isovelocity curves this gives a jump between the curves of 0.20 m/s. Maximum streamfunction in fig. 8.25 is $\Psi_{max} = 1.86 \cdot 10^{-5}$ m^2/s and minimum is $\Psi_{min} = 0$ m^2/s. With evenly distrubuted curves this gives a jump of $2.07 \cdot 10^{-7}$ m^2/s between each curve.

Due to uncertainty of the measurements and not very good plots of the measured data it must be stated that the calculated data and the corresponding plots are much more accurate than data and plots from measurements. The Newtonian fluid water which has been used in all the calculations so far can to

full extend be calculated in the geometries used.

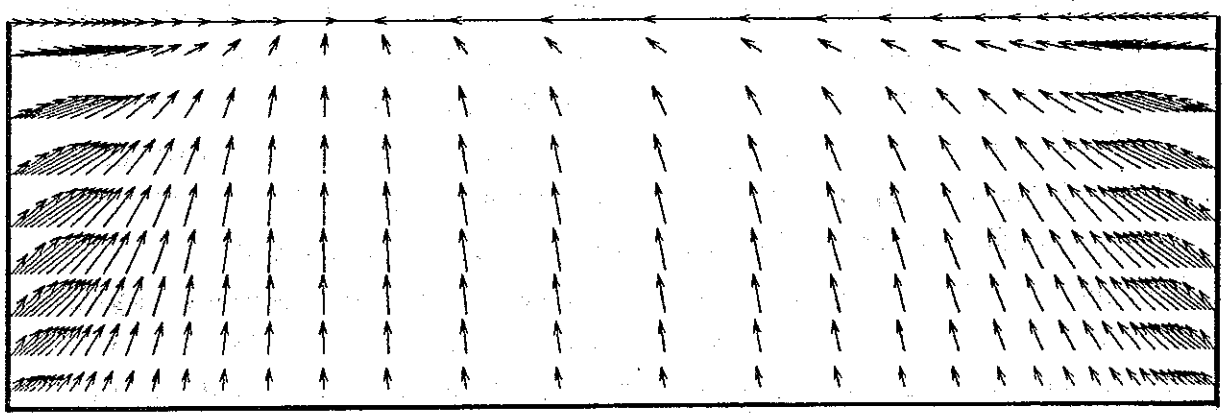

Fig. 8.18a *Vector plot at $\theta = 1.5^0$; $Re = 64$; 10×40 control volumes.*

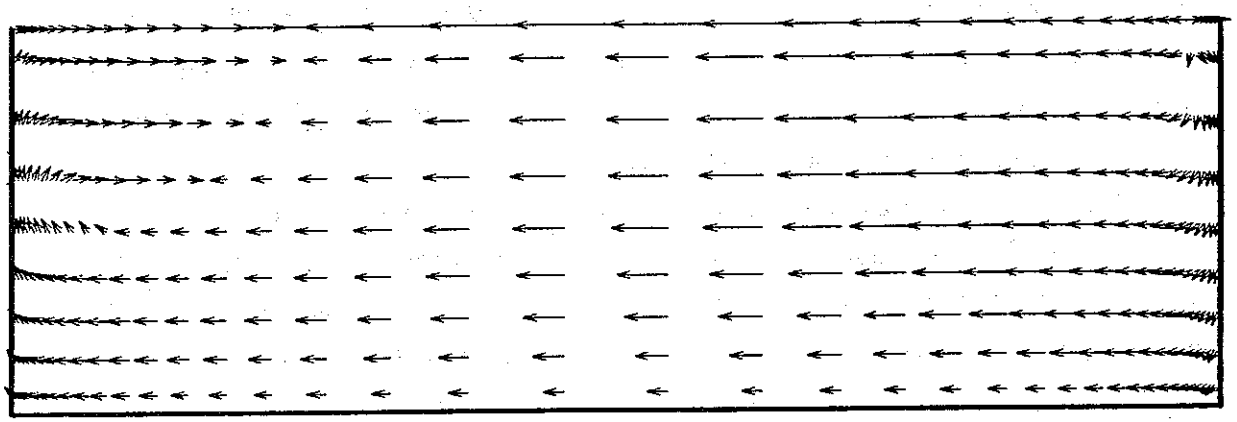

Fig. 8.18b *Vector plot at $\theta = 5.8^0$; $Re = 64$; 10×40 control volumes.*

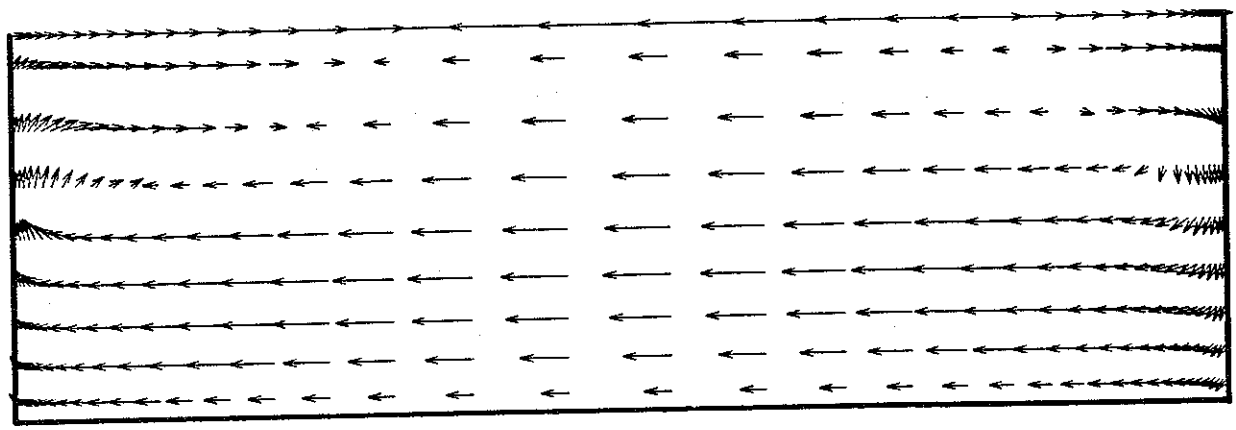

Fig. 8.18c *Vector plot at $\theta = 11.2^0$; $Re = 64$; 10×40 control volumes.*

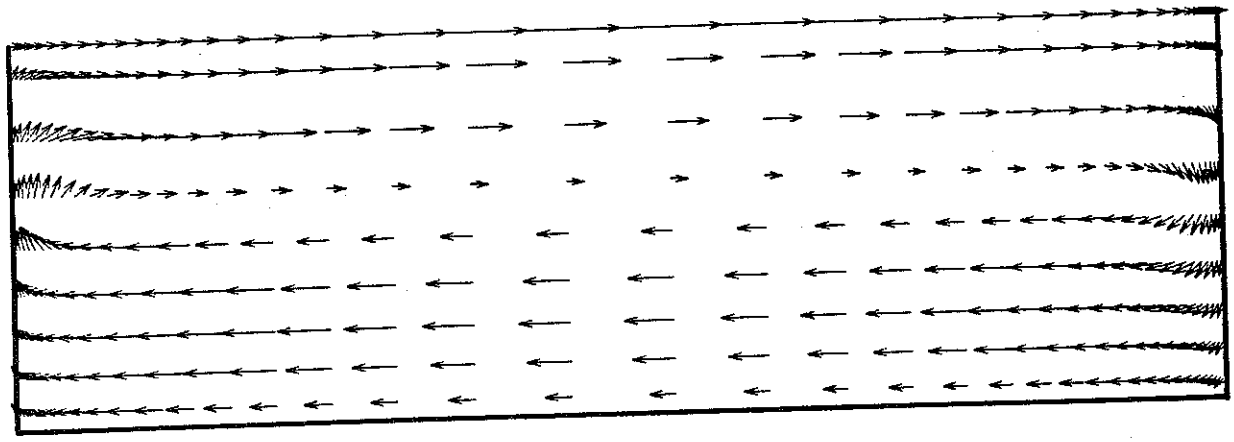

Fig. 8.18d *Vector plot at $\theta = 23.6^0$; $Re = 64$; 10×40 control volumes.*

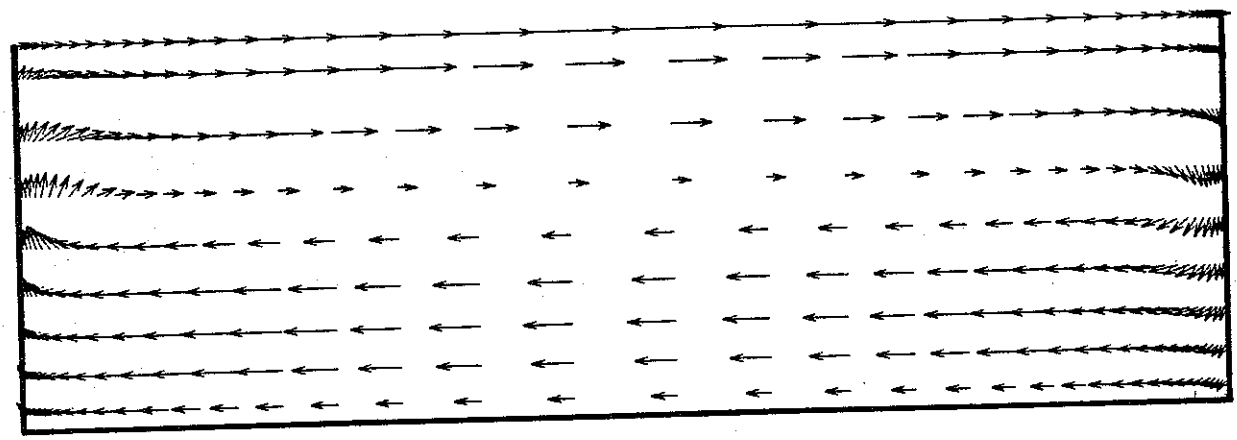

Fig. 8.18e *Vector plot at $\theta = 91.4^0$; $Re = 64$; 10×40 control volumes.*

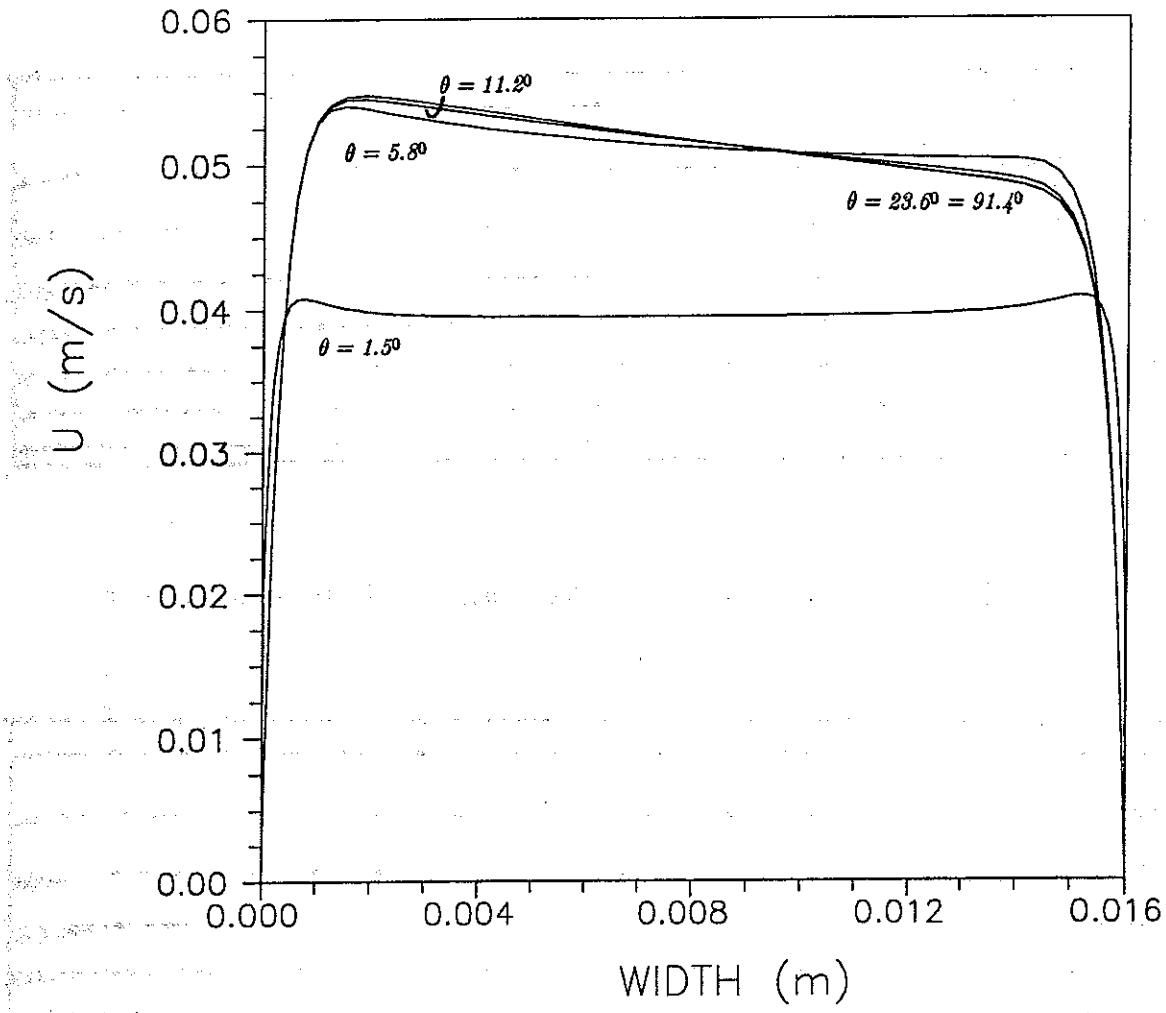

Fig. 8.19 *Primary flow shown at midplane of height along the width; Re = 64.*

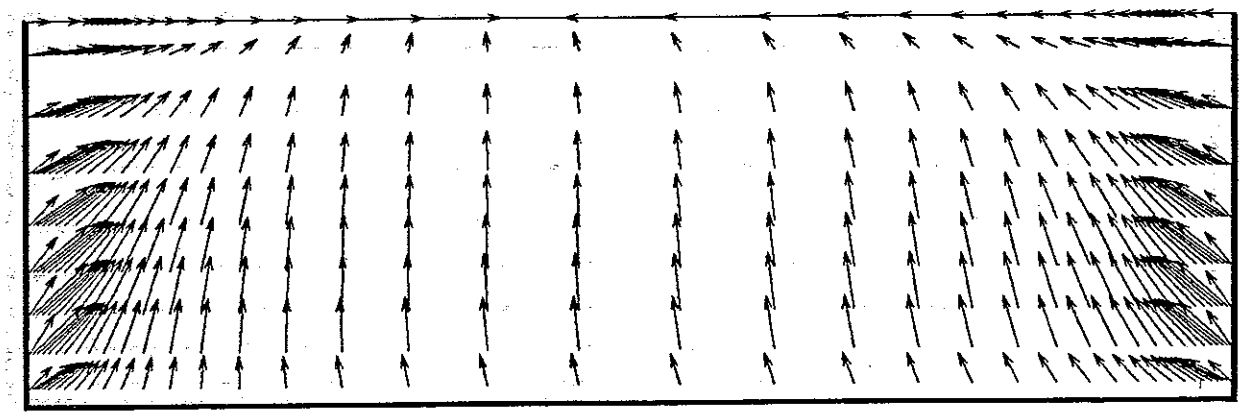

Fig. 8.20a *Vector plot at θ = 1.5⁰; Re = 1886; 10×40 control volumes.*

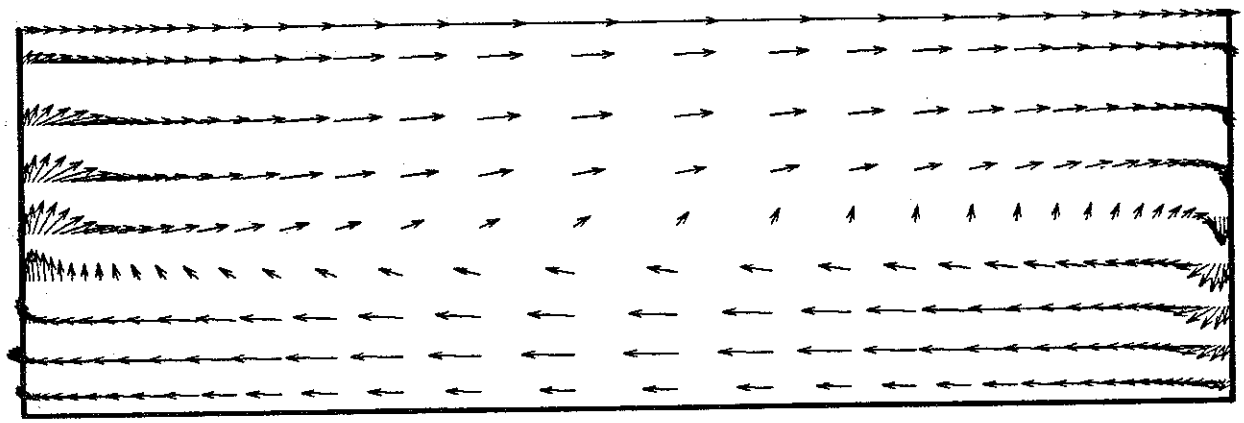

Fig. 8.20b *Vector plot at $\theta = 5.8^0$; Re = 1886; 10×40 control volumes.*

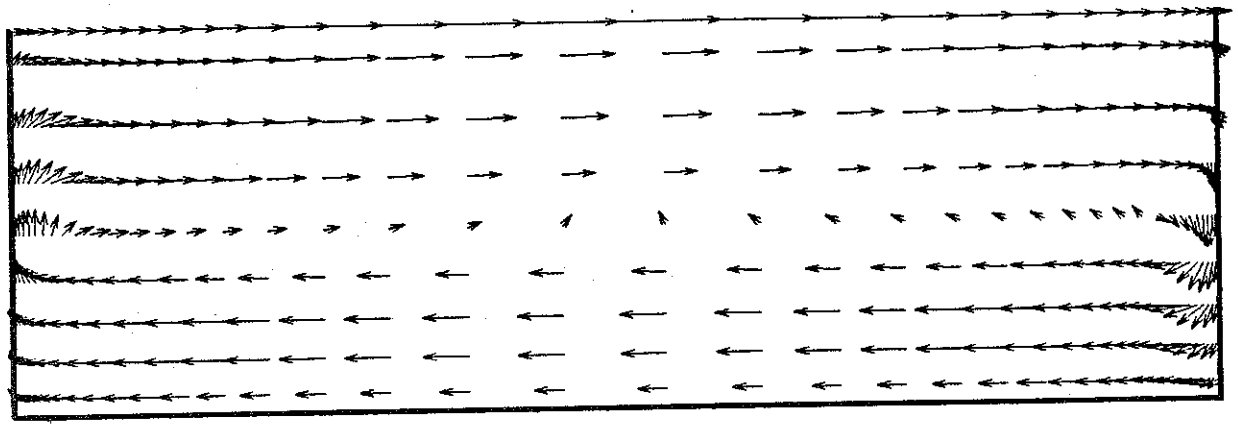

Fig. 8.20c *Vector plot at $\theta = 11.2^0$; Re = 1886; 10×40 control volumes.*

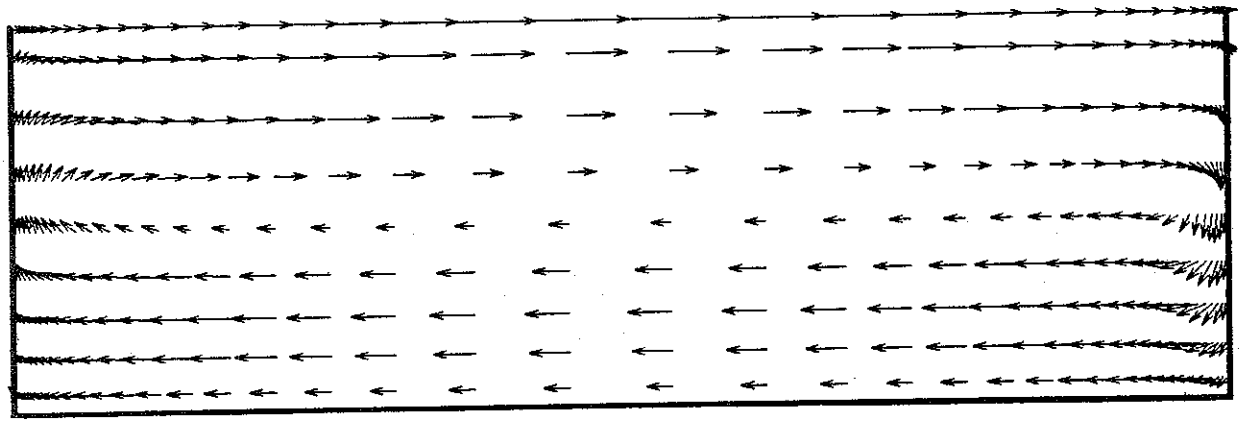

Fig. 8.20d *Vector plot at $\theta = 23.6^0$; Re = 1886; 10×40 control volumes.*

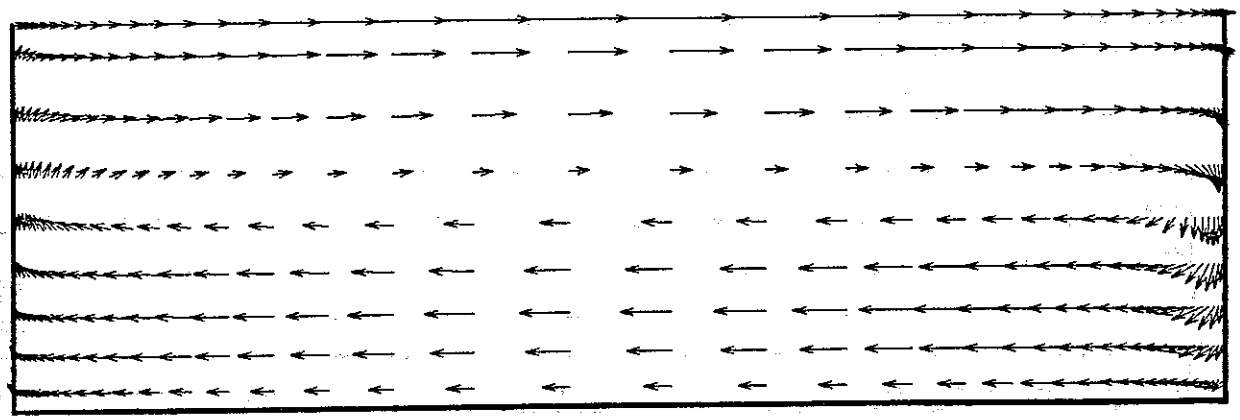

Fig. 8.20e *Vector plot at $\theta = 91.4^0$; Re = 1886; 10×40 control volumes.*

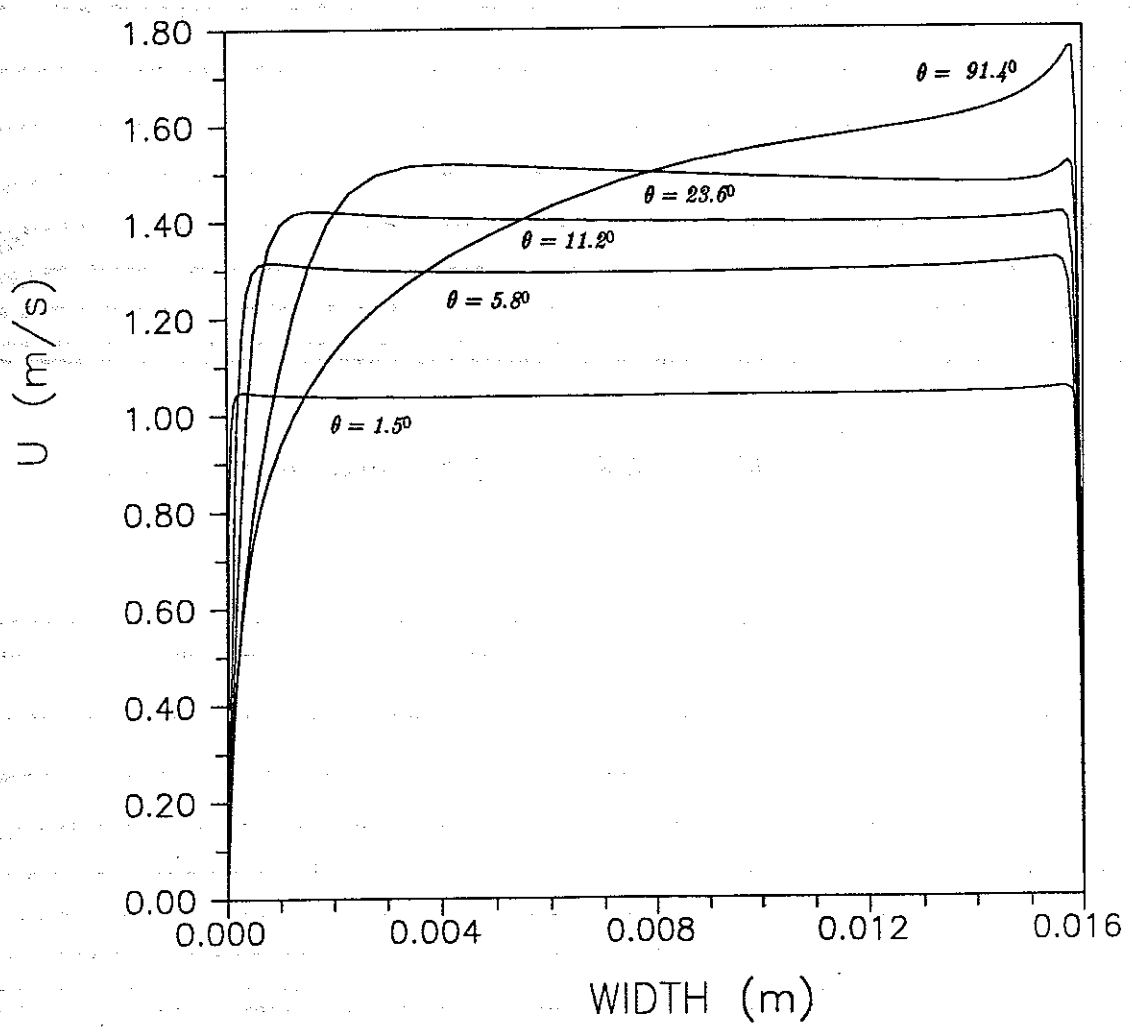

Fig. 8.21 *Primary flow shown at midplane of height along the width; Re = 1886.*

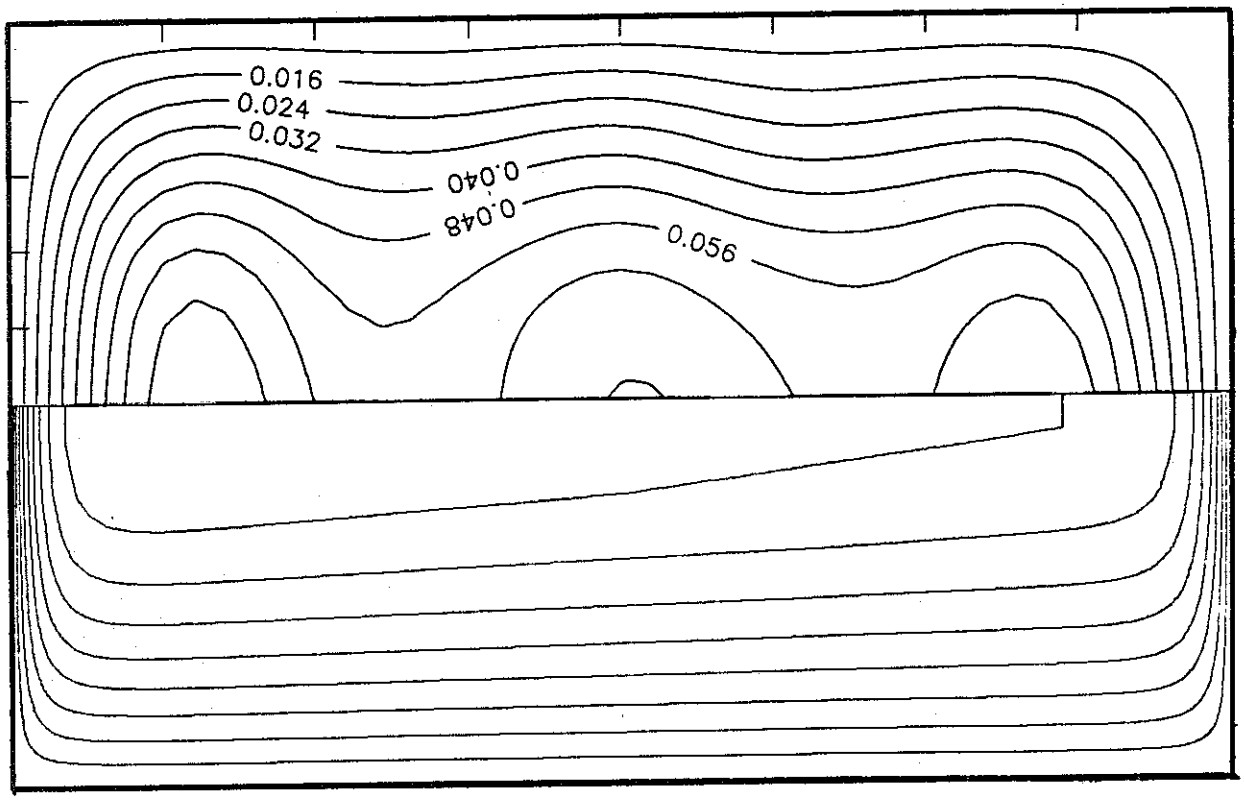

Fig. 8.22 *Calculated (a) and measured (b) isovelocity curves; Re = 64.*

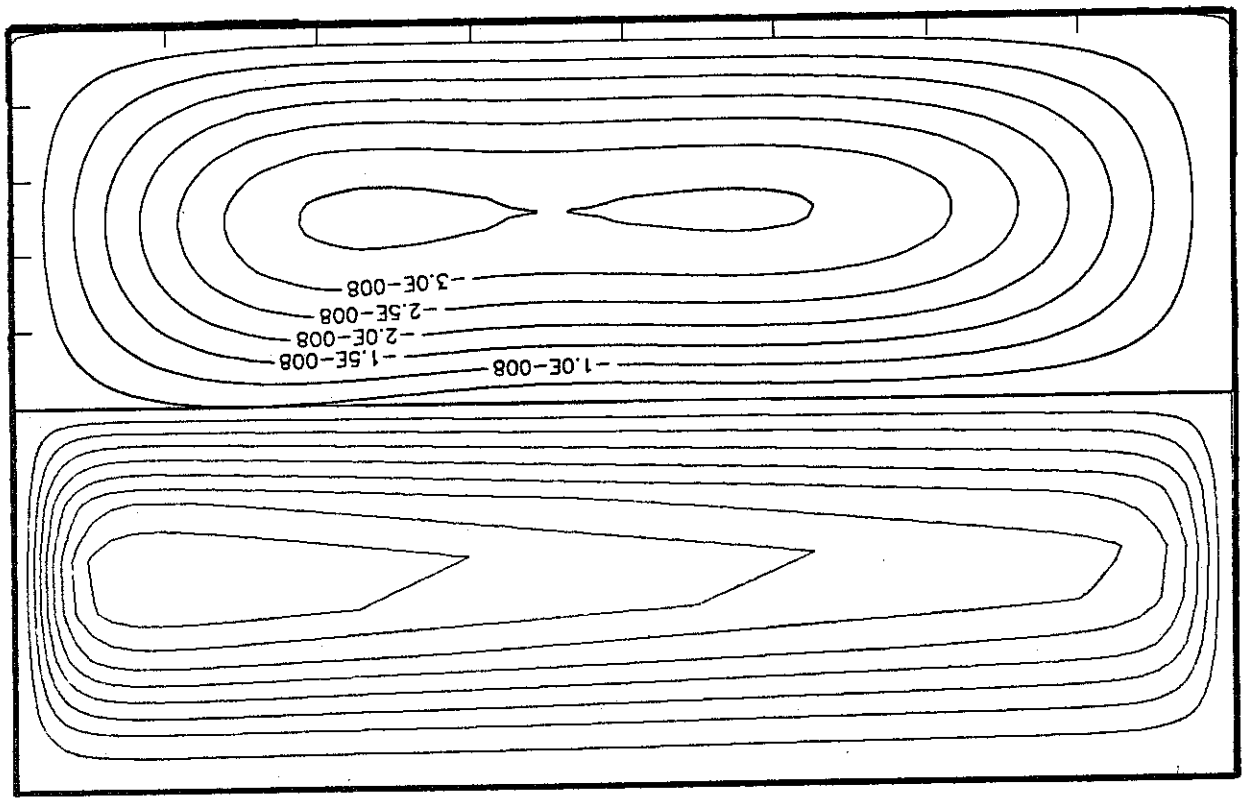

Fig. 8.23 *Calculated (a) and measured (b) streamlines; Re = 64.*

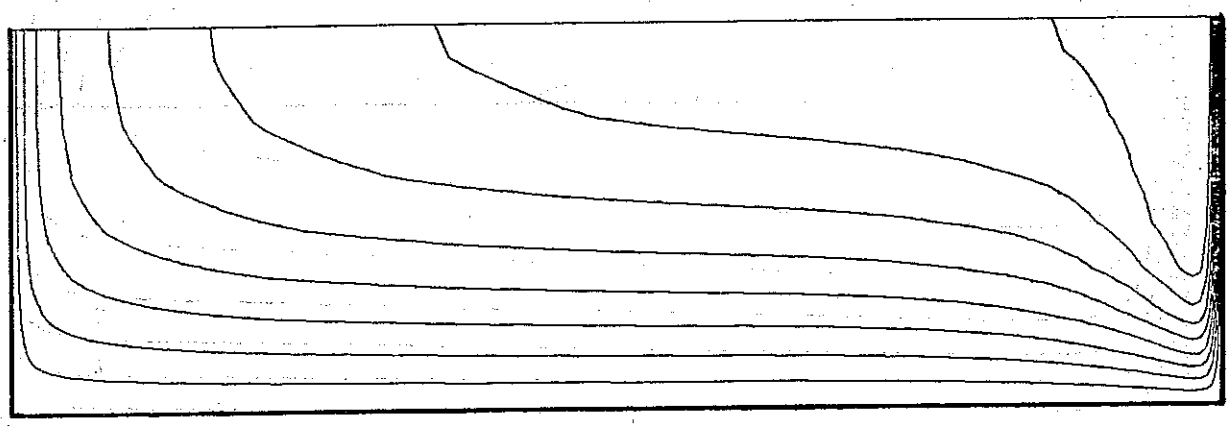

Fig. 8.24 *Calculated isovelocity curves, half cross section shown; Re = 1886.*

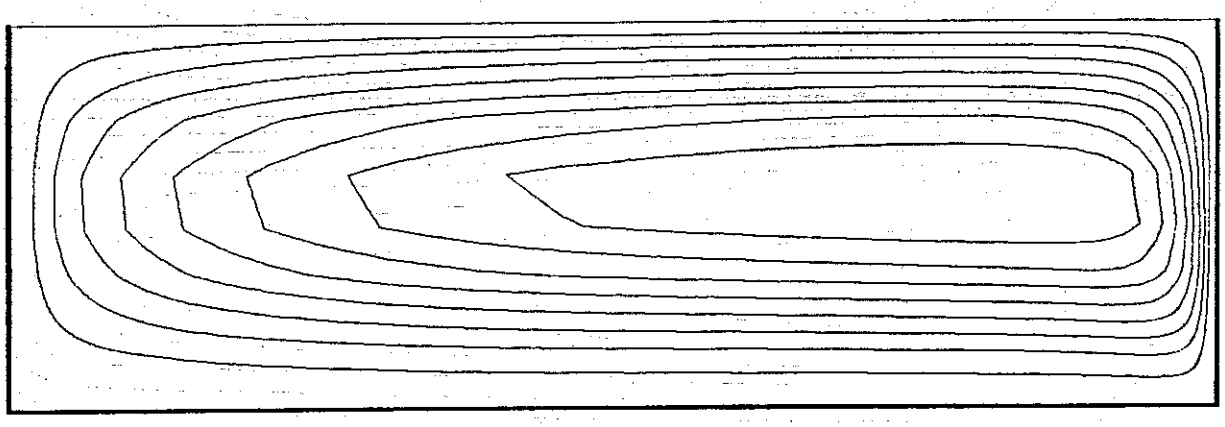

Fig. 8.25 *Calculated streamlines, half cross section shown; Re = 1886.*

8.3 SIMULATION OF VISCARIN IN DUCTS

Determination of the three viscometric functions.

Simulating water at a constant temperature required only the density and viscosity given as constants. This is not the case when viscarin is simulated. In chapter two the CEF–equation, which is going to be used as the Non–Newtonian model, was outlined. It was shown that besides the constant density three viscometric functions were needed. These are the shear rate dependent viscosity η and the first and second normal stress coefficients Ψ_1 and Ψ_2, respectively, each of which also dependents on the shear rate. All three viscometric functions are modelled with a powerlaw where, for example, the viscosity takes the form

$$\eta = k \cdot \dot{\gamma}^{n-1}.$$

At the University College of Wales (UCW) an extensive measurement programme, searching for model fluids for milk, has been carried out. This was set up as a part of a BRITE project as mentioned in chapter one. In trying to find a model fluid which will behave like some milk products the behaviour of several Non–Newtonian fluids were investigated in three basic rheometrical flows, Walters et al (1987)

- steady simple shear flow;
- small amplitude oscillatory shear flow;
- extensional flow.

The model fluid used for the present work is a 2% viscarin solution which is a suitable substitute for 40% full cream homogenized milk as far as $\eta(\dot{\gamma})$ is concerned, but it shows higher normal stress differences than milk. Plots showing the viscosity as function of shear rate has been prepared at UCW, see Walters et al (1987), from which the n and k values can be deduced. At 20^{0}C it was found that $n = 0.37$ and $k = 8.5$ Pa$\cdot$s^n. Neither the first nor the second normal stress coefficient are measured directly. The first normal stress coefficient has to be deduced directly from measurement of the first normal stress difference. In fig 8.26 measured and extrapolated data from UCW are shown. The measured data are marked with asterisks and the extrapolated data with circle. The extrapolated

data are used in order to find the second normal stress difference in a wider range than that in which the first normal stress difference has been measured. The curve giving the lowest values of Ψ_1 is based on measured and extrapolated data from UCW whereas the curve giving the highest values is an extrapolation obtained at TUD based on the measured data from UCW. The curve obtained at TUD is used in a sensitivity analysis of the secondary flow, section 8.3.1.

From the measured and extrapolated data for the first normal stress difference obtained at UCW the first normal stress coefficients is deduced. Values of Ψ_1 are plotted in fig. 8.27 from which a powerlaw of the form $\Psi_1 = k_1 \dot{\gamma}^{n_1}$ is obtained. Here, the constants are found to be $n_1 = -1.35$ and $k_1 = 5.96$ Pa·s$^{n_1+2}$. The ability to measure the viscometric functions η and Ψ_1 has become a standard feature of many modern commercial rheometers, but accurate results for the second normal stress coefficient have not yet been possible. Walters (1975) discusses approximate methods of determining the second normal stress difference N_2. For the present work a relation between N_1 and N_2 of $N_2 = -0.15 \cdot N_1$ based on work at UCW is used.

Throughout the simulations, the three viscometric functions are used with the values given above and the density is set to 1000 kg/m^3. Only in the sensitivity analysis of the secondary flow other values than the above mentioned are used. To summarize, the viscometric functions are given by

$$\eta = k\dot{\gamma}^{n-1}; \quad k = 8.5 \text{ Pa·s}^n, \; n = 0.37,$$

$$\Psi_1 = k_1 \dot{\gamma}^{n_1}; \quad k_1 = 5.96 \text{ Pa·s}^{n_1+2}, \; n_1 = -1.35, \tag{8.1}$$

$$\Psi_2 = -0.15 \cdot \Psi_1.$$

8.3.1 STRAIGHT DUCTS

In chapter two, the CEF–equation was set up to handle the stress distribution in a viscometric flow of which rectilinear shear flow is a class. One requirement of rectilinear shear flow was that the fluid particle pathlines are straight lines. It is well known that pathlines of a Newtonian fluid follow straight lines in a fully developed flow in straight ducts. This is usually not the case for a

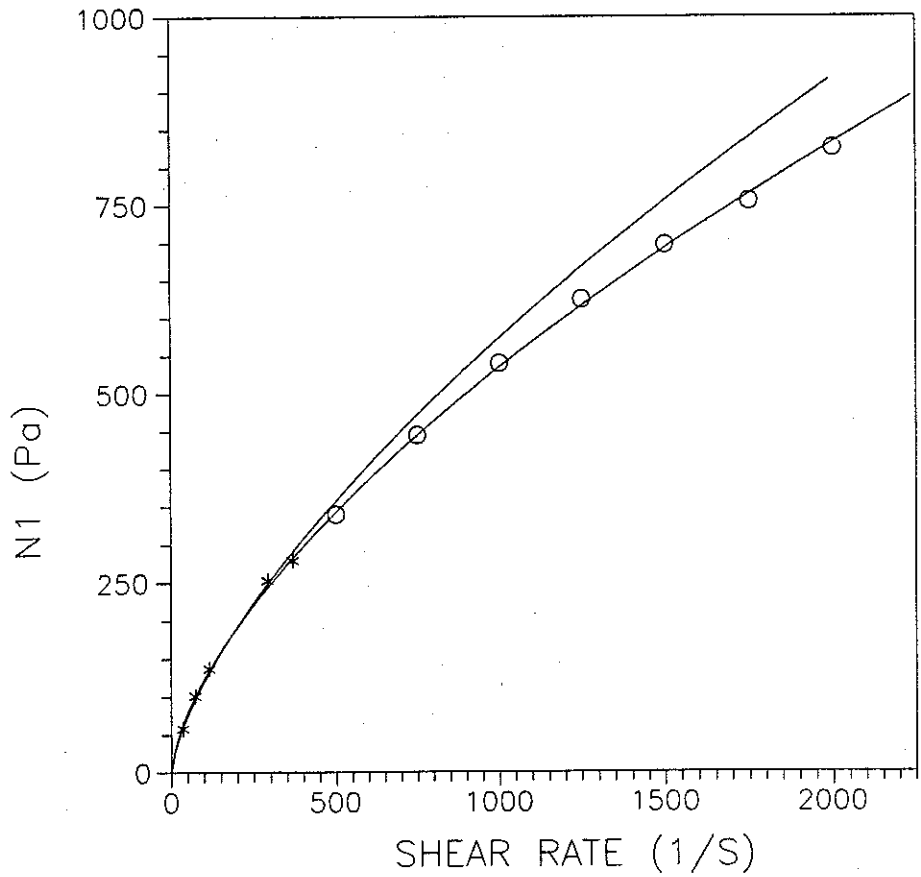

Fig. 8.26 *First normal stress difference versus shear rate.*
* *measured data*, o *extrapolated data* (*UCW*), – *extrapolated data* (*TUD*).

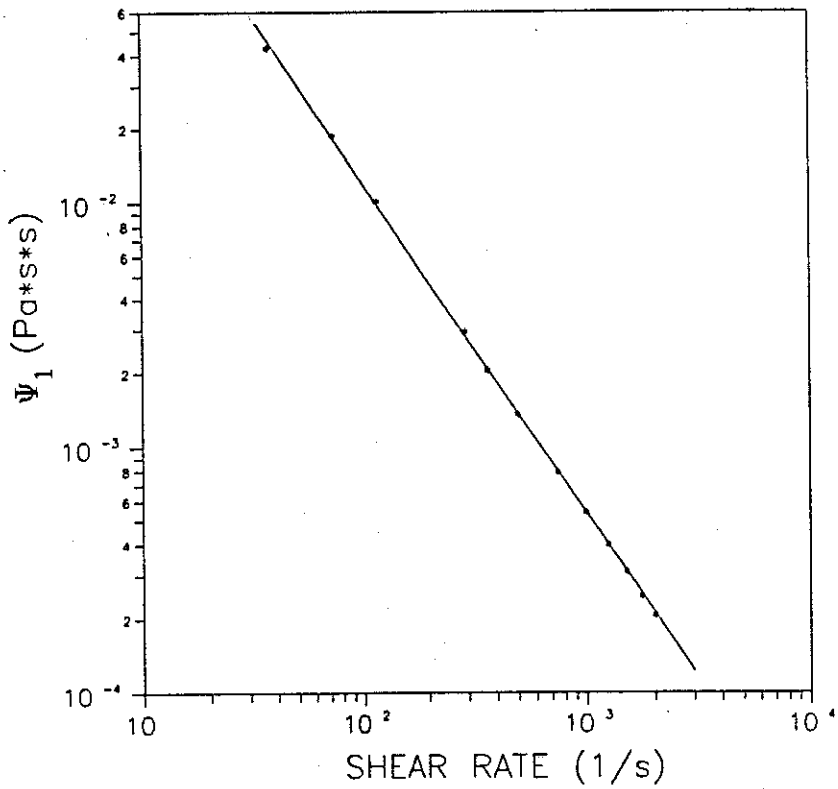

Fig. 8.27 *First normal stress coefficient versus shear rate.*

Non–Newtonian fluid and some secondary flow is to be expected. The stress distribution of the non–viscometric flow situation will be discribed with the CEF–equation and it is hoped that an equation which is exact for viscometric flow may also be (approximately) valid for nearly viscometric flows, Dodson et al (1973).

Fully developed primary flow.

The fully developed solution of duct flow with rectangular cross section is calculated for four different aspect ratios. The aspect ratios are 4×4 mm, 3×5.33 mm, 2×8 mm, and 1×16 mm, all having a cross section of $16 \cdot 10^{-6}$ m^2. For the Newtonian fluid water, the fully developed velocity profile at midplane of height and midplane of width in a duct with cross section 1×16 mm and mean velocity of 0.5 m/s were shown in figs. 8.4 and 8.5. The same calculation is made with the Non–Newtonian fluid 2% viscarin and the results are given in figs. 8.28 and 8.29. The figures show the primary velocity profiles at the same positions and for the same mean velocity as figs. 8.4 and 8.5 calculated with both the powerlaw model and the CEF–equation. It is seen that the primary velocity does not change whether the powerlaw model or the CEF–equation is used which indicates that for the chosen geometry and mean velocity the secondary flow which arises using the CEF–equation, see later in this section, does not have any influence on the primary flow or at least it can not be seen graphically. Comparing figs. 8.28 and 8.29 with the same plots for water, figs. 8.4 and 8.5, it is seen that the velocity profile along the height has a steeper gradient along the walls and consequently a lower maximum value. The velocity profile along the width is nearly the same, but with a wider "shoulder" area and similar to the other plot a lower maximum value.

An analytical expression for the velocity profile obtained for the fully developed flow between parallel plates separated the height of the duct can, for a powerlaw fluid, be written

$$u/u_{mean} = \frac{2n + 1}{n + 1} \left[1 - \tilde{\zeta}^{(n+1)/n}\right],$$

where $\tilde{\zeta} = \zeta/h$ having origo halfway between the plates.

It is seen that if n takes the value of one the velocity profile is a parabola. For lower values of n the velocity profile becomes more flat near the center and

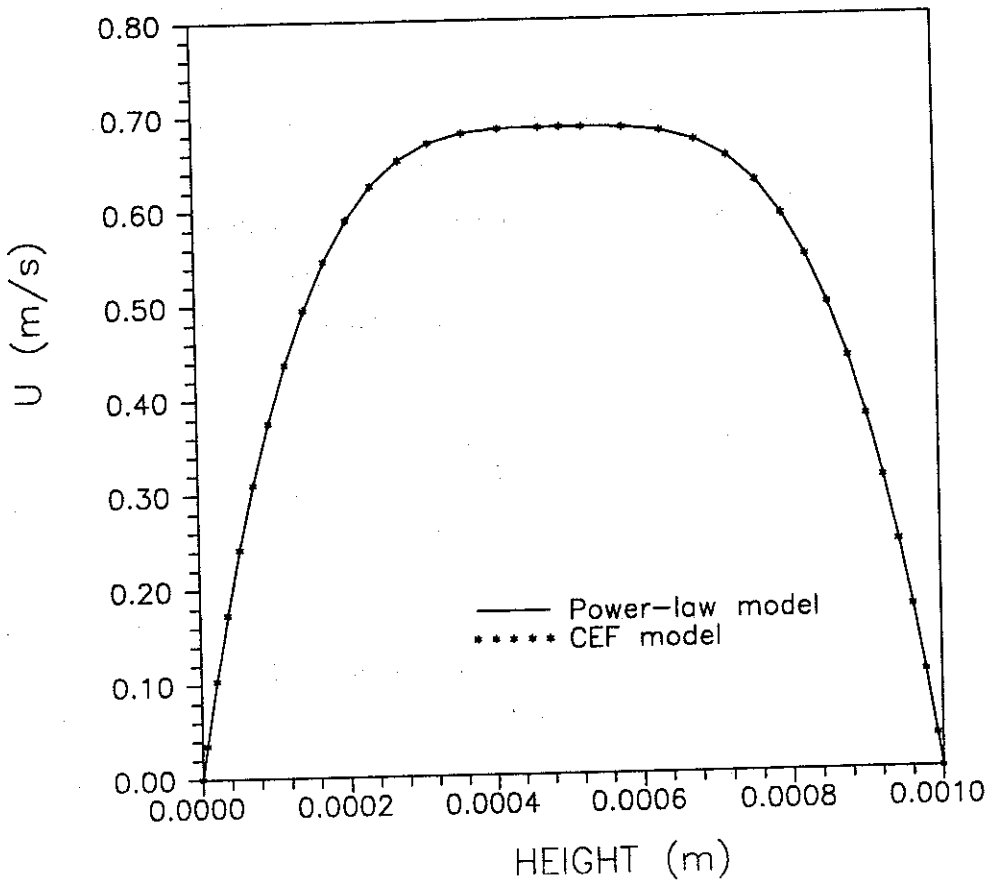

Fig. 8.28 *Primary velocity profile shown at half the width along the height.*

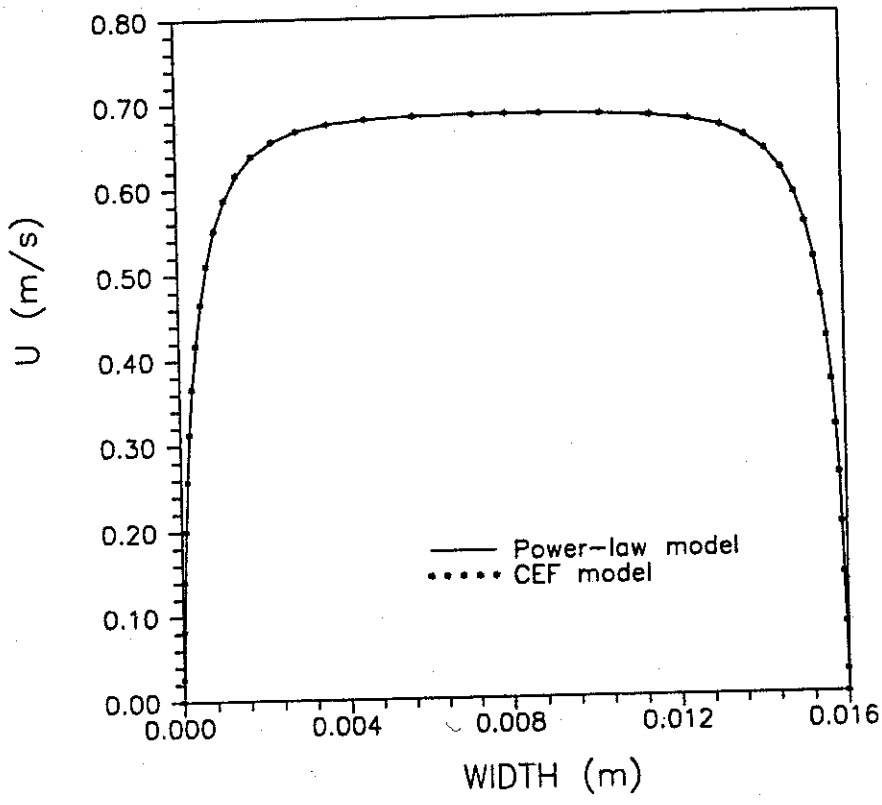

Fig. 8.29 *Primary velocity profile shown at midplane of height along the width.*

steeper near the walls. This is the well known powerlaw profile and Fig. 8.28 shows the characteristica of a powerlaw profile.

Even if figs. 8.28 and 8.29 are calculated for the same mean velocity as figs. 8.4 and 8.5 the Reynolds number is different. For a powerlaw fluid the Reynolds number in a developed flow between parallel plates is defined as, Larsen & Christensen (1985),

$$Re_{n,k} = \frac{\rho u_m^{2-n}(4h)^n}{k} \frac{3/2}{8^{n-1}} \left[\frac{2n}{2n+1}\right]^n . \tag{8.2}$$

For ducts with large aspect ratios eq. (8.2) is taken as a good approximation for the actual Reynolds number. For the flow shown in figs. 8.28 and 8.29 the Reynolds number becomes $Re_{n,k} = 15.5$ which should be compared to a Reynolds number of $Re = 993$ for the same mean velocity using water.

Fully developed secondary flow.

The behaviour of Non–Newtonian fluids in ducts has been paid much consideration in the past, where most of the attention has been designated to the "nature" of the secondary flow and to the role of secondary flow on the total flow rate. In a paper by Dodson et al (1973) the role of secondary flow in straight ducts of non–circular cross section was studied using a perturbation method where terms were expanded in powers of Ψ_2. The velocity distribution was of the form

$$\begin{aligned} u &= u_0 + \epsilon \bar{u}_1, \\ v &= \epsilon \bar{v}_1, \\ w &= \epsilon \bar{w}_1, \end{aligned} \tag{8.3}$$

where $\epsilon = \Psi_2$. Equation (8.3) is simply a perturbation about the rectilinear velocity field. With Ψ_2 taken as a constant in the perturbation analysis a quardratic shear rate dependence on the second normal stress difference is obtained. This was not the case in the work by Townsend et al (1976) where derivatives of Ψ_2 with respect to shear rate were also possible and ϵ in eq. (8.3) was taken as a separate quantity. With the work done by Dodson et al (1973) they concluded that the direction of streamlines reverse if the sign on Ψ_2 was

changed, but by the work of Townsend et al (1976) it was implied that it was the magnitude of departure of Ψ_2 from a constant multiple of η that determines the direction and strength of the secondary flow and consequently, if Ψ_2 is a constant multiple of η, there will be no secondary flow.

The constitutive equation used by both Dodson et al (1973) and Townsend et al (1976) was the CEF–equation. For the present work we use the same constitutive equation to model the non–linear rheology, but we do not use a perturbation method. Instead we model the full CEF–equation as described in chapter two. This, as will be seen later, gives a more detailed information of the secondary flow, thus extending earlier work.

First, a 2% viscarin solution is simulated in 4 straight ducts of rectangular cross section of same area and same mean velocity $u_m = 0.5$ m/s of primary flow. For each aspect ratio a set of 3 plots are shown. The *a* plots show velocity vector plots, the *b* plots show streamlines, and the *c* plots show perspective of the streamfunction of secondary flow. All plots are shown for one quadrant due to the symmetry along midplane of height and midplane of width.

All the *a* plots show that fluid is streaming along the walls towards the corner and leaving the corner in order to form two vortices. The two vortices differ in magnitude and size depending on aspect ratio, but at the large aspect ratio of 16 (1×16 mm) an additional very weak vortex appears. This vortex may be of a similar type as the additional vortex structure known from a driven cavity flow of increasing aspect ratio. Examination of the computational results in figs. 8.30 to 8.33 (shown at the end of this chapter) suggests a systematic parametric trend where the large, dominant vortex for large aspect ratios moves away from the corner to make room for the initially small vortex at the short end wall. At unity aspect ratio these two vortices take the same size as seen in fig. 8.30.

In order to understand the physics of the vortices we use the CEF–equation to obtain the relevant stress distribution in the cross plane including only first order terms,

$$\tau_{\eta\eta} - \tau_{\zeta\zeta} = \left[\left[\frac{\partial u}{\partial \eta}\right]^2 - \left[\frac{\partial u}{\partial \zeta}\right]^2\right] \cdot \Psi_2. \qquad (8.4)$$

Using eq. (8.4) along the line AB in fig. 8.34 it is seen that $\partial u/\partial \zeta$ varies less than $\partial u/\partial \eta$ (this must be a good assumption when considering the velocity profiles in fig. 8.28 and 8.29). Introducing this assumption together with the equation of Ψ_2 into eq. (8.4) the stress distribution in the cross plane takes the form

$$\tau_{\eta\eta} - \tau_{\zeta\zeta} \sim -\left[\frac{\partial u}{\partial \eta}\right]^2 \cdot \left\{\sqrt{\left[\left[\frac{\partial u}{\partial \eta}\right]^2 + \left[\frac{\partial u}{\partial \zeta}\right]^2\right]}\right\}^{n_1}, \qquad (8.5)$$

where $n_1 = -1.35$ for 2% viscarin. Equation (8.5) shows that the difference of $\tau_{\eta\eta} - \tau_{\zeta\zeta}$ along the line AB depends mainly on the difference of $\partial u/\partial \eta$ (remember $\partial u/\partial \zeta$ is assumed nearly constant). Due to the great velocity variation moving away from the wall, as seen in figs. 8.28 and 8.29, the stress difference $\tau_{\eta\eta} - \tau_{\zeta\zeta}$ has a greater negative value in A than B (remember the negative sign of Ψ_2 introduced in eq. (8.1)). With the sign convention used in eq. 2.2b, stress being positive in compression, eq. (8.5) indicates that the greater negative value of $\tau_{\eta\eta} - \tau_{\zeta\zeta}$ in A compared to the value in B makes the fluid move from B towards A. The same argumentation can be used along a line of constant η (sketched in fig. 8.34) and consequently, fluid will flow along the walls towards the corner as sketched in fig. 8.34 and as already seen in figs. 8.30 to 8.33 (shown at the end of this chapter).

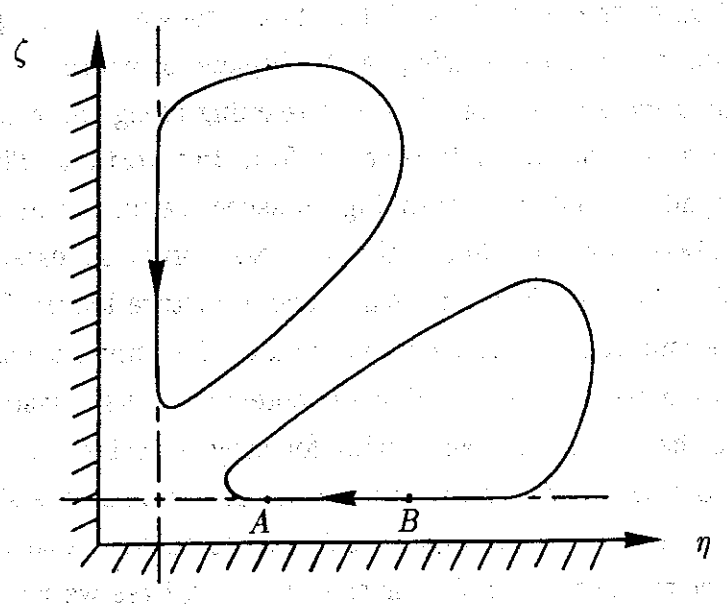

Fig. 8.34 *Sketch of streamlines near a corner.*

In order to demonstrate the legality or the illegality of eq. (8.5) and the conclusions stated by Townsend et al (1976) the programme was tested for different values of n_1 (the exponent in the powerlaw model of Ψ_1 and thereby also in the powerlaw model of Ψ_2). First, it was tested if the secondary flow disappeared if Ψ_2 is a constant multiple of η. A "test" fluid with $n_1 = n$ and $k_1 = 0.9$ Pa·s$^{n_1+2}$ was simulated and the results are, among other results, given in tabel 8.2. Table 8.2 shows the maximum and minimum values of the v-component and the streamfunction, respectively, and it is clearly seen that the secondary

flow is extremely small for the "test" fluid. The numerical prediction of any secondary flow may be due to the higher order terms in the CEF–equation (and round–off errors). The lower value used for the k_1 compared to the value used when viscarin is simulated was necessary in order to obtain convergence. The reason for that is not clear, but the values of Ψ_1 and $|\Psi_2|$ increase dramatically as n_1 is altered from –1.35 to –0.63 for the same shear rate and it caused loss of convergence if k_1 was not lowered.

In order to see how the variation of Ψ_2 with shear rate affects the strength and direction of the secondary flow the programme was tested with $n_1 = -1.2$ and $n_1 = -2.8$ for the same geometry (3×5.33) and the same mean velocity ($u_m = 1.0$ m/s). With use of eq. (8.5) it is expected that the secondary flow becomes stronger with $n_1 = -1.2$ which is clearly seen in table 8.2. A higher negative value will consequently make the secondary flow weaker, but again with use of eq. (8.5) for a certain high negative value of n_1 it is expected that the flow direction should reverse (for $\partial u/\partial\zeta$ set to zero it is, according to eq. (8.5), expected that the secondary flow will reverse whenever n_1 becomes smaller than –2). The reversal of the secondary flow was not observed, only a weakening. Even if the whole secondary flow field did not reverse the structure did change. The smallest vortex became smaller and the greater vortex became greater. This is viewed in fig. 8.35. For the chosen geometry and mean velocity the variation of Ψ_2 (obtained upon variation of n_1 and k_1) did <u>not</u> affect the direction of the secondary flow, <u>only</u> the strength. A reversal was <u>only</u> obtained by changing the sign of Ψ_2. The reversal of the secondary flow which was expected for high negative values of n_1 was based on eq. (8.5) which again was based on no or little variation of $\partial u/\partial\zeta$ from A to B in fig. 8.34 and including only first order terms. These limitations might very well be of importance for high negative values of n_1 where the actual value of Ψ_2 becomes lower with respect to shear rate even if the variation of Ψ_2 becomes greater.

The flow pattern for the geometry with cross section of 3×5.33 mm is shown in figs. 8.36 and 8.37 for two different mean velocities of 0.1 m/s and 10 m/s, respectively. It is seen that the center of the greater vortex moves towards the longest wall for the high mean velocity. This creates a little jet of fluid moving along the longest wall towards the corner and leaving the little vortex in an even more squeezed "world". The proportion of the maximum value of the streamfunctions of the little vortex becomes 111 whereas it becomes 140 for the greater vortex indicating that the greater vortex is growing faster than the little vortex. The actual magnitude of the maximum and minimum of the

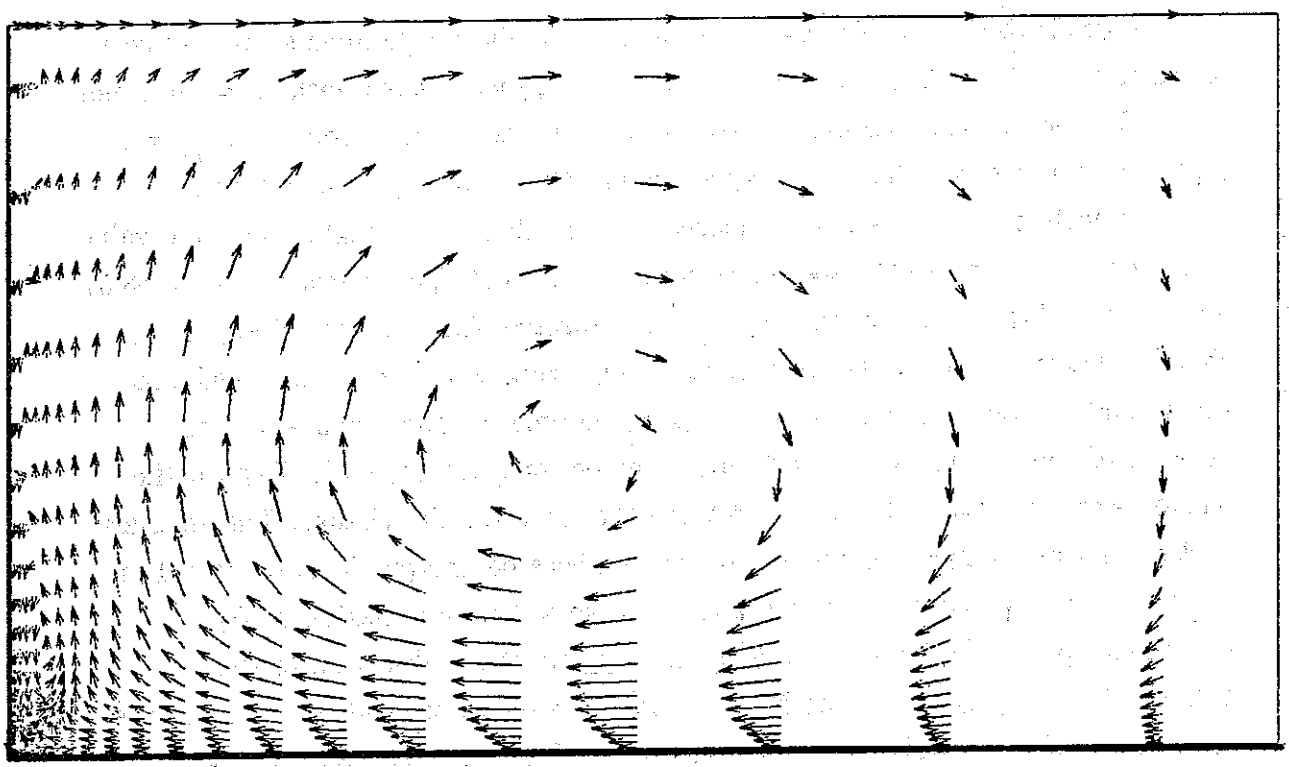

Fig. 8.35 *Change of streamline pattern for high negative values of* n_1. *The little vortex disappears leaving extra space for the great vortex.*

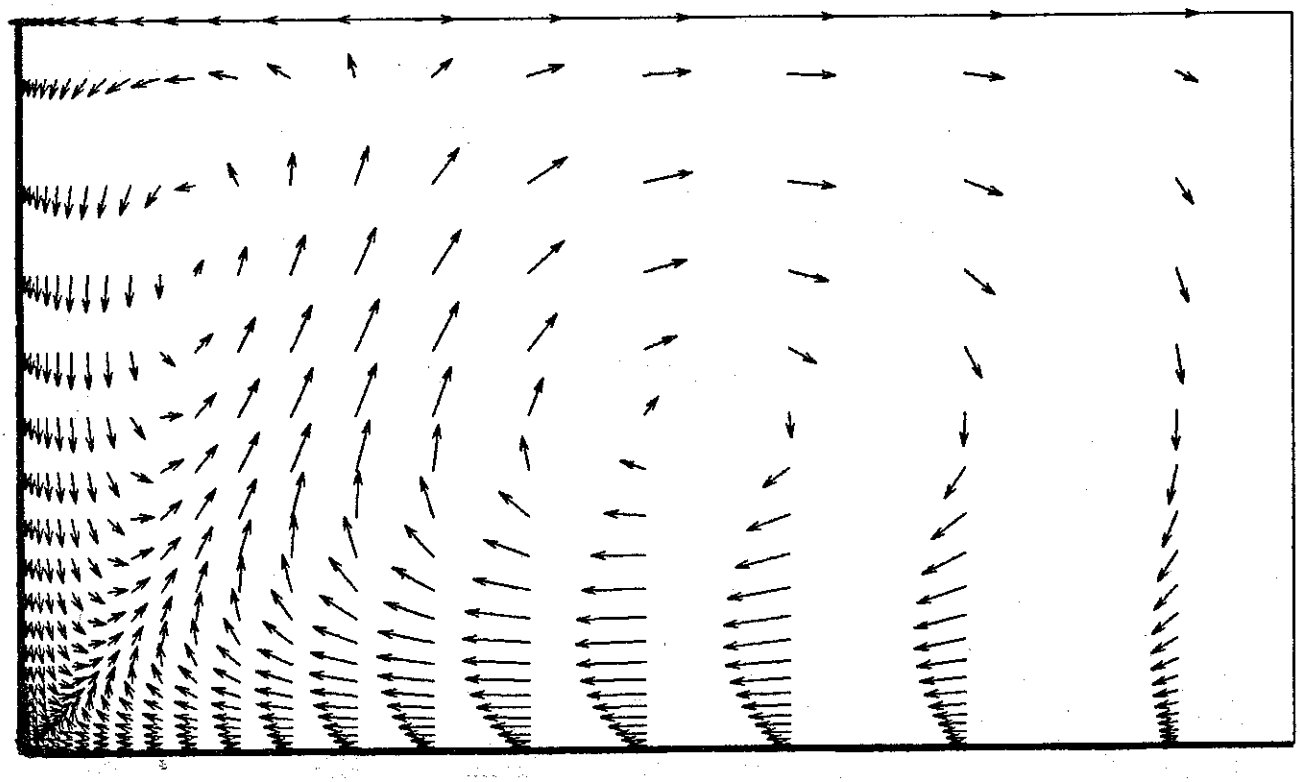

Fig. 8.36a *Velocity vector plot. Geometry: 3×5.33 mm.* $u_m = 0.1$ *m/s.*

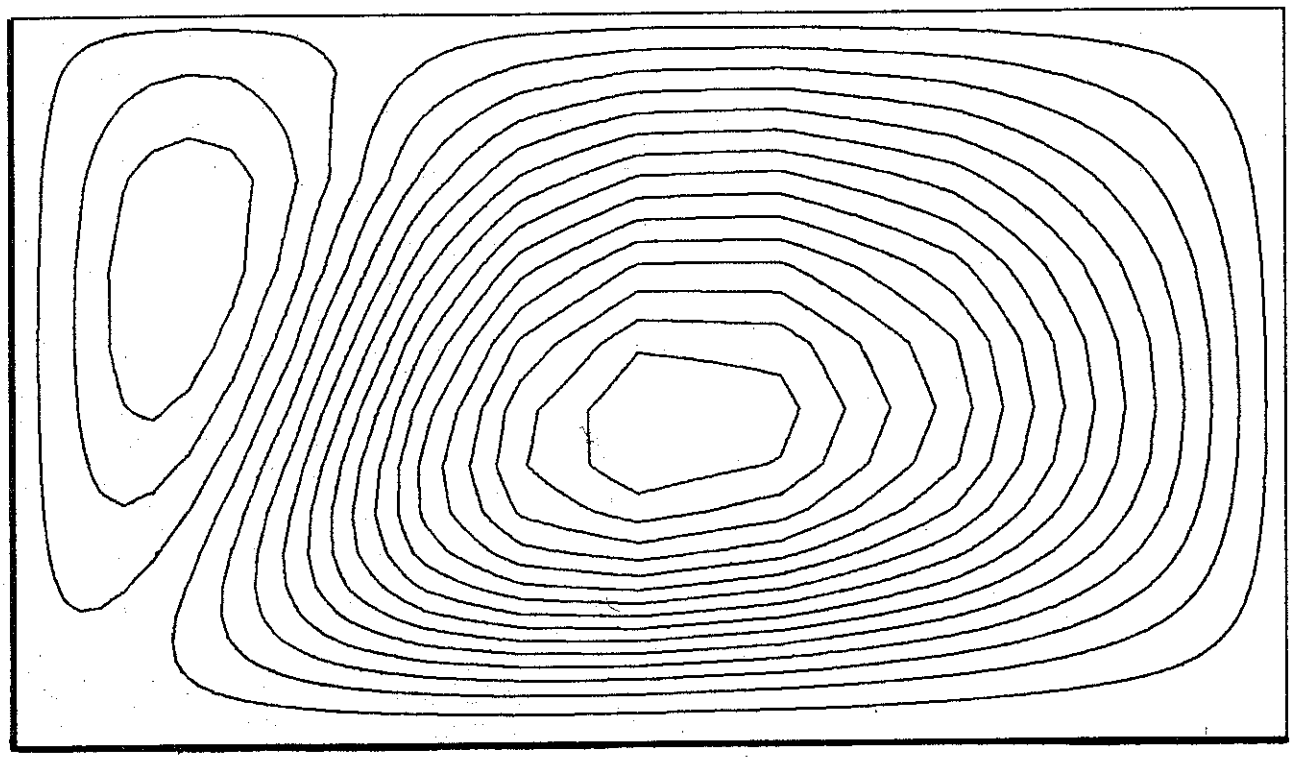

Fig. 8.36b *Streamline plot. Geometry: 3×5.33 mm.* $u_m = 0.1$ *m/s.*

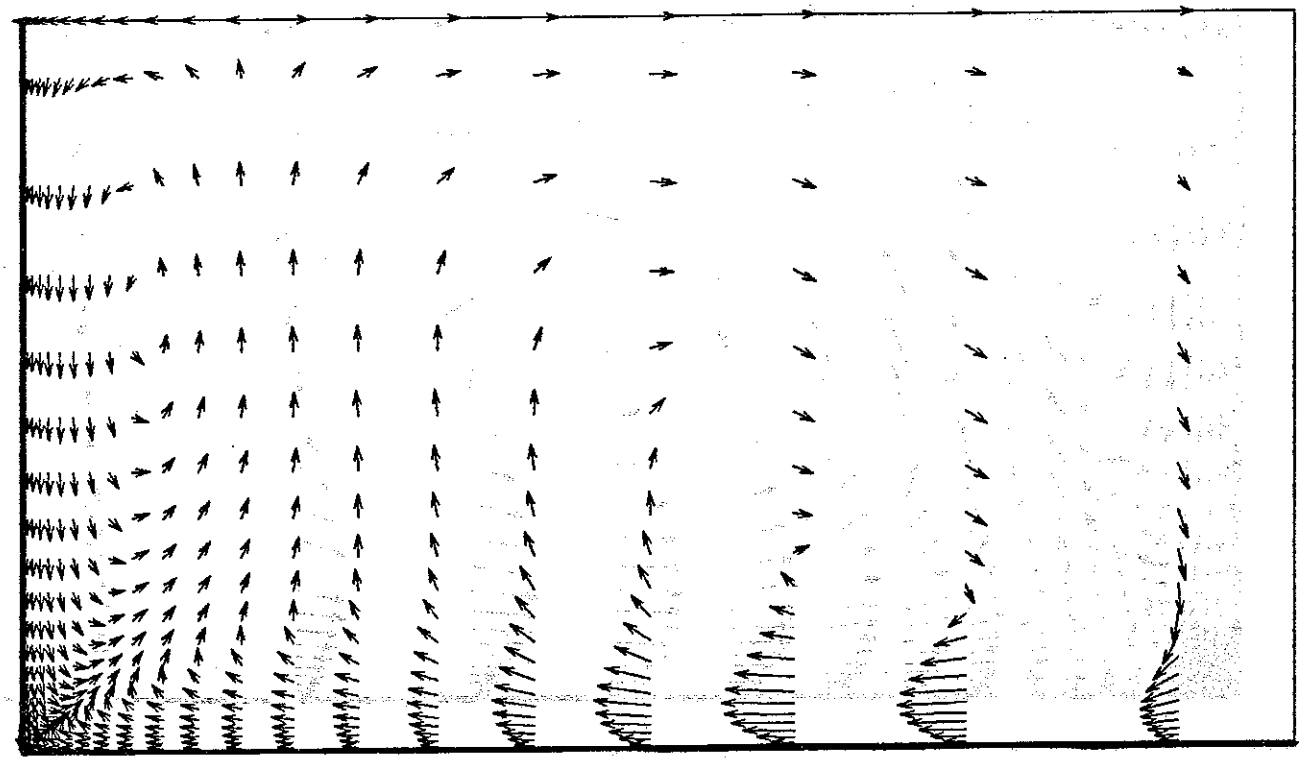

Fig. 8.37a *Velocity vector plot. Geometry: 3×5.33 mm.* $u_m = 10.0$ *m/s.*

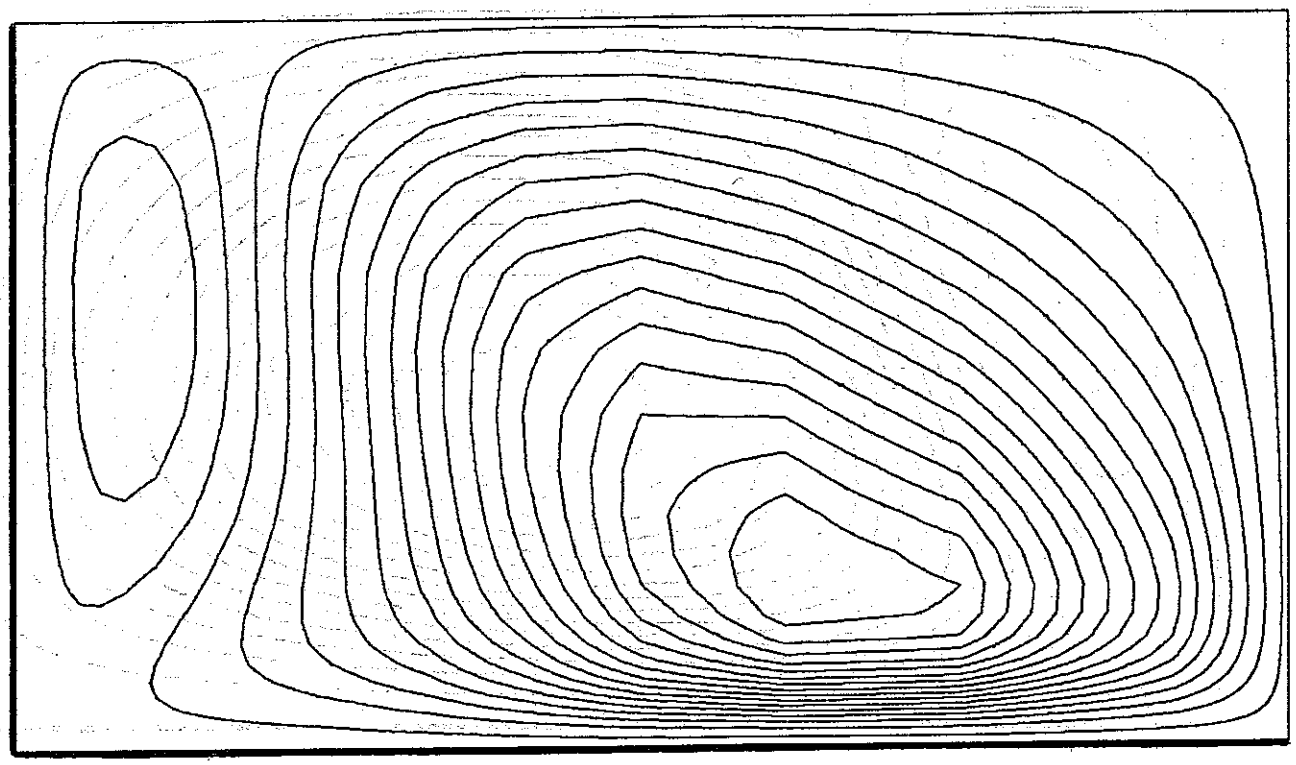

Fig. 8.37b *Streamline plot. Geometry: 3×5.33 mm.* $u_m = 10.0$ *m/s.*

streamfunctions and the v-components are shown in table 8.2 where values for other primary mean velocities are also shown. The cross section geometry is 3×5.33 mm.

u_{mean} (m/s)	v_{max} (m/s)	v_{min} (m/s)	*Streamfunction* $_{max}$ (m^2/s)	*Streamfunction* $_{min}$ (m^2/s)
0.1	$8.46 \cdot 10^{-4}$	$-1.43 \cdot 10^{-3}$	$1.19 \cdot 10^{-7}$	$-5.61 \cdot 10^{-7}$
0.3	$3.41 \cdot 10^{-3}$	$-5.82 \cdot 10^{-3}$	$4.89 \cdot 10^{-7}$	$-2.27 \cdot 10^{-6}$
0.5	$6.59 \cdot 10^{-3}$	$-1.12 \cdot 10^{-2}$	$9.24 \cdot 10^{-7}$	$-4.38 \cdot 10^{-6}$
1.0	$1.63 \cdot 10^{-2}$	$-2.72 \cdot 10^{-2}$	$2.04 \cdot 10^{-6}$	$-1.06 \cdot 10^{-5}$
1.0 $n_1=n=-0.63$ $k_1=0.9$	$1.18 \cdot 10^{-7}$	$-1.44 \cdot 10^{-7}$	$4.52 \cdot 10^{-16}$	$-7.63 \cdot 10^{-11}$
1.0 $n_1=-1.2$	$3.14 \cdot 10^{-2}$	$-3.17 \cdot 10^{-2}$	$4.20 \cdot 10^{-6}$	$-2.11 \cdot 10^{-5}$
1.0 $n_1=-2.8$	$1.31 \cdot 10^{-5}$	$-1.30 \cdot 10^{-5}$	$1.77 \cdot 10^{-11}$	$-8.72 \cdot 10^{-9}$
3.0	$5.89 \cdot 10^{-2}$	$-1.14 \cdot 10^{-2}$	$4.73 \cdot 10^{-6}$	$-4.03 \cdot 10^{-5}$
5.0	$8.26 \cdot 10^{-2}$	$-2.33 \cdot 10^{-1}$	$6.73 \cdot 10^{-6}$	$-6.20 \cdot 10^{-5}$
10.0	$1.00 \cdot 10^{-1}$	$-4.96 \cdot 10^{-1}$	$1.33 \cdot 10^{-5}$	$-7.87 \cdot 10^{-5}$

Table 8.2 *Calculated maximum and minimum values for the v-components and the streamfunctions for different corresponding* u_{mean} *values. Unless other is stated* $n_1 = -1.35$ *and* $k_1 = 5.96$ $Pa \cdot s^{2+n_1}$. *The cross section is 3×5.33 mm.*

Grid.

In order to determine the secondary flow to a high order of accuracy several grid densities were tried. The velocity profile along the width at midplane of height for the duct with cross section geometry of 3×5.33 mm is plotted in fig. 8.38 for three different grid densities. It is seen that the two grid densities 22×22 and 44×44 give the same results whereas the 11×11 grid gives a result which

differs from the others. The chosen grid used for the 3×5.33 geometry is taken as the grid involving 22×22 gridpoints (20×20 control volumes) and shown in fig. 8.39 (remember that the computation takes place in only one quadrant of the cross section). The number of grid points and the ratio between successive grid cell lengths in each direction used in the computations for the 4 different cross sections are shown in table 8.3.

Geometry (mm)	Aspect ratio	Grid points η	ζ	Cell length ratio η	ζ
4×4	1	22	22	1.2	1.2
3×5.33	1.78	22	22	1.22	1.18
2×8	4	22	22	1.23	1.14
1×16	16	22	18	1.25	1.10

Table 8.3 *Grid points and cell length ratio for 4 different the cross sections.*

Convergence and cpu consumption.

In order to get a fast convergence it was preferable to start the computation including only the shear rate dependent viscosity (powerlaw model) in the constitutive equation and after the residual is lowered a factor 1000, or so, the extra terms in the CEF–equation were coupled to the powerlaw. In order to start the computation with the full CEF–equation employed it was necessary to use excessively small relaxation parameters except for the duct with aspect ratio 1 where the relaxation parameter for the u–velocity was set to $\lambda_u = 0.85$ and for the v and w–velocity they were set to $\lambda_v = \lambda_w = 0.75$. A typical plot of residual versus number of iterations is shown in fig. 8.40 for a duct with aspect ratio of 1 and primary mean velocity of $u_m = 0.5$ m/s. The residual is the highest normalized residual defined in chapter seven where the residual could be either the residual from one of the momentum equations or from the pressure corrector equation. For the present residual plot, the residual is the normalized residual of

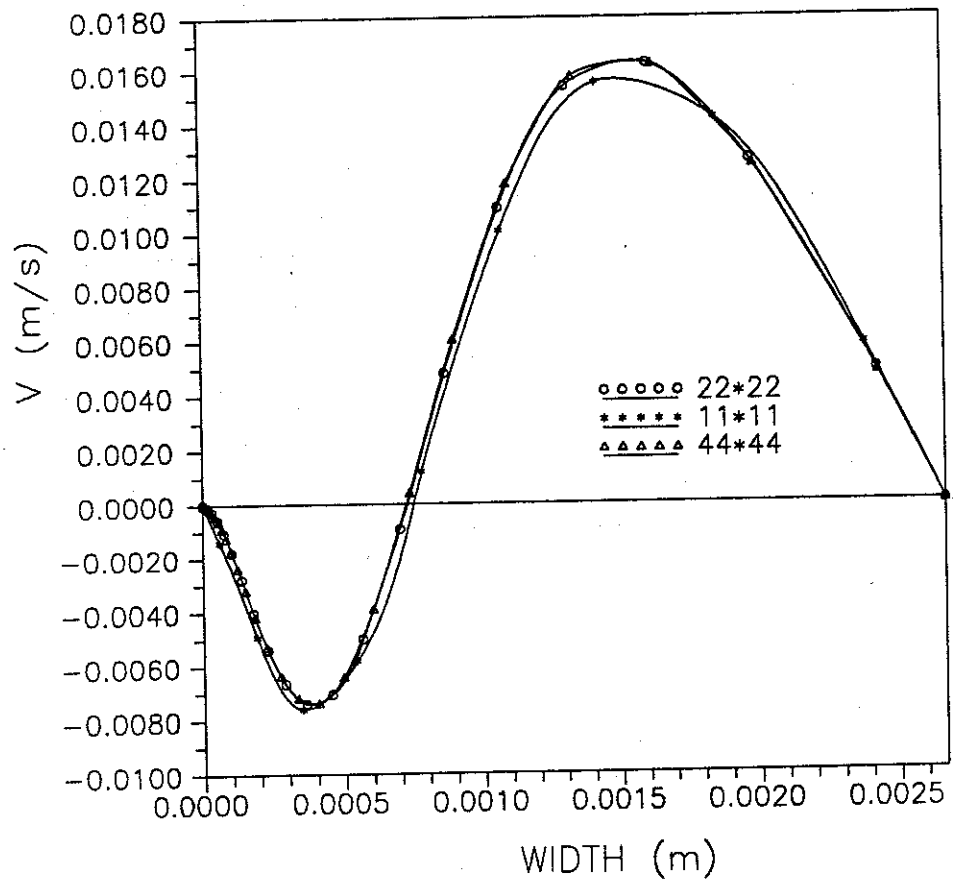

Fig. 8.38 *Secondary flow for different grid densities.*

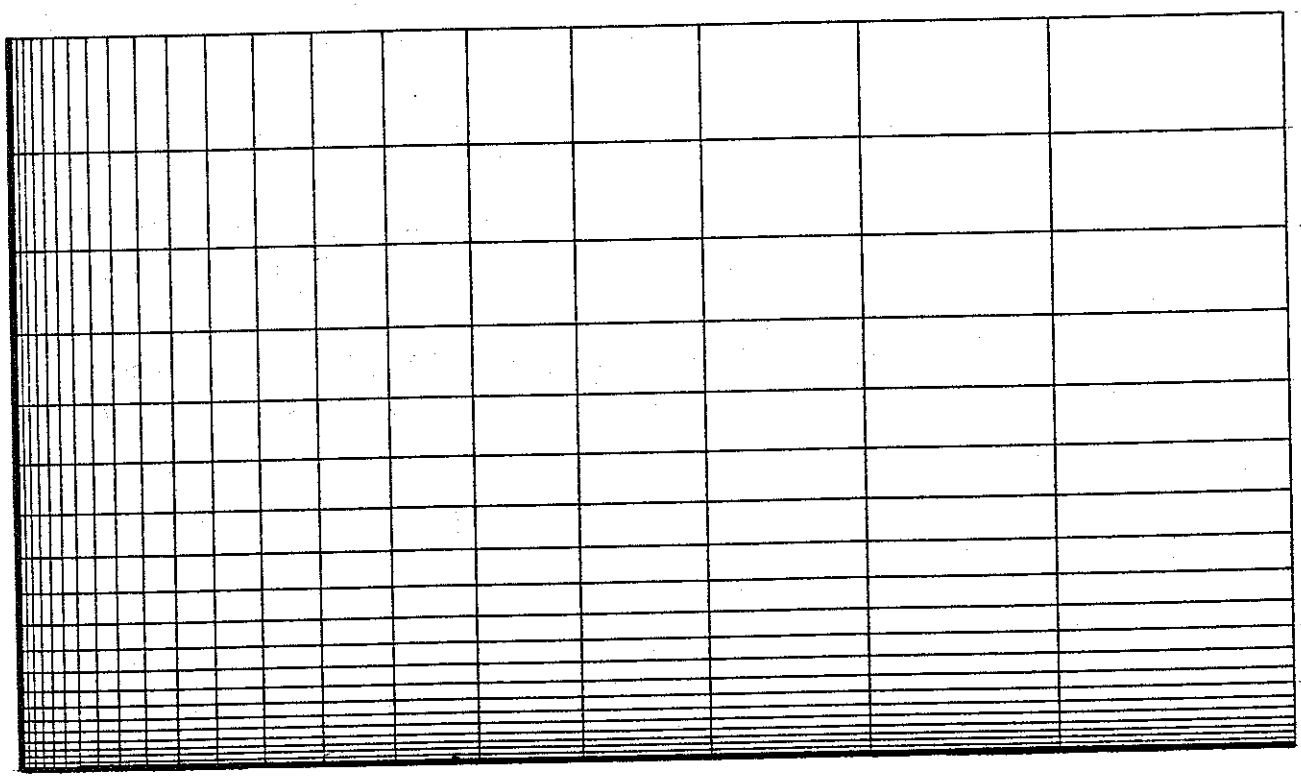

Fig. 8.39 *Grid for the cross section 3×5.33 mm.*

the u–momentum equation which is the leading residual for this type of duct computations. The bend in the residual curve seen after nearly 20 iterations has to do with the way the inlet–outlet conditions are treated. As stated, earlier in order to find the inlet condition the inlet condition is cyclic related to the outlet condition which is fed in as a new inlet condition at each iteration until the flow repeats itself. The outlet condition is treated as if the flow were parabolic. After nearly 20 iterations the changes in the flow is as in a developing flow. The rate of convergence could be raised if the relaxation parameters were changed to a higher value after 20 iterations.

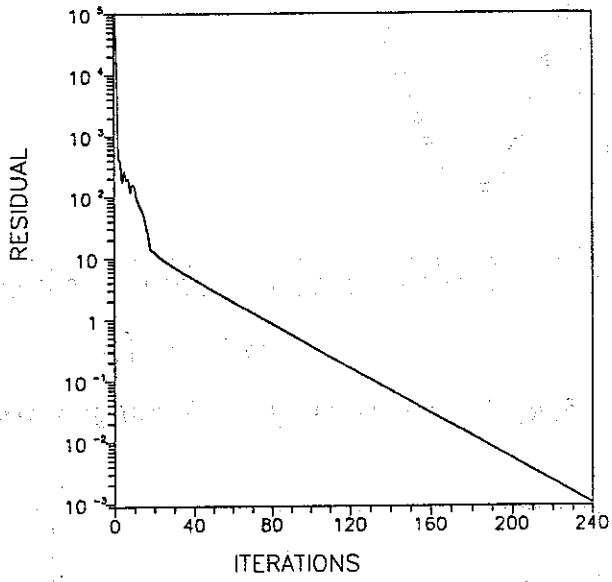

Fig. 8.40 *Residual historie. Geometry: 4×4 mm. Fluid: 2% viscarin.*

The cpu consumption for a computation involving 22×22 grid points, aspect ratio 1, and u_m = 0.5 m/s with the residual historie shown in fig. 8.40 is 200 sec on an Amdahl 5890 model 180E. This gives a cpu consumption of $200/(20\times20\times240) = 6.9\cdot10^{-4}$ sec/point/iteration. For comparison, the calculation made with water of a developing flow in a curved duct the consumption of $5\cdot10^{-5}$ sec/point/iteration. This indicates that the Non–Newtonian fluid requires about an order of magnitude more cpu consumption than the Newtonian fluids. The main reason is that the constitutive equation is updated after each outer loop making the viscosity and the normal stress coefficients lag behind the flow and pressure field. Another factor, when comparing convergence rates of water and viscarin, is that the same mean velocity does not give the same Reynolds number. Flow of polymer solutions as viscarin is usually characterized by low Reynolds numbers indicating high amounts of diffusive fluxes which usually require more computation than flows at a high Reynolds number in the laminar range.

Sensitivity analysis and evaluation of accuracy.

The accuracy of the flow field can be divided into two groups. One which has to do with accuracy of the primary flow and one which has to do with accuracy of the secondary flow. The Navier–Stokes equations can completely describe the nature of Newtonian fluids whereas the CEF–equation can only describe the stress distribution of viscarin (it is assumed that the flow is of a viscometric type) if the three viscometric functions are known to a high level of accuracy. LDA measurements of both primary flow and secondary flow in straight ducts are made by Bardur et al (1987) and Hansen et al (1988) where it is seen that the measured primary flow agrees very well with the calculated primary flow. The fully developed solution of 2% viscarin in a straight duct can, with the CEF–equation or the powerlaw model used as the constitutive equation, completely describe the nature of the primary flow. The appearance of secondary flow does not alter the primary flow noticably,as seen in figs. 8.28 and 8.29. This means that each model will nearly describe the nature of the primary flow of viscarin to the same accuracy as the Navier–Stokes equations describe water. This, with the conclusions made for water, tells that the primary flow can to full extend be described in the geometries used and the level of accuracy is higher than the accuracy obtainable from measurements.

The most interesting flow is the secondary flow where high level of accuracy is a big challenge both the experimentalist who is interested in LDA and the experimentalist who is interested in rheometry. If it is believed that the CEF–equation can describe the stress distribution in a straight duct even if the flow is not a viscometric flow the accuracy depends on the level of accuracy of the three viscometric functions where Ψ_2 is the most difficult one to measure, Walters (1975).

The secondary flow was studied for different Ψ_1–functions and different Ψ_2–functions as shown in fig. 8.41. The two functions of Ψ_1 found by UCW and TUD based on measurents and extrapolated data of N_1 was earlier shown in fig. 8.26. The Ψ_1–function found by TUD is $\Psi_1 = 5.2 \cdot \dot{\gamma}^{-1.32}$ and Ψ_2 is still used as $\Psi_2 = -0.15\Psi_1$. It is seen that hardly any difference is observed using Ψ_1 found by TUD compared to the one found by UCW. Even if hardly any difference was observed using two different functions of Ψ_1 a great difference is observed when Ψ_2 is changed which also was expected because Ψ_2 is directly related to the secondary flow. Also, Ψ_2–values are known only to within 50% accuracy or even less.

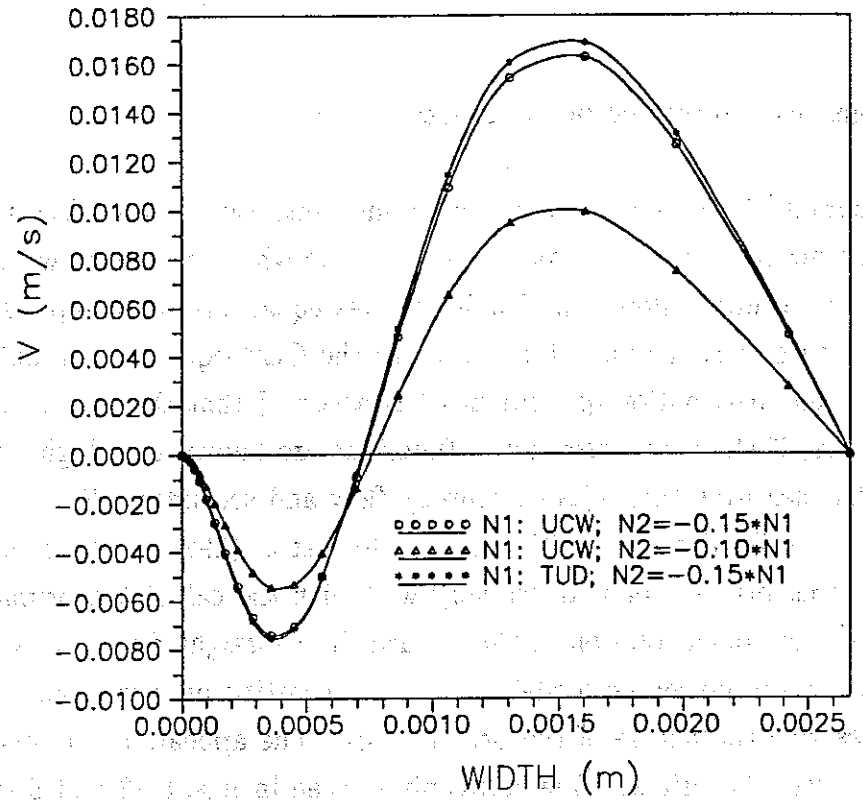

Fig. 8.41 *Sensitivity analysis of secondary flow.*

In order to evaluate the calculated results of the secondary flow in duct with aspect ratio 1.78 and $u_m = 1$ m/s the v-component along the width 1.1 mm from the wall was compared with measured results. The measured results (Christensen & Larsen, 1989) are shown in fig. 8.42 and the calculated results in fig 8.43. Due to the symmetry condition only half of the width is shown in fig. 8.43. Exactly the same trend is seen in both the plots where a small negative value is seen near the wall changing to a high positive value moving along the width ending at zero value at the symmetry line. The very few measured data near the walls are due to the extend of the measuring volume which prevents one from going closer to the wall. Even if the trend is the same in figs. 8.42 and 8.43 the values and thereby the strength of the secondary flow is not the same. This must due to the very great uncertainty of both the measured velocity data and the measured rheology data for N_2. The uncertainty of the measured velocity data comes mainly from the great difference in magnitude of the velocity component of the primary flow and the secondary flow which makes it extremly difficult to measure the secondary flow without some blending of the primary flow. Even if the viscometric functions were measured to a higher level of accuracy it is also necessary to measure them in a higher range of shear rates. The shear rates in the duct of aspect ratio 16 are higher than 20000 1/s which should be compared to the measured values in fig. 8.26 where the highest shear rate is in the order of

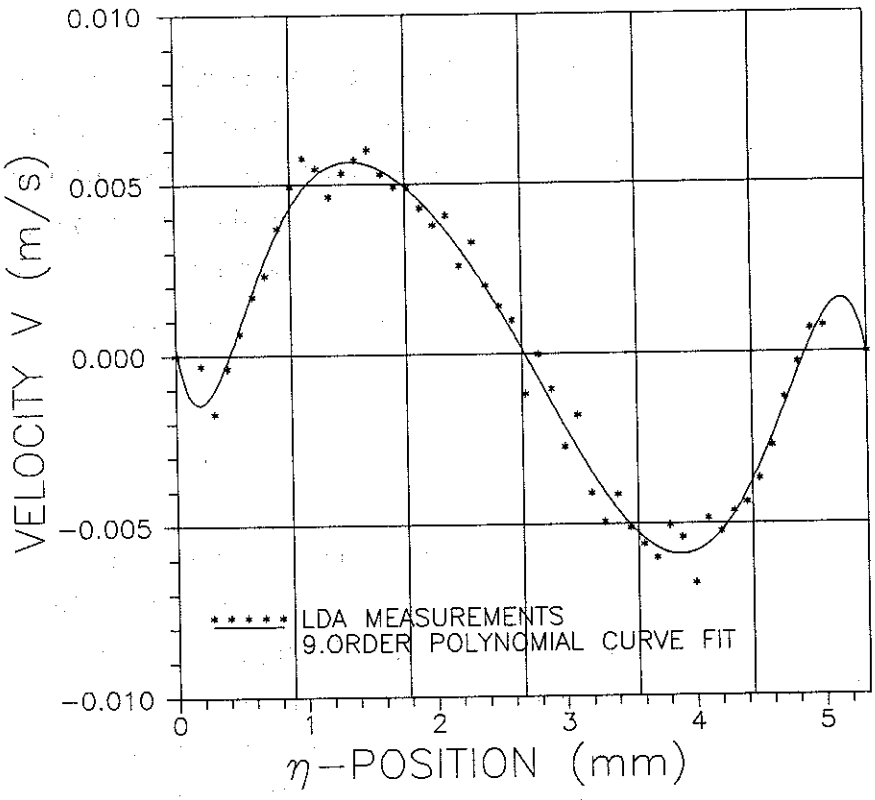

Fig. 8.42 *Measured v-component along the width 1.1 mm from the wall.*

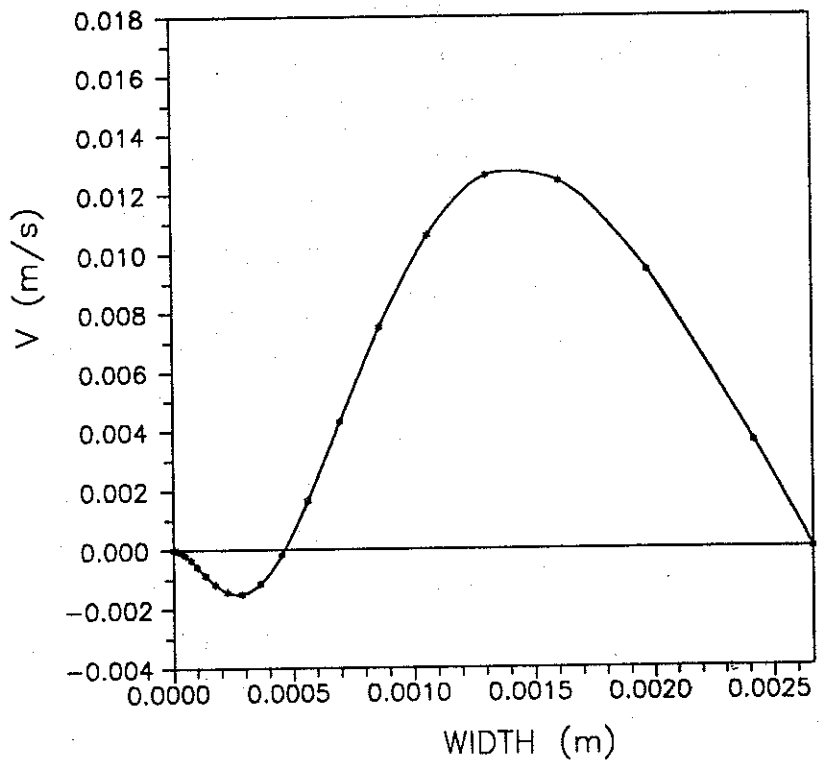

Fig. 8.43 *Calculated v-component along the width 1.1 mm from the wall.*

500 1/s. Due to the great uncertainty of both the measured velocities and the measured viscometric functions the calculated strength of the secondary flow can not be verified, but it is believed that the behaviour of the secondary flow is accurate since both the calculated and measured data show the same trend. Even if only one plot of measured data will be shown the same trend as seen in fig. 8.42 and 8.43 was also observed for other aspect ratios and mean velocities.

8.3.2 CURVED DUCTS

To extend the study of flow in straight ducts to curved ducts the same constitutive equation is used. The flow is surely not a viscometric flow any more due to secondary flow initiated from curvature effects, but again we hope that an equation which is exact for viscometric flow may also be (approximately) valid for nearly viscometric flows. The calculations are carried out over half the cross section of the duct due to the symmetry condition along the width at half height. The primary flow along width at half height in a duct with aspect ratio 16 is shown in fig. 8.44 for 3 different primary mean velocities. The 3 different mean velocities are 0.01 m/s, 0.1 m/s, and 1.2 m/s, respectively, with corresponding Reynolds numbers of 0.04, 1.6, and 92, respectively, obtained from eq. (8.2). The *b* plot shows the primary flow calculated with both the powerlaw model and the CEF–equation indicating that the secondary flow has no noticable influence of the primary flow. This also was seen in the straight duct. It is clearly seen that the highest velocity appears near the inner wall which also was expected when remembering the same plots for water at low Reynolds numbers.

Isovelocity curves for the primary flow for $u_m = 1.2$ m/s is shown in fig. 8.45 for both calculated and measured data. Maximum velocity in fig. 8.45 is 1.81 m/s and minimum is 0 m/s for the calculated isovelocity curves. With evenly distibuted isovelocity curves this gives a jump between the curves of 0.23 m/s. The measured data are taken from Nielsen (1989). Due to the limited number of measured data points near the inner and outer wall the agreement is not as good as could have been expected, but elsewhere the agreement is fine.

Streamlines of the secondary flow for the same geometry and mean velocity is shown in fig. 8.46 where both plots obtained from measured data and calculated data are shown. It is seen that the strongest vortex situated near the inner wall is shown for both the measured data and the calculated data and consequently the weakest vortex is situated near the outer wall. The main

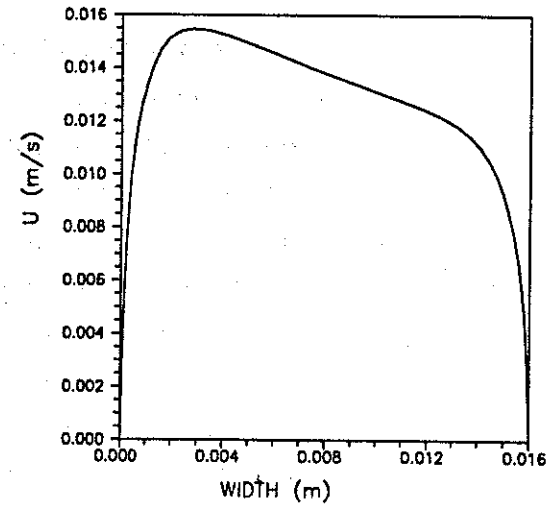

Fig. 8.44a *Primary velocity plot along width at half height.* $u_m = 0.01$ *m/s.*

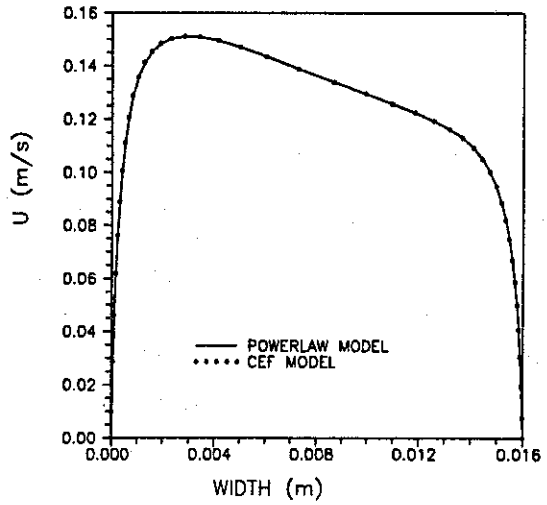

Fig. 8.44b *Primary velocity plot along width at half height.* $u_m = 0.1$ *m/s.*

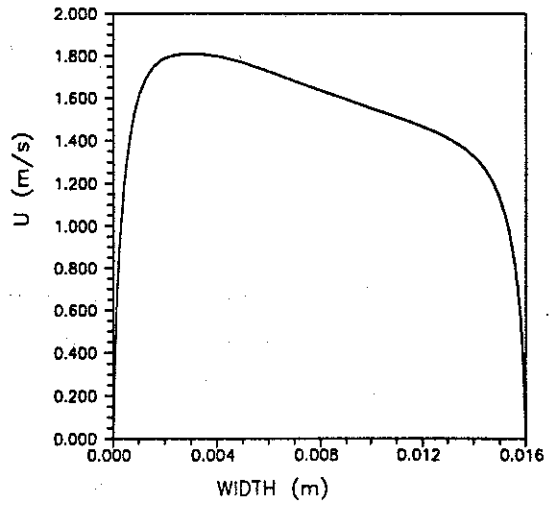

Fig. 8.44c *Primary velocity plot along width at half height.* $u_m = 1.2$ *m/s.*

difference on the measured and calculated data are the extend to which the vortices reach into the domain. The strong vortex extends over the greatest domain when the measured data are considered whereas it is opposite for the calculated data. At first glance, it seems most logical that the strongest vortex extends the furthest, but no conclusion will be given here. In addition to the vortices already discussed an extra little vortex is calculated very near the inner wall. This is easily seen in fig. 8.47b which shows the streamfunction in perspective. Fig. 8.47a shows a velocity vector plot of the same situation. Similar results as shown in figs. 8.46 and 8.47 have been obtained for u_m = 0.1 m/s and u_m = 0.01 m/s, but only the calculated data will be given. Table 8.4 shows the maximum value for all three velocity components and the maximum and minimum values for the streamfunctions for the three mean velocities of 1.2 m/s, 0.1 m/s, and 0.01 m/s, respectively.

u_{mean} (m/s)	u_{max} (m/s)	v_{max} (m/s)	w_{max} (m/s)	*Streamfunction* $_{max}$ (m^2/s)	*Streamfunction* $_{min}$ (m^2/s)
0.01	.0155	$8.11 \cdot 10^{-5}$	$4.5 \cdot 10^{-5}$	$8.34 \cdot 10^{-9}$	$-1.28 \cdot 10^{-8}$
0.1	0.151	$1.52 \cdot 10^{-3}$	$8.8 \cdot 10^{-4}$	$1.59 \cdot 10^{-7}$	$-2.45 \cdot 10^{-7}$
1.2	1.81	$3.80 \cdot 10^{-2}$	$2.0 \cdot 10^{-2}$	$3.79 \cdot 10^{-6}$	$-6.23 \cdot 10^{-6}$

Table 8.4 *Maximum u, v, and w components and maximum and minimum streamfunction for cross section of 1×16 mm and different mean velocities.*

8.4 PRESSURE DROP – MEASUREMENTS & CALCULATIONS

In order to calculate the effect of secondary flow on the pressure drop in straight ducts a measurement programme was set–up on an already existing test section for LDA measurements. The experimental set–up will not be described only the results of the measurements.

The pressure drop in 4 ducts with cross section of 4×4 mm, 3×5.33 mm, 2×8 mm, and 1×16 mm were measured for mean velocities ranging from 0.05 m/s to 3 m/s. The fluid was 2% viscarin. Fig. 8.48 shows measured and calculated data

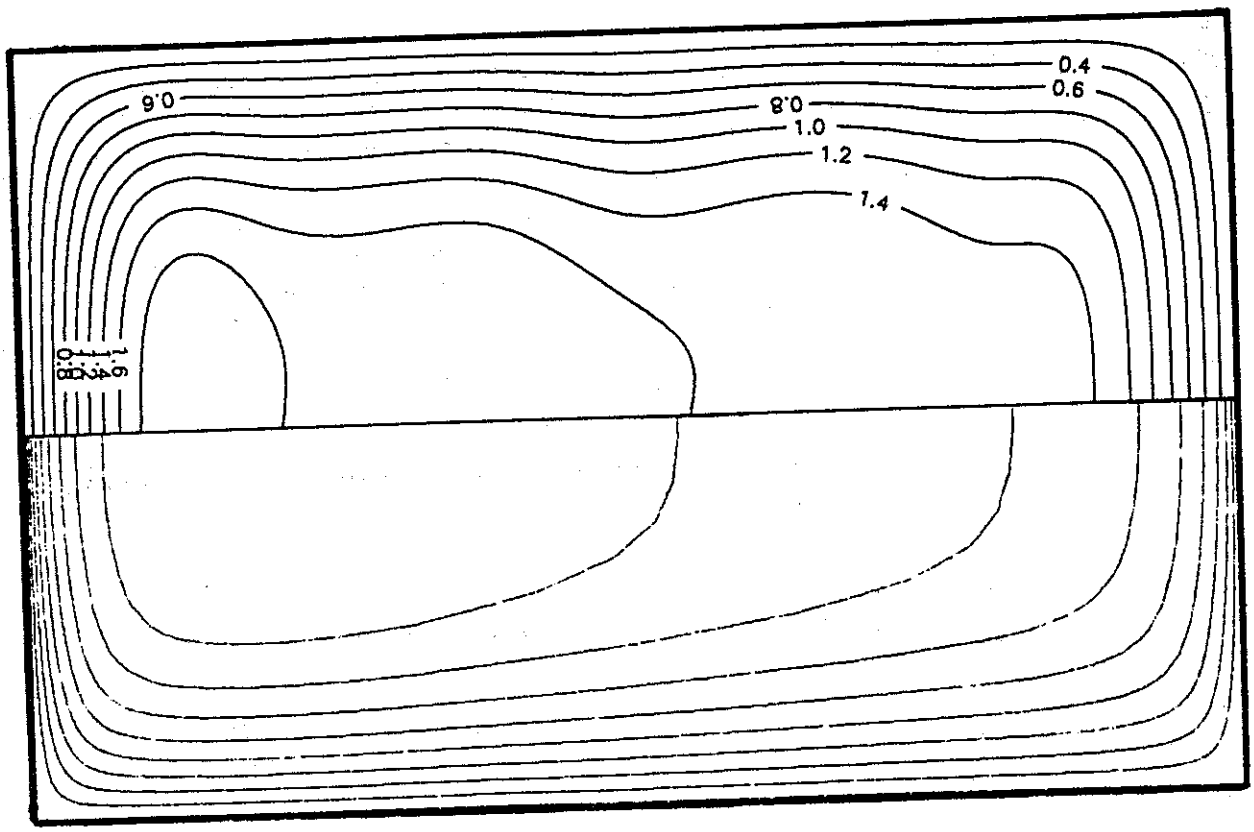

Fig. 8.45 *Calculated (a) and measured (b) isovelocity curves,* $u_m = 1.2\ m/s$.

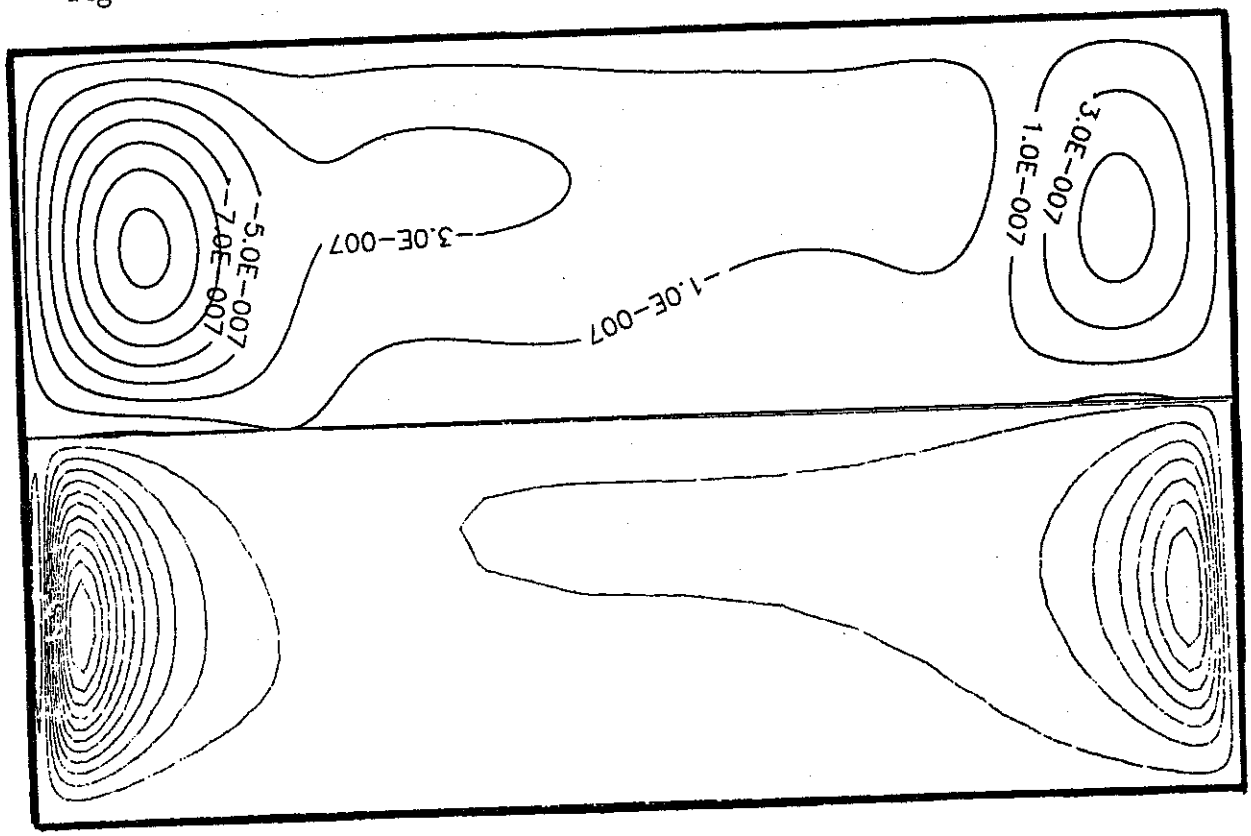

Fig. 8.46 *Calculated (a) and measured (b) streamline plot,* $u_m = 1.2\ m/s$.

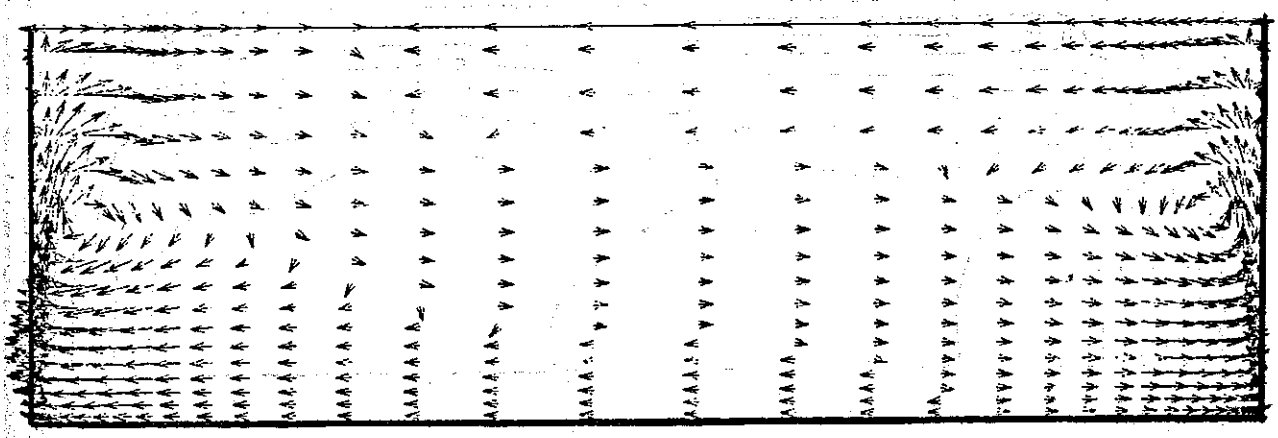

Fig. 8.47a *Vector plot, u_m = 1.2 m/s, geometry: 1×16 mm.*

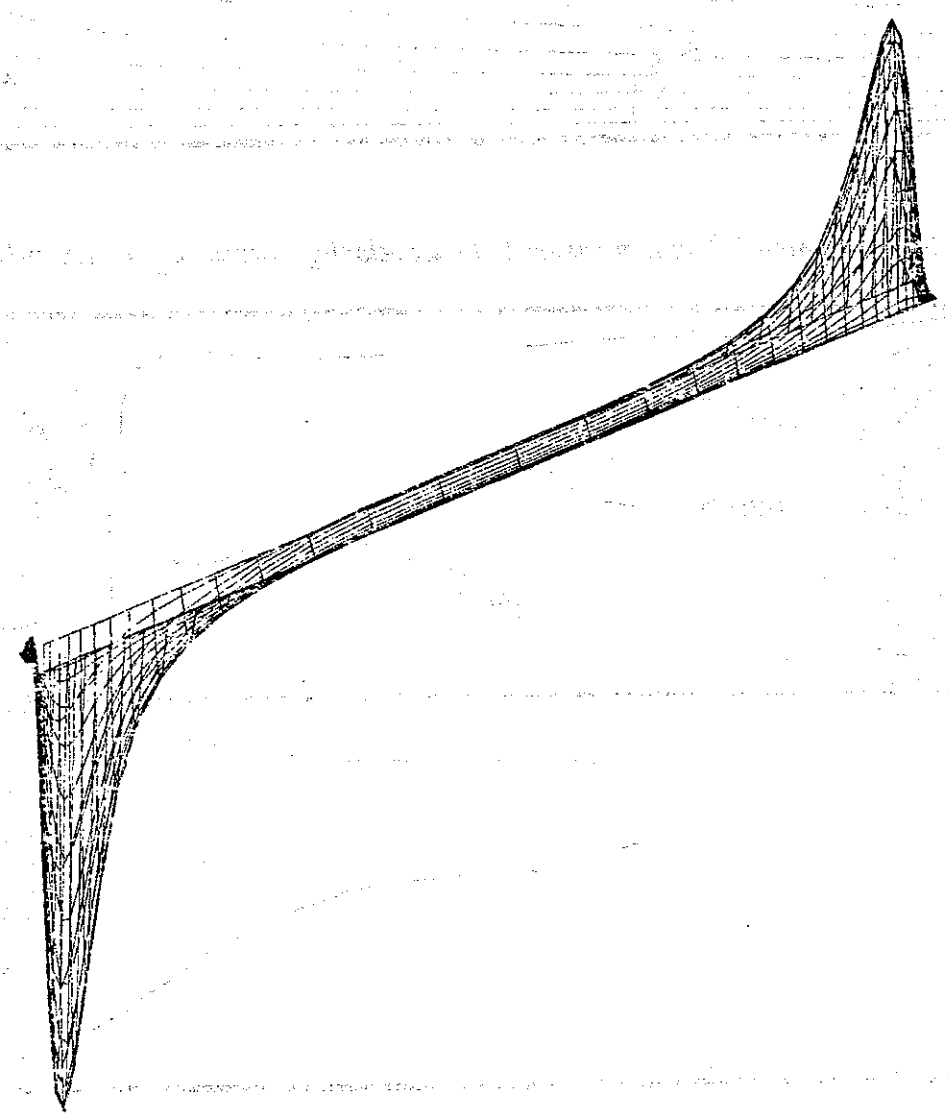

Fig. 8.47b *Streamfunction shown in perspective, u_m = 1.2 m/s, geo.: 1×16 mm.*

where open symbols indicate the measured data and asterisks and cross symbols indicate the calculated data. The straight lines are based on curved fit of the measured data.

For a powerlaw fluid, fully developed laminar flow in straight ducts can be shown to have the relation between mean velocity and pressure drop of

$$-\frac{\partial p}{\partial \xi} = F(n,k,h,H)\cdot u_m^n. \tag{8.6}$$

It is seen from the data that for each geometry F is a constant. The relations between the mean velocity and pressure drop obtained from the curve fits of the measured data are shown in table 8.5. It is seen that the agreement on the measured exponent obtained from pressure drop measurements and the exponent extracted from viscosity measurements is indeed very fine (remember that n was found to be $n = 0.37$ obtained from UCW measurements). The increase of the function F was expected for increasing aspect ratios.

Geomerty (mm)	F–function Pa(s/m)^n	Exponent (–)
4×4	1.49	0.369
3×5.33	1.59	0.379
2×8	2.29	0.363
1×16	5.36	0.369

Table 8.5 *Constants in eq.* (8.6) *obtained from measurements.*

Two set of calculations were made. One set which concentrated on one mean velocity of $u_m = 0.5$ m/s and all the geometries and one which concentrated on one geometry with cross section of 3×5.33 mm. Using eq. (8.2), the Reynolds number for $u_m = 0.5$ m/s is $Re_{n,k} = 15.5$ for the aspect ratio → ∞. This number must be a good approximation for the aspect ratio of 16. Note that Reynolds number increases as unit aspect ratio is approached due to the increase of hydraulic diameter. It is seen that calculated pressure drop (indicated by crosses in fig. 8.48) is slightly lower than those measured, indicating that the constant in

the powerlaw model may be too small. Earlier measurements made at TUD showed that the constant should be $k_{TUD} = 9.6$ Pa·s^n. Calculations with this value showed a slightly higher pressure drop than measured. This indicates that the value of k should be between 8.5 Pa·s^n and 9.6 Pa·s^n. Only the calculations for the set of all geometries show lower values than measured whereas the calculations for the cross section geometry of 3×5.33 mm show high level of agreement for a high fange of velocities. This indicates, that if it is believed that the measurements have been carried out with a too low value of k the 3×5.33 mm duct must be expected to have a slightly greater cross section that stated.

The measured pressure drop in the ducts for $u_m = 0.5$ m/s is shown in table 8.6. The pressure drop is calculated using both the powerlaw model and the CEF–equation showing a slightly higher pressure drop using the powerlaw model than the CEF–equation. This is believed to due to the extra shear thinning arising from the secondary flow.

Geometry	Pressure drop (–bar/m)	
(mm)	Powerlaw	CEF
4×4	1.1077	1.1074
3×5.33	1.2122	1.2117
2×8	1.7149	1.7142
1×16	3.9960	3.9955

Table 8.6 *Calculated pressure drop using the powerlaw model and the CEF–equation.* $u_m = 0.5$ m/s.

Comparing the results from table 8.6 with the results in table 8.7, showing the pressure drop in the duct with cross section 3×5.33 mm for different mean velocities, it is seen that pressure drop using the CEF–equation is also lower than the pressure drop using the powerlaw model for low mean velocities whereas it is higher for high mean velocities. This means that at high velocities the effect of having vortices, which carry high momentum fluid from the center of the duct out near the walls and low momentum fluid from the corners into the middle of the duct, has a greater effect on the pressure losses than the shear thinning effect

from the secondary flow.

Mean velocity (m/s)	Pressure drop (-bar/m)	
	Powerlaw	CEF
0.1	0.66825	0.66814
0.3	1.0035	1.0031
0.5	1.2122	1.2117
1.0	1.5667	1.5661
3.0	2.3525	2.4077
5.0	2.8423	3.1262
10.0	3.6730	4.6986

Table 8.7 *Calculated pressure drop using the powerlaw model and the CEF-equation. Geometry:* 3×5.33 mm.

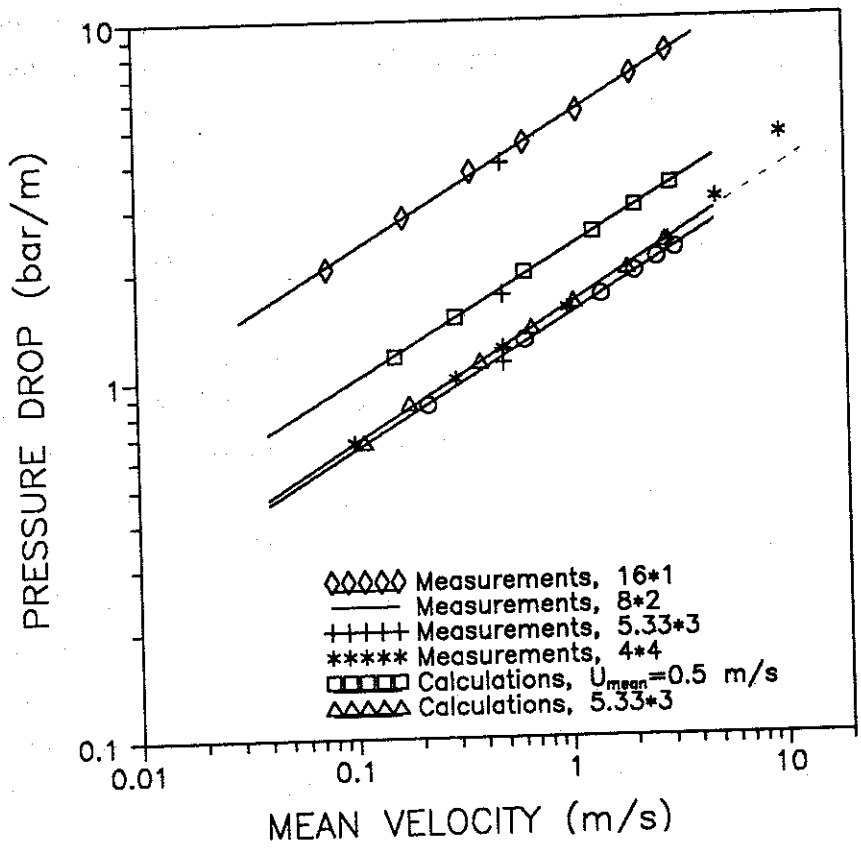

Fig. 8.48 *Measured and calculated pressure drop in straight ducts.*

Since the secondary flow has very little influence on the pressure drop in the parameter range studied the measurements can mainly be used to check that the exponent in the powerlaw is right (it is believed that the exponent is right considering the great accordance of the exponents in table 8.5 and the exponent extracted from the UCW data). Unfortunately it was not possible to measure the pressure drop for high mean velocities, but the significant deviation at high mean velocities between calculated pressure drop and extrapolated pressure drop (indicated by a dashed line) seems to justify that the secondary flow has a significant influence on the pressure drop at high mean velocities. Equation (8.2) gives a Reynolds number of 2040 for $u_m = 10$ m/s, but due to change in hydraulic diameter the Reynolds number is higher, indicating that the computation may be carried out in the transition range, hence these results should be interpreted with caution.

8.5 CLOSURE

Calculated results in straight and curved ducts with moderate and large aspect ratios for the Newtonian fluid water and the Non–Newtonian fluid viscarin have been compared with measurements. The main study has been that of secondary flow due to either curvature effect or non–linear rheology or both.

The incompressible, steady Navier–Stokes equations describe to full extent the "nature" of water, hence the calculated results are believed to be more accurate than the measured results. In curved ducts with water, the well known secondary flow pattern with fluid flowing from the outer wall towards the inner wall along the top and bottom walls and going back into itself flowing from the inner wall to the outer wall in the middle of the duct was seen. This flow pattern is set up through a balance of centrifugal forces, pressure forces, and viscous forces. The influence of secondary flow on primary flow in a fully developed flow change considerably with Reynolds number. At low Reynolds numbers, hardly any influence is observed and the primary flow has the highest values near the inner wall which is expected since the constant pressure gradient in the primary flow direction acts over a shorter distance at the inner wall than at the outer wall. This is also the case at high Reynolds numbers. However, due to influence of the secondary flow high momentum fluid is carried towards the outer wall increasing primary flow here.

In developing flow of water in a curved duct, the secondary flow is set up

very late in the developing phase for low Reynolds numbers whereas it starts early at high Reynolds numbers. Even if the secondary flow starts early, the influence on the primary flow is first seen when the fluid at the center of the duct has been accelerated to its maximum value.

The Non–Newtonian fluid 2% viscarin, showing normal stress differences in a steady simple shear flow, has been simulated for fully developed flow using the CEF–equation as the constitutive equation to give the stress distribution. The second normal stress difference gives rise to secondary flow in the cross plane.

With a negative second normal stress coefficient all the calculations showed that fluid is flowing along the walls towards the corner leaving the corners in order to form two vortices in each quadrant. The two vortices differ in magnitude and size depending on aspect ratio, but at the large aspect ratio of 16 an additional very weak vortex appears giving a total of 12 vortices over the cross section. At unity aspect ratio the two vortices formed in each quadrant take the same size and strength.

In the curved duct, three vortices are found at each half section of the duct with aspect ratio of 16. An extremely small vortex is found close to the inner wall in addition to two larger ones where one is found near the small one and the other one near the outer wall. The vortex near the outer wall has the greatest size.

Comparison of calculated and measured secondary flow in straight ducts shows the same pattern for all geometries, but higher values are calculated than measured. The difference between measured and calculated data are due to great uncertainty of both the measured velocity data and the measured rheology data for the second normal stress difference.

The effect of secondary flow on pressure drop in straight ducts was calculated and found to be negligible. Experiments also showed no significant effect in the range of velocities measured. For high velocities the calculations showed a significant difference between the results obtained using the powerlaw model and the results obtained using the CEF–equation. The measured results were mainly used to check that the exponent used in the powerlaw model for the viscosity was right.

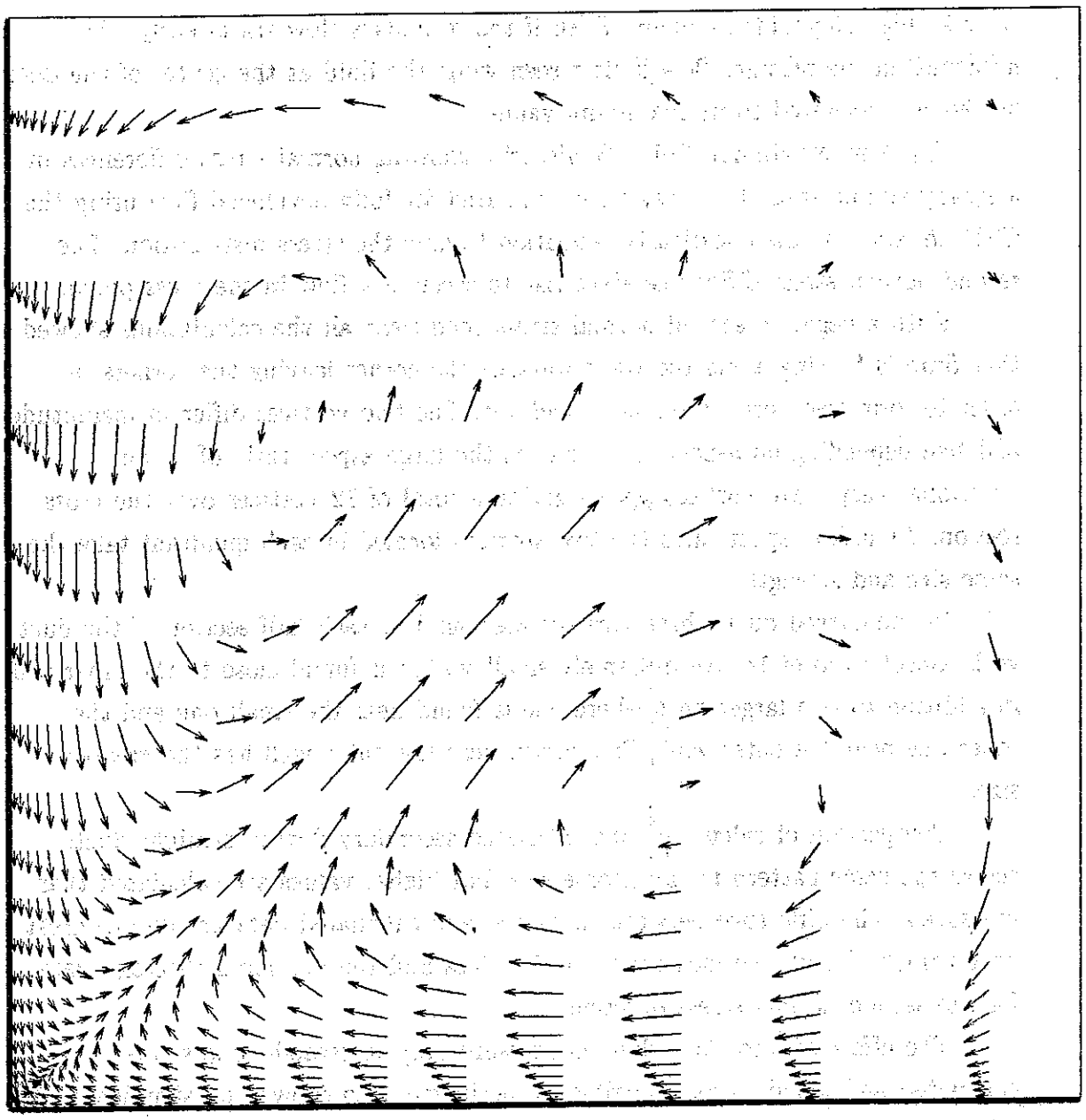

Fig. 8.30a *Velocity vector plot of secondary flow in straight channel, fully developed flow. Geometry: 4×4 mm² (one quarter of the cross section is shown, symmetri condition on 2 sides), Fluid: 2% viscarin.* $u_{mean} = 0.5$ *m/s,* $u_{max} = 0.815$ *m/s,* $v_{max} = 5.02 \times 10^{-3}$ *m/s,* $w_{max} = 4.86 \times 10^{-3}$ *m/s*

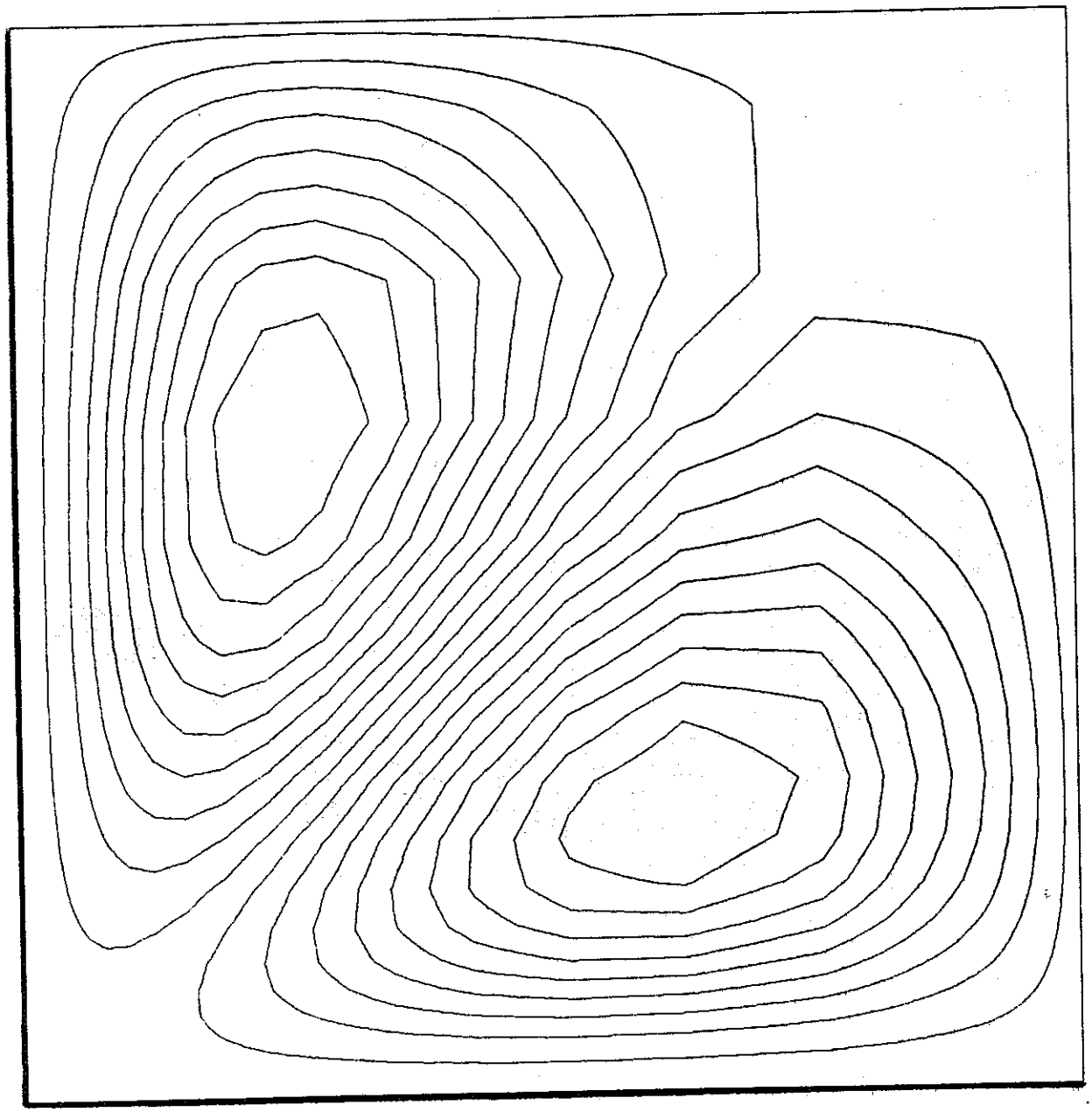

Fig. 8.30b *Streamline plot of secondary flow in straight channel, fully developed flow. Geometry: 4×4 mm² (one quarter of the cross section is shown, symmetri condition on 2 sides), Fluid: 2% viscarin.* $u_{mean} = 0.5$ *m/s,* $\Psi_{max} = 2.11\times10^{-6}$ *m²/s,* $\Psi_{min} = -2.14\times10^{-6}$ *m²/s*

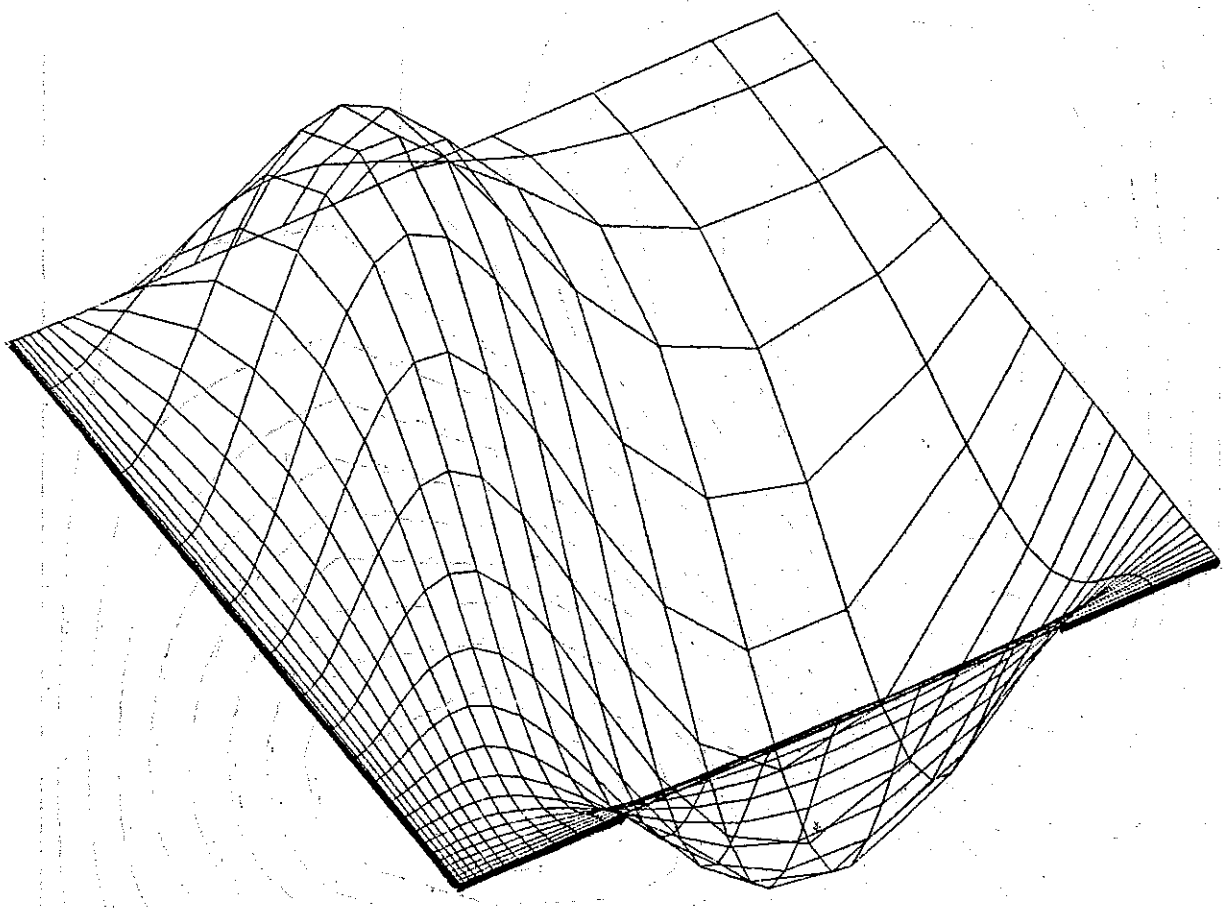

Fig. 8.30c *Conditions as in fig. 8.30b. Plot shown in perspective.*

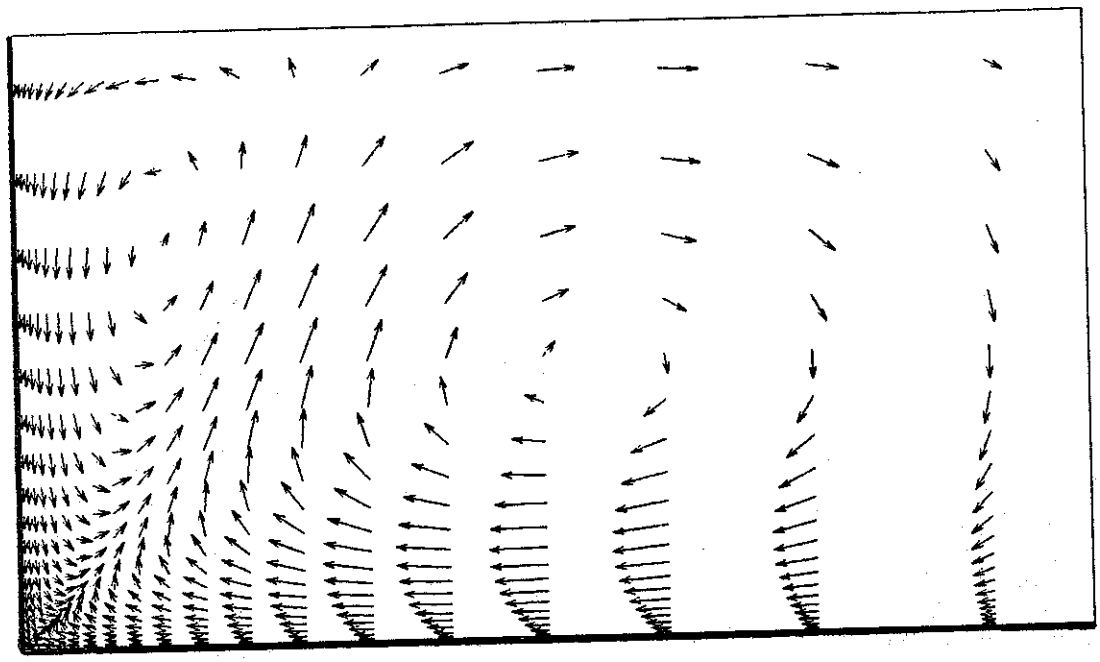

Fig. 8.31a *Velocity vector plot of secondary flow in straight channel, fully developed flow. Geometry: 3×5.33 mm² (one quarter of the cross section is shown, symmetri condition on 2 sides), Fluid: 2% viscarin.* $u_{mean} = 0.5$ *m/s,* $u_{max} = 0.802$ *m/s,* $v_{max} = 6.17\times10^{-3}$ *m/s,* $w_{max} = 7.08\times10^{-3}$ *m/s*

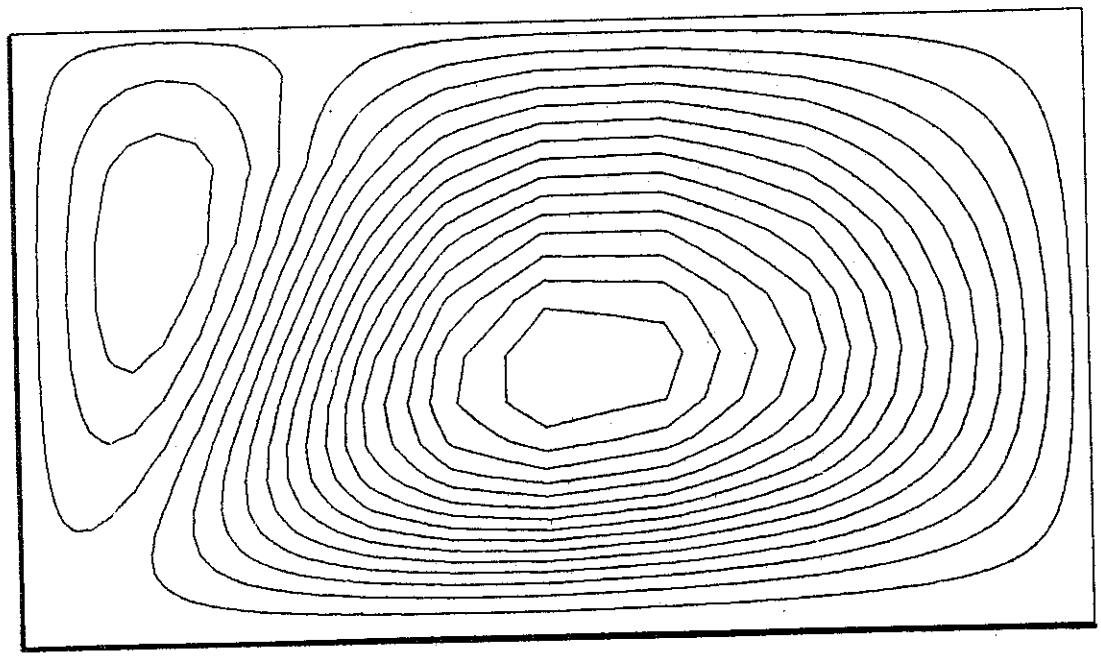

Fig. 8.31b *Streamline plot of secondary flow in straight channel, fully developed flow. Geometry: 3×5.33 mm² (one quarter of the cross section is shown, symmetri condition on 2 sides), Fluid: 2% viscarin.* $u_{mean} = 0.5$ *m/s,* $\Psi_{max} = 8.66\times10^{-7}$ *m²/s,* $\Psi_{min} = -4.10\times10^{-6}$ *m²/s*

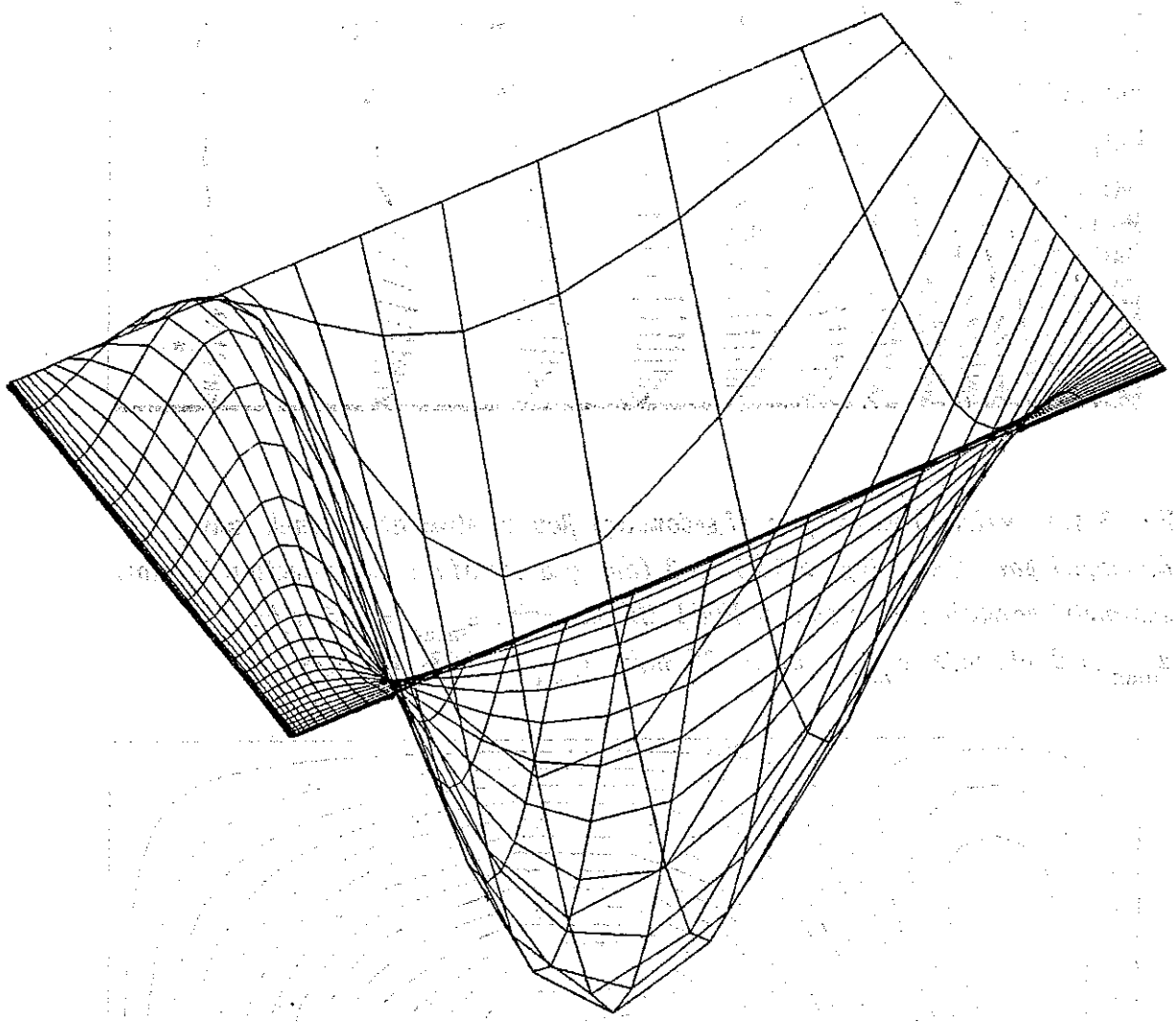

Fig. 8.31c *Conditions as in fig. 8.31b. Plot shown in perspective.*

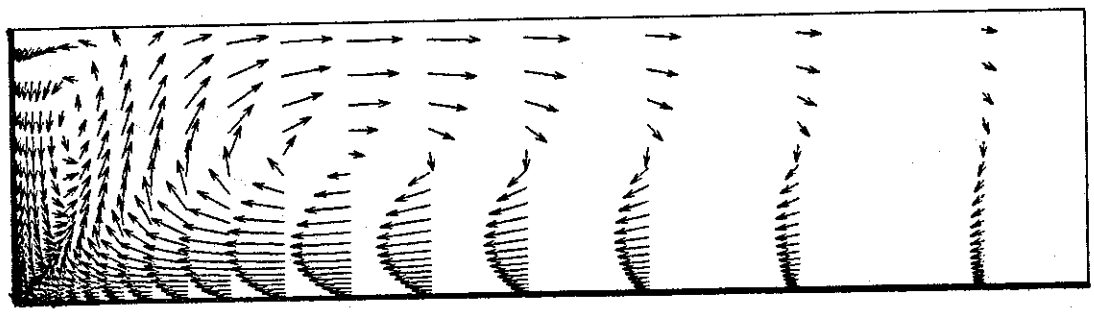

Fig. 8.32a *Velocity vector plot of secondary flow in straight channel, fully developed flow. Geometry: 2×8 mm² (one quarter of the cross section is shown, symmetri condition on 2 sides), Fluid: 2% viscarin.* $u_{mean} = 0.5$ *m/s,* $u_{max} = 0.779$ *m/s,* $v_{max} = 1.02\times10^{-2}$ *m/s,* $w_{max} = 6.44\times10^{-3}$ *m/s*

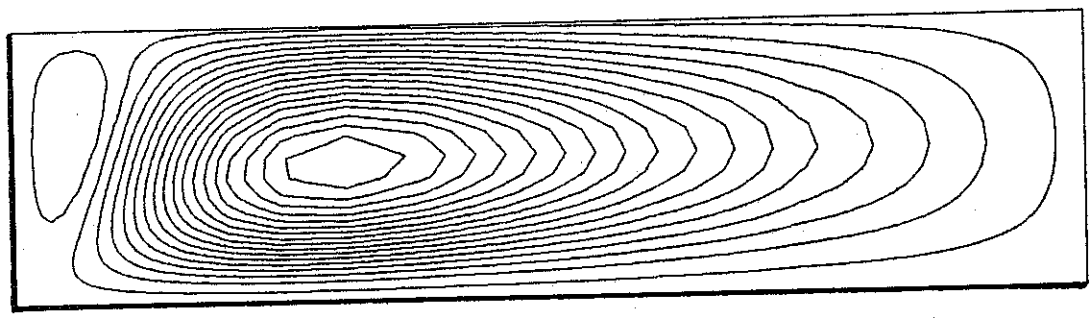

Fig. 8.32b *Streamline plot of secondary flow in straight channel, fully developed flow. Geometry: 2×8 mm² (one quarter of the cross section is shown, symmetri condition on 2 sides), Fluid: 2% viscarin.* $u_{mean} = 0.5$ *m/s,* $\Psi_{max} = 3.20\times10^{-7}$ *m²/s,* $\Psi_{min} = -3.54\times10^{-5}$ *m²/s*

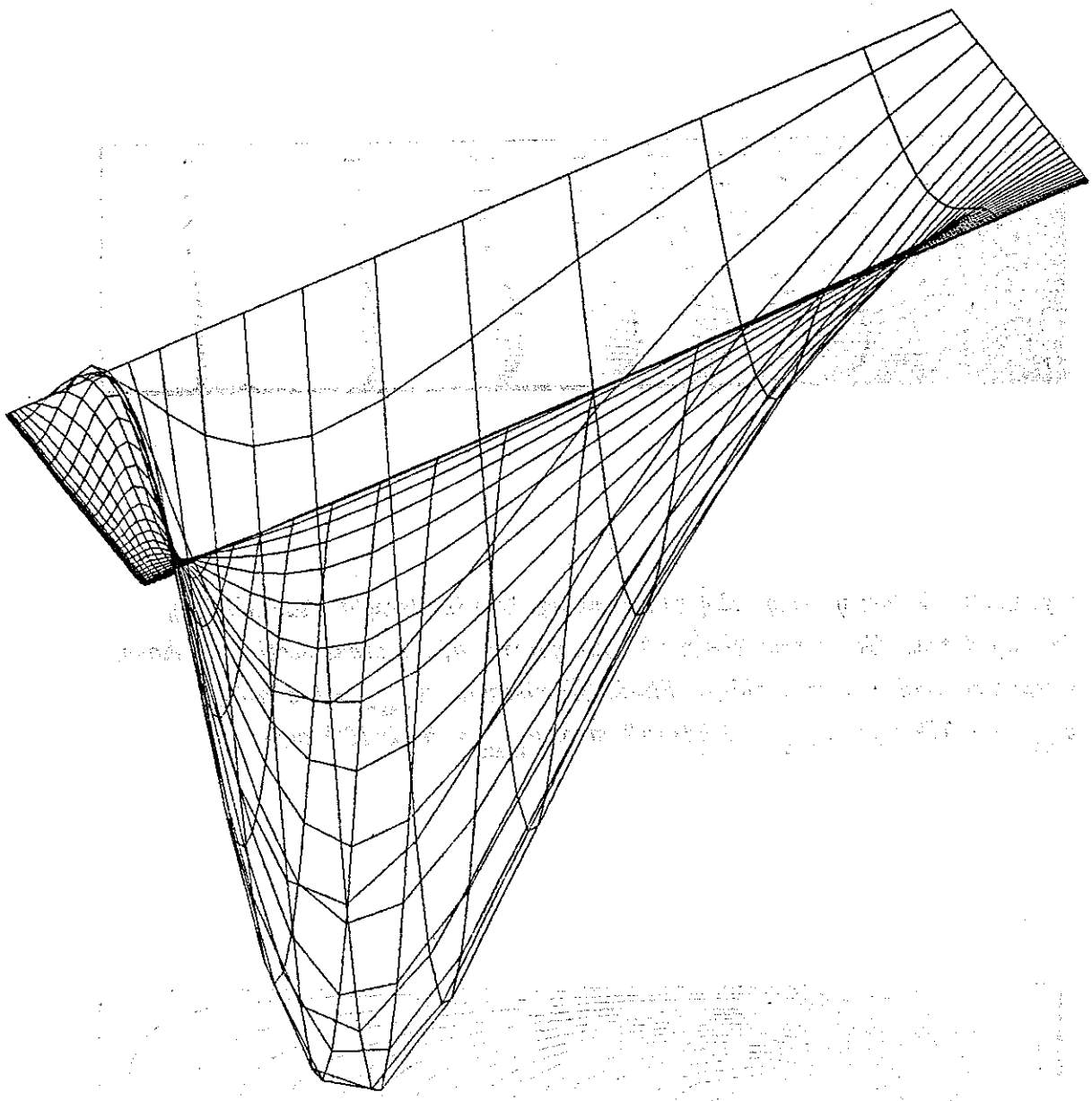

Fig. 8.32c *Conditions as in fig. 8.32b. Plot shown in perspective.*

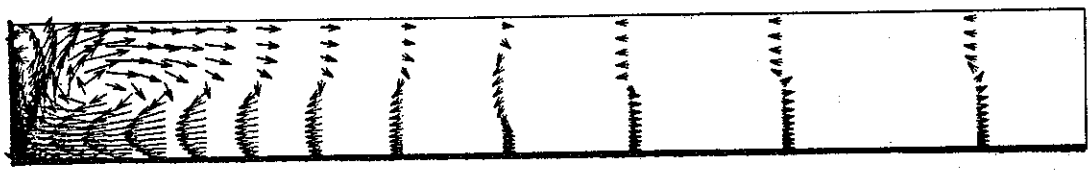

Fig. 8.33a *Velocity vector plot of secondary flow in straight channel, fully developed flow. Geometry: 1×16 mm² (one quarter of the cross section is shown, symmetri condition on 2 sides – the height is scaled 1:2),*
Fluid: 2% viscarin. $u_{mean} = 0.5$ *m/s,* $u_{max} = 0.685$ *m/s,*
$v_{max} = 9.59\times10^{-3}$ *m/s,* $w_{max} = 5.64\times10^{-3}$ *m/s*

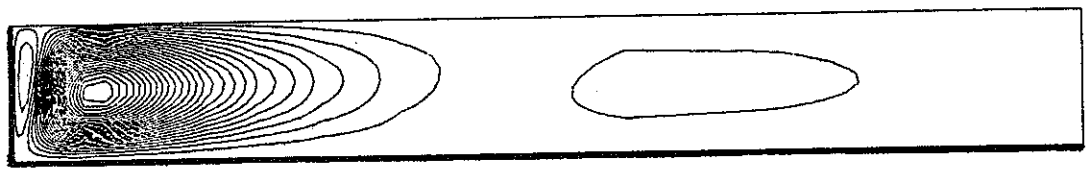

Fig. 8.33b *Streamline plot of secondary flow in straight channel, fully developed flow. Geometry: 1×16 mm² (one quarter of the cross section is shown, symmetri condition on 2 sides – the height is scaled 1:2), Fluid: 2% viscarin.*
$u_{mean} = 0.5$ *m/s,* $\Psi_{max} = 1.37\times10^{-7}$ *m²/s,* $\Psi_{min} = -1.61\times10^{-4}$ *m²/s*

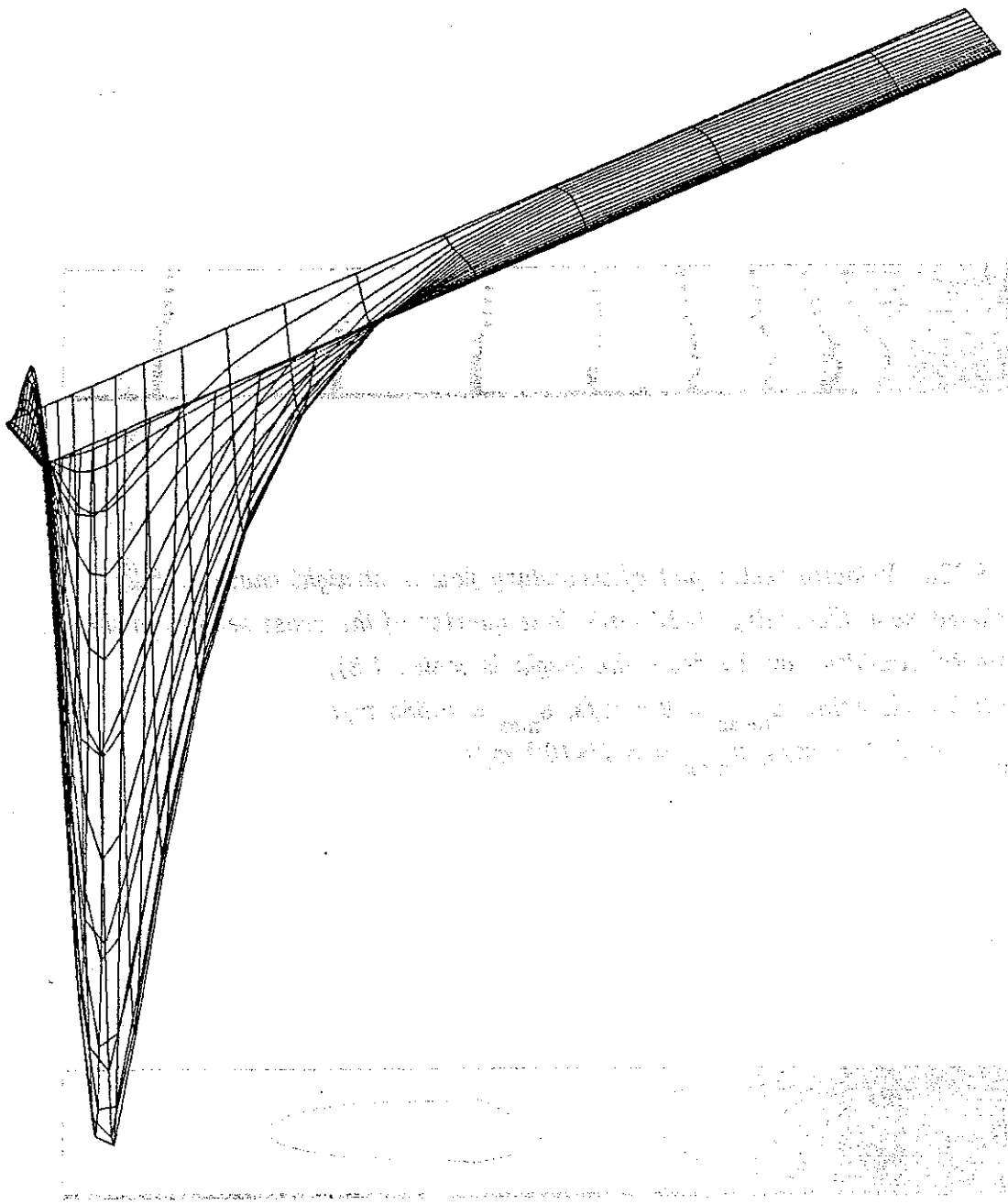

Fig. 8.33c *Conditions as in fig. 8.33b, but without scaling. Plot shown in perspective.*

CHAPTER 9

SUMMARY AND CONCLUSIONS

The prediction of secondary flow due to either curvature effects or non–linear rheology in straight and curved ducts of moderate and large aspect ratios forms a major part of the present work. In addition to the fluid dynamic aspects of the work the numerical part has been aimed towards fast linear solvers for sparce matrix systems.

The fluid dynamic model incorporates the finite volume method combined with an orthogonal curvilinear coordinate formulation of the governing equations in semi–strong conservative form (the developed computer code is based on experience with the ROBOT code developed at Imperial College, London). The fluxes are discretised by finite differences. The orthogonal curvilinear coordinate system employed is general curvilinear orthogonal in two dimensions and cartesian orthogonal in the third. The incompressible, steady Navier–Stokes equations are solved using a velocity–pressure coupling based on the PISO method (Pressure Implicit with Splitting of Operators) which is a predictor–corrector method using two corrector steps to satisfy divergence free velocity field at each outer loop. In order to solve the momentum equations at the predictor level an ADI solver is used. At each corrector level a Poisson type of equation obtained for the pressure–corrector equation has to be solved. A preconditioned conjugate gradient method is used. Several preconditioning matrices were tried and the one used is a relaxed block incomplete Cholesky factorization. Only laminar flows are simulated in ducts having a cross section area of $16 \cdot 10^{-6}$ m^2. The 4 different cross sections considered are 4×4 mm, 3×5.33 mm, 2×8 mm, and 1×16 mm.

In order to handle Non–Newtonian fluids in addition to the Newtonian fluids the CEF–equation is used to obtain the stress distribution in the ducts. The CEF–equation can to full extend describe the stress distribution in a steady simple shear flow for a Non–Newtonian fluid where the stress distribution is described through knowledge of the shear rate dependent viscosity and the first and second normal stress differences. The first and second normal stress coefficients used to describe the normal stress differences are modelled, as the viscosity, by a powerlaw function of the shear rate. In general the CEF–equation can describe the stress distribution whenever the flow is a viscometric flow. Rectilinear shear flow is a type of viscometric flow. It is well known that

pathlines of a Newtonian fluid follow straight lines in a fully developed flow in straight ducts and thus form a rectilinear flow. This is usually not the case for a Non–Newtonian fluid and some secondary flow is to be expected. The presence of secondary flow makes the flow a non–viscometric flow, but due to the small deviation from a rectilinear flow the CEF–equation is used to describe the stress distribution of the Non–Newtonian fluids 2% viscarin investigated.

Results obtained simulating water.

Mainly, the secondary flow in curved ducts using water was studied. The well known pattern of fluid flowing from the outer wall towards the inner wall along the top and bottom walls and going back into itself, flowing from the inner wall to the outer wall in the middle of the duct was seen. This flow pattern is set up through a balance of centrifugal forces, pressure forces, and viscous forces. The influence of secondary flow on primary flow in a fully developed flow changes with Reynolds number. At low Reynolds numbers the pressure gradient in the primary flow direction dominates the flow and the highest values are observed near the inner wall. This is not the case for high Reynolds numbers where the strong increase in secondary flow now is able to move high momentum fluid out towards the outer wall increasing the primary flow here.

In developing flow of water in a curved duct the secondary flow is set up very late in the developing phase for low Reynolds numbers whereas it starts early at high Reynolds numbers. Even if the secondary flow starts early, the influence on the primary flow is first seen when the fluid at center of the duct has been accelerated to its maximum value.

The calculated results have been compared with LDA measurements where fine agreement is observed. It is believed that for the range of velocities simulated the calculated results are more accurate than the measurements.

Results obtained simulating 2% viscarin.

The model fluid used in the simulations of a Non–Newtonian fluid is a polymeric solution of 2% viscarin in water. The model fluid is a suitable substitute for 40% full cream homogenized milk as far as the shear rate dependent viscosity is concerned, but it shows higher normal stress differences than milk.

The second normal stress coefficient is given as a small, negative constant multiplied by the first normal stress coefficient. However, the coefficient is very difficult to measure to a high level of accuracy leaving the secondary flow, which is primarily dependent on the second normal stress coefficient, difficult to calculate accurately.

With the negative second normal stress coefficient all the calculations showed that fluid is flowing along the walls towards the corner leaving the corner in order to form two vortices in each quadrant. The two vortices differ in magnitude and size depending on aspect ratio, but at the large aspect ratio of 16 a additional very weak vortex appears, giving a total of 12 vortices over the cross section. At unity aspect ratio the two vortices formed in each quadrant take the same size and strength. In order to determine the dependence of the second normal stress coefficient on the flow direction the coefficients in the powerlaw of the second normal stress coefficient were altered in order to seen any effect. For high negative values of the exponent in the powerlaw model for the second normal stress coefficient the secondary flow was weakened and the smaller vortex at aspect ratios different from unity became smaller in size. Equating the exponent in the powerlaw model for the viscosity and the second normal stress coefficient made the secondary flow nearly disappear in full agreement with the observations made by Townsend et al (1976). The only way to change the direction of the streamlines was to change the sign of the second normal stress coefficient.

Comparison between the measured and calculated secondary flow show the same pattern, but higher values are calculated than measured. The difference between the measured and calculated data are due to the very high uncertainty of the measured velocity data and, as already mentioned, the uncertainty in measuring the second normal stress difference.

The effect of secondary flow on pressure drop in straight ducts was calculated and found to be negligible. Experiments also showed no significant effect in the range of velocities measured. For high velocities the calculations showed a significant difference between the results obtained using the powerlaw model and the results obtained using the CEF–equation. The measured results were mainly used to check that the exponent used in the powerlaw model for the viscosity was right.

REFERENCES

Ames, W.F., Numerical Methods for Partial Differential Equations, Academic Press, New York, 1977.

Anderson, D.A., Tannehill, J.C., & Pletcher, R.H., Computational Fluid Mechanics and Heat Transfer, Hemisphere, New York, 1984.

Antonopoulos, K., Gosman, A.D., & Issa, R.I., "The ROBOT code for the detailed analysis of three–dimensional turbulent recirculating flow in rod bundles", Department of Mechanical Engineering, Imperial College, London, 1976.

Aris, R., Vectors, Tensors, and the Basic Equations of Fluid Dynamics, Prentice–Hall, Englewood Cliffs, N. J., 1962.

Arpaci, V.S. & Larsen, P.S., Convection Heat Transfer, Prentice–Hall, Englewood Cliffs, New Jersey, 1984.

Axelsson, O., "A General Incomplete Block–Matrix Factorization Method", Linear Algebra and its Applications, 74, 179–190, 1986.

Axelsson, O. & Barker, V.A., Finite Element Solution of Boundary Value Problems, Academic Press, 1984.

Axelsson, O., Brinkkemper, S., & Il'in V.P., "On some version of Incomplete Block–Matrix Factorization Iterative Method", Linear Algebra and its Applications, 58, 3–15, 1984.

Barker, V.A., "Iterative Solution of Singular Systems of Equations Arising from Ergodic Markov Chains", Report No. 366, DCAMM, The Technical University of Denmark, 1987.

Barker, V.A., Personal communication, 1988.

Berge, G., "Numerisk programsystem basert på fleirdimensjonale ortogonale

koordinatar for simulering av forbrenning, masse og varmetransport" (in Norwegian), Ph.D. Thesis, University of Trondheim, 1982.

Berger, S.A., Talbot, L., & Yao, L.S., "Flow in curved pipes", Ann. Rev. Fluid Mech., 15, 461, 1983.

Bird, R.B., Stewart, W.E., & Lightfoot, E.N., Transport Phenomena, Wiley, New York, 1960.

Bird, R.B., Armstrong, R.C., & Hassager, O., Dynamics of Polymeric Liquids, Second Edition, Volume 1, Wiley, 1987.

Brandt, A, "Guide to Multigrid Development" in Multigrid Methods, Proceedings, Koln–Porz, 1981, ed. by W. Hackbusch and U. Trottenberg, Springer, 1982.

Buzbee, B.L., Golub, G.H., & Nielsen, C.W., "On Direct Methods for Solving Poisson's Equations", SIAM J. Numer. Anal., 7, 627–656, 1970.

Carrier, G.F. & Pearson, C.E., Partial Differential Equations, Academic Press, London, 1976.

Cheng, K.C., Nakayama, J., & Akiyama, M., "Effects of Finite and Infinite Aspect Ratios on Flow Patterns in Curved Rectangular Channels", in Flow Visualization, Hemisphere Publ. Corp. & McGraw Hill, 1979, ed. by Asanuma, T.

Christensen, E.M. & Larsen, P.S., Personal communication, 1989.

Coleman, B.D., Markovitz, H., & Noll, W., Viscometric Flows of Non–Newtonian Fluids, Springer, New York, 1966.

Collins, P., Personal communication, 1988.

Concus, P., Golub, G.H., & Meurant, G., "Block Preconditioning for the Conjugate Gradient Method, SIAM J. Sci. Stat. Comput. 6, 220–252, 1985.

Criminale, W.O., Jr., Ericksen, J.L., & Filbey, G.L., Jr., "Steady Shear Flow of Non–Newtonian Fluids", Arch. Rational Mech. Anal., 1, 410–417, 1958.

Crochet, M.J., Davies, A.R., & Walters, K., Numerical Simulation of Non–Newtonian Flow, Elsevier, 1984.

Dodson, A.G., Townsend, P., & Walters, K., "Non–Newtonian Flow in Pipes of Non–Circular Cross Section", Computers and Fluids, 2, 317–338, 1973.

Dorr, Fred W., "The Direct Solution of the Discrete Poisson Equation on a Rectangle", SIAM Review, 12, 248–263, 1970.

Enni, B., Christensen, E.M., & Larsen, P.S., The Fluid Mechanics of Membrane Filtration, Report AFM–MF–P1–87, Dept. of Fluid Mechanics, Techn. Univ. of Denmark, 1987.

Enni, B., Christensen, E.M., & Larsen, P.S., The Fluid Mechanics of Membrane Filtration, Report AFM–MF–P2–87, Dept. of Fluid Mechanics, Techn. Univ. of Denmark, 1987.

Flügge, W., Tensor Analysis and Continuum Mechanics, Springer, 1972.

Fröberg, Carl–Erik, Introduction to Numerical Analusis, Addison–Wesley Publishing Company, Inc., 1965.

Gervang, B., "Solution of Discretised equations", under preparation, 1990.

Golub, G.H. & Van Loan, C.F., Matrix Computations, The Johns Hopkins University Press, 1983.

Gosman, A.D., Pun, W.M., Runchal, A.K., Spalding, D.B., & Wolfstein, M., Heat and Mass Transfer in Recirculation Flows, Academic Press, London, 1969.

Gustafsson, I., "Modified Incomplete Cholesky (MIC) Methods" in Preconditioning Methods, Theory and Applications, (Evans, D.J., ed.). New York, London, Paris: Gordon and Breach Science 1983.

Hageman, L.A. & Young, D.M., Applied Iterative Methods, Academic Press, 1981.

Hansen, C.B., Christensen, E.M., & Larsen, P.S., The Fluid Mechanics of Membrane Filtration, Report AFM–MF–P3–88, Dept. of Fluid Mechanics, Techn. Univ. of Denmark, 1988.

Harlow, F.H. & Welch, J.E., "Numerical Calculatio of Time-dependent Viscous Incompressible Flow of Fluid with Free Surface", The Physics of Fluids, 8, 1965.

Harten, A., Engquist, B., Osher, S., & Chakravarthy, S.R., "Uniformly High Order Accurate Essentially Non–oscillatory Schemes, III", Journal of Computational Physics 71, 231–303, 1987.

Hawkins, G.A. Multilinear Analysis for Students in Engineering and Science, Wiley, 1963.

Hedberg, P.K.M., "NONDIF: A method to avoid numerical diffusion and over– and undershoots", 6th Int. Conf. Numerical Methods in Lam. and Turb. Flow, Swansea, 1989.

Hestenes, M.R. & Stiefel, E., "Methods of Conjugate Gradients for Solving Linear Systems", J. Res. Nat. Bur. Standards Sect. B 49, 409–436, 1952.

Hirsch, C., Numerical Computation of Internal and External Flows, Wiley, 1988

Hockney, R.W., "Rapid Elliptic Solvers" in Numerical Methods in Applied Fluid Dynamics, ed. B. Hunt, 1980.

Humphrey, J.A.C., Taylor, A.M.K., & Whitelaw, J.H., "Laminar flow in a square duct of strong curvature", J. Fluid Mech., 83, part 3, 509–527, 1977.

Issa, R.I., "J. Comput. Phys.", 61, 1985.

Issa, R.I., Gosman, A.D., & Watkins, A.P., "J. Comput. Phys.", 61, 1985.

Jang, D.S., Jetli, R., & Acharya, S., "Numerical Heat Transfer", 10, 1986.

Jennings, Alan, Matrix Computation for Engineers and Scientists, John Wiley & Sons, 1977.

Jonsson, G., "Boundary Layer Phenomena during Ultrafiltration of Dextran and Whey Protein Solutions", Desalination, 51, 61–77, 1984.

Lai, K.Y.M., "Numerical Analysis of Fluid Transport Phenomena", Ph.D. Thesis, University of London, 1983.

Larsen, P.S., Personal communication, 1989.

Latimer, B.R. & Pollard, A., "Numerical Heat Transfer", 8, 1985.

Madsen, R.F., Hyperfiltration and Ultrafiltration in Plate–and–Frame Systems, Elsevier, Amsterdam, 1977.

Meijerink, J.A. & Van der Vorst, H.A., "An iterative Solution Method for Linear Systems of Which the Coefficient Matrix is a Symmetric *M*–matrix", Math. Comput. 31, 148–152, 1977.

Miyake, Y, Kajishima, T., & Inaba, T., "Numerical Experiment of Laminar Flow in Curved Ducts of Rectangular Cross–section", in Experimental Heat Transfer, Fluid Mechanics, and Thermodynamics, Elsevier, 1988, ed. by Shah, R.K., Ganic, E.N., and Yang, K.T.

Morse, P.M. & Feshbach, H., Methods of Theoretical Physics, Mcgraw–Hill, 1953.

Munksgaard, Niels, Solution of General Sparse Symmetric Sets of Linear Equations. Report No. NI–78–02. Institute for Numerical Analysis, Technical University of Denmark, 1978.

Patankar, S.V., Numerical Heat Transfer and Fluid Flow, Hemiphere, Washington, D.C., 1980.

Patankar, S.V. & Spalding, D.B., "A Calculation Procedure for Heat, Mass and Momentum Transfer in Three Dimensional Parabolic Flows", Int. J. Heat Mass Transfer, 15, 1972.

Peaceman D.W. & Rachford H.H.,"The Numerical Solution of Parabolic and Elliptic Differential Equations",SIAM Journal, 3, 1955.

Peric, M., "A Finite–Volume Method for the Prediction of Three–Dimensional Fluid Flow in Complex Ducts", Ph.D. Thesis, University of London, 1985.

Peric, M., Kessler, R., & Scheuerer, G., "Comparison of Finite–volume Numerical Methods with Staggered and Colocated Grids", Computers & Fluids, 16, No 4, 1988.

Prager, W., Introduction to Mechanics of Continua, Ginn, Lexington, Mass., 1961.

Raithby, G.D., "A Critical Evaluation of Upstream Differencing Applied to Problems Involving Fluid Flow", Comp. Meth. Appl. Mech. Eng., 9, 75–103, 1976.

Raithby, G.D., "Skew Upstream Differencing Schemes for Problems Involving Fluid Flow", Comp. Meth. Appl. Mech. Eng., 9, 153–164, 1976.

Raithby, G.D. & Schneider, G.E., "Numerical Solution of Problems in Incompressible Fluid Flow; Treatment of the Velocity–Pressure Coupling", Numerical Heat Transfer, 2, No 2, 1979.

Roache, P.J., Computational Fluid Dynamics, Hermosa Publishers, Albuquerque New Mexico, 1976

Runchal, A.K., "CONDIF: A Modified Central–differencing Scheme with Unconditional Stability and very low Numerical Diffusion", Proceedings of The Eight International Heat Transfer Conference,

San Francisco, 1986.

Schlichting, H., Boundary–Layer Theory, McGraw–Hill, 7 ed., 1979.

Soh, W.Y., "Developing fluid flow in a curved duct of square cross–section and its fully developed dual solutions", J. Fluid Mech., 188, 337–361, 1988.

Soh, W.Y. & Berger, S.A., "Laminar entrance flow in a curved pipe", J. Fluid Mech., 148, 109–135, 1984.

Spalding, D.B., "A Novel Finite–difference Formulation for Differential Expressions Involving both First and Second Derivatives", Int. J. Num. Meth. Eng., 4, 551–559, 1972.

Stewart, G.W., "The convergence of the Method of Conjugate Gradients at Isolated Extreme Points of the Spectrum", Numer. Math., 24, 85–93, 1975.

Stone, H.L., "Iterative Solution of Implicit Approximations of Multidimensional Partial Differential Equations", SIAM J. Numer. Anal., 5, 1968.

Stuben, K. & Trottenberg, U., "Multigrid Methods: Fundamental Algorithms, Model Problem Analysis and Applications" in Multigrid Methods, Proceedings, Koln–Porz, 1981, ed. by W. Hackbusch and U. Trottenberg, Springer, 1982.

Sugiyama, S., Aoi, T., Yamamoto, M., Narisawa, N., & Miyake, Y., "Measurements on Developing Laminar Flow in a Curved Rectangular Duct by Means of LDV" in Experimental Heat Transfer, Fluid Mechanics, and Thermodynamics, Elsevier, 1988, ed. by Shah, R.K., Ganic, E.N., and Yang, K.T.

Swartztrauber, Paul N., "The Methods of Cyclic Reduction, Fourier Analysis and the FACR Algorithm for the Discrete Solution of Poisson's Equation on a Rectangle", SIAM Review, 19, 490–501, 1977.

Sørensen, J.N. & Loc, T.P., "Inflow and Outflow Boundary Conditions for Incompressible, Axisymmetric Flows", 6th Int. Conf. Numerical Methods in Lam. and Turb. Flow, Swansea, 1989.

Taylor, A.M.K.P., Whitelaw, J.H., & Yianneskis, M., " Curved Ducts With Strong Secondary Motion: Velocity Measurements of Developing Laminar and Turbulent Flow", Journal of Fluids Engineering, 104, 1982.

Thiart, G.D., "A Finite Difference Scheme for the Numerical Solution of Fluid Flow and Heat Transfer Problems on Nonstaggered Grids", Proc. Symposium on Computational Fluid Dynamics, S482, CSIR, 1988.

Thiart, G.D., "A New Finite Difference Scheme for the Numerical Solution of Convection–diffusion Problems on Nonstaggered Grids", 6th Int. Conf. Numerical Methods in Lam. and Turb. Flow, Swansea, 1989.

Townsend, P., Waterhouse, W.M., & Walters, K., "Secondary Flows in Pipes of Square Cross–Section and the Measurement of the Second Normal Stress Difference", Journal of Non–Newtonian Fluid Mechanics, 1, 107–123, 1976.

Tsui, Y.Y., "Calculation of Three–dimensional Flow in Motored Engines", Ph.D. Thesis, University of London, 1987.

Van Doormal, J.P. & Raithby, G.D., "Enhancements of the SIMPLE Method for Predicting Incompressible Fluid Flows", Numerical Heat Transfer, 7, 1984.

Walter, K.T. & Larsen, P.S., "The FON–method for the Steady Two–dimensional Navier–Stokes Equations", Computers & Fluids, 9, 365–376, 1981.

Walters, K., Rheometry, Halsted Press, 1975.

Walters, K., Jones, W.M., & Jones, S.H., Contribution to Brite Project, Department of Mathematics, University College of Wales, Aberystwyth, 1987.

APPENDIX A

SCALE FACTORS

In using Gibbs notation to describe the conservation of the transport equations in fluid dynamics, the equations are valid for any coordinate system. Let us define x_1, x_2, and x_3 to be a set of coordinate lines in an orthogonal curvilinear coordinate system with the corresponding unit vectors e_1, e_2, and e_3, which are mutually orthogonal, and let y_1, y_2, and y_3 be the cartesian system with unit vectors i_1, i_2, and i_3, see fig. A1.

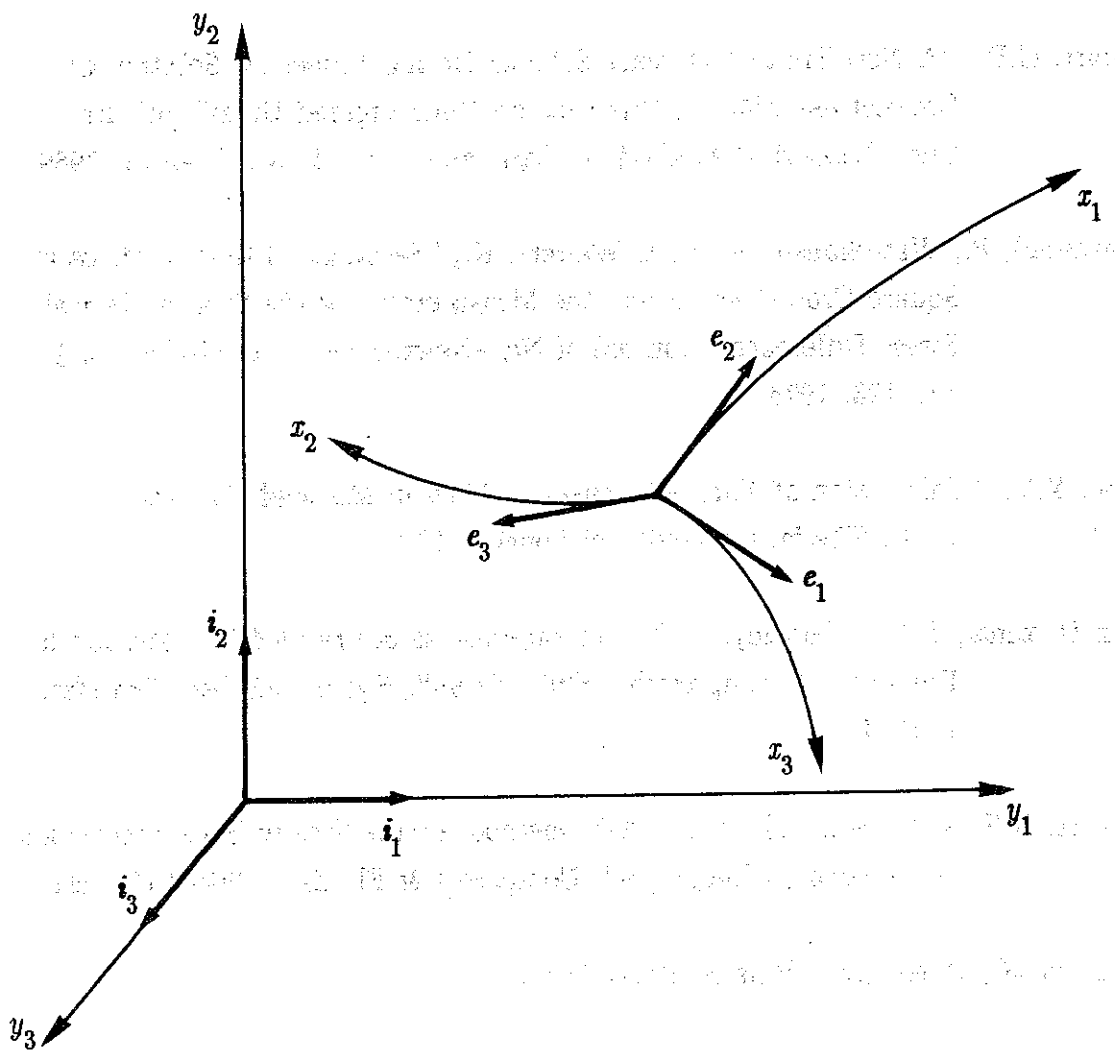

Fig. A1 *Orthogonal curvilinear coordinate system.*

The cartesian coordinates are related to the curvilinear coordinates by the transformation

$$\begin{aligned} y_1 &= y_1(x_1,x_2,x_3) \\ y_2 &= y_2(x_1,x_2,x_3) \\ y_3 &= y_3(x_1,x_2,x_3) \end{aligned} \tag{A1}$$

and if the Jacobian J, see Anderson et al (1984),

$$J = \frac{\partial(y_1,y_2,y_3)}{\partial(x_1,x_2,x_3)}$$

is nonzero, then the inverse transformation exists

$$\begin{aligned} x_1 &= x_1(y_1,y_2,y_3) \\ x_2 &= x_2(y_1,y_2,y_3) \\ x_3 &= x_3(y_1,y_2,y_3). \end{aligned} \tag{A2}$$

The relation between the X–system and the Y–system is given through either eq. (A1) or eq. (A2), but often the scale factors or the metrics are introduced. Let us look at the elemental arc length which in cartesian coordinates are given by

$$(ds)^2 = (dy_1)^2 + (dy_2)^2 + (dy_3)^2. \tag{A3}$$

Differentiation of eq. (A1) takes the form, in matrix notation,

$$\begin{bmatrix} \frac{\partial y_1}{\partial x_1} & \frac{\partial y_1}{\partial x_2} & \frac{\partial y_1}{\partial x_3} \\ \frac{\partial y_2}{\partial x_1} & \frac{\partial y_2}{\partial x_2} & \frac{\partial y_2}{\partial x_3} \\ \frac{\partial y_3}{\partial x_1} & \frac{\partial y_3}{\partial x_2} & \frac{\partial y_3}{\partial x_3} \end{bmatrix} \begin{bmatrix} dx_1 \\ dx_2 \\ dx_3 \end{bmatrix} = \begin{bmatrix} dy_1 \\ dy_2 \\ dy_3 \end{bmatrix}, \tag{A4}$$

where each column represents the components of the "natural" base vectors. The "natural" base vectors are tangential to their coordinate line x_i, and are, as the unit vectors e_1, e_2, and e_3, mutually orthogonal and differ only in length. With the introduction of eq. (A4) in eq. (A3), and using that the

matrix in eq. (A4) is the Jacobian J, the elemental arc length is described in matrix notation as

$$(ds)^2 = (d\boldsymbol{x})^{\mathrm{T}} J^{\mathrm{T}} J (d\boldsymbol{x}), \tag{A5}$$

which takes the form

$$(ds)^2 = (d\boldsymbol{x})^{\mathrm{T}} \begin{bmatrix} h_1^2 & 0 & 0 \\ 0 & h_2^2 & 0 \\ 0 & 0 & h_3^2 \end{bmatrix} d\boldsymbol{x} \tag{A6}$$

or

$$(ds)^2 = (h_1 dx_1)^2 + (h_2 dx_2)^2 + (h_3 dx_3)^2, \tag{A7}$$

where

$$h_1^2 = \left[\frac{\partial y_1}{\partial x_1}\right]^2 + \left[\frac{\partial y_2}{\partial x_1}\right]^2 + \left[\frac{\partial y_3}{\partial x_1}\right]^2,$$

$$h_2^2 = \left[\frac{\partial y_1}{\partial x_2}\right]^2 + \left[\frac{\partial y_2}{\partial x_2}\right]^2 + \left[\frac{\partial y_3}{\partial x_2}\right]^2,$$

$$h_3^2 = \left[\frac{\partial y_1}{\partial x_3}\right]^2 + \left[\frac{\partial y_2}{\partial x_3}\right]^2 + \left[\frac{\partial y_3}{\partial x_3}\right]^2.$$

The metric is given through the scale factors h_1, h_2, and h_3. The off–diagonal elements in the matrix in eq. (A6) are zero because the base vectors are mutually orthogonal. In a non–orthogonal system the off–diagonal elements are in general not zero. The importance of the scale factors can be viewed by looking at the physical distance along a coordinate line.

In general, the distance $\Delta\xi$ between the points with orthogonal curvilinear coordinates x_1, x_2, x_3 and x_1+dx_1, x_2, x_3 is not given by dx_1, but by $\Delta\xi = h_1 dx_1$, where h_1 is a function of the coordinates x_1, x_2, and x_3.

In the following, $\Delta\xi$, $\Delta\eta$, and $\Delta\zeta$ denote the distance in physical dimension of length in the x_1, x_2, and x_3 direction, respectively, and are given by

$$\begin{aligned} \Delta\xi &= h_1 dx_1, \\ \Delta\eta &= h_2 dx_2, \\ \Delta\zeta &= h_3 dx_3. \end{aligned} \tag{A8}$$

The symbol Δ is used instead of d because finite distances are used in practical computation.

The square root of the determinant of J is written h and takes the form

$$h = \sqrt{J} = \sqrt{h_1^2 h_2^2 h_3^2} = h_1 h_2 h_3.$$

In physical dimensions a finite volume is given by

$$\Delta V = h_1 h_2 h_3 dx_1 dx_2 dx_3 = h dx_1 dx_2 dx_3 = \Delta\xi\Delta\eta\Delta\zeta.$$

Physical components of a vector.

As already mentioned, the "natural" base vectors e_i(natural) are tangential to their coordinate line x_i and are defined as

$$e_i(\text{natural}) = \frac{\partial y_j}{\partial x_i} \mathbf{i}_j \tag{A9}$$

Any vector $\boldsymbol{v}$ may then be resolved into components according to

$$\boldsymbol{v} = v^i e_i(\text{natural}). \tag{A10}$$

The components v^i are called the contravariant components and represents then the components of a vector $\boldsymbol{v}$ along the "natural" base vectors.

Another base, the "dual natural" base, represents the base in which e^i(dual) are normal to the coordinate surfaces of constant x_i, and are defined as

$$e^i(\text{dual}) = \frac{\partial x_i}{\partial y_j} \mathbf{i}_j \tag{A11}$$

The components of a vector $\boldsymbol{v}$ resolved into components according to

$$\boldsymbol{v} = v_i \boldsymbol{e}^i(\text{dual}) \tag{A12}$$

are called the covariant components of the vector $\boldsymbol{v}$.

It is seen that the base vectors $\boldsymbol{e}_i(\text{natural})$ and $\boldsymbol{e}^i(\text{dual})$ collapse in an orthogonal system, but do not necessarily have the same length. In non–orthogonal systems the base vectors do not collapse.

In general, the base vectors are normally neither nondimensional, nor unit vectors, and hereby it is seen that neither the contravariant nor the covariant components of a vector $\boldsymbol{v}$ have the same dimension as the vector which is resolved.

In a polar coordinate system, for example, where $x^1 = r$ and $x^2 = \theta$, the first one has the dimension of length and the second one has no dimension. Thus the contravariant velocity components $v^i = dx^i/dt$ would not have the same dimensions. The associated covariant vectors are in no better position. However, to make the components of a vector $\boldsymbol{v}$ have the same dimensions as $\boldsymbol{v}$ itself, we write

$$|\boldsymbol{v}|^2 = (h_1 v^1)^2 + (h_2 v^2)^2 + (h_3 v^3)^2 \tag{A13}$$

where $h_i v^i$ have the same physical dimensions as the magnitude of the vector $\boldsymbol{v}$. Equation (A13) is evidently given by Pythagoros' theorem (it is the counterpart to eq. (A7)). The components $h_i v^i$ are called the physical components of a vector $\boldsymbol{v}$ and the components are written $v(i)$ in order to distinguish them from the contravariant and covariant components. With the physical components $v(i)$ a vector $\boldsymbol{v}$ may be resolved as

$$\boldsymbol{v} = v(1)\boldsymbol{e}_1 + v(2)\boldsymbol{e}_2 + v(3)\boldsymbol{e}_3, \tag{A14}$$

where $\boldsymbol{e}_i$ are the unit contravariant nondimensional base vectors and according to eq. (A13) and eq. (A14) they are obtained as

$$\boldsymbol{e}_i = \boldsymbol{e}_i(\text{natural})/h_i \qquad \text{(no summation)}. \tag{A15}$$

In eq. (A13) the contravariant components were used, but if the covarient components were used the physical components would be given by

$$v(i) = \frac{v_i}{h_i} \qquad \text{(no summation)} \qquad \text{(A16)}$$

and the nondimensional unit base vectors through

$$e^i = e^i(\text{dual})h_i \qquad \text{(no summation).} \qquad \text{(A17)}$$

Since the base vectors $e_i(\text{natural})$ and $e^i(\text{dual})$ collapse in an orthogonal curvilinear coordinate system and only differ in length it is convenient to work with the unit base vectors e_i (= e^i for an orthogonal system) which resolve all vectors in physical components, see fig. A2 for the geometrical representation of contravariant base vectors and covariant base vectors.

A more thorough description of tensor algebra may be found in books by Aris (1962), Hawkins (1963), and Flügge (1972).

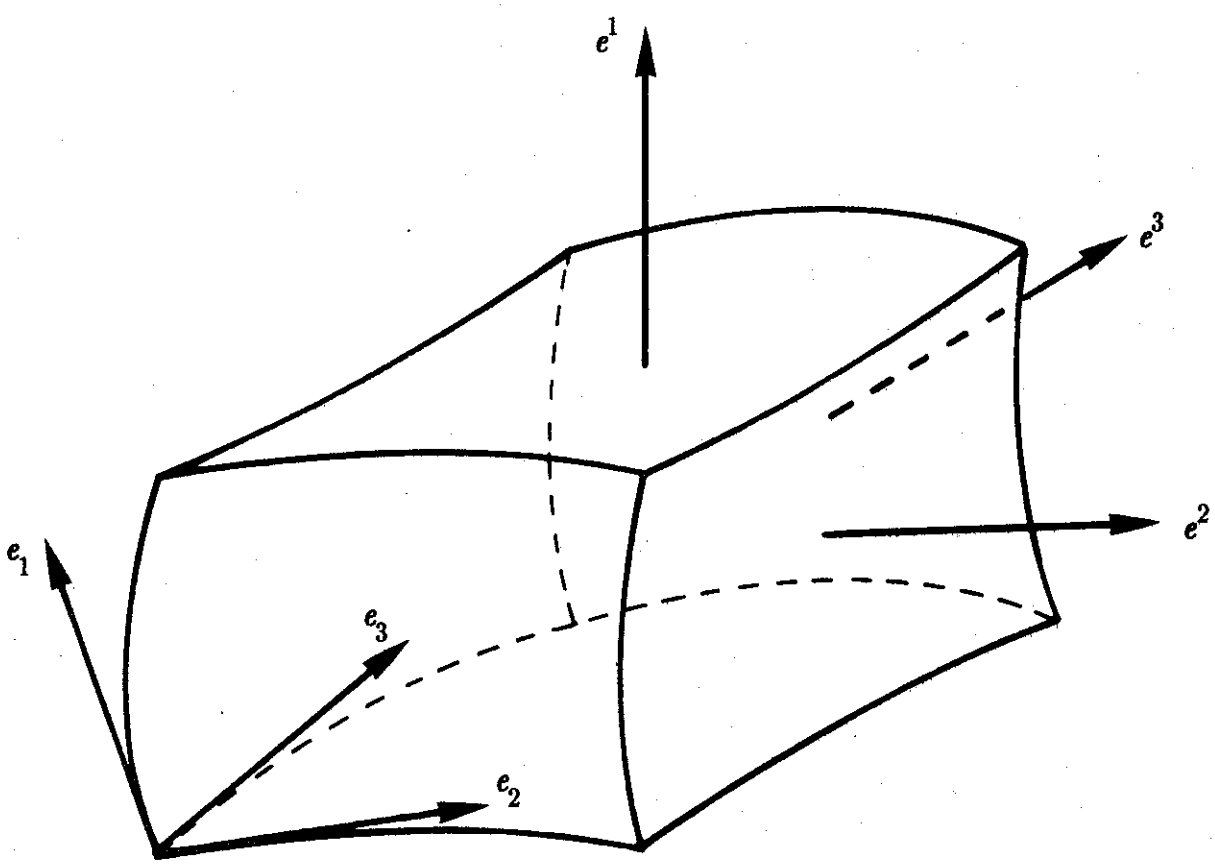

Fig. A2 *Geometrical representation of contravariant base vectors* (e_i) *and covariant base vectors* (e^i).

APPENDIX B

COMPONENTS OF THE CEF-MODEL

The extra-stress tensor in the CEF-equation in chapter 2 was given by

$$\tau = -\eta(\dot{\gamma})\dot{\gamma} + \tfrac{1}{2}\Psi_1(\dot{\gamma})\overset{\Delta}{\dot{\gamma}} - (\Psi_1 - \Psi_2)\{\dot{\gamma}\cdot\dot{\gamma}\} \tag{B1}$$

where $\dot{\gamma}$ is given by eq. (2.18), and

$$\overset{\Delta}{\dot{\gamma}} = \frac{D}{Dt}\dot{\gamma} + \{(\nabla v)^{\mathrm{T}}\cdot\dot{\gamma} + \dot{\gamma}\cdot(\nabla v)\}.$$

The components of the second and third terms will be outlined where, in the general transport equation, they will appear as expressions in the source term.

The second term, assuming steady state, is given by

$$\tfrac{1}{2}\Psi_1\overset{\Delta}{\dot{\gamma}}_{ik} = \tfrac{1}{2}\Psi_1\Big\{v(j)\Big[\frac{\partial^2 v(i)}{\partial x_j \partial x_k} + \frac{\partial^2 v(k)}{\partial x_j \partial x_i}\Big] + 2\frac{\partial v(j)}{\partial x_k}\frac{\partial v(j)}{\partial x_i} + \frac{\partial v(j)}{\partial x_i}\frac{\partial v(k)}{\partial x_j} + \frac{\partial v(j)}{\partial x_k}\frac{\partial v(i)}{\partial x_j}\Big\}, \tag{B2}$$

where each component of the tensor $\dot{\gamma}_2$ takes the form

$$\tfrac{1}{2}\Psi_1\overset{\Delta}{\dot{\gamma}}_{11} = \tfrac{1}{2}\Psi_1\Big\{2v(1)\frac{\partial^2 v(1)}{\partial x_1 \partial x_1} + 2v(2)\frac{\partial^2 v(1)}{\partial x_2 \partial x_1} + 2v(3)\frac{\partial^2 v(1)}{\partial x_3 \partial x_1} + 4\frac{\partial v(1)}{\partial x_1}\frac{\partial v(1)}{\partial x_1} + 2\frac{\partial v(2)}{\partial x_1}\frac{\partial v(2)}{\partial x_1} + 2\frac{\partial v(3)}{\partial x_1}\frac{\partial v(3)}{\partial x_1} + 2\frac{\partial v(2)}{\partial x_1}\frac{\partial v(1)}{\partial x_2} + 2\frac{\partial v(3)}{\partial x_1}\frac{\partial v(1)}{\partial x_3}\Big\},$$

$$\tfrac{1}{2}\Psi_1\overset{\Delta}{\dot{\gamma}}_{12} = \tfrac{1}{2}\Psi_1\Big\{v(1)\Big[\frac{\partial^2 v(1)}{\partial x_1 \partial x_2} + \frac{\partial^2 v(2)}{\partial x_1 \partial x_1}\Big] + v(2)\Big[\frac{\partial^2 v(1)}{\partial x_2 \partial x_2} + \frac{\partial^2 v(2)}{\partial x_2 \partial x_1}\Big] + v(3)\Big[\frac{\partial^2 v(1)}{\partial x_3 \partial x_2} + \frac{\partial^2 v(2)}{\partial x_3 \partial x_1}\Big] + 3\frac{\partial v(1)}{\partial x_2}\frac{\partial v(1)}{\partial x_1} + 3\frac{\partial v(2)}{\partial x_2}\frac{\partial v(2)}{\partial x_1} +$$

$$2\frac{\partial v(3)}{\partial x_2}\frac{\partial v(3)}{\partial x_1} + \frac{\partial v(1)}{\partial x_1}\frac{\partial v(2)}{\partial x_1} + \frac{\partial v(3)}{\partial x_1}\frac{\partial v(2)}{\partial x_3} + \frac{\partial v(2)}{\partial x_2}\frac{\partial v(1)}{\partial x_2} +$$

$$\frac{\partial v(3)}{\partial x_2}\frac{\partial v(1)}{\partial x_3}\Big\},$$

$$\tfrac{1}{2}\Psi_1\overset{\Delta}{\dot{\gamma}}_{13} = \tfrac{1}{2}\Psi_1\Big\{v(1)\Big[\frac{\partial^2 v(1)}{\partial x_1\partial x_3} + \frac{\partial^2 v(3)}{\partial x_1\partial x_1}\Big] + v(2)\Big[\frac{\partial^2 v(1)}{\partial x_2\partial x_3} + \frac{\partial^2 v(3)}{\partial x_2\partial x_1}\Big] +$$

$$v(3)\Big[\frac{\partial^2 v(1)}{\partial x_3\partial x_3} + \frac{\partial^2 v(3)}{\partial x_3\partial x_1}\Big] + 3\frac{\partial v(1)}{\partial x_3}\frac{\partial v(1)}{\partial x_1} + 2\frac{\partial v(2)}{\partial x_3}\frac{\partial v(2)}{\partial x_1} +$$

$$3\frac{\partial v(3)}{\partial x_3}\frac{\partial v(3)}{\partial x_1} + \frac{\partial v(1)}{\partial x_1}\frac{\partial v(3)}{\partial x_1} + \frac{\partial v(2)}{\partial x_1}\frac{\partial v(3)}{\partial x_2} + \frac{\partial v(2)}{\partial x_3}\frac{\partial v(1)}{\partial x_2} +$$

$$\frac{\partial v(3)}{\partial x_3}\frac{\partial v(1)}{\partial x_3}\Big\},$$

$$\tfrac{1}{2}\Psi_1\overset{\Delta}{\dot{\gamma}}_{21} = \tfrac{1}{2}\Psi_1\overset{\Delta}{\dot{\gamma}}_{12},$$

$$\tfrac{1}{2}\Psi_1\overset{\Delta}{\dot{\gamma}}_{22} = \tfrac{1}{2}\Psi_1\Big\{2v(1)\frac{\partial^2 v(2)}{\partial x_1\partial x_2} + 2v(2)\frac{\partial^2 v(2)}{\partial x_2\partial x_2} + 2v(3)\frac{\partial^2 v(2)}{\partial x_3\partial x_2} + 2\frac{\partial v(1)}{\partial x_2}\frac{\partial v(1)}{\partial x_2} +$$

$$4\frac{\partial v(2)}{\partial x_2}\frac{\partial v(2)}{\partial x_2} + 2\frac{\partial v(3)}{\partial x_2}\frac{\partial v(3)}{\partial x_2} + 2\frac{\partial v(1)}{\partial x_2}\frac{\partial v(2)}{\partial x_1} + 2\frac{\partial v(3)}{\partial x_2}\frac{\partial v(2)}{\partial x_3}\Big\},$$

$$\tfrac{1}{2}\Psi_1\overset{\Delta}{\dot{\gamma}}_{23} = \tfrac{1}{2}\Psi_1\Big\{v(1)\Big[\frac{\partial^2 v(2)}{\partial x_1\partial x_3} + \frac{\partial^2 v(3)}{\partial x_1\partial x_2}\Big] + v(2)\Big[\frac{\partial^2 v(2)}{\partial x_2\partial x_3} + \frac{\partial^2 v(3)}{\partial x_2\partial x_2}\Big] +$$

$$v(3)\Big[\frac{\partial^2 v(2)}{\partial x_3\partial x_3} + \frac{\partial^2 v(3)}{\partial x_3\partial x_2}\Big] + 2\frac{\partial v(1)}{\partial x_3}\frac{\partial v(1)}{\partial x_2} + 3\frac{\partial v(2)}{\partial x_3}\frac{\partial v(2)}{\partial x_2} +$$

$$3\frac{\partial v(3)}{\partial x_3}\frac{\partial v(3)}{\partial x_2} + \frac{\partial v(1)}{\partial x_2}\frac{\partial v(3)}{\partial x_1} + \frac{\partial v(2)}{\partial x_2}\frac{\partial v(3)}{\partial x_2} + \frac{\partial v(1)}{\partial x_3}\frac{\partial v(2)}{\partial x_1} +$$

$$\frac{\partial v(3)}{\partial x_3}\frac{\partial v(2)}{\partial x_3}\Big\},$$

$$\tfrac{1}{2}\Psi_1\overset{\Delta}{\dot{\gamma}}_{31} = \tfrac{1}{2}\Psi_1\overset{\Delta}{\dot{\gamma}}_{13},$$

$$\tfrac{1}{2}\Psi_1 \overset{\Delta}{\dot{\gamma}}_{32} = \tfrac{1}{2}\Psi_1 \overset{\Delta}{\dot{\gamma}}_{23},$$

$$\tfrac{1}{2}\Psi_1 \overset{\Delta}{\dot{\gamma}}_{33} = \tfrac{1}{2}\Psi_1\Big\{2v(1)\frac{\partial^2 v(3)}{\partial x_1 \partial x_3} + 2v(2)\frac{\partial^2 v(3)}{\partial x_2 \partial x_3}\, 2v(3)\frac{\partial^2 v(3)}{\partial x_3 \partial x_3} + 2\frac{\partial v(1)}{\partial x_3}\,\frac{\partial v(1)}{\partial x_3} +$$

$$2\frac{\partial v(2)}{\partial x_3}\,\frac{\partial v(2)}{\partial x_3} + 4\frac{\partial v(3)}{\partial x_3}\,\frac{\partial v(3)}{\partial x_3} + 2\frac{\partial v(1)}{\partial x_3}\,\frac{\partial v(3)}{\partial x_1} + 2\frac{\partial v(2)}{\partial x_3}\,\frac{\partial v(3)}{\partial x_2}\Big\}.$$

The third term is given by

$$(\Psi_1 - \Psi_2)\{\dot{\gamma}_{ij}\dot{\gamma}_{jk}\} = (\Psi_1 - \Psi_2)\Big\{\frac{\partial v(j)}{\partial x_k}\,\frac{\partial v(i)}{\partial x_j} + \frac{\partial v(i)}{\partial x_j}\,\frac{\partial v(k)}{\partial x_j} + \frac{\partial v(j)}{\partial x_k}\,\frac{\partial v(j)}{\partial x_i} + \frac{\partial v(j)}{\partial x_i}\,\frac{\partial v(k)}{\partial x_j}\Big\}, \tag{B3}$$

and each component of the tensor takes the form

$$(\Psi_1 - \Psi_2)\{\dot{\gamma}_{1j}\dot{\gamma}_{j1}\} = (\Psi_1 - \Psi_2)\Big\{4\frac{\partial v(1)}{\partial x_1}\,\frac{\partial v(1)}{\partial x_1} + 2\frac{\partial v(2)}{\partial x_1}\,\frac{\partial v(1)}{\partial x_2} +$$

$$2\frac{\partial v(3)}{\partial x_1}\,\frac{\partial v(1)}{\partial x_3} + \frac{\partial v(1)}{\partial x_2}\,\frac{\partial v(1)}{\partial x_2} + \frac{\partial v(1)}{\partial x_3}\,\frac{\partial v(1)}{\partial x_3} +$$

$$\frac{\partial v(2)}{\partial x_1}\,\frac{\partial v(2)}{\partial x_1} + \frac{\partial v(3)}{\partial x_1}\,\frac{\partial v(3)}{\partial x_1}\Big\},$$

$$(\Psi_1 - \Psi_2)\{\dot{\gamma}_{1j}\dot{\gamma}_{j2}\} = (\Psi_1 - \Psi_2)\Big\{2\frac{\partial v(1)}{\partial x_2}\,\frac{\partial v(1)}{\partial x_1} + 2\frac{\partial v(2)}{\partial x_2}\,\frac{\partial v(1)}{\partial x_2} +$$

$$\frac{\partial v(3)}{\partial x_2}\,\frac{\partial v(1)}{\partial x_3} + 2\frac{\partial v(1)}{\partial x_1}\,\frac{\partial v(2)}{\partial x_1} + \frac{\partial v(1)}{\partial x_3}\,\frac{\partial v(2)}{\partial x_3} +$$

$$2\frac{\partial v(2)}{\partial x_2}\,\frac{\partial v(2)}{\partial x_1} + \frac{\partial v(3)}{\partial x_2}\,\frac{\partial v(3)}{\partial x_1} + \frac{\partial v(3)}{\partial x_1}\,\frac{\partial v(2)}{\partial x_3}\Big\},$$

$$(\Psi_1 - \Psi_2)\{\dot{\gamma}_{1j}\dot{\gamma}_{j3}\} = (\Psi_1 - \Psi_2)\Big\{2\frac{\partial v(1)}{\partial x_3}\,\frac{\partial v(1)}{\partial x_1} + \frac{\partial v(2)}{\partial x_3}\,\frac{\partial v(1)}{\partial x_2} +$$

$$2\frac{\partial v(3)}{\partial x_3}\frac{\partial v(1)}{\partial x_3} + 2\frac{\partial v(1)}{\partial x_1}\frac{\partial v(3)}{\partial x_1} + \frac{\partial v(1)}{\partial x_2}\frac{\partial v(3)}{\partial x_2} +$$

$$\frac{\partial v(2)}{\partial x_3}\frac{\partial v(2)}{\partial x_1} + 2\frac{\partial v(3)}{\partial x_3}\frac{\partial v(3)}{\partial x_1} + \frac{\partial v(2)}{\partial x_1}\frac{\partial v(3)}{\partial x_2}\Big\},$$

$$(\Psi_1 - \Psi_2)\{\dot\gamma_{2j}\dot\gamma_{j1}\} = (\Psi_1 - \Psi_2)\{\dot\gamma_{1j}\dot\gamma_{j2}\},$$

$$(\Psi_1 - \Psi_2)\{\dot\gamma_{2j}\dot\gamma_{j2}\} = (\Psi_1 - \Psi_2)\Big\{2\frac{\partial v(1)}{\partial x_2}\frac{\partial v(2)}{\partial x_1} + 4\frac{\partial v(2)}{\partial x_2}\frac{\partial v(2)}{\partial x_2} +$$

$$2\frac{\partial v(3)}{\partial x_2}\frac{\partial v(2)}{\partial x_3} + \frac{\partial v(2)}{\partial x_1}\frac{\partial v(2)}{\partial x_1} + \frac{\partial v(2)}{\partial x_3}\frac{\partial v(2)}{\partial x_3} +$$

$$\frac{\partial v(1)}{\partial x_2}\frac{\partial v(1)}{\partial x_2} + \frac{\partial v(3)}{\partial x_2}\frac{\partial v(3)}{\partial x_2}\Big\},$$

$$(\Psi_1 - \Psi_2)\{\dot\gamma_{2j}\dot\gamma_{j3}\} = (\Psi_1 - \Psi_2)\Big\{\frac{\partial v(1)}{\partial x_3}\frac{\partial v(2)}{\partial x_1} + 2\frac{\partial v(2)}{\partial x_3}\frac{\partial v(2)}{\partial x_2} +$$

$$2\frac{\partial v(3)}{\partial x_3}\frac{\partial v(2)}{\partial x_3} + \frac{\partial v(2)}{\partial x_1}\frac{\partial v(3)}{\partial x_1} + 2\frac{\partial v(2)}{\partial x_2}\frac{\partial v(3)}{\partial x_2} +$$

$$\frac{\partial v(1)}{\partial x_3}\frac{\partial v(1)}{\partial x_2} + 2\frac{\partial v(3)}{\partial x_3}\frac{\partial v(3)}{\partial x_2} + \frac{\partial v(1)}{\partial x_2}\frac{\partial v(3)}{\partial x_1}\Big\},$$

$$(\Psi_1 - \Psi_2)\{\dot\gamma_{3j}\dot\gamma_{j1}\} = (\Psi_1 - \Psi_2)\{\dot\gamma_{1j}\dot\gamma_{j3}\},$$

$$(\Psi_1 - \Psi_2)\{\dot\gamma_{3j}\dot\gamma_{j2}\} = (\Psi_1 - \Psi_2)\{\dot\gamma_{2j}\dot\gamma_{j3}\},$$

$$(\Psi_1 - \Psi_2)\{\dot\gamma_{3j}\dot\gamma_{j3}\} = (\Psi_1 - \Psi_2)\Big\{2\frac{\partial v(1)}{\partial x_3}\frac{\partial v(3)}{\partial x_1} + 2\frac{\partial v(2)}{\partial x_3}\frac{\partial v(3)}{\partial x_2} +$$

$$4\frac{\partial v(3)}{\partial x_3}\frac{\partial v(3)}{\partial x_3} + \frac{\partial v(3)}{\partial x_1}\frac{\partial v(3)}{\partial x_1} + \frac{\partial v(3)}{\partial x_2}\frac{\partial v(3)}{\partial x_2} +$$

$$\frac{\partial v(1)}{\partial x_3}\frac{\partial v(1)}{\partial x_3} + \frac{\partial v(2)}{\partial x_3}\frac{\partial v(2)}{\partial x_3}\Big\}.$$

APPENDIX C

ACCURACY OF PISO

This appendix follows the analysis made by Issa (1985)

In the following, the accuracy during each time step will be examined for a fixed spatial discretisation, based on a Taylor series analysis. The error on each level will be described as ϵ_u^k and ϵ_p^k for the velocity and pressure, respectively. ϵ_u^k is taken as

$$\epsilon_u^k = u_i^{n+1} - u_i^k, \tag{C1}$$

where k takes one of the values $*$, $**$, $***$ and ϵ_p^k is taken as

$$\epsilon_p^k = p^{n+1} - p^k, \tag{C2}$$

where k takes one of the values n, $*$, $**$.

The error at each level in a time step is estimated from the difference between the momentum and pressure fields at time step $n+1$ and the momentum and pressure fields at each intermediate level. The momentum equation at time step $n+1$ is given by eq. (5.14). A specific pressure equation at the same time step is given below.

The pressure at time step $n+1$ will be derived using eq. (5.14) and the discretised continuity equation. Using the momentum equation, eq. (5.14), as the u–momentum at the east face of a main grid volume, eq. (5.14) takes the form

$$\tilde{a}_p u_e^{n+1} = H_e^{n+1} + A_e(p_P - p_E)^{n+1} + b_e + f u_e^n, \tag{C3}$$

which can be written as

$$(\rho A u)_e^{n+1} = \tilde{H}_e^{n+1} + \tilde{A}_e(p_P - p_E)^{n+1} + \tilde{b}_e + \tilde{f} u_e^n, \tag{C4}$$

where

$$\tilde{H}_e^{n+1} = \frac{(\rho A H)_e^{n+1}}{\tilde{a}_p}; \quad \tilde{A}_e = \frac{(\rho A^2)_e}{\tilde{a}_p}; \quad \tilde{b}_e = \frac{(\rho A b)_e}{\tilde{a}_p}; \quad \tilde{f} = \frac{(\rho A f)_e}{\tilde{a}_p}.$$

An equation as (C4) can be written for all six faces and substituted into the discretised continuity equation to yield the pressure equation at time step $n+1$

$$p_P^{n+1}\Sigma\tilde{A} = \Sigma(p^{n+1}\tilde{A}) - \mathrm{div}(\tilde{H}^{n+1}) - \mathrm{div}(\tilde{b}) - \mathrm{div}(\tilde{f}u^n), \tag{C5}$$

where Σ is a summation over the neighbours to p_P. The pressure equation at the first and second corrector level, respectively, takes the form

$$p_P^*\Sigma\tilde{A} = \Sigma(p^*\tilde{A}) - \mathrm{div}(\tilde{H}^*) - \mathrm{div}(\tilde{b}) - \mathrm{div}(\tilde{f}u^n) \tag{C6}$$

and

$$p_P^{**}\Sigma\tilde{A} = \Sigma(p^{**}\tilde{A}) - \mathrm{div}(\tilde{H}^{**}) - \mathrm{div}(\tilde{b}) - \mathrm{div}(\tilde{f}u^n). \tag{C7}$$

At the corrector levels a pressure equation, as eq. (5.13), based on an increment equation for the velocity, eq. (5.17), was used. Equation (C6) and (C7), respectively, is based on the actual velocity field and does not require additional information, as compared to eq. (5.13), but is only another way of writting the pressure equation. A pressure equation on the form as eq. (5.13) is to be preferred because of reduction in computer time and storage, Issa (1985), and the pressure equation written on the form as eq. (C5) is only used in estimating the error.

The error introduced at the predictor level can be taken as

$$(a_p + \frac{\rho\Delta V}{\Delta t})\epsilon_u^* = H(\epsilon_u^*) + A\delta_i(\epsilon_p^n), \tag{C8}$$

which is obtained by subtracting the momentum equation, attained at the predictor level, eq. (5.15), from the original momentum equation, eq. (5.14). The error of the pressure is

$$\epsilon_p^n = p^{n+1} - p^n \tag{C9}$$

and, based on a Taylor series expansion, the error is written

$$\epsilon_p^n = p^n + O(\Delta t) - p^n = O(\Delta t), \tag{C10}$$

which states that the error of the pressure ϵ_p^n in eq. (C8) is of first order. The first order accuracy in the pressure field does introduce second order accuracy in the velocity field, however. This is seen by dividing every term in eq. (C8) by Δt and then letting Δt approach infinity. ϵ_u^* will only vanish if ϵ_u^* is of second order accuracy in Δt

$$\epsilon_u^* = O(\Delta t^2). \tag{C11}$$

At the first corrector level, the error introduced in the momentum and pressure equations, respectively, can be written as

$$(a_p + \frac{\rho \Delta V}{\Delta t})\epsilon_u^{**} = H(\epsilon_u^*) + A\delta_i(\epsilon_p^*) \tag{C12}$$

and

$$\epsilon_p^* \Sigma \tilde{A} = \Sigma(\tilde{A}\epsilon_p^*) - \mathrm{div}(\tilde{H}(\epsilon_u^*)). \tag{C13}$$

Equation (C12) is found by subtraction of eq. (5.16) from eq. (5.14) and eq. (C13) is found by substraction of eq. (C6) from eq. (C5). From eq. (C13) it is seen that ϵ_p^* decays with the same order as ϵ_u^* and hence ϵ_p^* is of order $O(\Delta t^2)$ which gives third order accuracy of ϵ_u^{**} in eq. (C12).

For the second corrector level, the error on the momentum and pressure equations can be found by subtraction of eq. (5.19) from eq. (5.14) and subtraction of eq. (C7) from eq. (C5), respectively, which is written as

$$(a_p + \frac{\rho \Delta V}{\Delta t})\epsilon_u^{***} = H(\epsilon_u^{**}) + A\delta_i(\epsilon_p^{**}) \tag{C14}$$

and

$$\epsilon_p^{**}\Sigma\tilde{A} = \Sigma(\tilde{A}\epsilon_p^{**}) - \mathrm{div}(\tilde{H}(\epsilon_u^{**})). \qquad \text{(C15)}$$

It is seen that ϵ_u^{***} is $O(\Delta t^4)$ and ϵ_p^{**} is $O(\Delta t^3)$. More corrector steps will increase the accuracy, but usually two corrector steps are enough because the original equations are discretised to second order accuracy, Issa (1985). The values obtained for the velocity and pressure fields at the second corrector step are taken as the values at step n+1.